PB-220 242

EVALUATION OF A DIFFUSION MODEL FOR PHOTOCHEMICAL SMOG SIMULATION

GENERAL RESEARCH CORP.

PREPARED FOR
ENVIRONMENTAL PROTECTION AGENCY

OCTOBER 1972

Distributed By:
NTIS
National Technical Information Service
U. S. DEPARTMENT OF COMMERCE

PB 220 242

EPA-R4-73-012, Vol. a

CR-1-273

EVALUATION OF A DIFFUSION MODEL FOR PHOTOCHEMICAL SMOG SIMULATION

FINAL REPORT
Contract No. 68-02-0336

by
A. Q. Eschenroeder
J. R. Martinez
R. A. Nordsieck

October 1972

Prepared for
Environmental Protection Agency

GENERAL
RESEARCH CORPORATION
P.O. BOX 3587, SANTA BARBARA, CALIFORNIA 93105

Reproduced by
NATIONAL TECHNICAL
INFORMATION SERVICE
U S Department of Commerce
Springfield VA 22151

BIBLIOGRAPHIC DATA SHEET

1. Report No. EPA-R4-73-012, Vol. a

2.

3. Recipient's Accession No. PB-220 242

4. Title and Subtitle
Evaluation of a Diffusion Model for Photochemical Smog Simulation

5. Report Date October 1972

6.

7. Author(s)
A.Q. Eschenroeder, J.R. Martinez, R.A. Nordsieck

8. Performing Organization Rept. No. CR-1-273

9. Performing Organization Name and Address
General Research Corporation
P. O. Box 3587
Santa Barbara, California 93105

10. Project/Task/Work Unit No.

11. Contract/Grant No. 68-02-0336

12. Sponsoring Organization Name and Address
ENVIRONMENTAL PROTECTION AGENCY
Research Triangle Park, North Carolina 27711

13. Type of Report & Period Covered Final

14.

15. Supplementary Notes

16. Abstracts

Extensive improvements have characterized this evaluation of the GRC Photochemical/Diffusion model. Despite the limitations of smog chamber experimental data, they have served an essential purpose toward updating the kinetics portion of the model. Consistency of rates and reactivities is now achievable using recently measured coefficients for a wide variety of systems. Model methodology revisions have enhanced the realism of the advective and diffusive descriptions. Previous assumptions regarding transverse (cross-streamline) horizontal diffusion have been confirmed by an exhaustive series of parametric tests. Photochemical/diffusion validations were successful for trajectories occurring during four days of the 1969 smog season in Los Angeles. Our measure of success is concentration-history fidelity with a minimum of adjustments of diffusion parameters. (Chemical coefficients were scaled from the smog chamber studies and held fixed for the simulations carried out to date). Future directions for air pollution model development are discussed in detail in an appendix as information supporting the experimental recommendations.

17. Key Words and Document Analysis. 17a. Descriptors

Air pollution
Mathematical models
Photochemical reactions
Diffusion
Advection
Trajectories
Reaction kinetics
Smog
Chambers
Validity

17b. Identifiers/Open-Ended Terms

Diffusion models
Atmospheric modeling

17c. COSATI Field/Group 13B

18. Availability Statement
Unlimited

19. Security Class (This Report) UNCLASSIFIED

20. Security Class (This Page) UNCLASSIFIED

21. No. of Pages ~~230~~ 226

22. Price $6.75/0.95

EPA-R4-73-012, Vol. a

CR-1-273

EVALUATION OF A DIFFUSION MODEL FOR PHOTOCHEMICAL SMOG SIMULATION

Final Report

Contract No. 68-02-0336

A. Q. Eschenroeder
J. R. Martinez
R. A. Nordsieck

October 1972

Prepared for
Environmental Protection Agency

ia

ANSTRACT

Extensive improvements have characterized this evaluation of the GRC Photochemical/Diffusion model. Despite the limitations of smog chamber experimental data, they have served an essential purpose toward updating the kinetics portion of the model. Consistency of rates and reactivities is now achievable using recently measured coefficients for a wide variety of systems. Model methodology revisions have enhanced the realism of the advective and diffusive descriptions. Previous assumptions regarding transverse (cross-streamline) horizontal diffusion have been confirmed by an exhaustive series of parametric tests. Photochemical/diffusion validations were successful for trajectories occurring during four days of the 1969 smog season in Los Angeles. Our measure of success is concentration-history fidelity with a minimum of adjustments of diffusion parameters. (Chemical coefficients were scaled from the smog chamber studies and held fixed for the simulations carried out to date.) Future directions for air pollution model development are discussed in detail in an appendix as information supporting the experimental recommendations.

CONTENTS

SECTION		PAGE
	ABSTRACT	i
	OVERVIEW AND SUMMARY OF THE WORK	1
1	STRUCTURE OF THE REPORT	9
2	ANALYSIS OF CHEMICAL KINETICS IN SMOG CHAMBER EXPERIMENTS	11
	2.1 Introduction	11
	2.2 Chemical Mechanism	11
	2.3 Methodology of Adjustments and Evaluations	17
	2.4 Experimental Data Base	18
	2.5 Results of Smog Chamber Validations	20
	2.6 Adaptation of Chemical Model to Atmospheric Modeling	43
3	MODEL METHODOLOGY IMPROVEMENTS	51
	3.1 Perspectives on Model Updating	51
	3.2 Advective Air Trajectories	51
	3.3 Vertical and Horizontal Eddy Diffusion Coefficients	58
	3.4 Emission Flux Histories	65
4	TRANSVERSE DIFFUSION AND ITS EFFECT ON THE GRC MODEL	66
	4.1 Lateral Diffusion Between Neighboring Streamtubes	66
	4.2 Lateral Diffusion Effects in the Vicinity of High-Flux Elevated Point Sources	72
5	VALIDATION STUDIES	79
	5.1 Selection of Days for Model Tests	79
	5.2 Program Conversion	82

Preceding page blank

CONTENTS (Cont.)

SECTION		PAGE
	5.3 Atmospheric Validation Tests	84
	5.4 Techniques for Model Operation	148
	5.5 Sources of Uncertainty Due to Solar Radiation and Particulate Reactions	152
6	CONCLUDING REMARKS	162
APPENDIX A	A VIEW OF FUTURE PROBLEMS IN AIR POLLUTION MODELING	167
	REFERENCES	207

ILLUSTRATIONS

NO.		PAGE
2.1	Experiment 329, Propylene/NO_x. Plot of Propylene, NO, NO_2	23
2.2	Experiment 329, Propylene/NO_x. Plot of Ozone and PAN	24
2.3	Experiment 253, Toluene/n-Butane/NO_x. Plot of NO and NO_2	27
2.4	Experiment 253, Toluene/n-Butane/NO_x. Plot of Ozone and PAN	28
2.5	Experiment 253, Toluene/n-Butane/NO_x. Plot of Toluene and n-Butane	29
2.6	Experiment 251, Toluene/n-Butane/NO_x. Plot of NO and NO_2	30
2.7	Experiment 271, Toluene/NO_x. Plot of Toluene, NO, and NO_2	32
2.8	Experiment 271, Toluene/NO_x. Plot of Ozone and PAN	33
2.9	Experiment 231, Dilute Auto Exhaust (Controlled Vehicle). Plot of NO and NO_2	38
2.10	Experiment 231, Dilute Auto Exhaust (Vehicle with Emission Controls). Simulation of Reactive Hydrocarbon Decay	39
2.11	Experiment 222, Dilute Auto Exhaust (Uncontrolled Vehicle). Plot of NO and NO_2	41
2.12	Experiment 222, Dilute Auto Exhaust (Uncontrolled Vehicle). Plot of Ozone and PAN	42
2.13	Experiment 336. Dilution Model Compared with Measured Ethane Concentration	47
2.14	Experiment 336. Effect of Dilution on Propylene Concentration. (Curves Computed using a Single set of Rate Constants)	48
3.1	Air Trajectory in the Los Angeles Basin	53
3.2	Comparison of Ground Trajectory with Tetroon Trajectory	54
3.3	Comparison of Wind Speed Measurements at El Monte	56

ILLUSTRATIONS (Cont.)

NO.		PAGE
3.4	Comparison of Wind Direction Measurements at El Monte	57
3.5	Vertical Diffusivity Versus Wind Speed	60
3.6	Vertical Diffusivity Versus Vertical Temperature Gradient	61
3.7	Vertical Diffusivity Profiles	63
3.8	Lateral Separation of Simultaneously Released Tetroon Pairs as a Function of Time Since Release	65
4.1	CO Flux Histories on Two Neighboring Trajectories	67
4.2	Eddy Diffusivity Profile for Neighboring Streamtube Analysis	67
4.3	CO Concentration Histories on Right-Hand (Commerce) Trajectory	68
4.4	CO Concentration Histories on Left-Hand (Synthetic) Trajectory	68
4.5	Superposed CO Flux Histories for 24 Trajectories	69
4.6	Bounding CO Flux Histories for Parallel Trajectory Analysis	70
4.7	CO Concentration Histories for Worst-Case Parallel Trajectories	70
4.8	Superposed NO Flux Histories for 24 Trajectories	72
4.9	Eddy Diffusivity Profile for Elevated Point Source/Lateral Diffusion Analysis	73
4.10	Ground Concentration Effects of Elevated Point Sources: 10 kg/hr/km^2 Background Flux	75
4.11	Ground Concentration Effects of Elevated Point Sources: 15 kg/hr/km^2 Background Flux	76
4.12	Ground Concentration Effects of Elevated Point Sources: 20 kg/hr/km^2 Background Flux	77
5.1	Air Quality and Meteorological Monitoring Network in the Los Angeles Basin	86

ILLUSTRATIONS (Cont.)

NO. PAGE

5.2 Interpolated and Observed Ozone Concentration at a Monitoring Station in the West San Gabriel Valley on September 29, 1969 93

5.3 Interpolated and Observed Ozone Concentration at a Monitoring Station in the West San Gabriel Valley on November 4, 1969 94

5.4 Observed Versus Computed Carbon Monoxide Concentration 97

5.5 Observed Versus Computed Ozone Concentration 98

5.6 September 11, 1969 Trajectory Starting at Commerce at 0530 100

5.7 Trajectory No. 1--Computed and Observed CO Concentrations 101

5.8 Trajectory No. 1--Computed and Observed NO and NO_2 Concentrations 101

5.9 Trajectory No. 1--Computed and Observed Ozone Concentrations 101

5.10 September 11, 1969 Trajectory Starting at Commerce at 0630 102

5.11 Trajectory No. 2--Computed and Observed CO Concentrations 103

5.12 Trajectory No. 2--Computed and Observed NO and NO_2 Concentrations 103

5.13 Trajectory No. 2--Computed and Observed Ozone Concentrations 103

5.14 September 11, 1969 Trajectory Starting in Downtown Los Angeles at 0530 104

5.15 Trajectory No. 3--Computed and Observed CO Concentrations 105

5.16 Trajectory No. 3--Computed and Observed NO and NO_2 Concentrations

5.17 Trajectory No. 3--Computed and Observed Ozone Concentrations 105

5.18 September 11, 1969 Trajectory Starting in Downtown Los Angeles at 0630 106

5.19 Trajectory No. 4--Computed and Observed CO Concentration 107

ILLUSTRATIONS (Cont.)

NO.		PAGE
5.20	Trajectory No. 4--Computed and Observed NO and NO_2 Concentrations	107
5.21	Trajectory No. 4--Computed and Observed Ozone Concentrations	107
5.22	September 29, 1969 Trajectory Starting at Commerce at 0530	108
5.23	Trajectory No. 5--Computed and Observed CO Concentrations	109
5.24	Trajectory No. 5--Computed and Observed NO and NO_2 Concentrations	109
5.25	Trajectory No. 5--Computed and Observed Ozone Concentrations	109
5.26	September 29, 1969 Trajectory Starting at Commerce at 0630	110
5.27	Trajectory No. 6--Computed and Observed CO Concentrations	111
5.28	Trajectory No. 6--Computed and Observed NO and NO_2 Concentrations	111
5.29	Trajectory No. 6--Computed and Observed Ozone Concentrations	111
5.30	September 29, 1969 Trajectory Starting in Downtown Los Angeles at 0530	112
5.31	Trajectory No. 7--Computed and Observed CO Concentrations	113
5.32	Trajectory No. 7--Computed and Observed NO and NO_2 Concentrations	113
5.33	Trajecotry No. 7--Computed and Observed Ozone Concentrations	113
5.34	September 29, 1969 Trajectory Starting Near the Coast at 0230	114
5.35	Trajectory No. 8--Computed and Observed CO Concentrations	115
5.36	Trajectory No. 8--Computed and Observed NO and NO_2 Concentrations	115
5.37	Trajectory No. 8--Computed and Observed Ozone Concentrations	115
5.38	September 30, 1969 Trajectory Starting at Commerce at 0530	116

ILLUSTRATIONS (Cont.)

NO.		PAGE
5.39	Trajectory No. 9--Computed and Observed CO Concentrations	117
5.40	Trajectory No. 9--Computed and Observed NO and NO_2 Concentrations	117
5.41	Trajectory No. 9--Computed and Observed Ozone Concentrations	117
5.42	September 30, 1969 Trajectory Starting at Commerce at 0630	118
5.43	Trajectory No. 10--Computed and Observed CO Concentrations	119
5.44	Trajectory No. 10--Computed and Observed NO and NO_2 Concentrations	119
5.45	Trajectory No. 10--Computed and Observed Ozone Concentrations	119
5.46	September 30, 1969 Trajectory Starting in Downtown Los Angeles at 0430	120
5.47	Trajectory No. 11-Computed and Observed CO Concentrations	121
5.48	Trajectory No. 11--Computed and Observed NO and NO_2 Concentrations	121
5.49	Trajectory No. 11--Computed and Observed Ozone Concentrations	121
5.50	September 30, 1969 Trajectory Starting in Downtown Los Angeles at 0530	122
5.51	Trajectory No. 12--Computed and Observed CO Concentrations	123
5.52	Trajectory No. 12--Computed and Observed NO and NO_2 Concentrations	123
5.53	Trajectory No. 12--Computed and Observed Ozone Concentrations	123
5.54	October 29, 1969 Trajectory Starting in Downtown Los Angeles at 0530	124
5.55	Trajectory No. 13--Computed and Observed CO Concentrations	125
5.56	Trajectory No. 13--Computed and Observed NO and NO_2 Concentrations	125

ILLUSTRATIONS (Cont.)

NO.		PAGE
5.57	Trajectory No. 13--Computed and Observed Ozone Concentrations	125
5.58	October 29, 1969 Trajectory Starting at 0630 in Downtown Los Angeles	126
5.59	Trajectory No. 14--Computed and Observed CO Concentrations	127
5.60	Trajectory No. 14--Computed and Observed NO and NO_2 Concentrations	127
5.61	Trajectory No. 14--Computed and Observed Ozone Concentrations	127
5.62	October 29, 1969 Trajectory Starting at Commerce at 0630	128
5.63	Trajectory No. 15--Computed and Observed CO Concentrations	129
5.64	Trajectory No. 15--Computed and Observed NO and NO_2 Concentrations	129
5.65	Trajectory No. 15--Computed and Observed Ozone Concentrations	129
5.66	October 29, 1969 Trajectory Starting at El Monte at 0830	130
5.67	Trajectory No. 16--Computed and Observed CO Concentrations	131
5.68	Trajectory No. 16--Computed and Observed NO and NO_2 Concentrations	131
5.69	Trajectory No. 16--Computed and Observed Ozone Concentrations	131
5.70	October 30, 1969 Trajectory Starting at Pasadena at 0	132
5.71	Trajectory No. 17--Computed and Observed CO Concentrations	133
5.72	Trajectory No. 17--Computed and Observed NO and NO_2 Concentrations	133
5.73	Trajectory No. 17--Computed and Observed Ozone Concentrations	133
5.74	October 30, 1969 Trajectory Starting at Commerce at 0630	134
5.75	Trajectory No. 18--Computed and Observed CO Concentrations	135
5.76	Trajectory No. 18--Computed and Observed NO and NO_2 Concentrations	135

ILLUSTRATIONS (Cont.)

NO. PAGE

5.77 Trajectory No. 18--Computed and Observed Ozone Concentrations 135

5.78 October 30, 1969 Trajectory Starting at El Monte at 0630 136

5.79 Trajectory No. 19--Computed and Observed CO Concentrations 137

5.80 Trajectory No. 19--Computed and Observed NO and NO_2 Concentrations 137

5.81 Trajectory No. 19--Computed and Observed Ozone Concentrations 137

5.82 October 30, 1969 Trajectory Starting in Downtown Los Angeles at 0830 138

5.83 Trajectory No. 20--Computed and Observed CO Concentrations 139

5.84 Trajectory No. 20--Computed and Observed NO and NO_2 Concentrations 139

5.85 Trajectory No. 20--Computed and Observed Ozone Concentrations 139

5.86 November 4, 1969 Trajectory Starting at Commerce at 0530 140

5.87 Trajectory No. 21--Computed and Observed CO Concentrations 141

5.88 Trajectory No. 21--Computed and Observed NO and NO_2 Concentrations 141

5.89 Trajectory No. 21--Computed and Observed Ozone Concentrations 141

5.90 November 4, 1969 Trajectory Starting at Commerce at 0630 142

5.91 Trajectory 22-Computed and Observed CO Concentrations 143

5.92 Trajectory No. 22--Computed and Observed NO and NO_2 Concentrations 143

5.93 Trajectory No. 22--Computed and Observed Ozone Concentrations 143

5.94 November 4, 1969 Trajectory Starting in Pasadena at 0530 144

5.95 Trajectory No. 23--Computed and Observed CO Concentrations 145

ILLUSTRATIONS (Cont.)

NO.		PAGE
5.96	Trajectory No. 23--Computed and Observed NO_2 Concentrations	145
5.96	Trajectory No. 23--Computed and Observed NO and NO_2 Concentrations	145
5.97	Trajectory No. 23--Computed and Observed Ozone Concentrations	145
5.98	November 4, 1969 Trajectory Starting in Downtown Los Angeles at 0530	146
5.99	Trajectory No. 24--Computed and Observed CO Concentrations	147
5.100	Trajectory No. 24--Computed and Observed NO and NO_2 Concentrations	147
5.101	Trajectory No. 24--Computed and Observed Ozone Concentrations	147
5.102	NO_2 Photolysis Rate Constant, k_1, for September 11, 1969	154
5.103	NO_2 Photolysis Rate Constant, k_1, for September 29, 1969	155
5.104	NO_2 Photolysis Rate Constant, k_1, for September 30, 1969	156
5.105	NO_2 Photolysis Rate Constant, k_1, for October 29, 1969	157
5.106	NO_2 Photolysis Rate Constant, k_1, for October 30, 1969	158
5.107	NO_2 Photolysis Rate Constant, k_1, for November 4, 1969	159
A.1	($NO + NO_2$) - Concentration Ground Level Huntington Park	170
A.2	CO/NO_x Ratios for Huntington Park 1968	171
A.3a	Chemiluminescent Measurements in New York - 1970	184
A.3b	Chemiluminescent Measurements in New York - 1970	184
A.4	Quasiequilibrium Test for 1969 Ground Data at El Monte--High NO Levels	187
A.5	Ozone Inaccuracies Needed to Explain the Departures from Quasiequilibrium in Fig. A.4	188

ILLUSTRATIONS (Cont.)

NO.		PAGE
A.6	Quasiequilibrium in a Simulated Smog Chamber Experiment	189
A.7	LAPS Coordinate System	197
A.8	Cross Section of Depressed Six-Lane Freeway	199
A.9	Wind-Oriented Coordinate System	199
A.10	CO Concentration Profiles Normal to Roadway at Various Wind Aspect Angles	200
A.11	Ozone and Nitric Oxide in an Air Mass Moving Over a Roadway	200

TABLES

NO. PAGE

2.1 Basic Kinetic Model 16

2.2 Experimental Data 19

2.3 Rate Constants Used in Propylene Simulations 21

2.4 Rate Constants for Toluene/n-Butane Simulation 31

2.5 Rate Constants for Toluene Experiment 271 35

2.6 Initial Hydrocarbon Concentrations (PPM) for Auto Exhaust Experiments 36

2.7 Rate Constants Used in Simulation of Experiment 231, Dilute Exhaust from a Vehicle with Emission Control 40

2.8 Rate Constants Used for Simulating Experiment 222, Dilute Exhaust from a Vehicle Without Emission Control 44

2.9 Mole-Weighted Reactivity of Atmospheric and Smog Chamber Hydrocarbon Mixtures 49

4.1 "Worst Case" Bounding Error Fractions Due to Omission of Lateral Diffusion in Urban Modeling Assuming Zero Initial Concentration of Carbon Monoxide 71

4.2 "Worst Case" Bounding Error Fractions Due to Omission of Lateral Diffusion in Urban Modeling, Assuming an Initial Concentration of Carbon Monoxide of 10 ppm 71

4.3 Maximum Fractional Contribution of an Elevated Point Source at a Ground Location Two Miles from the Plume Centerline 78

5.1 Directory of Air Quality and Meteorological Monitoring Stations in the Los Angeles Basin 87

5.2 Trajectory Identification Table 89

5.3 Initial Concentrations Used in Atmospheric Simulations 90

PRECEDING PAGE BLANK

TABLES (Cont.)

NO.		PAGE
5.4	Correlation Coefficients for CO and Ozone	96
5.5	Regression Equations for CO and Ozone	99
5.6	Rate Constants Used in Atmospheric Modeling Studies	149
A.1	Concentrations (ppm) and Gas Phase Rate Constant Assumed for Comparative Analysis	178
A.2	Upper Limit of (Surface Rate/Gas Phase Rate) Ratio	180
A.3	Ford/New York Data (First 20 Minutes)	185
A.4	Air Quality Effects for 1974 Trajectory	195

OVERVIEW AND SUMMARY OF THE WORK

For the past several years, General Research Corporation (GRC) has been developing and refining a photochemical/diffusion model for the US Environmental Protection Agency (EPA) and its predecessor agency. The application of this model is the prediction of air quality in terms of pollutant emission patterns and meteorological features of a particular airshed. Tracing from our first steps down to now, the efforts have balanced the emphasis between fidelity in the air chemistry and realism in the fluid dynamic transport. Unlike earlier static models based on superposition of plumes, ours is based on time-dependent processes. Therefore, one significant improvement has been treatment of unsteady diffusion and another has been the finite-difference formulation to allow for atmospheric transformation processes.

The work described in this report combines another round of model improvements with a controlled evaluation first of chemistry alone, and finally chemistry combined with diffusion. The evaluation has been done in parallel with two other contractors, Pacific Environmental Services and Systems Applications, Inc., who are pursuing similar tests on their models, each of which is somewhat different from ours. It should be emphasized that these evaluation studies are carried out in parallel with the only interaction between contractors being an exchange of monthly progress letters and occasional informal meetings.

Before summarizing our findings in a point-by-point narrative, it is helpful to digress here and review briefly just what the GRC photochemical/diffusion model does and how. We take an initial state for an airshed to be the spatial distributions of the concentrations of pollutants of interest; e.g., the parts per million of carbon monoxide, ozone, hydrocarbon, nitrogen dioxide, and nitric oxide. We must also specify the boundary conditions that control how the system evolves from its initial state. Strictly speaking, the boundary conditions are limited to temporal and spatial emission source distributions of the various pollutants just named. In an indirect fashion, the kinematics of airflow including both advection and diffusion are the fundamental boundary conditions for our model, since we follow an air mass-center as it is guided by the winds from place to place around the air basin. Where it goes will influence what pollutant emissions it receives.

We also trace the upward spread of pollutants in the air mass as they are introduced at the ground by emission sources. The ongoing chemical changes are simultaneously calculated. By stratifying the air vertically in the computation, we determine pollutant concentration as a function of height so that our output takes the form of concentration profiles in the air mass as functions of time-from-initial-state (or, equivalently, location in the air basin). To generate concentrations on a horizontal grid, we need to compute many air mass trajectories and to interpolate concentrations at prescribed time intervals.

Returning to the summary of the present evaluation study, let us now examine the findings of the chemical calculations. The approach is to formulate a functional list of reactions that describe phenomenologically the main observable species in a laboratory smog chamber experiment. With an eye toward atmospheric application, we work to minimize the computing load by collapsing some of the reaction chains into a single rate-controlling step with overall stoichiometry specified. Similarly, parallel reactions involving analogous members of an organic species family are lumped into a single composite step that involves a single class of generic reactants, a composite rate constant, and a single class of generic products. Our adopted ground rules required:

1. Initial determination of chain stoichiometry (which thereafter is held fixed),
2. Maintenance of reported rate constants within their measured intervals (except where reasons exist to believe otherwise), and
3. Adjustment of a minimum number of the unknown rate constants.

Following this procedure, we obtained simplified mechanisms for fourteen chemical systems (dilute hydrocarbon/nitric oxide mixtures in air) undergoing photooxidation in smog chamber experiments. A single prototype reaction mechanism involving twelve species and sixteen reaction steps was used for all systems. Different hydrocarbons were characterized by different rate constants in the hydrocarbon oxidation reactions. The ratios of rate constants followed ratios of the hydrocarbon reactivity reported elsewhere. This confirmed our earlier practice of scaling laboratory systems to the atmosphere according to these ratios.

In evaluating the photochemical kinetic model, we had to compensate for certain aspects that are peculiar to the smog chamber. Surface-to-volume ratios are much higher in the laboratory than in the atmosphere and an appropriate reaction chain has to be included beginning with ozone reacting with nitrogen dioxide and ending with nitric acid on the chamber wall. Another artificial feature of the smog chamber is the dilution of the reaction sample by removal of sizable samples for analysis and replacement with "clean" air. In certain cases, this correction became so large as to obscure the effects of some reactions; therefore, it is our recommendation that all future smog chamber work utilize in situ measurements. (The use of long-path infrared cells for many smog studies in the past has demonstrated the feasibility of in situ measurements.)

A striking example of the need for gas-solid reactions is found in the analysis of dilute automobile exhaust in the smog chamber results. Despite its small surface area compared with that of the walls, the fine suspended particulate matter in the exhaust forced the addition of an (NO_2 + particles)-reaction in order to account for nitrogen loss from the pollutant fraction in the gas phase. This was not necessary for the synthetic hydrocarbon/NO_x mixture experiments that were essentially free of particulate material.

Moving from laboratory experiments to polluted atmospheres, we added several improvements and carried out further cross-checks on the

GRC photochemical diffusion model that was briefly outlined above. In preparation for the eventual coding of the air trajectory calculation, we established the logic for objective determination of advection paths of air mass-centers. Certain intrinsic weaknesses in the data and in the use of ground winds suggest that high degrees of refinement are unwarranted. Very poor agreement was found between wind directions and wind speeds measured at two stations set up in the same area. Likewise, very poor agreement was noted between a computed ground track using station data and the measured trajectory of a tetroon* flying with the wind at a few hundred meters altitude.

In the past, our vertical eddy diffusivity values were based on wind speed, but a more detailed analysis of the data showed that vertical temperature gradient was better than wind speed or Richardson number for correlating measured diffusivities. Based on these findings, we adopted five vertical profiles of eddy diffusivity, each characterized by a range of vertical temperature gradients. Subsequent diffusion calculations for nonreactive species required some downward adjustments of the diffusivity values; however, they were still within the range of observational uncertainty. Horizontal diffusivities were obtained from radar measurements of tetroons as reported in the literature.

The pollution source program was updated by further automating the generation of emission fluxes and by introducing the new numbers provided by Systems Applications, Inc. The bearings and speeds for one-hour trajectory segments are fed into this auxiliary program. Given a geographical and temporal starting point, the program generates a data deck that supplies boundary conditions for the photochemical/diffusion model. Most of the numerous revisions given to us were incorporated in the pollutant emissions calculations.

A three-dimensional (vertical displacement, transverse displacement, and streamwise displacement) time-dependent diffusion code was used to assess the importance of neglecting transverse horizontal diffusion in the photochemical/diffusion model. The 3-D code's coordinate frame follows the air, but Gaussian spread lateral to the air motion is considered, for each time step as well as vertical diffusion using flux/gradient relationships. Air parcels moving parallel to one another were assumed to pass over emission fluxes differing widely from one another. For the worst case, errors between 27% and 39% were noted for CO-increments over a five-hour period; however, the errors in CO-concentration after five hours would scale down to only 10% to 20% because of the addition of initial concentrations (usually 5 to 10 ppm) for high air pollution conditions. Another assessment of horizontal spread was made for an air mass-center passing, at closest approach, one grid distance* away from a stack emitting oxides of nitrogen. A trajectory model would omit the subsequent spread of the plume that, in reality, would raise ground concentration somewhere downwind. Calculations showed that moderate values of stack emission and distributed ground-based source emissions give a maximum error of 5% due to omission of the stack plume contribution.

---

*A neutral bouyancy balloon that floats with the air along levels approximating constant ambient density.

The heart of our evaluation study is a series of tests of the simulation model against real-world air quality measurements. If there is any return on our investment in development and refinement efforts, it must show up as successful predictions of contaminant concentrations in the atmosphere. Extensive groundwork in chemical and meteorological improvement has been summarized above. Our test design will now be outlined and the results will be summarized.

Six days in the 1969 Los Angeles smog season (September-November) were designated for the data base. In addition to having two instrumental trailers in operation measuring detailed aerometric data, on those six days airborne studies were conducted yielding numerous detailed temperature profiles. The profiles are needed to obtain the vertical eddy diffusivity of pollutants. Ordinarily, only one or two soundings are available each day from instrumented balloons which telemeter information back to a station.

---

*"Grid distance" refers to the cell size that specifies the spatial resolution of the emission-source inputs to the model. At the present time, this distance is 2 miles.

Three of the days are designated "hands-off" days and the other three, "hands-on" days. The intent of the test design is to adjust parameters and to develop a set of operating rules for optimal model performance based on "hands-on" data. Then the test proceeds without any further model manipulation for the "hands-off" days to see how well the predictions are made. Each test of the model involves taking measured initial contaminant levels early in the morning (0230 to 0830 for our tests) and computing the concentration histories through the morning and early afternoon hours to exercise both the photochemical and meteorological parts of the model. For "hands-on" operation, the diffusional parts of the model are examined in the absence of chemistry by checking against carbon monoxide measurements. This has the combined advantage of being a nearly-inert tracer and of being essentially all derived from widely distributed (vehicular) sources.

Normalizing the diffusional parts of the simulation against carbon monoxide highlights the chemical aspects in subsequent exercises of the full model. For example, the peaking of nitric oxide levels during the morning commute-rush reflects first, the inability of the air to dilute the material; and later, the effects of dispersion and transformation to nitrogen dioxide that combine to cause a decay as they overcome the weakening emission sources as cars leave the road. Without the advance tests of diffusion, the interpretation of the nitric oxide tests would be ambiguous, at least, because of uncertainties in meteorological dispersion superimposed on uncertainties in chemistry.

Despite these seemingly difficult obstacles that must be overcome, the test results were consistently more accurate than were the exercises of previous versions of the model. The report presents the detailed data, but the general findings are as follows:

1. The chemistry we used to model smog chamber experiments is applicable to the atmosphere if the hydrocarbon rate constants are appropriately chosen[*] and the (NO_2 + particulate)-rate is decreased.

2. The diffusion in the vertical is described well by using a set of profiles determined directly from inert gas dispersion data found in the literature providing that diffusivity profiles for stable atmospheric conditions are uniformly decreased by factors of two or three. This degree of uncertainty is not unusual for vertical diffusivities.

3. The source emission inputs give results consistent with the materials balances observed in the atmosphere with the conspicuous exception of nitric oxide. Its fluxes had to be reduced by 75% (as in tests of previous versions of the model[1]) in order to achieve observed loadings of NO + NO_2. Carbon monoxide (and previously hydrocarbon[1]) require no adjustment. No physical mechanisms have been specifically identified to explain this deficit; however, surface uptake of NO appears to be a strong possibility that must be investigated in future field programs.

4. Curves of individual species fit the interpolated measurements[**] rather well during the peaking phases; however, both

---

[*] Automobile exhaust runs in the smog chamber were modeled by stratifying all the reactive hydrocarbons into two groups based on speed of oxidation rate. Good atmospheric results were obtained using rates derived for the slower of the two groups of hydrocarbon.

[**] Since the air parcel trajectories generally cut between monitoring stations rather than going right over them, we must use some inverse-distance-weighted averages to interpolate among the station measurements.

carbon monoxide and nitrogen dioxide are overpredicted at the ends of trajectories where their levels are relatively low. Inadequate accounting for the mixing is likely responsible for these discrepancies. Furthermore, in the case of nitrogen dioxide, heterogeneities can cause large errors since the chemistry in the model is treated homogeneously.

5. Ozone, one of the main pollutants, is relatively well predicted in its time-phasing for net production and its level. This success is especially fortunate because ozone is the subject of much control planning activity and is a very sensitive indicator of validity for photochemical models.

In an appendix to the report, we indicate two areas where future research is needed to build confidence in applying photochemical smog models. One deals with gas-solid interactions and the other, with the interference of finite mixing rates with the reaction kinetics. Gas-solid interactions include aerosol reactions and adsorption to urban surfaces. These processes may well be responsible for the difficulty in achieving a nitrogen balance in morning air samples. Surface uptake of pollutants will assume growing importance in the analysis of large-scale urban/rural air pollution. The turbulence interference phenomenon occurs when chemistry proceeds rapidly compared with mixing. Experimental evidence is analyzed to demonstrate that the magnitude of this effect could lead to significant modeling errors. Both of these new problem areas must receive more attention in field studies before the modeling methods can be further advanced to deal with them.

1 STRUCTURE OF THE REPORT

This report describes the rationale behind and the evaluation of various advances in the existing GRC photochemical/diffusion model. The model's objectives and methodology have been discussed in detail in the preceding Overview and Summary; therefore, we will emphasize the near-term goals and activities without repeating the background discussions.

Briefly, our immediate purposes are, first, to make changes that should improve the chemistry and physics used in the GRC photochemical/diffusion model and, second, to subject the updated model to controlled evaluations using measured data. A subsidiary objective is to convert the program to an IBM system and create manuals to afford US Environmental Protection Agency (EPA) personnel the opportunity to operate the model. Improving the model's physical and chemical content necessitates some refinement and some innovation. Refinements in source inventories are available from other recent work in the field.

A brief preview of the remaining sections in this document is given below.

Section 2. Chemical kinetic improvements are introduced in three ways: (1) updating input values to incorporate newly measured rate constants, (2) adding or deleting reactions based on recent findings, and (3) exercising the kinetics submodel for smog chamber conditions over a wider span of systems and mixture ratios than that used previously.

Section 3. The meteorological innovations are based on better choices of diffusion coefficients and systematized (but still manual) wind field analysis.

Section 4. The introduction of chemical and meteorological improvements is followed by controlled evaluations of modeling assumptions adopted previously, i.e., the neglect of crosswind diffusion and the treatment of large point sources in the framework of a source model laid out on a two-mile grid. Of particular concern is the omission of plumes from off-trajectory point sources in inputs to the moving control volume. These plumes are left out if the mass center of the air parcel never actually transects the grid square containing the source. This plume error and lateral diffusion error from area source nonuniformities are assessed using the three dimensional LAPS code* developed at GRC.

Section 5. Model tests for six days were undertaken first for diffusion of CO and subsequently for major species undergoing diffusion combined with photochemistry. Although the objective was four six-hour trajectories per day, some modifications had to be incorporated in the form of tradeoffs between numbers and lengths of trajectories. (An auxiliary study of transportation control abatement strategies was performed using three of the trajectories. The results of this task are reported in a separate volume.)

---

*Appendix A, Sec. A.3.2.

2 ANALYSIS OF CHEMICAL KINETICS IN SMOG CHAMBER EXPERIMENTS

2.1 INTRODUCTION

The mathematical model of smog photochemistry described below is a lumped-parameter model which is a key element of a larger model of polluted atmospheres. In developing and validating such a chemical model, the following objectives have guided our approach:

1. Reproduction of the essential features of smog chamber experiments
2. Capability to simulate experiments using a variety of hydrocarbons and hydrocarbon/NO_x mixtures
3. Ease of adaptation to atmospheric modeling
4. Retaining physical plausibility by using rate constant values which are in agreement with experimental data
5. Maintaining computational simplicity by using lumped parameters
6. Explicit consideration of surface reaction effects that may be peculiar to smog chambers

In the following sections, we shall deal with the validation of the model using smog chamber data. First, we describe the kinetic model itself in some detail. The methodology used for validation is reported next. Then the smog chamber data and the results are described. Finally, we discuss criteria used in adapting the chemical model for simulating atmospheric chemistry.

2.2 CHEMICAL MECHANISM

2.2.1 Reaction Steps

The basic mechanism is composed of sixteen reactions. Some of the reactions are elementary and in some cases a set of elementary reactions has been reduced to a single step, hence the lumped-parameter nature of the model. The reactions included in the model are shown below.

Following the inorganic cycle

$$\left.\begin{array}{l} h\nu + NO_2 \rightarrow NO + O \\ \\ O + O_2 + M \rightarrow O_3 + M \end{array}\right\} \begin{array}{l} \text{implies}^{*} \\ h\nu + NO_2 \rightarrow NO + O_3 \end{array} \qquad (2.1)$$

$$NO + O_3 \rightarrow NO_2 + O_2 \qquad (2.2)$$

we have the hydrocarbon oxidation chain initiators

$$O + HC \rightarrow (b_1)RO_2 \qquad (2.3)$$

$$OH + HC \rightarrow (b_2)RO_2 \qquad (2.4)$$

$$O_3 + HC \rightarrow (b_3)RO_2 \qquad (2.5)$$

Reactions (2.3)-(2.5) are lumped reactions which represent the oxidation chains which have been postulated to occur.[2-6] HC denotes a generic hydrocarbon and RO_2 is an organic radical. The b's denote branching factors which account for the fact that the oxidation chain produces a multiplicity of radicals. In reaction (2.4) we have treated the radical attacking HC as OH because of its likely dominance.[7,8]

---

[*] Because the reaction $O + O_2 + M \rightarrow O_3 + M$ is known to be very fast, the two reactions shown in (2.1) can be combined into a single reaction whose net product is $NO + O_3$, i.e., $h\nu + NO_2 \rightarrow NO + O_3$. This is equivalent to assuming O-atom quasistationarity.

The conversion of NO to NO_2 occurs via the chain-carrying reaction

$$RO_2 + NO \rightarrow NO_2 + (y)OH \tag{2.6}$$

where (y) is a yield factor which represents that fraction of the conversion which returns OH to the system. The yield factor is less than one because all R's are not H .

Note that reactions (2.4) and (2.6) form essentially a closed loop early in the reaction and stability requirements call for $b_2 y < 1 + \alpha$, where α is a positive function of other rate constants and concentrations which is small compared to 1 at early times and gradually increases throughout the reaction. Imposition of this constraint prevents RO_2 runaway during the early part of the reaction.

Chain-termination steps consist of the lumped reaction

$$RO_2 + NO_2 \rightarrow PAN^* \tag{2.7}$$

and the elementary reactions

$$OH + NO \rightarrow HONO \tag{2.8}$$

$$OH + NO_2 \rightarrow HNO_3 \tag{2.9}$$

The photodissociation of HONO has been suggested as a possible source of OH-radical[7,8]

$$h\nu + HONO \rightarrow OH + NO \tag{2.10}$$

---

*PAN denotes peroxyacetylnitrate.

Formation of HONO is assisted by the reaction

$$NO + NO_2 + H_2O \rightarrow 2HONO \qquad (2.11)$$

which is likely to proceed in two steps

$$NO + NO_2 \rightarrow N_2O_3$$

$$N_2O_3 + H_2O \rightarrow 2HONO$$

as suggested by Altshuller and Bufalini.[4] The N_2O_3 reacts with H_2O so rapidly that the two reactions can be lumped into reaction (2.11). The late-time behavior of O_3 and NO_2 is best reproduced when the following reaction is included

$$NO_2 + O_3 \rightarrow NO_3 + O_2 \qquad (2.12)$$

Nitrogen imbalances in smog chambers have prompted various investigators to attempt to track down the fate of the nitrogen compounds. Gay and Bufalini[9] report that a large fraction of the nitrogen loss can be accounted for by nitrate formation on the walls of the chamber. Following their suggestions as well as those of Dodge,[10] the reactions shown below have been included in the mechanism.

$$NO_3 + NO_2 \rightarrow N_2O_5 \qquad (2.13)$$

$$N_2O_5 \rightarrow NO_3 + NO_2 \qquad (2.14)$$

$$N_2O_5 + H_2O \xrightarrow{\text{wall}} 2HNO_3 \qquad (2.15)$$

It should be noted that up to now no HNO_3 has been observed in the gas phase in smog chambers.[9] This prompted us to compare the relative efficiency of reactions (2.9) and (2.15). In our simulations, the result was that for 50% relative humidity reaction (2.15) is about six times faster than reaction (2.9), so one would expect to find significantly more HNO_3 on the walls of the chamber than in the gas phase. As a final comment, we note that the significance of reactions (2.13)-(2.15) for atmospheric modeling is not clear at this time.

Aerosol was observed in the chamber experiments with dilute auto exhaust. The disappearance of NO_x from the system differed significantly from that observed in the other experiments in which no aerosol was present. This prompted the suggestion by Dodge[11] that a first-order reaction of the form

$$NO_2 + \text{particulates} \rightarrow \text{products} \qquad (2.16)$$

be added to the system to account for the observed effects. Inclusion of this reaction has improved the simulation of the auto-exhaust experiments. Also, this reaction may be helpful in atmospheric modeling since aerosol is observed in the real world.

Previous versions of our kinetic model also contained the reaction

$$RO_2 + NO_3 \rightarrow PAN \qquad (2.17)$$

This reaction has been suggested by Hanst[12] as likely to be important in the formation of PAN. Such likelihood was supported by our earlier modeling work.[13] However, the increase of rate constants for reactions (2.4), (2.7) and (2.8) which was required by recently available measurements[7,14,15] caused reaction (2.17) to become unimportant in our model and thus it has been dropped.

Table 2.1 shows a list of all the reactions in our current kinetic model along with rate constants for which measurements exist. The rate constants obtained by repeated trials from the simulations are reported in the section on results of the adjustments and tests.

TABLE 2.1

BASIC KINETIC MODEL

	Reaction	Experimental Rate Constant Values†	Ref. No.
1.	$h\nu + NO_2 \rightarrow NO + O$	2.67(-1)min^{-1}	
1a.	$O + O_2 + M \rightarrow O_3 + M$	1.32(-5)ppm^{-2}min^{-1}	16
2.	$NO + O_3 \rightarrow NO_2 + O_2$	2.2(+1) to 4.4(+1)ppm^{-1}min^{-1}	17
3.	$O + HC \rightarrow (b_1)RO_2$	*	
4.	$OH + HC \rightarrow (b_2)RO_2$	*	
5.	$O_3 + HC \rightarrow (b_3)RO_2$	*	
6.	$RO_2 + NO \rightarrow NO_2 + (y)OH$		
7.	$RO_2 + NO_2 \rightarrow PAN$		
8.	$OH + NO \rightarrow HONO$	1.5(+3)ppm^{-1}min^{-1}	14
9.	$OH + NO_2 \rightarrow HNO_3$	3.0(+3)ppm^{-1}min^{-1}	15
10.	$h\nu + HONO \rightarrow OH + NO$		
11.	$NO + NO_2 \xrightarrow{H_2O} 2HONO$		
12.	$NO_2 + O_3 \rightarrow NO_3 + O_2$	5(-2) to 1.25(-1)ppm^{-1}min^{-1}	18
13.	$NO_3 + NO_2 \rightarrow N_2O_5$	4.5(+3)ppm^{-1}min^{-1}	19
14.	$N_2O_5 \rightarrow NO_3 + NO_2$	1.4(+1)min^{-1}	18
15.	$N_2O_5 + H_2O \rightarrow 2HNO_3$	2.5(-3)ppm^{-1}min^{-1}**	20
16.	NO_2 + particulates → products		

---

† The number in parentheses denotes the power of ten by which the coefficient must be multiplied, e.g., 2.67(-1) = 2.67 × 10^{-1} .

* Experimental values for these rate constants are often known for particular hydrocarbons and will be reported in Sec. 2.5.

** For the validation process, k_{15} was converted to a pseudo-first-order rate constant by lumping water vapor content of air at 50% relative humidity into k_{15} since the smog chamber experiments were conducted at this level of humidity. The resulting rate constant is 60.5 min^{-1}.

2.2.2 Quasistationarity Assumptions

Several of the species included in our kinetic model can be assumed to be in a quasistationary state with respect to the other species. Apart from the computational advantages of this assumption, quasistationarity can be justified on physical grounds by examining the relative rates of the various reactions involved. Such a check has revealed that it is likely that O-atom, RO_2 , OH , NO_3 , and N_2O_5 are in a quasistationary state. O-atom quasistationarity can be justified on the basis that the removal of O-atom by the reaction $O + O_2 + M \rightarrow O_3 + M$ is known to be very fast. We have tested quasistationarity assumptions for RO_2 , OH , NO_3 , and N_2O_5 by solving parallel cases with and without stationarity. The results of the tests showed that assuming stationarity has a negligible effect on the computed concentration of all the species. A similar test for HONO yielded negative results, thus HONO has been retained as an active species.

2.3 METHODOLOGY OF ADJUSTMENTS AND EVALUATIONS

Two kinds of adjustable parameters are available to us: rate constants and branching factors. However, the number of free parameters is limited by the fact that several elementary rate constants have been measured. Our approach is to keep the values of the measured rate constants within the range of experimental uncertainties. The unknown values of nonelementary, i.e., lumped, rate constants are then estimated from comparisons with analogous reactions, if they exist, and during the simulation process itself. Indeed, the object of the simulation is to determine the values of these unknown constants. In cases where rate-controlling processes can be identified, the rate constants are sometimes available. These are also confined to ranges of measurement wherever possible.

The branching factors of the model are determined by the NO and HC decay prior to the NO_2 peak and before the ozone buildup. The branching factor is estimated from

$$b_2 = \frac{d[NO]/dt}{d[HC]/dt} \qquad (2.18)$$

In Eq. (2.18), it is implied that most of the HC decay is due to the reaction $OH + HC \rightarrow (b_2)RO_2$. This is justified by virtue of the fact that reaction (2.3) is slow compared to (2.4) and that early in the reaction the ozone is essentially zero and thus (2.5) plays no role in HC decay. Since $NO \rightarrow NO_2$ conversion occurs via reaction (2.6), the relation shown in (2.18) can be used because RO_2 is in stationary state.

Thus, using the available data, we obtained linear least-squares fits of the NO and HC to estimate their respective decay rates. Then from Eq. (2.18), we estimated b_2 prior to any adjustment of rate constants. We then chose a value of b_2 from among the various values obtained for each experiment set. Subsequently, we set $b_1 = b_2$. The value of b_3 was obtained by modeling the late-time behavior of the system. Once set, the values of the branching factors remain constant throughout the simulation.

2.4 EXPERIMENTAL DATA BASE

Experiments on different mixtures of the following four systems in air were used in the validation process:

1. Propylene/NO_x
2. Toluene/n-Butane/NO_x
3. Toluene/NO_x
4. Dilute auto exhaust/NO_x

These four groups comprised a total of fourteen experiments which were used in testing the kinetic model. The number of experiments in each group was four, three, five, and two, respectively. Table 2.2 shows a detailed breakdown of the experimental data used in our simulations. The experiment numbers shown on the table are the same ones used by EPA in their laboratory procedures.

TABLE 2.2

EXPERIMENTAL DATA

Group	Exp. No.	Initial Concentrations, ppm			Average Fractional Dilution Rate ($\times 10^{-4}$ min^{-1})*
		NO	NO_2	HC	
Propylene	321	1.23	.09	.275	7.52
	325	.30	.04	.45	7.33
	329	.29	.01	.24	7.22
	336	1.14	.04	.61	7.03
Toluene/ n-Butane	251	1.11	.11	1.60/3.02	6.17
	253	.53	.11	1.43/3.42	6.22
	257	.27	.07	1.29/2.97	4.90
Toluene	250	1.17	.08	1.53	5.78
	258	.35	.04	2.88	4.88
	263	.54	.06	1.71	5.80
	271	.32	.04	1.20	6.05
	305	1.26	.06	3.14	5.76
Auto Exhaust	CUE 222**	1.94	.10	1.06/1.15†	5.65
	CE 231***	2.73	.23	.39/.20†	5.98

---

*To obtain average volumetric dilution rate multiply by the chamber volume (335 ft^3) (see Sec. 2.6.1 for a detailed discussion of dilution effects in smog chambers).

**Exhaust from a vehicle without exhaust hydrocarbon and CO emission controls.

***Exhaust from a vehicle with exhaust hydrocarbon and CO emission controls.

†The multiple hydrocarbon mixture has been aggregated into two classes: high and low reactivity hydrocarbon. The fraction shown here gives the ppm of each class in the order high-reactivity/low-reactivity.

2.5 RESULTS OF SMOG CHAMBER VALIDATIONS

In this section, we discuss the results of the validation tests which were performed on our chemical model. The goal of these validation tests was to simulate smog chamber experiments performed in EPA laboratories. The experimental data used for comparison with the model's results has been described in Sec. 2.4. The outcome of the tests is presented by means of graphs that are representative of the group of tests performed. In addition, a table of the rate constants used in the validation tests is presented for several experiments. Finally, the branching factors for the various simulations are also given.

2.5.1 Propylene Experiments

The simulation of the propylene experiments was carried out by varying a single rate constant within the framework of a basic set of parameters. Thus, after determining the branching factors and setting values for the other rate constants, it was sufficient to adjust k_4 (the OH attack on HC) to reproduce the experimental results obtained for the various propylene/NO_x mixtures. Two of the experiments (nos. 321 and 329) required $k_4 = 6 \times 10^4\ ppm^{-1}min^{-1}$. Experiments number 325 and 336 required $k_4 = 2 \times 10^4$ and $k_4 = 3 \times 10^4$, respectively. Table 2.3 shows the rate constants used in the four cases. The branching factors were determined to be $b_1 = b_2 = 4$ and $b_3 = 1$. The yield factor for OH in reaction (2.6) is set to 0.25. It should be noted that Stedman[7] measured the rate constant of the hydroxyl-propylene reaction and obtained $k_4 = 2.5 \times 10^4\ ppm^{-1}min^{-1}$. (If this experimental value of k_4 were used for all the simulations, the reaction would be slowed down in experiments 321, 329, and 336, and it would be speeded up in 325.) Thus, our model values for k_4 agree well with the measured quantity, which is a hundred times greater than a previous estimate of Westberg[4] of $k_4 = 244\ ppm^{-1}min^{-1}$. In our previous modeling work, we had lowered this estimate to $80\ ppm^{-1}min^{-1}$. To preserve the good agreement between data and simulation, we had to raise k_6 from $1500\ ppm^{-1}min^{-1}$ to 10^5, and k_7 from 6 to 600. (It will be recalled that k_8 was increased

TABLE 2.3

RATE CONSTANTS USED IN PROPYLENE SIMULATIONS

Reaction Number	Rate Constant*
1	2.67(-1)min^{-1}
1a	1.32(-5)ppm^{-2}min^{-1}
2	2.67(+1)
3	6.1(+3)**
4 (experiment 321 and 329)	6.0(+4)
4 (experiment 325)	2.0(+4)
4 (experiment 336)	3.0(+4)
5	9.27(-3)**
6	1.0(+5)
7	6.0(+2)
8	1.5(+3)
9	3.0(+3)
10	1.0(-3)min^{-1}
11	1.0(-4)
12	5.0(-3)
13	4.5(+3)
14	1.4(+1)min^{-1}
15	6.05(+1)min^{-1}
16	0 min^{-1}

---

*Units in ppm^{-1}min^{-1} unless otherwise specified.

**Measured rate constant from Ref. 2.

from 10 to 1500 and k_9 from 30 to 3000 in order to be consistent with experimental values.[14,15]) The success of this procedure is especially significant, since it shows that a workable set of rate constants is far from unique. However, this is not surprising in view of the highly nonlinear character of the system.

Referring to Tables 2.1 and 2.3, we note that $k_{12} = 5 \times 10^{-3}$ in Table 2.3 and this is a factor of 10 lower than the lower bound of the experimental value shown on Table 2.1. This had to be done in order not to impair greatly the late-time behavior of NO_2 and O_3. The same effect was encountered in modeling the other experiments with various types of hydrocarbons and HC/NO_x mixtures. In the present model, reaction (2.12), $NO_2 + O_3 \rightarrow NO_3 + O_2$, is rate-controlling late in the reaction. Furthermore, the computed concentrations of NO_2 and O_3 are very sensitive to small changes in k_{12}. Thus this parameter is very important and the availability of a very accurate value would be a boon for the modeler.

Figures 2.1 and 2.2 illustrate results obtained in the simulation of experiment 329. Note that the data are closely approximated by the model. The ozone plot shown in Fig. 2.2 exhibits lower concentrations than are indicated by the data late in the reaction. This discrepancy is due to dilution effects in the model and cannot be resolved by plausible adjustments in rate constants. Omission of dilution terms from the model results in ozone concentrations which provide a better fit to the data. However, omitting dilution terms also results in markedly poorer fits for the hydrocarbon and NO_2. Thus it seems that the inclusion of dilution both benefits and hinders the results. One possible explanation of this apparent paradox is that the continuous-dilution approximation used in the model is not accurate enough to simulate those cases where the dilution rate becomes large compared with the chemical rate. (See Sec. 2.6.1 for a detailed discussion of dilution effects in smog chambers.)

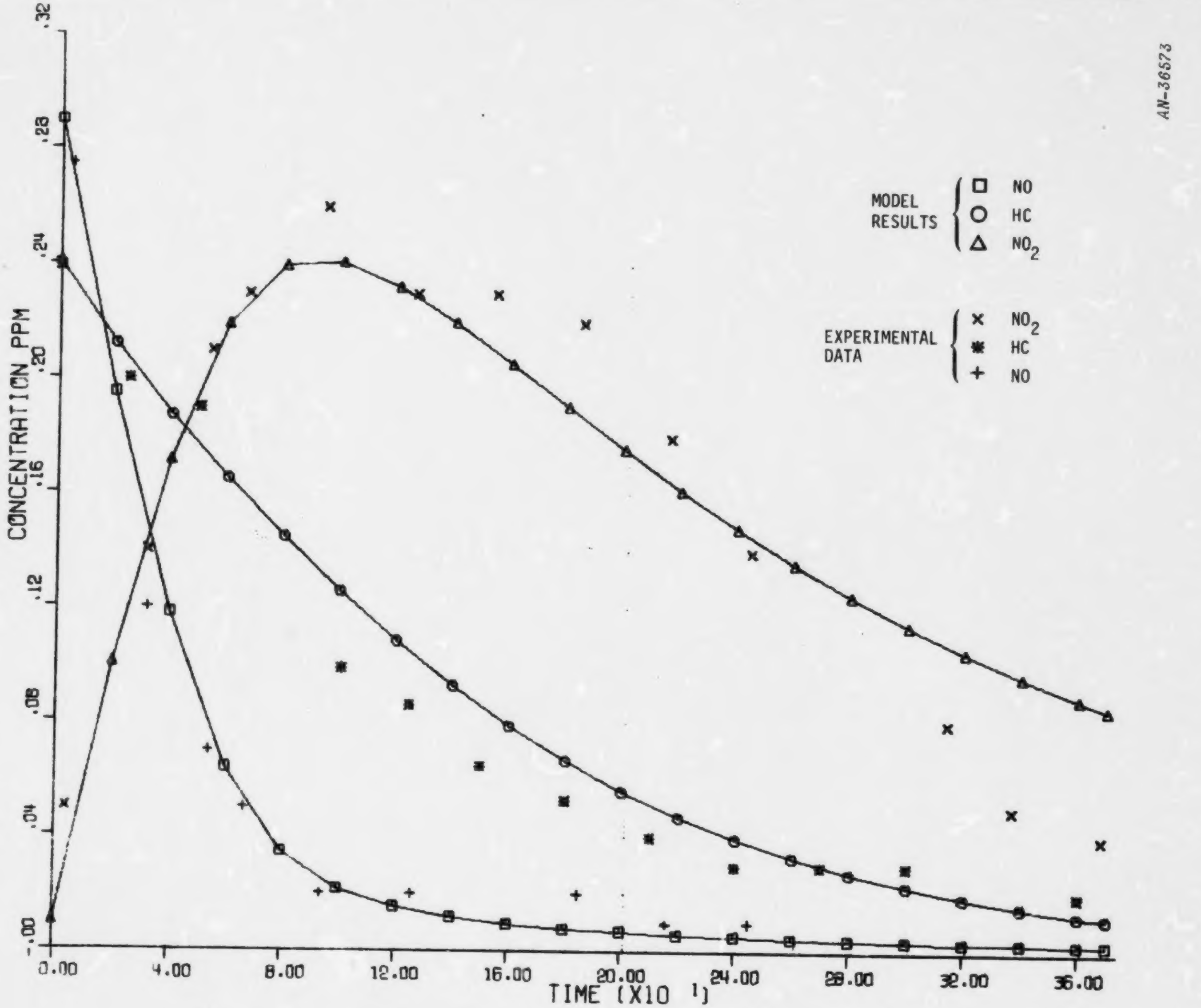

Figure 2.1. Experiment 329, Propylene/NO_x. Plot of Propylene, NO, NO_2

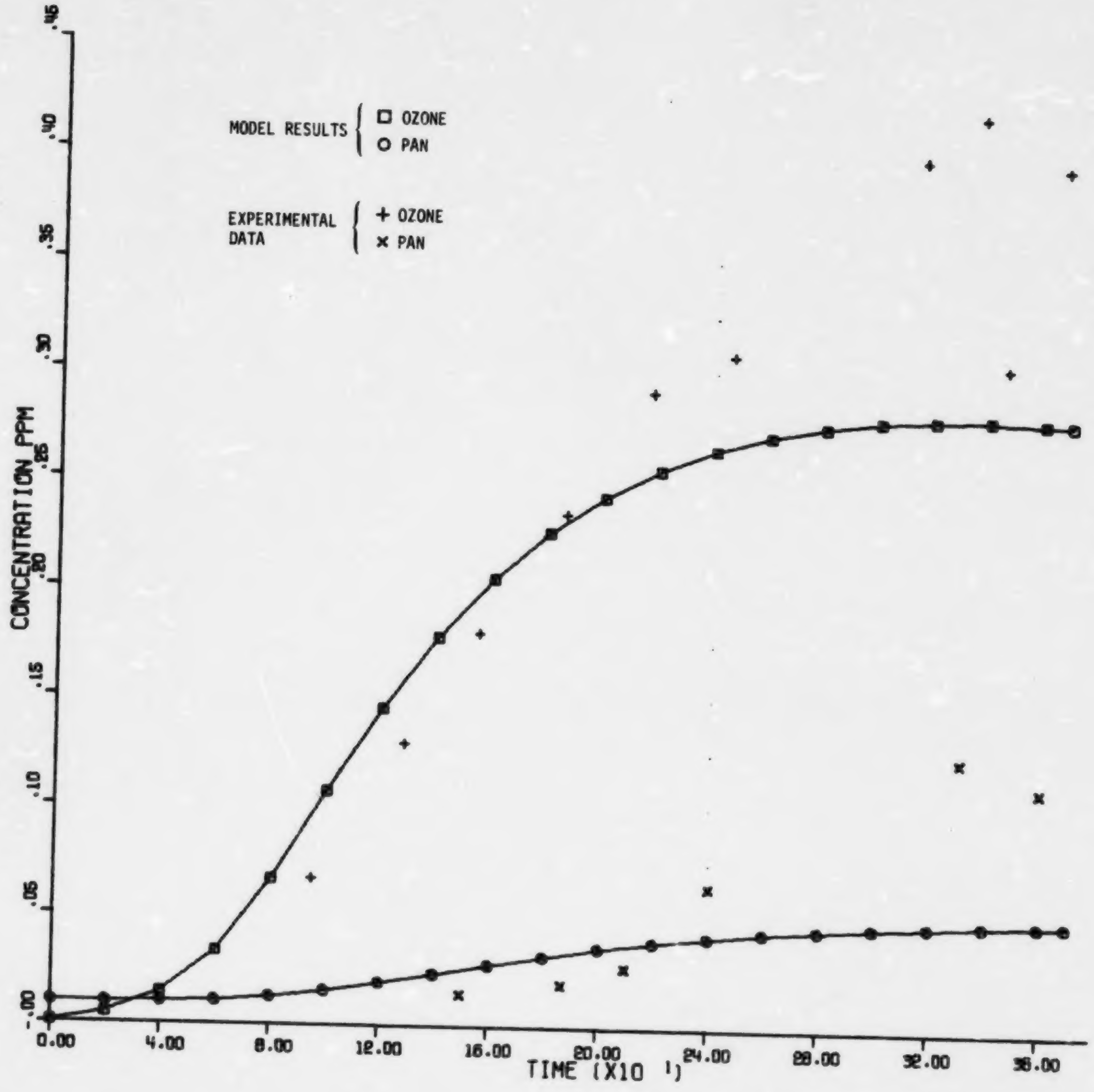

Figure 2.2. Experiment 329, Propylene/ NO_x. Plot of Ozone and PAN

2.5.2 Toluene/n-Butane Data

The simulations of this binary hydrocarbon mixture were very successful. Most remarkable is the fact that we were able to reproduce accurately all three experiments with a single set of parameters. This contrasts with the propylene tests where k_4 had to be varied. It should be noted that two sets of hydrocarbon reactions were used in these simulations.

Some remarks are in order about the rate constants for reactions (2.3)-(2.5). Published rate constant data were found for both toluene and n-butane only for reaction (2.3).[2,6] For reaction (2.4), a measured rate constant could be located[6,21] only for n-butane. The rate constant for toluene in reaction (2.4) was estimated from the literature value of k_4 for propylene using the relative reactivity of the two hydrocarbons. This initial estimate of k_4 was then adjusted until agreement between computed results and chamber data was obtained.

No literature data for toluene or n-butane ozonolysis was found. Nevertheless, the rate constants for the ozonolysis of these hydrocarbons are expected to be low, as indicated by the low values given for aromatics such as xylene. For example, Niki,[6] in a scale of relative rate constants (with propylene as unity), gives xylene ozonolysis an upper bound of 0.2 compared with relative rates ranging from 2 to 62 for the olefins. Reactivity scales are not useful for obtaining estimates for k_5 since hydrocarbon reactivity and k_5 do not correlate well for other than olefinic compounds, as has been pointed out by Niki, et al.[6] For purposes of the simulation, we chose some initial low value for the ozonolysis rate constant and subsequently adjusted it to obtain good agreement with chamber measurements. The resulting values remained low, 3×10^{-4} ppm^{-1}min^{-1} for toluene and 10^{-4} ppm^{-1}min^{-1} for n-butane. These values should be compared with 9.27×10^{-3} ppm^{-1}min^{-1} which is used for propylene.

Based on relative reactivity considerations, the OH + HC rate constants for toluene and n-butane were maintained at a 2:1 ratio with a rate constant for toluene of 2×10^4. Although this rate constant is higher than the one used in the pure toluene experiments, this result is not surprising inasmuch as we have synergistic effects to account for.

Figures 2.3-2.5 illustrate a simulation of experiment 253. We can see that NO_x, both hydrocarbons, and O_3 are reproduced very well indeed. In contrast with the pure toluene runs (see Fig. 2.8), the ozone buildup has both the correct time phasing and magnitude. Similar results were obtained for the other two experiments in the set. However, as shown in Fig. 2.6, the NO_2 buildup occurs late for experiment 251, although the shape of the curve is similar to that shown in the data.

Table 2.4 shows a list of the parameters used for these cases. The branching factors used are $b_1 = b_2 = 2$ and $b_3 = 1$. The yield factor for OH in reaction (2.6) was set to 0.5.

2.5.3 Toluene Experiments

The results of the simulations of the toluene experiments were fair. The main problem encountered was that too much ozone was produced in the simulation. Moreover, it seems that no plausible adjustments of the rate constants remedied the situation. The reproduction of toluene and NO histories was generally good, but the NO_2 tended to linger late in the reaction. Figures 2.7 and 2.8 illustrate one such simulation, in this case for experiment 271. Note that although the NO decay is well modeled, the simulated O_3 buildup is about 40 minutes too late. Since the interaction between NO and O_3 is so strong, efforts aimed at speeding up the O_3 buildup are bound to impair the modeling of NO and vice versa. Finally, typical OH + toluene rate constants used in these simulations were $10^4\ ppm^{-1}min^{-1}$. This compares with the range 2×10^4 to 6×10^4 used for propylene and with 2×10^4 used in the toluene/n-butane case.

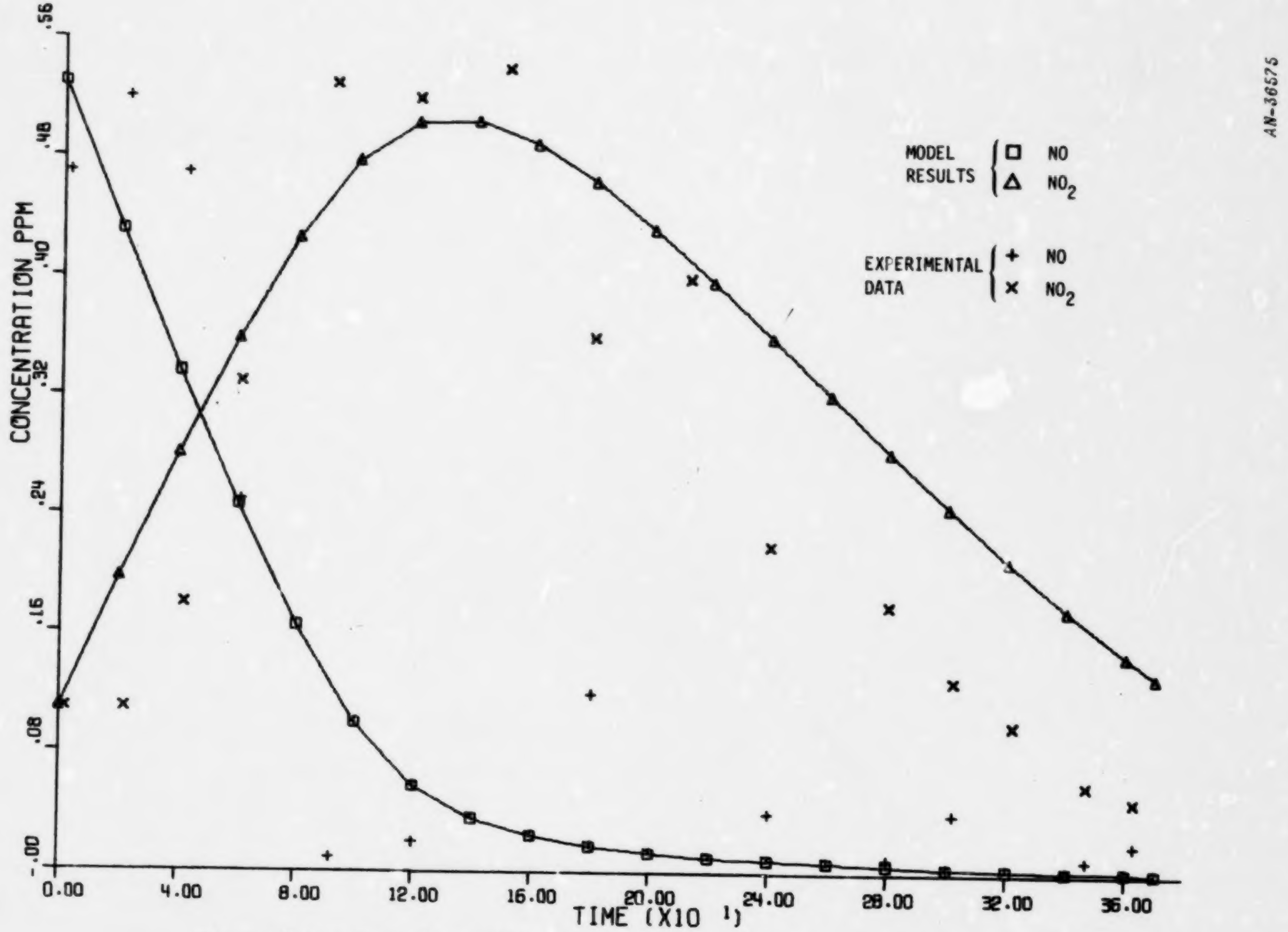

Figure 2.3. Experiment 253, Toluene/n-Butane/NO_x. Plot of NO and NO_2

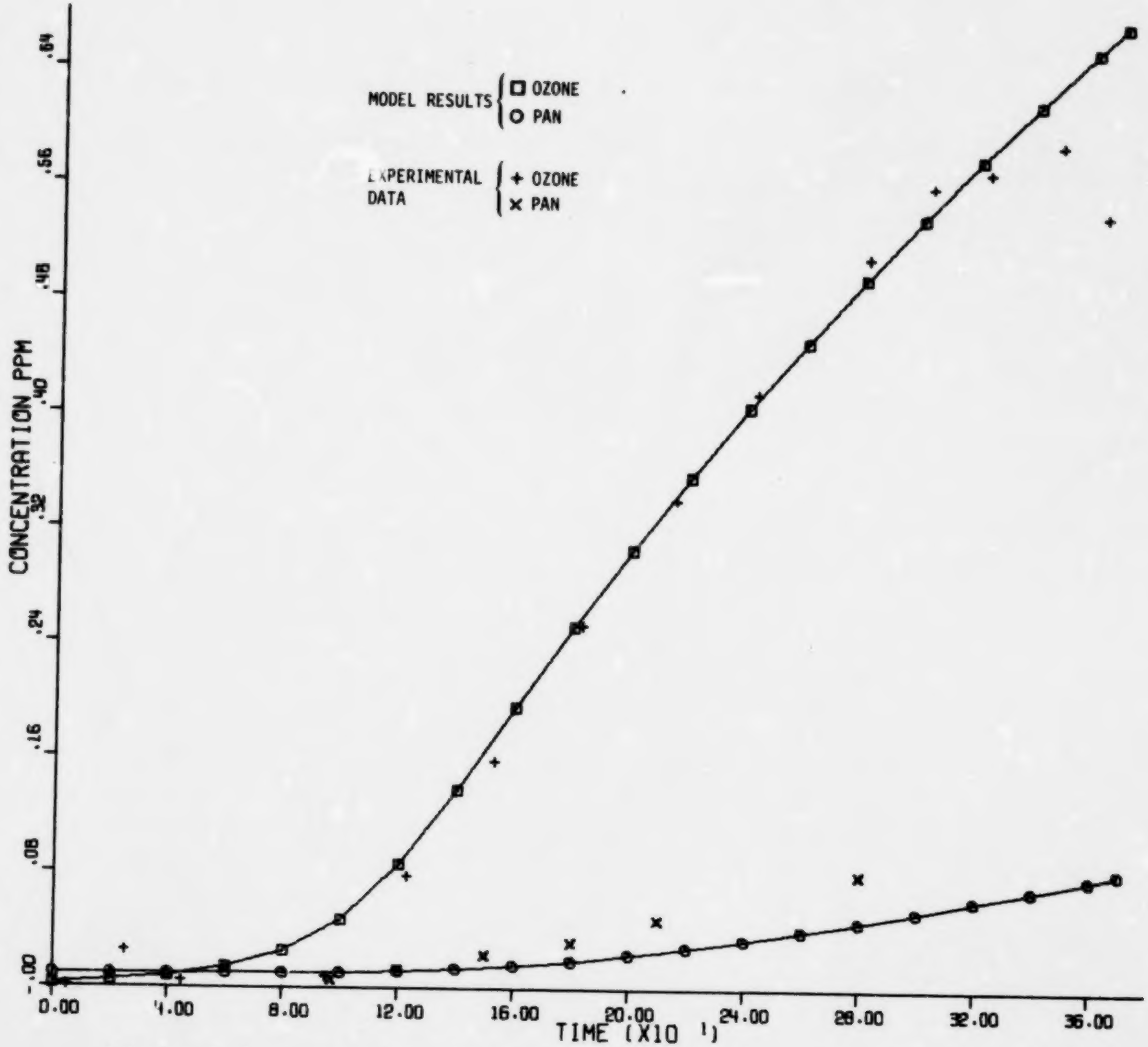

Figure 2.4. Experiment 253, Toluene/n-Butane/NO_x. Plot of Ozone and PAN

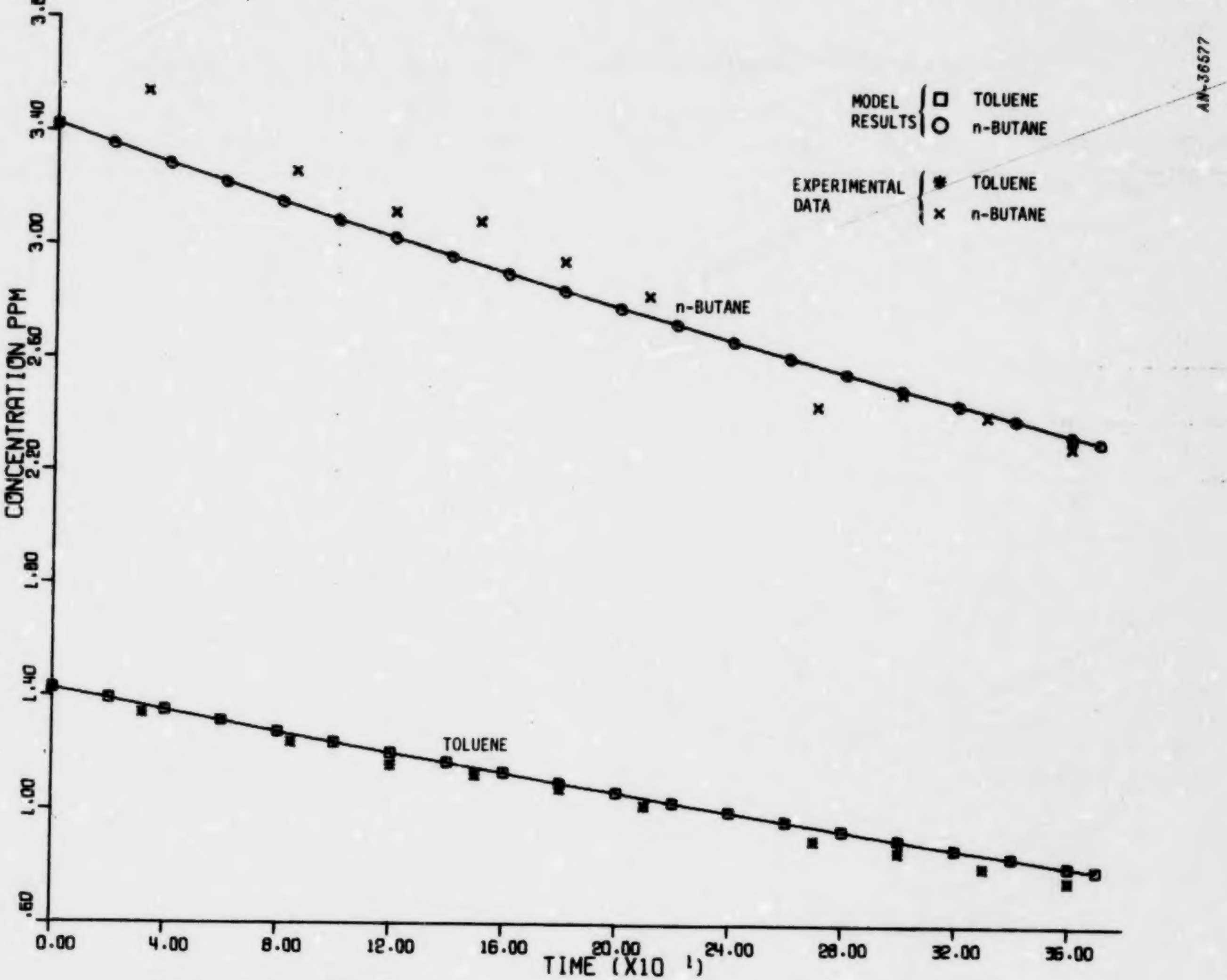

Figure 2.5. Experiment 253, Toluene/n-Butane/NO_x. Plot of Toluene and n-Butane

AN-36578

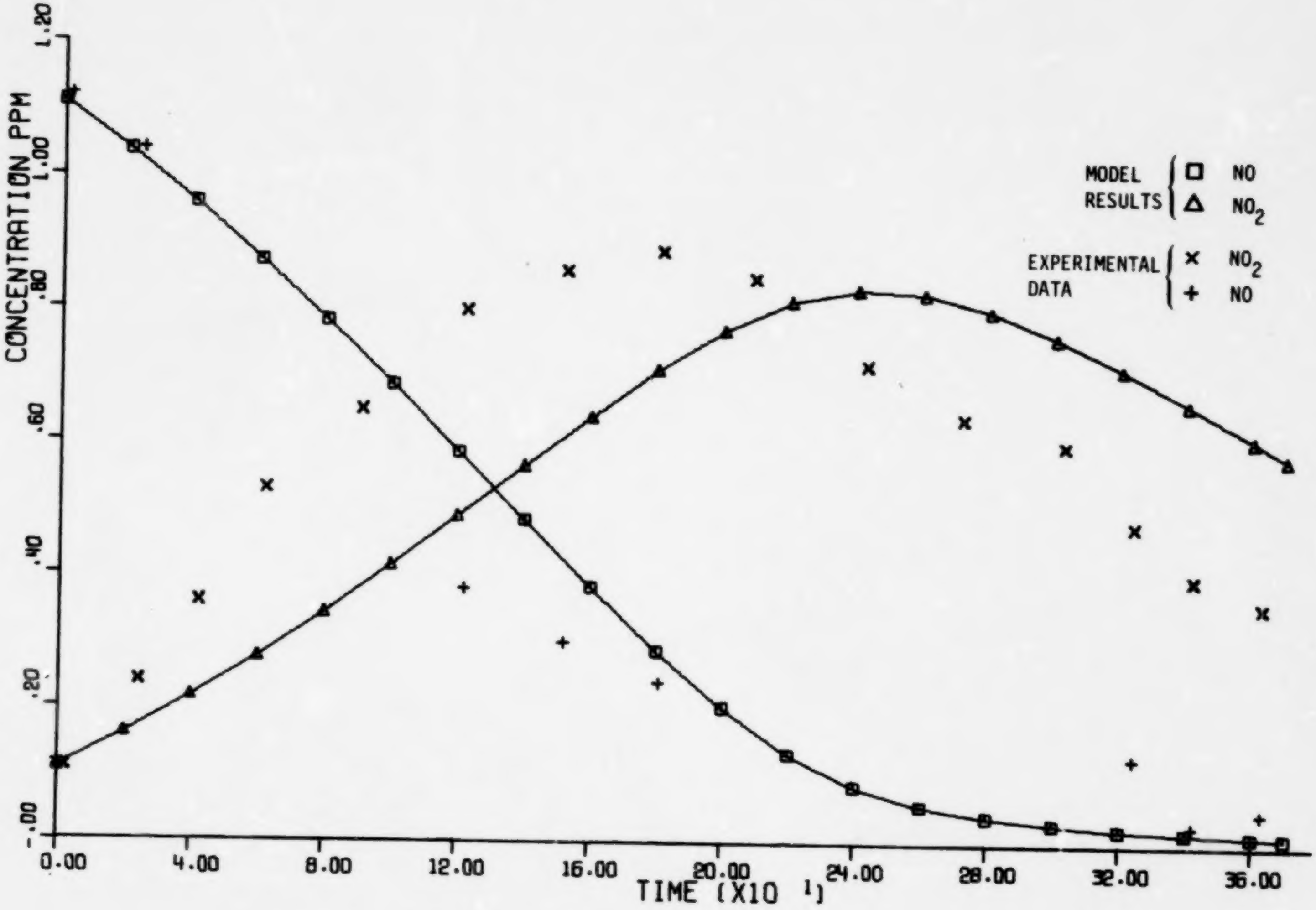

Figure 2.6. Experiment 251, Toluene/n-Butane/NO_x. Plot of NO and NO_2

TABLE 2.4
RATE CONSTANTS FOR TOLUENE/n-BUTANE SIMULATION

	Reaction Number	Rate Constant Used in Validation*
	1	$2.67(-1)\,\text{min}^{-1}$
	1a	$1.32(-5)\,\text{ppm}^{-2}\text{min}^{-1}$
	2	2.67(+1)
Toluene	3	1.69(+2)**
	4	2.0(+4)
	5	3.0(-4)
n-Butane	3	1.4(+1)**
	4	1.0(+4)
	5	1.0(-4)
	6	1.0(+5)
	7	2.0(+2)
	8	1.5(+3)
	9	3.0(+3)
	10	$1.0(-3)\,\text{min}^{-1}$
	11	1.0(-3)
	12	5.0(-3)
	13	4.5(+3)
	14	$1.4(+1)\,\text{min}^{-1}$
	15	$6.05(+1)\,\text{min}^{-1}$
	16	$0\,\text{min}^{-1}$

---

*Units are $\text{ppm}^{-1}\text{min}^{-1}$ unless otherwise specified.

**Measured values obtained from Refs. 2 and 6, respectively.

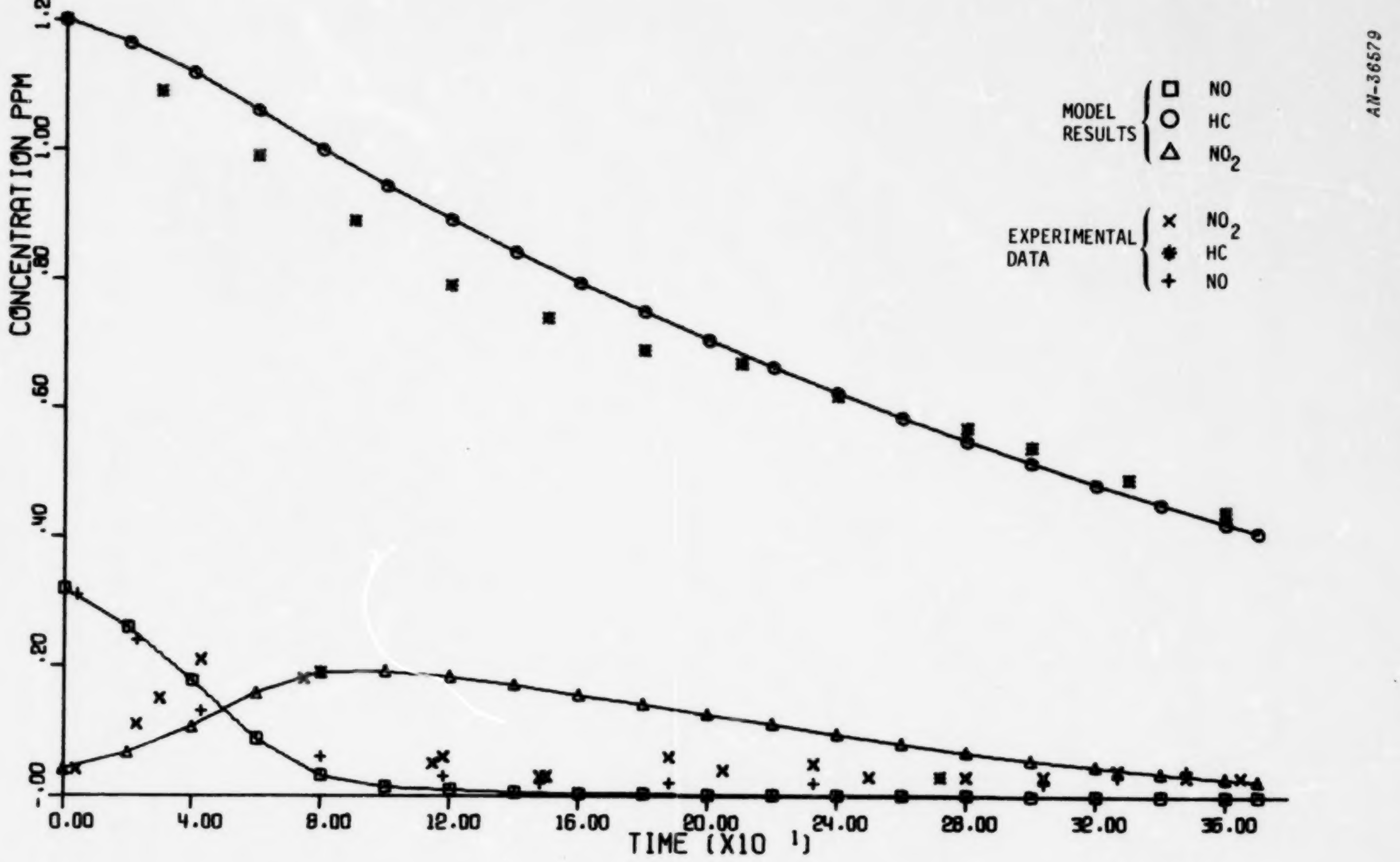

Figure 2.7. Experiment 271, Toluene/NO_x. Plot of Toluene, NO, and NO_2

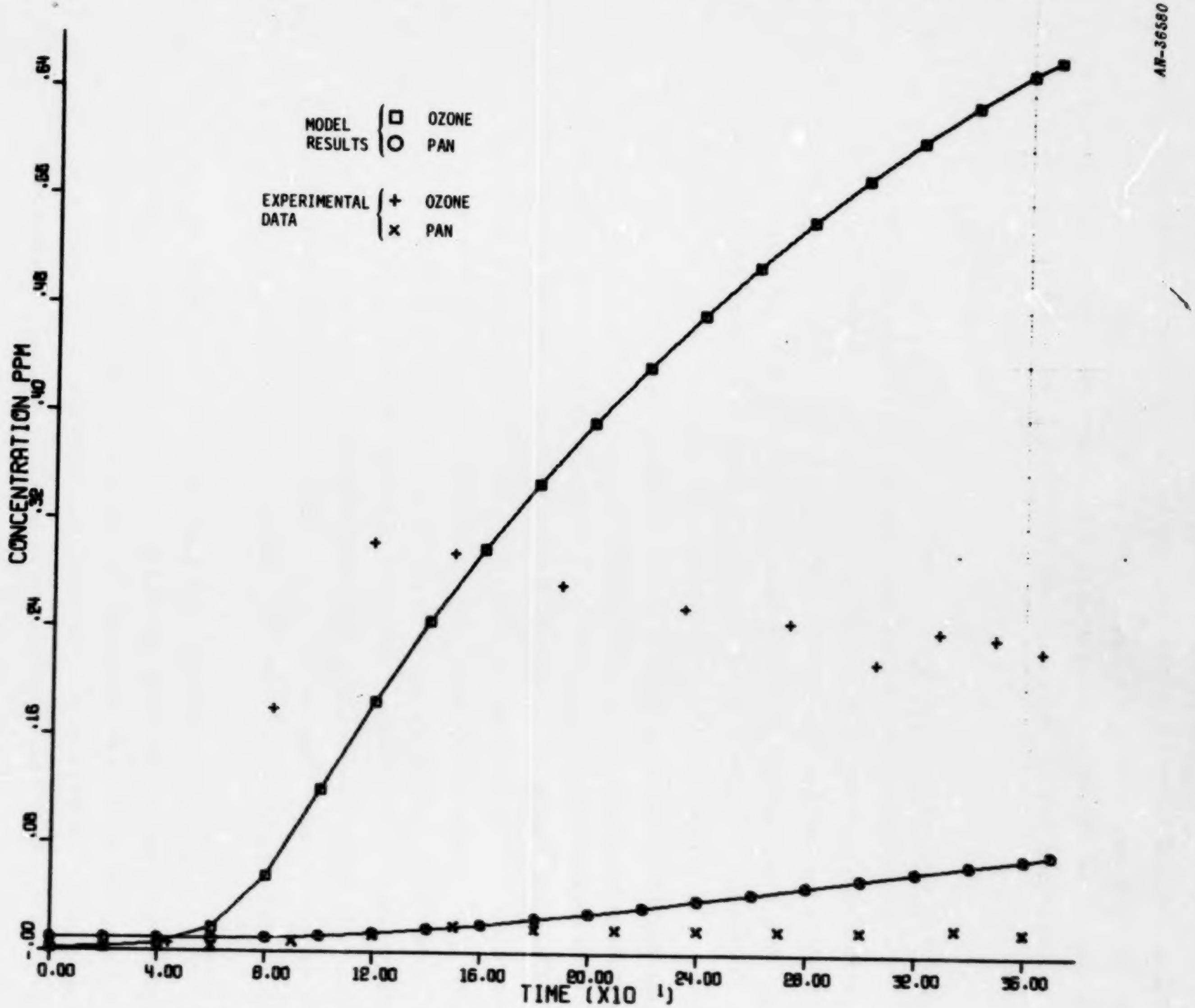

Figure 2.8. Experiment 271, Toluene/NO_x. Plot of Ozone and PAN

The rate constant data used to simulate experiment 271 are given in Table 2.5. No additional data are shown for the other toluene experiments because the results obtained do not warrant it. See Sec. 2.5.2 for a discussion of the rate constant data for toluene reactions. The branching factors used are $b_1 = b_2 = 2$ and $b_3 = 1$. The yield factor for OH is 0.5.

2.5.4 Auto Exhaust Validations

The experiments with dilute auto exhaust introduced the additional complication of having to deal with a multiplicity of hydrocarbons. Also, particulate matter was observed in these experiments, but was not observed in the previous experiments. The auto exhaust data also exhibited $NO \rightarrow NO_2$ conversion with relatively small amounts of hydrocarbon having reacted. To account for NO_x disappearance in the presence of aerosol it was suggested[11] that reaction (2.16) be added to the model, the rate constant to be determined by adjustments during the simulation. Because of the multiple hydrocarbon mixture, the branching factors were increased to reflect the increased length of the hydrocarbon oxidation chains with its concomitant increase in organic radicals. Finally, since it is not feasible to consider each hydrocarbon individually, the mixture was aggregated into three types: nonreactive and low- and high-reactivity hydrocarbons. Hydrocarbons considered nonreactive were ignored in the simulation. Thus the modeling runs were conducted using the two reactive hydrocarbon groups. The initial hydrocarbon concentrations were obtained from an analysis by Dodge[11] and are reproduced in Table 2.6.

The initial rate constants for each group were obtained by mole-weighted averages of the rate constants for typical members of each group. Thus for group I, we used n-butane and toluene to represent the paraffins and aromatics, respectively. For group II, ethylene and propylene were used. Again, these rate constants were adjusted during the simulation.

TABLE 2.5

RATE CONSTANTS FOR TOLUENE EXPERIMENT 271

Reaction Number	Rate Constant Used in Validation*
1	2.67(-1)min^{-1}
1a	1.32(-5)ppm^{-2}min^{-1}
2	2.67(+1)
3	1.69(+2)**
4	1.0(+4)
5	5.0(-4)
6	1.0(+5)
7	2.0(+2)
8	1.5(+3)
9	3.0(+3)
10	1.0(-3)min^{-1}
11	5.0(-2)
12	5.0(-3)
13	4.5(+3)
14	1.4(+1)min^{-1}
15	6.05(+1)min^{-1}
16	0 min^{-1}

---

*Units are ppm^{-1}min^{-1} unless otherwise specified.

**Measured constant obtained from Ref. 2.

TABLE 2.6

INITIAL HYDROCARBON CONCENTRATIONS (PPM) FOR AUTO EXHAUST EXPERIMENTS

Group		Hydrocarbon Type	Experiment Number	
			222	231
I.	Low-Reactivity	C_4 + paraffins	0.68	0.11
		Aromatics (excluding benzene)	0.47	0.09
II.	High-Reactivity	Ethylene	0.48	0.22
		Olefins (excluding ethylene)	0.58	0.17

It should be noted that rather large amounts of CO were present in the mixtures described above. The data provided for these experiments show that for Exp. 222, the concentration of CO was 53 ppm, and for Exp. 231, it was 12 ppm. Dodge[11] has pointed out that CO may be partly responsible for the oxidation of NO and that this would explain, at least in part, why the $NO \rightarrow NO_2$ conversion occurs so rapidly even though very little hydrocarbon has reacted. The CO effect could come about via the following steps:

$$OH + CO \rightarrow CO_2 + H \tag{2.19}$$

$$H + O_2 + M \rightarrow HO_2 + M \tag{2.20}$$

$$HO_2 + NO \rightarrow OH + NO_2 \tag{2.21}$$

$$HO_2 + NO_2 \rightarrow HNO_2 + O_2 \tag{2.22}$$

Reaction (2.21) is analogous to reaction (2.6) and would be the step responsible for part of the $NO \rightarrow NO_2$ conversion. Our model does not include reactions (2.19)-(2.22), of course, and so if CO reactions are indeed significant, we will have to compensate for them by other means such as increasing branching factors and k_4. We note, however, that previous work with CO (Refs. 4, 5, 8, 22-24), appears to indicate that CO concentrations of the order of 100 ppm are required before CO can be considered to play a significant role in the oxidation of NO. Thus CO is probably not important in experiment 231, but may be a significant factor in experiment 222.

Figure 2.9 shows the results for NO and NO_2 obtained for the controlled exhaust case, experiment 231. No ozone results are shown because this experiment produced very small amounts of ozone and the simulation behaved accordingly. This is due to the relatively large concentrations of NO that exist throughout the experiment. As the graph shows, the NO is well modeled but the NO_2 buildup in the model is not as fast as the data would indicate. It is puzzling, however, that the data appear to show a rapid buildup of NO_2 even though NO decays very little in the interval 0-80 min. Nevertheless, we note that the NO_2 achieves its correct magnitude late in the reaction. The effect of reaction (2.16) is to take NO_2 out of the system to simulate the NO_x decay. The NO_x plot shown in Fig. 2.9 illustrates that the NO_x removal is well modeled. Note that the correspondence between computed NO_x and the (smoothed) NO_x data provided by EPA[11] (denoted by the asterisks) is very close. It should be noted, however, that in this simulation 20% of the difference between initial and final NO_x concentration is accounted for by dilution.

Figure 2.10 shows a plot of the computed reactive hydrocarbon for experiment 231. The intent here is not to reproduce the hydrocarbon data, but rather to show that relatively little hydrocarbon has reacted. The experimental data show a final concentration of 0.3 ppm and the model yields 0.26 ppm at 360 minutes. As was the case with NO_x, dilution accounts for 20% of the concentration change from initial to final value. Thus the main characteristics of this experiment (NO_x disappearance, hardly any ozone production, and a slow reactive-hydrocarbon decay) are reproduced well by the model.

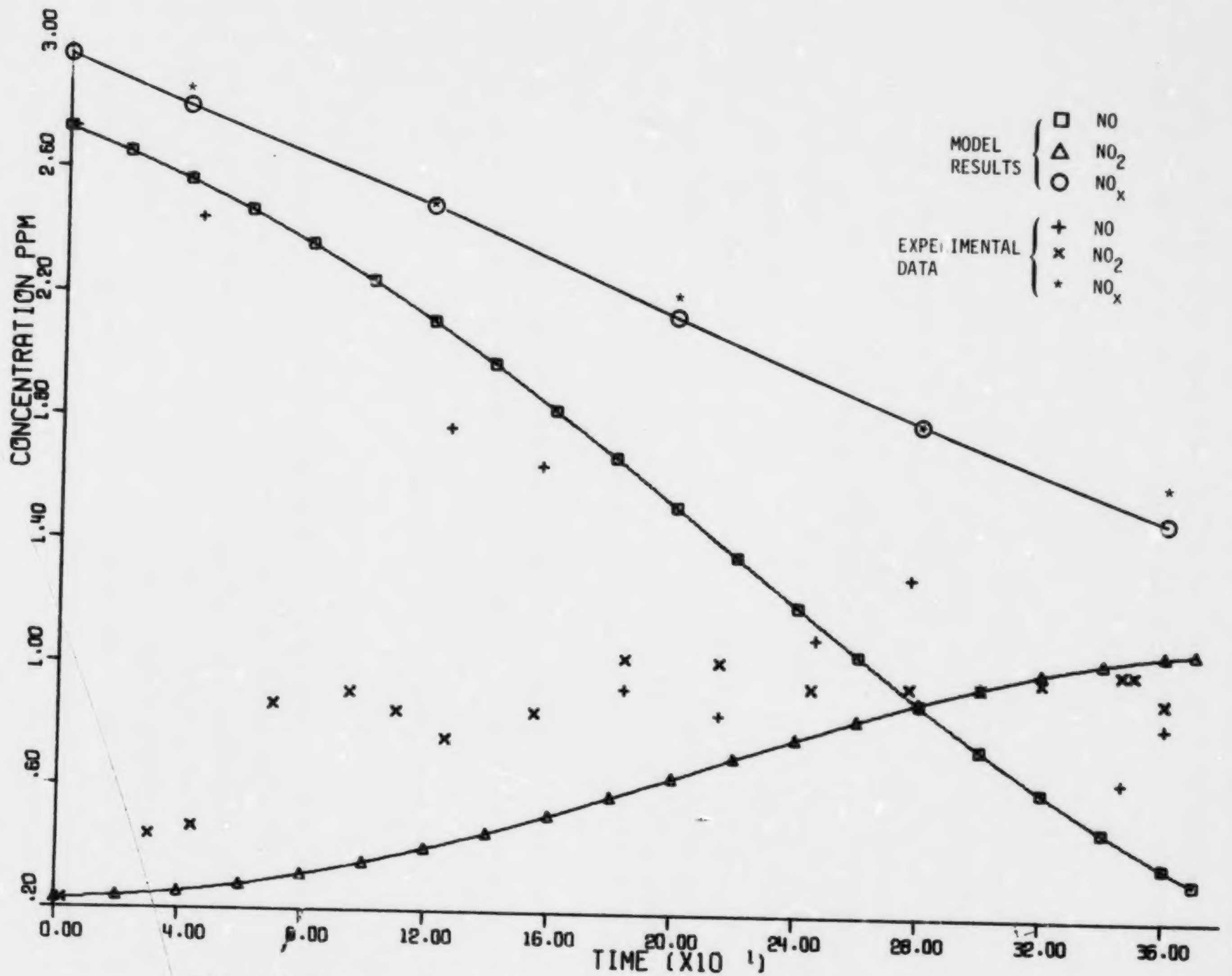

Figure 2.9. Experiment 231, Dilute Auto Exhaust (Controlled Vehicle). Plot of NO and NO_2

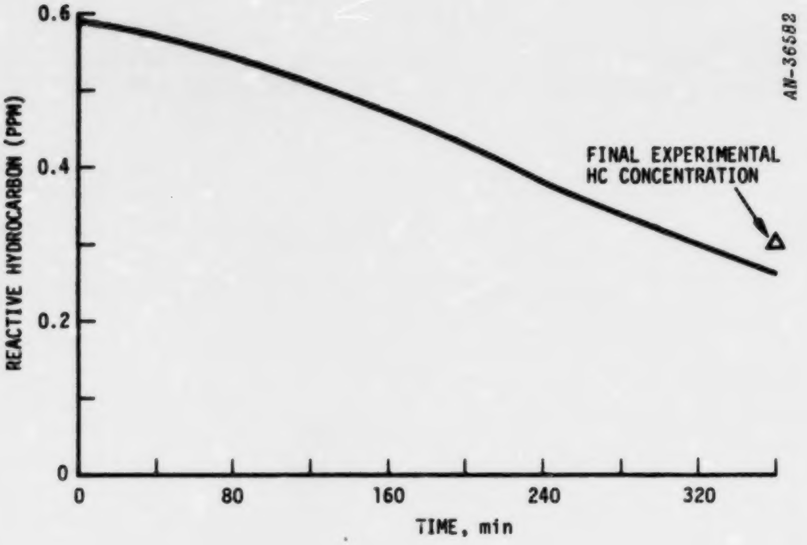

Figure 2.10. Experiment 231, Dilute Auto Exhaust (Vehicle with Emission Controls). Simulation of Reactive Hydrocarbon Decay

Table 2.7 contains the rate constants used in the simulation. Note that the ratio k_{4a}/k_4 is 2.5, a plausible value in view of the relative reactivity of the components of each hydrocarbon group. Note also that the value of k_4 is the same as that used for n-butane in the binary mixture experiments, whereas $k_{4a} = 2.5 \times 10^4$ lies in the range used for propylene. It is also interesting to note that the value of k_{16} is only three times greater than the dilution "rate constant" of 5.98×10^{-4}. Finally, the branching factors were increased considerably from previous values, with $b_1 = b_2 = 8$ and $b_3 = 1$ for both hydrocarbon groups. This was to be expected in view of the increased length of the chains. The OH yield factor was set to $y = 1/8$.

Figures 2.11 and 2.12 show the results obtained for experiment 222. It can be seen that the time phasing of the NO_2 peak is off, the peak occurring about 50 minutes late. This of course affects the concentration-time curve for NO_x and for this reason, it has not been plotted.

TABLE 2.7

RATE CONSTANTS USED IN SIMULATION OF EXPERIMENT 231 DILUTE EXHAUST FROM A VEHICLE WITH EMISSION CONTROL

	Reaction Number	Rate Constant*
	1	$2.67(-1)\text{min}^{-1}$
	1a	$1.32(-5)\text{ppm}^{-2}\text{min}^{-1}$
	2	2.67(+1)
Low-Reactivity Hydrocarbon	3	8.39(+1)
	4	1.0(+4)
	5	2.8(-4)
High-Reactivity Hydrocarbon	3a	2.82(+3)
	4a	2.5(+4)
	5a	7.56(-3)
	6	1.0(+5)
	7	2.0(+2)
	8	1.5(+3)
	9	3.0(+3)
	10	$1.0(-3)\text{min}^{-1}$
	11	1.0(-3)
	12	5.0(-3)
	13	4.5(+3)
	14	$1.4(+1)\text{min}^{-1}$
	15	$6.05(+1)\text{min}^{-1}$
	16	$2.0(-3)\text{min}^{-1}$

---

*Units are $\text{ppm}^{-1}\text{min}^{-1}$ unless otherwise specified.

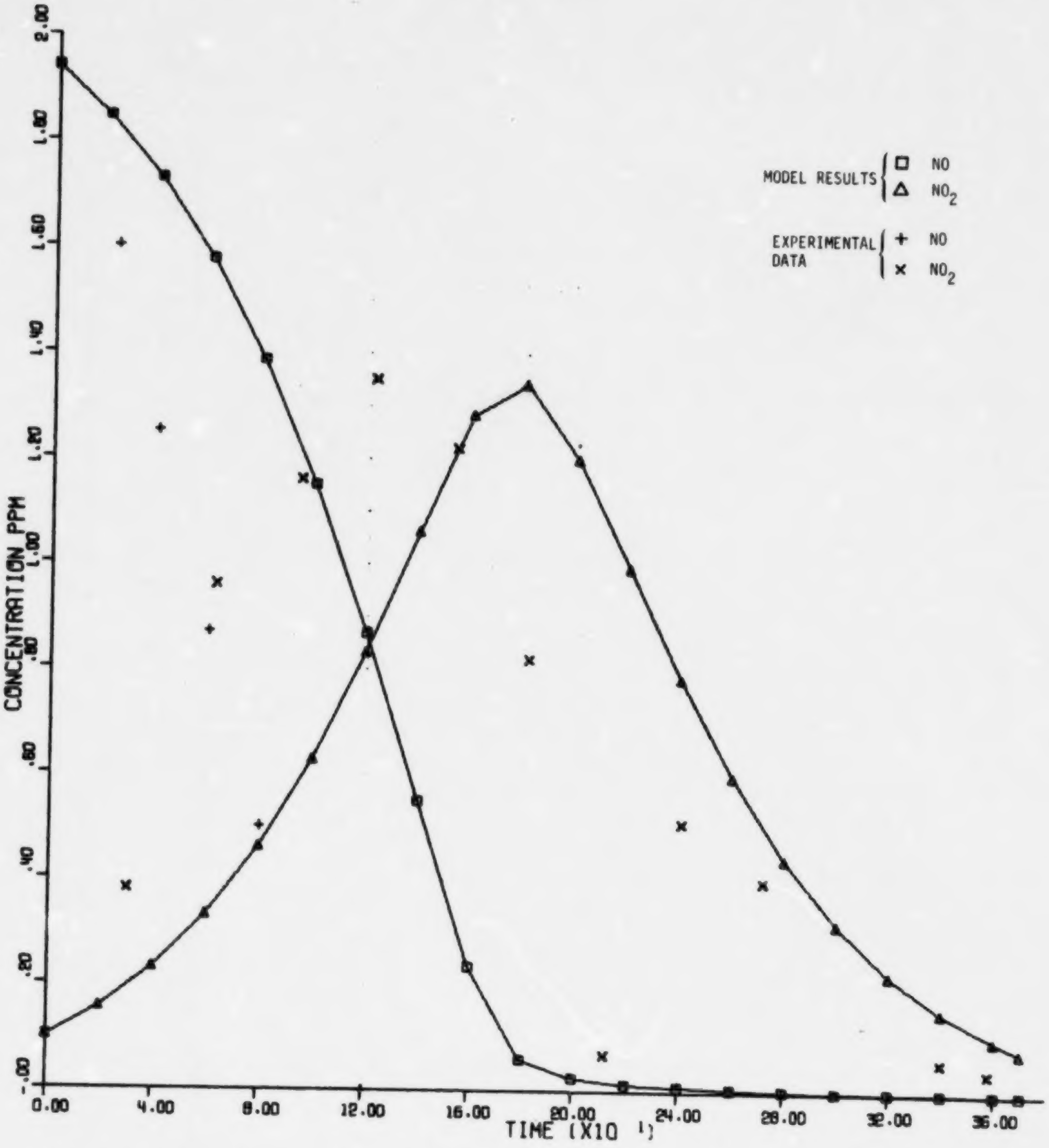

Figure 2.11. Experiment 222, Dilute Auto Exhaust (Uncontrolled Vehicle). Plot of NO and NO_2

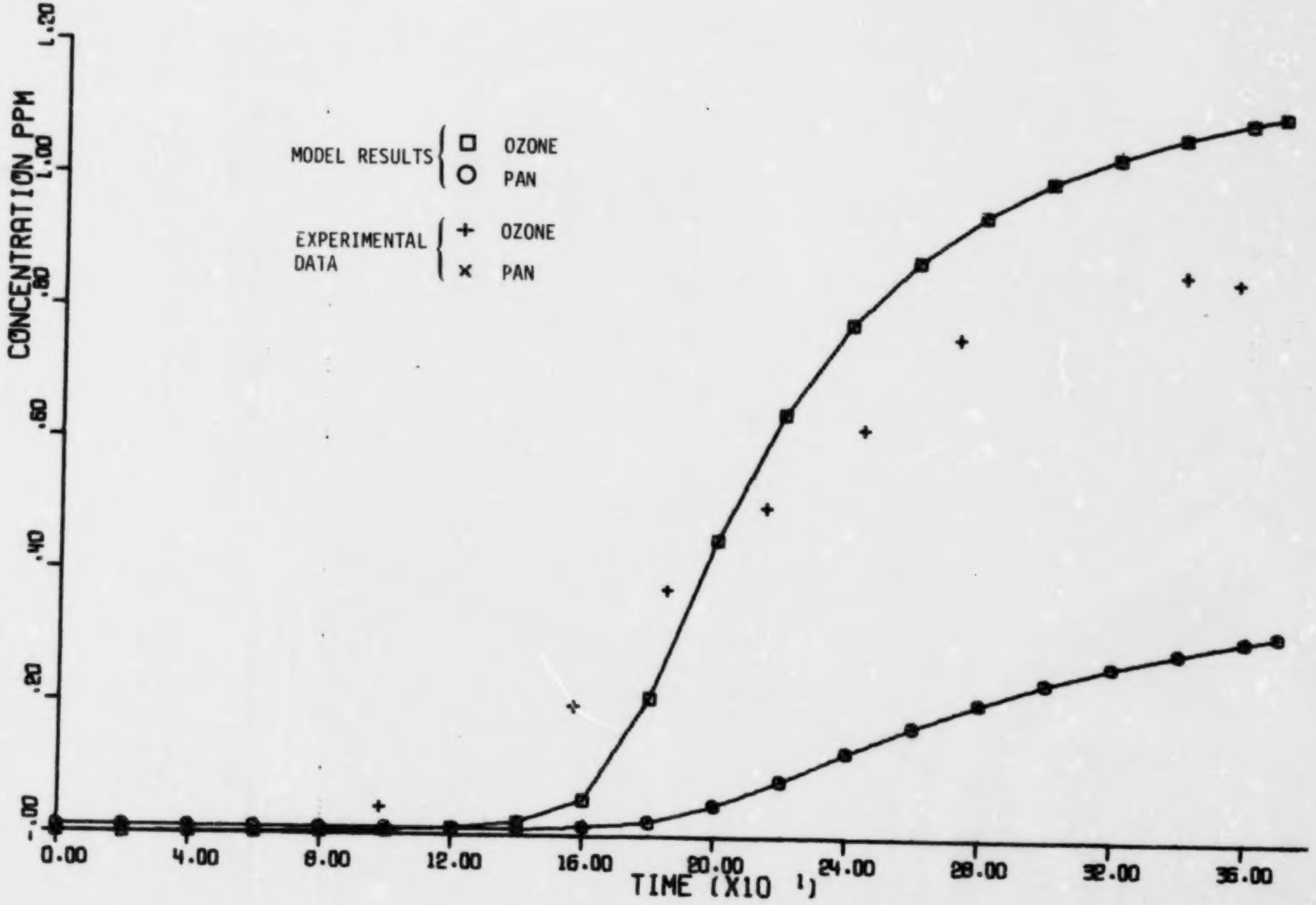

Figure 2.12. Experiment 222, Dilute Auto Exhaust (Uncontrolled Vehicle). Plot of Ozone and PAN

However, the NO_x levels occurring late in the experiment agree well with the measured values. Furthermore, the NO_2 peak has the correct magnitude. Equally important is the reproduction of the ozone data. Figure 2.12 shows that the time phasing and the magnitude approximate well the experimental data. Although it is not shown, the final concentration of reactive hydrocarbon is 0.86 ppm compared with 0.7 ppm for the data.

Table 2.8 contains all the rate constants used for simulating experiment 222. Note that $k_{4a}/k_4 = 2$ and that k_{16} has the same value used in experiment 231. The values of the branching factors are $b_1 = b_2 = 5$ and $b_1 = b_2 = 10$ for low- and high-reactivity hydrocarbons, respectively. The branching factor b_3 is unity for both hydrocarbon groups. The OH yield factor is equal to 0.1.

2.6 ADAPTATION OF CHEMICAL MODEL TO ATMOSPHERIC MODELING

The parameters of the chemical system obtained from the smog chamber simulation tests must be modified when we move from the smog chamber to the atmosphere. What one hopes to obtain from smog chamber experiments is a qualitative agreement between laboratory and atmospheric observables. Modeling the smog chamber experiments then gives us an indication that the physical mechanism proposed for modeling these observables contains the most important features of the highly complex phenomena which take place in reality. The evaluation process using smog chamber data also gives us an understanding of the model's sensitivity to various parameters.

Having obtained this information about the model using laboratory data, the quantitative link with atmospheric observables must come from attempts to model the atmospheric processes themselves. In order to do this, we must identify those features of the chemical model which are most likely to be heavily influenced by smog chamber conditions. We must also find out the degree of correlation which exists between the chamber and atmospheric mixtures.

TABLE 2.8

RATE CONSTANTS USED FOR SIMULATING EXPERIMENT 222 DILUTE EXHAUST FROM A VEHICLE WITHOUT EMISSION CONTROL

	Reaction Number	Rate Constant*
	1	2.67(-1)min^{-1}
	1a	1.32(-5)$\text{ppm}^{-2}\text{min}^{-1}$
	2	2.67(+1)
Low-Reactivity Hydrocarbon	3	7.76(+1)
	4	1.5(+4)
	5	2.6(-4)
High-Reactivity Hydrocarbon	3a	3.45(+3)
	4a	3.0(+4)
	5a	8.54(-3)
	6	1.0(+5)
	7	2.0(+2)
	8	1.5(+3)
	9	3.0(+3)
	10	1.0(-3)min^{-1}
	11	1.0(-3)
	12	5.0(-3)
	13	4.5(+3)
	14	1.4(+1)min^{-1}
	15	6.05(+1)min^{-1}
	16	2.0(-3)min^{-1}

---

*Units are $\text{ppm}^{-1}\text{min}^{-1}$ unless otherwise specified.

2.6.1 Wall Effects and Dilution Effects in Smog Chambers

Two factors characteristic of smog chambers which are most likely to influence the parameters as well as the nature of the chemical model are dilution effects due to sampling in the smog chamber and wall effects. Omitting dilution from the model has the effect of requiring unrealistically high values for some of the adjustable rate constants. This is especially significant with k_4-adjustments needed to obtain satisfactory simulations.

Wall effects influence the nature of the model. In our particular case, three reactions, (2.13)-(2.15), have been added to try to account for the nitrogen imbalance which is presumably due to NO_2 reacting on the chamber walls. Whether these reactions will play any role under atmospheric conditions is not known, but intuitively one would expect them not to be significant. Hopefully, the evaluation process under atmospheric conditions will yield an answer to this question.

The concerns we expressed earlier regarding the importance of wall reactions as an NO_x sink were confirmed by comparison of absolute reaction rates throughout the simulation. The reaction of N_2O_5 with water on the wall to form nitric acid dominated the NO_x removal as would be expected from prior experimental findings.[9] Specifically, this reaction rate exceeded the gas phase production of nitric acid by about a factor of 6. In the course of checking out sensitivity of the system to the chain breaking reactions, we individually varied reaction rate constants in reactions (2.12), (2.13), (2.14), and (2.15). A measure of the sensitivity was the influence on nitrogen dioxide decay at late time. The greatest sensitivity of all was exhibited with respect to variation in k_{12}. A threefold increase in this rate constant, for example, resulted in a fourfold decrease of end-point NO_2 concentration in the simulation. The next reaction in the sequence, that between nitrogen dioxide and nitrogen trioxide, had a lesser effect. Perhaps counter to intuition, an increase in k_{14} by a factor of three actually resulted in a slight (less than 10%) increase in end-point nitrogen dioxide concentration. Rather large changes in the wall reaction rate k_{15} were introduced, but these had virtually no influence on the system.

Samples were periodically withdrawn during each smog chamber experiment to analyze the composition of the gas. "Clean" air replaced the sample in each case. In our evaluation process, we have found that this dilution can play a significant role in smog chamber experiments. Thus dilution was accounted for in all of the simulations discussed previously.

Given an average volumetric dilution rate for an experiment, the first step was to convert this rate to a first-order "rate constant" by dividing by the chamber volume. Then we subtract a factor due to dilution from each chemical rate equation as shown below:

$$\frac{dc_i}{dt} = R_i - \delta c_i \tag{2.23}$$

where c_i = ith species concentration

R_i = chemical rate for ith species

δ = average fractional dilution = average volumetric dilution rate/chamber volume

To test the validity of our approach for simulating dilution effects, we used the ethane concentration data in the propylene experiments, since ethane can be considered to be essentially unreactive. The predicted and observed ethane concentrations for one such experiment, experiment 336, are shown in Fig. 2.13. It can be seen that the two sets of data agree closely. The maximum error is 5%. Additional checks with other experiments produced similar results.

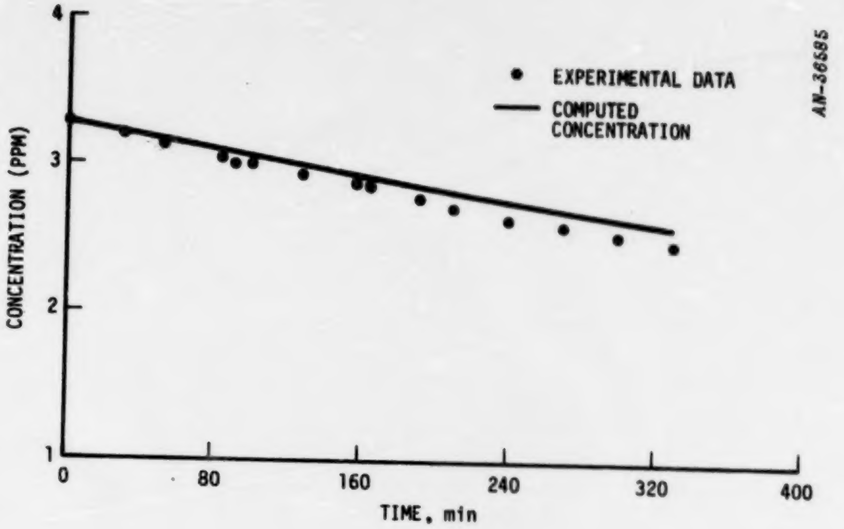

Figure 2.13. Experiment 336. Dilution Model Compared with Measured Ethane Concentration

---

The effects of dilution on the reactive species can be seen in Fig. 2.14 which contains a plot of propylene concentration with and without dilution. The effect on other species was similar but the degree of influence varies for each species. Thus for nitric oxide, the dilution effect is generally small due to the rapid decay of NO by chemical reaction, i.e., $R_{NO} >> \delta c_{NO}$ in Eq. (2.23). On the other hand, for ozone, dilution has been observed to play a large role late in the reaction.

Dilution can also account for some of the discrepancy found in the nitrogen balance in smog chambers. Our simulations indicate that dilution effects can account for up to 25% of the nitrogen loss for those experiments used in these model validations.

From the above remarks, it is clear that dilution can have a significant impact on the whole reaction. Furthermore, because of system

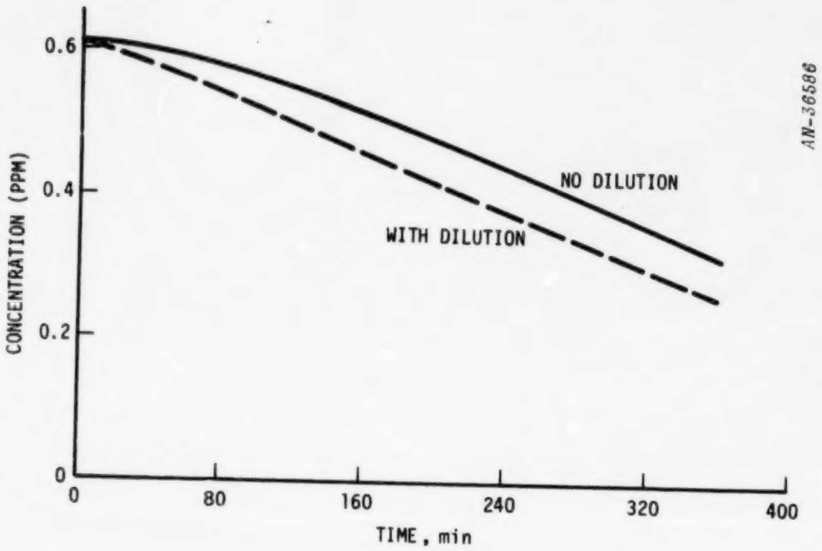

Figure 2.14. Experiment 336. Effect of Dilution on Propylene Concentration. (Curves Computed using a Single set of Rate Constants)

nonlinearities, simple scaling cannot be used to compensate for dilution effects. Thus caution must be exercised when attributing changes in species concentration to chemical causes alone. Therefore, it is imperative that dilution data be included when experiments are reported in the literature.

As a final comment, we note that the approach described above assumes a uniformly distributed dilution which implies a continuous sampling process. This is, of course, not the case, since sampling is done at irregular intervals and no dilution takes place between sampling points. Whether approximating the discontinuous sampling process by a continuous one has any significant effects on the simulation remains to be determined.

2.6.2 Smog Chamber vs Atmospheric Mixtures

The reactivity of the mixture is one measure that can be used as a guide to estimate the magnitude of the modifications in the rate constants of the hydrocarbon reactions. We have followed this approach in previous work.[24] Table 2.9 shows the mole-weighted reactivity of the hydrocarbon mixtures in the atmosphere and in the smog chamber experiments previously described. The measure of reactivity is based on a hydrocarbon-consumption scale due to Altshuller.[25] The reactivity of the Los Angeles atmosphere was obtained from our previous study of Los Angeles atmospheric reaction data.[26]

It is obvious from the table that the dilute auto exhaust approximates the reactivity of the Los Angeles atmosphere. So we expect these experiments to yield the most useful rate constant data for the model. Our previous approach of using a chemical model validated only for propylene and dividing its hydrocarbon rate constants by three for atmospheric modeling purposes is, of course, a result of the reactivity

TABLE 2.9

MOLE-WEIGHTED REACTIVITY OF ATMOSPHERIC
AND SMOG CHAMBER HYDROCARBON MIXTURES

Mixture	Reactivity*
Los Angeles Atmosphere	6 ± 2
Propylene	17
Toluene	3
Toluene/n-Butane	1.6
Auto Exhaust--With HC and CO exhaust	6.8
Auto Exhaust--Without HC and CO exhaust	6

---

*Based on a hydrocarbon consumption scale.[25]

relationship shown in Table 2.9. Finally, we note that the reason for the controlled vehicle exhaust to be slightly more reactive than the uncontrolled vehicle exhaust is due to the fact that the propylene content of the former is a larger fraction of the total hydrocarbon mix than is the case for the uncontrolled exhaust.

3 MODEL METHODOLOGY IMPROVEMENTS

3.1 PERSPECTIVES ON MODEL UPDATING

Initially,[27] our model treated a constant-thickness air layer with a very compact lumped kinetic scheme. Generalization of the model introduced advection and more realistic chemistry, but ground-fixed coordinate systems led to unacceptable numerical diffusion errors and the chemistry still needed more chain-termination steps. Subsequent work[24] used scaling parameters from actual air data[26] for hydrocarbon reactivity adjustments and for nitric oxide emission adjustments. These adjustments have been necessary in past work to convert theoretical estimates to the values that better approximate what actually occurs in the atmosphere. Further model development saw the replacement of the Eulerian coordinate system by the semi-Lagrangian system now used. Substantial improvements in computing efficiency and accuracy were also made by introducing Padé approximant numerical techniques.

Still, some lingering questions remained unanswered. The present work addresses these questions. Chemical refinements were described in the previous section. These studies confirmed the validity of our earlier approaches in converting smog chamber findings to the atmosphere. Moreover, the main structure of the model must necessarily deal with the advection, diffusion, and the array of sources as they all interact in air masses moving through regions where air pollution is to be predicted. The following subsections deal individually with the current round of improvements in modeling these phenomena.

3.2 ADVECTIVE AIR TRAJECTORIES

The speed and direction of the air mass-center are determined, as before,[24] by taking weighted averages of wind speeds and directions from neighboring measurement stations. It is useful to examine the theoretical basis for the weighting and its detailed application in the current phases of our work.

Reciprocal distance weighting of wind station readings is used as a theoretical basis of interpolation. The rationale for reciprocal-distance over reciprocal-distance-square stems from the nature of fluid dynamic singularities in plane flows.

Because of the comparisons of horizontal and vertical scales in the atmospheric boundary layer problem, the flow may be regarded more nearly planar than three-dimensional. Clearly, three-dimensional effects occur at convergences and do generate vertical velocities, but horizontal advection seems to be the most important character of the lower atmospheric flow fields we are treating. This being the case, it can be conceived that any velocity field can be generated by the cumulative effect of plane singularities such as sources, sinks, and vortex elements. Classical fluid dynamics shows that the dependence of the influence of each one of these singularities upon distance is reciprocal in the distance from the flow element. Thus, if the flow at a field point is assumed to be the superposition of flows described at neighboring points, it follows that the relative weight given to each neighboring point should be proportional to its reciprocal distance from the field point.

The output of hand calculations of air trajectories takes the form of schedules describing hourly magnitude and direction of successive trajectory segments. For each node point in the trajectory, air-quality weighting factors are derived in addition to wind weighting factors. These were applied to concentration data from the two or three nearest-neighboring air monitoring stations (which do not generally correspond to the neighboring wind measurement stations). This gives an estimated hourly history of air quality along the trajectory, thereby affording a much larger data base than merely the end point concentrations. The net effect of the expanded base is to impose stricter standards on validation compared with end point receptor-oriented calculations.

Figure 3.1 shows two typical Los Angeles morning trajectories. (Stations having hydrocarbon data were chosen as origins for the trajectory to minimize uncertainties in initial conditions.) In this case, the Air Pollution Control District (APCD) Downtown station has hourly total hydrocarbon and methane concentrations. The computed crossing of trajectories may not have occurred had there been data which would allow the use of a shorter interval size in the calculation. The sampling station located at the City of Commerce has gas chromatographic data commencing in the early morning hours. The validation runs for these trajectories can be checked against interpolated air quality data from nearby monitoring stations.

Figure 3.2 illustrates a study comparing the surface wind trajectory calculations with winds aloft tracked by an ESSA tetroon. In this example,

---

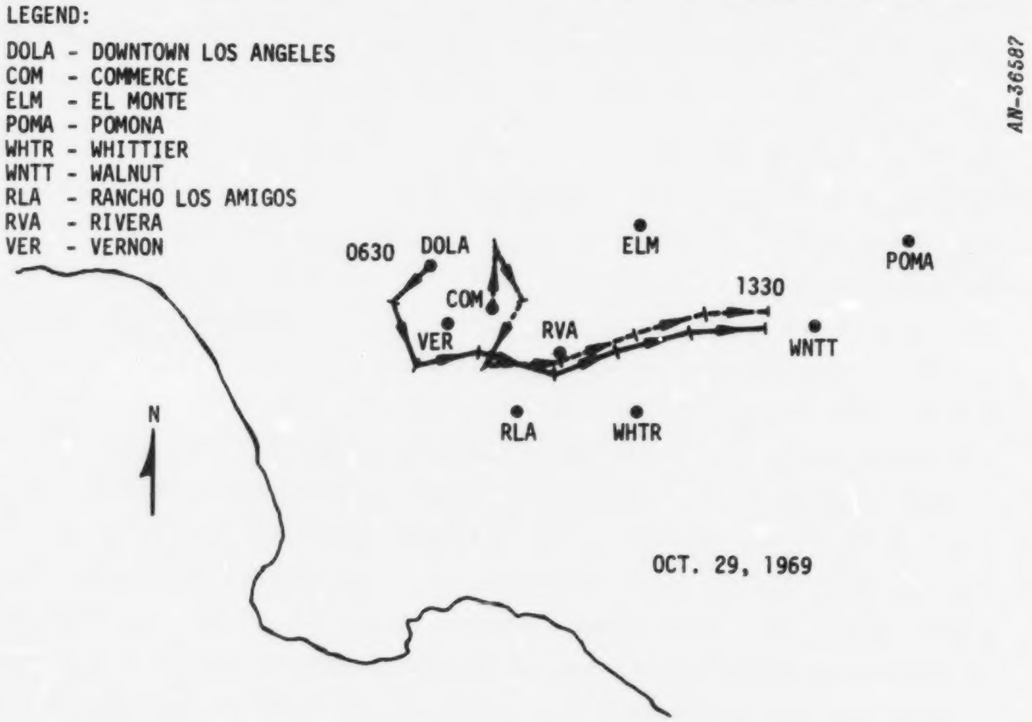
LEGEND:
DOLA - DOWNTOWN LOS ANGELES
COM - COMMERCE
ELM - EL MONTE
POMA - POMONA
WHTR - WHITTIER
WNTT - WALNUT
RLA - RANCHO LOS AMIGOS
RVA - RIVERA
VER - VERNON
AN-36587
0630
DOLA
ELM
POMA
1330
COM
VER
RVA
WNTT
RLA
WHTR
N
OCT. 29, 1969

Figure 3.1. Air Trajectory in the Los Angeles Basin

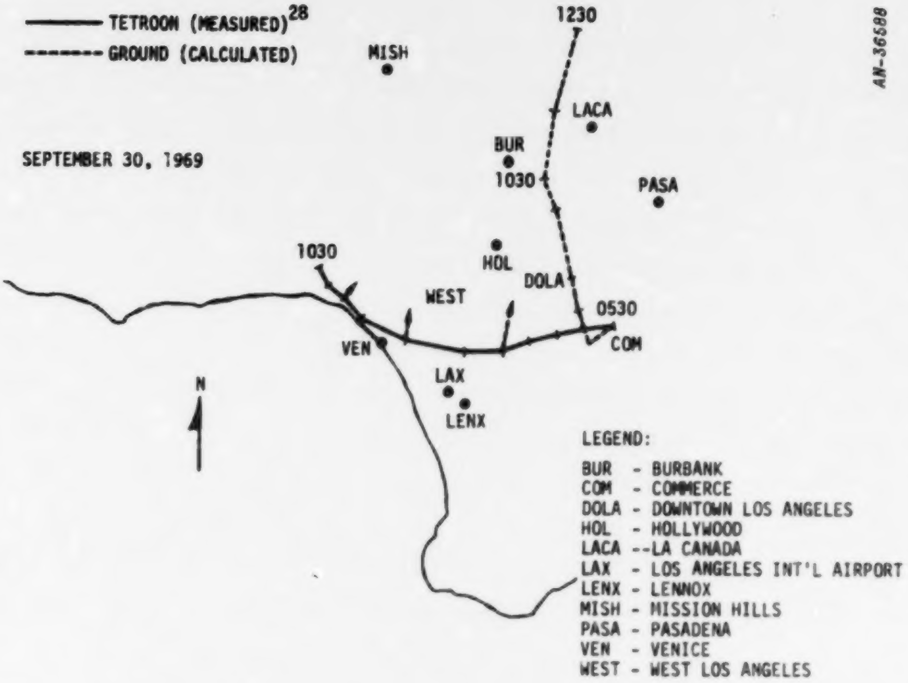

TETROON (MEASURED)28
GROUND (CALCULATED)
MISH
1230
AN-36588
LACA
SEPTEMBER 30, 1969
BUR
1030
PASA
1030
HOL
DOLA
WEST
0530
VEN
COM
LAX
LENX
N
LEGEND:
BUR - BURBANK
COM - COMMERCE
DOLA - DOWNTOWN LOS ANGELES
HOL - HOLLYWOOD
LACA --LA CANADA
LAX - LOS ANGELES INT'L AIRPORT
LENX - LENNOX
MISH - MISSION HILLS
PASA - PASADENA
VEN - VENICE
WEST - WEST LOS ANGELES

Figure 3.2. Comparison of Ground Trajectory with Tetroon Trajectory

---

the solid line is the tetroon path and the dashed line is the calculated surface trajectory. Short dashed arrows along the tetroon trajectory show one-hour segments computed from wind station data. Except for the initial segment, the computed surface winds have a rightward heading from the tetroon path (looking in the direction of tetroon motion). The result is the surface trajectory heading north through Cahuenga Pass, over Burbank and into the Verdugo Hills, while the tetroon travels due west in an offshore direction until it veers inland over Santa Monica late in the morning; therefore, it appears that these differences between surface and elevated winds can be especially distinct. Although Angell, et al.,[28] analyze such disparities in their paper, their comparisons exhibited a higher degree of correspondence between paths than ours. The difficulties in neglecting height-dependence of advection are obvious to the modeler; however, neither theoretical nor empirical corrections are presently available. The means for handling this effect may come out of boundary layer meteorological researches.

Even at a single location, variations in wind speeds and directions appear to occur due to localized effects. Figures 3.3 and 3.4 show plots of Los Angeles Air Pollution Control District data versus Scott Research Laboratories data. Both sets of data were reportedly taken at El Monte, California. Because of topographic setting and instrumental differences, the simultaneous readings show wide variances. This may be due to hourly averages of the Scott data versus instantaneous readings of the Los Angeles APCD (LAAPCD) station. In evaluating any air pollution simulation model, this sort of deviation must be considered, as well as that described in the preceding paragraph. Confronted with these conflicts, we attempted to resolve the differences by taking arithmetic means.

An objective technique for approximating continuous wind fields from discrete data will be needed in the near future. In the course of carrying out the hand calculations, we have developed the following logical structure on which such a technique might be based:

1. Forward differencing is the zero order approximation; that is, each segment is laid out based on the hourly averaged wind that is interpolated from station data surrounding its origin-point.
2. Higher approximations will require interpolation of wind data to the midpoint of the zeroth order segment and then refining the magnitude and direction of the segment in the first approximation.
3. Reiteration of the segment calculation may be coded with either an iteration counter or a convergence criterion to terminate the succession of approximations for the segment. (Discreteness of wind data may prevent convergence if proximity tests intervene in the sequence and alter the selection of wind stations utilized for interpolation).
4. Beyond some maximum distance, wind stations must be rejected even if it means reducing the number of input stations.

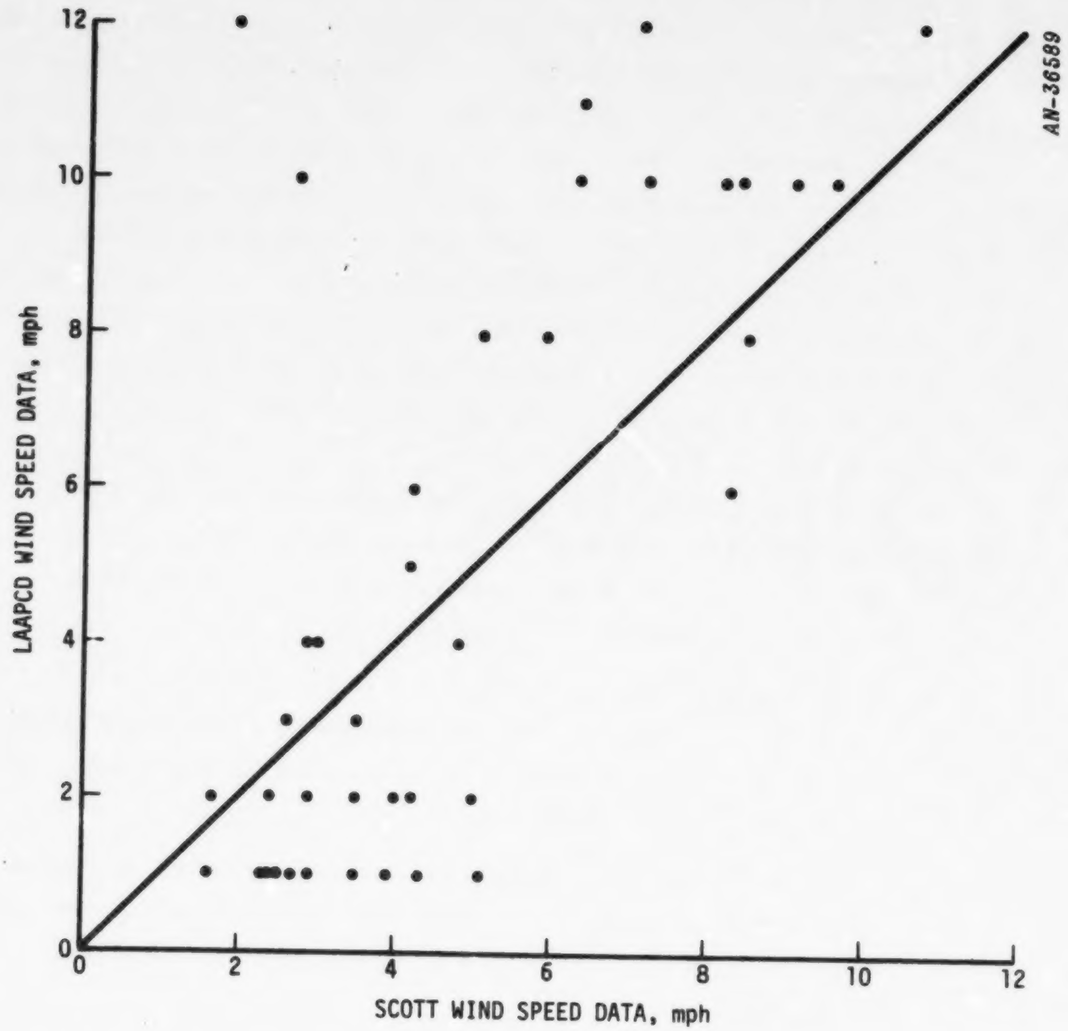

Figure 3.3. Comparison of Wind Speed Measurements at El Monte (Mornings in 1969)

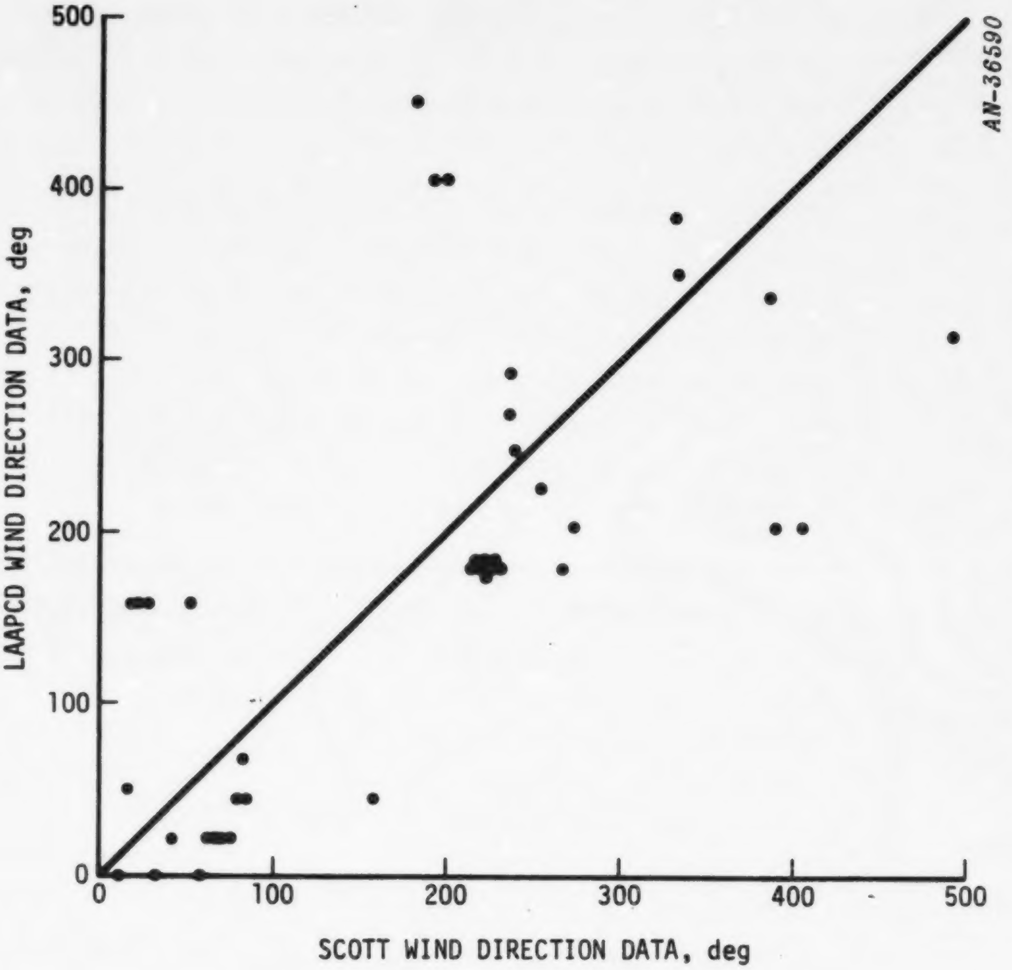

Figure 3.4. Comparison of Wind Direction Measurements at El Monte (Mornings in 1969)

5. Closer than some minimum distance, a single station's wind vector should be used directly.

6. If all station distances from the region of interest exceed a certain threshold (input) for a certain number of segments (also input) the computation should be terminated with an exit flag.

7. Numerical experiments with directional weighting should be conducted for both trajectory generation and for interpolated air quality at a trajectory point; for example, the air quality should be more sensitive to where it has been than to where it is going. For improving the zero-order wind motion approximation, direction and magnitude of a trajectory segment will be more sensitive to station readings near its future path than those it is moving away from.

8. Numerical experiments should be conducted on the relative merits of r^{-1}-weighting versus r^{-2}-weighting. This is done most directly by using a wind station as an unknown point. Then the three nearest neighbors (obeying the distance and barrier selection laws) are weighted by each power and the merit of each is evaluated by some measure such as least sum of square residuals between predicted and measured values.

3.3 VERTICAL AND HORIZONTAL EDDY DIFFUSION COEFFICIENTS

In the evaluation phase of developing the GRC photochemical/diffusion model, greater emphasis is placed on the use of temperature profiles for the test days. This led us to reappraise our earlier formulation[27] of the eddy diffusivity profile by incorporating more of the measured data that have been reported in the literature.

Up to now, the eddy diffusivity profile has been assumed to be trapezoidal from the "ground"* up to the mixing depth (previously set at the inversion base). Following Estoque,[29] the ramp portions of the profile extends to a height of 50 meters and nonvanishing values are set at the bottom and top of the vertical mesh. Assigning the flat portion of the profile of value of K_{z_∞}, the vertical diffusivity, we used the formula $K_{z_\infty} \approx 8300\ (u + 500)\ \mathrm{cm}^2/\mathrm{second}$, where u is the wind speed in cm/second. The approximation was based on a fit of scattered data from various sources cited in our 1969 paper.[27]

A key element in the review of this approach is the use of Hosler's[30] vertical diffusivity data (for a 0 to 90 m height interval) to determine a useful method of calculation that can be based on available data. Figures 3.5 and 3.6 show the vertical diffusivity plotted versus wind speed and vertical temperature gradient. The widely scattered values in either case are discouraging to the theorist who wishes to use finite difference diffusion terms. Note on Fig. 3.5 that the wind velocity dependence previously chosen for K_z is inconsequential compared to the two-order-of-magnitude scatter of the data. In contrast, an examination of Fig. 3.6 reveals a relatively systematic dependence on vertical temperature gradient. The velocity formula plotted on Fig. 3.5 gives an estimate of vertical diffusivity lying largely in the neutral stability range. This may be expected to approximate conditions averaged over space and time in the marine layer overlaid by an inversion layer.

On the other hand, temperature gradient inputs are apparently far more influential than wind speed inputs in determining vertical diffusivity values. As an improvement on our earlier approach, we have reconstructed

---

*Because of the assumption of uniform horizontal velocity profiles, we take our "ground" elevation to be something like mean rooftop height where the air sampler inlets were located on the Scott stations. This is equivalent to setting $z = 0$ at elevations an order of magnitude or two greater than roughness heights.

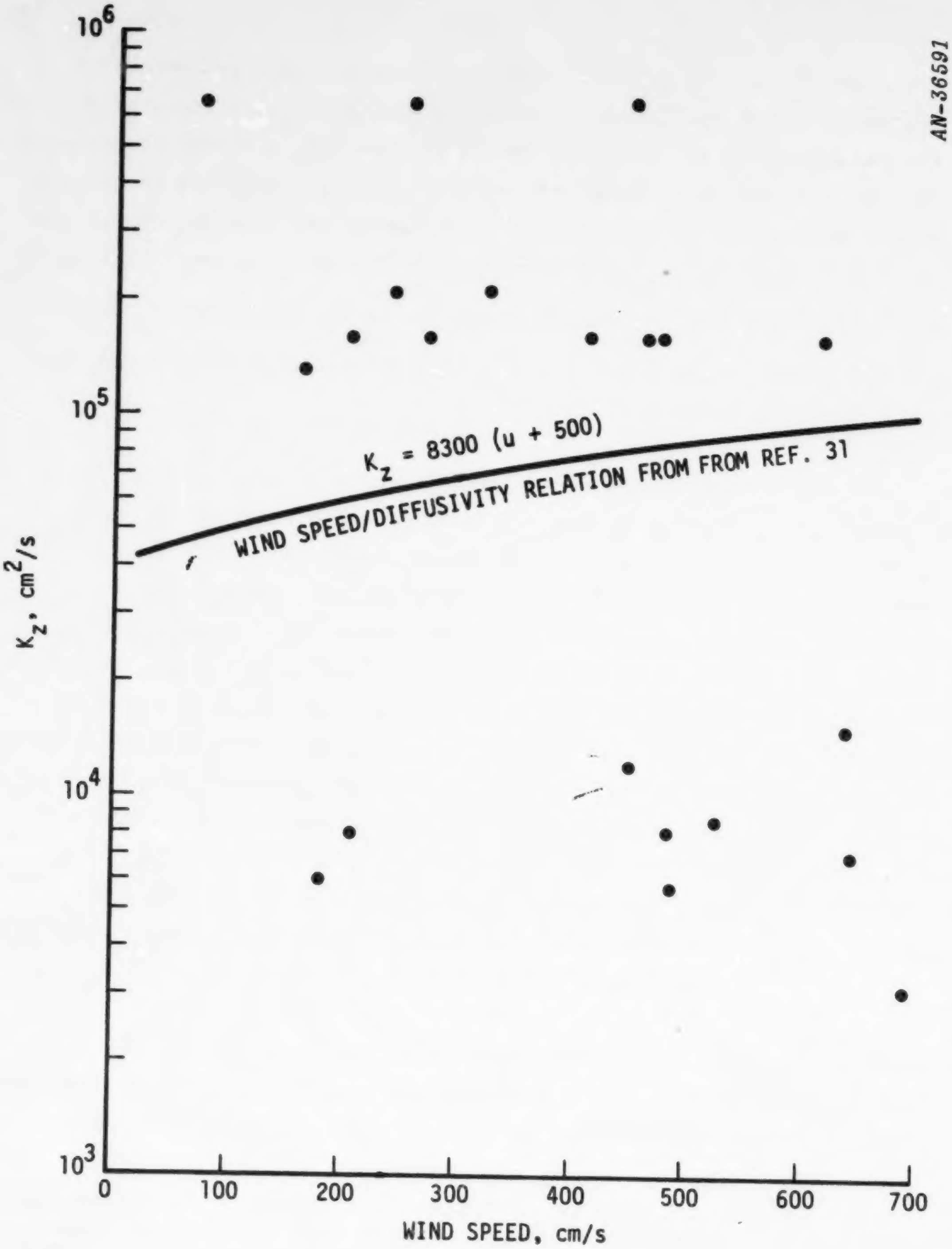

Figure 3.5. Vertical Diffusivity Versus Wind Speed (Ref. 30)

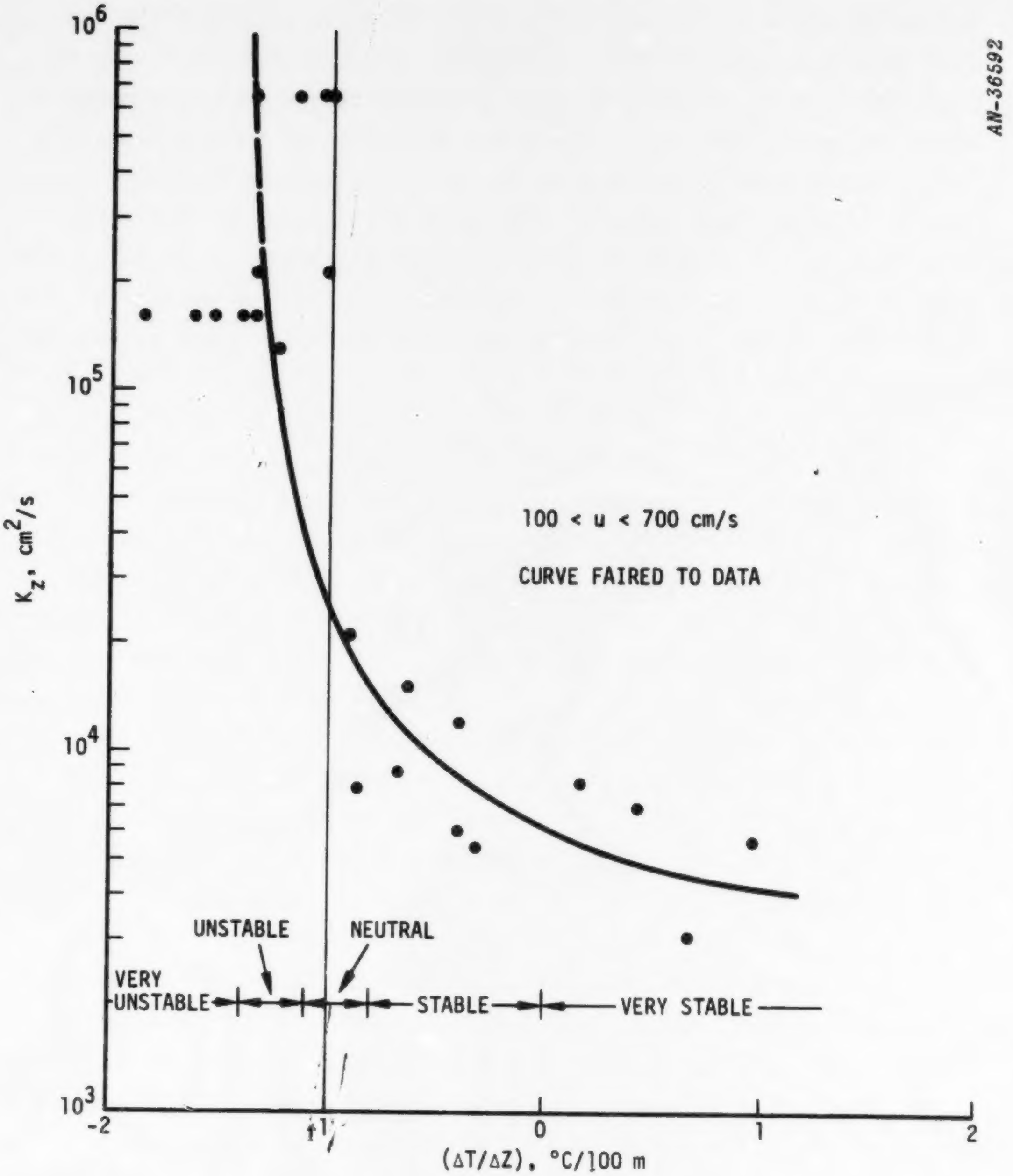

Figure 3.6. Vertical Diffusivity Versus Vertical Temperature Gradient (After Ref. 30)

the diffusivity profiles to represent the broad stability categories delineated along the bottom of Fig. 3.6. Dropping the dependence on wind speed and introducing the dependence on temperature gradient, we might expect a larger dynamic range of diffusivity values throughout any given simulation run. It is difficult to justify any more elaboration on the diffusivity calculation on the basis of the body of theory that depends on fluxes and stresses. The guesses necessary to arrive at a Richardson number or a Monin-Obukhoff length parameter cannot be seriously expected to yield better results than the correlation shown in Fig. 3.6 (especially in view of the poor correlations with Richardson number cited by Hosler).[30]

Having a guide to the choice of the plateau value of vertical diffusivity, we now turn our attention to assigning a ground value for diffusivity. Surface shear stresses typically vary from 1 to 10 dynes·cm^{-2} leading to friction velocity u^* values of 20 to 90 cm/second. For neutral stability conditions $K_z \approx ku^*z$ assuming that the vertical diffusivity approximately equals the eddy viscosity. Typically, the coefficient k takes on values about 0.4 if $u^* \approx 50$ cm/second. Assuming the "ground" plane to be at about 5 meters, we get $K(0) \approx 10^4$ cm^2/second. Considering the larger roughness for urban areas as compared with the surfaces in Table 3.1 on p. 72 of Pasquill's book,[32] this falls just above the range of K values listed there. For very stable conditions as defined on Fig. 3.6, the value of $K(0)$ is likely to be far less than 10^4 cm^2/second.

Translating the ground values and the elevated values of vertical diffusivity (Fig. 3.6) into profiles, we arrive at the data shown on Fig. 3.7. The choice of 50 m for the knee height illustrates a nominal value. Because of uncertainties, this height is taken to be the first mesh point above the ground in a five-point mesh. For mesh ranges typically varying from 100 to 300 m, the knee will be 25 m to 75 m above the ground. Details of K-profile shape at the top of the mesh have little

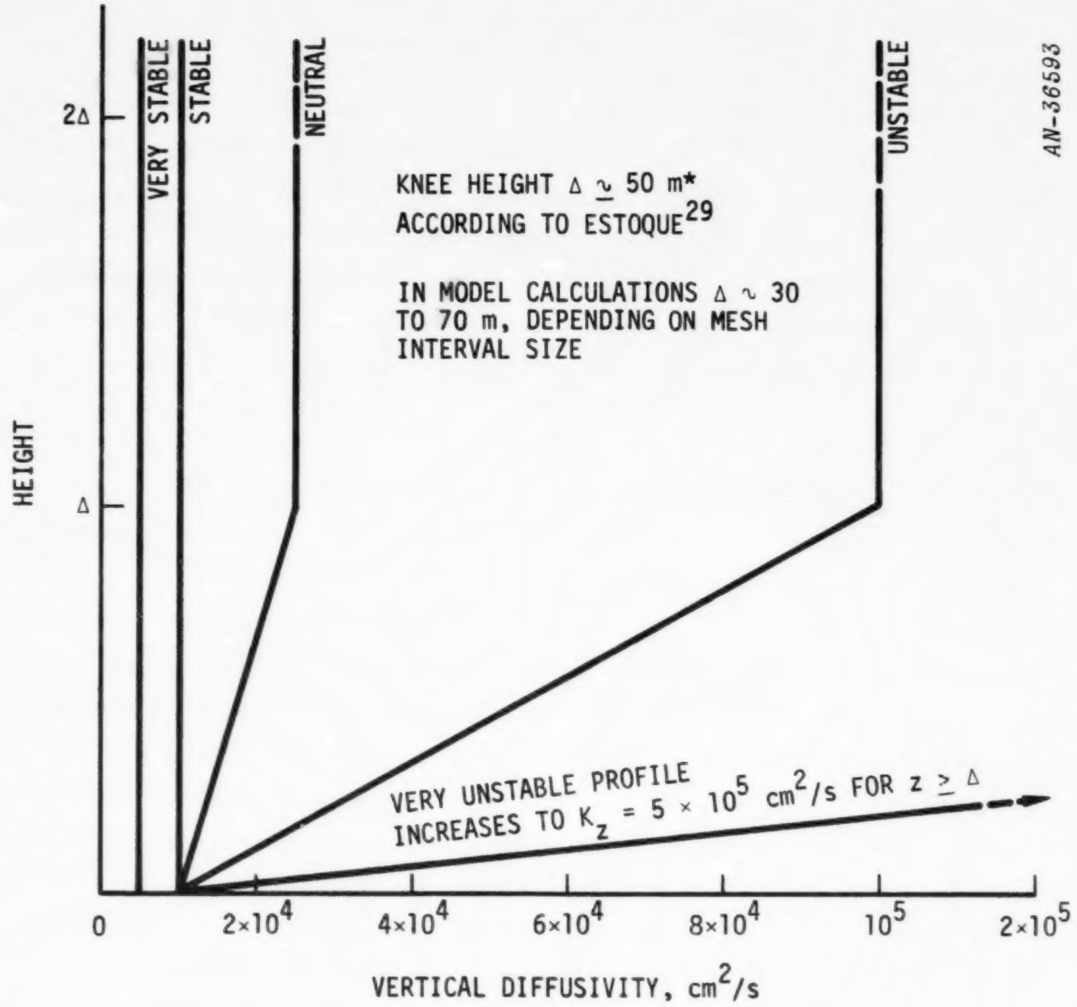

*IN URBAN AREAS OF VERY TALL BUILDING HEIGHTS, ESTOQUE'S ESTIMATE MAY BE TOO LOW; HOWEVER, THIS EXCEEDS ROUGHNESS HEIGHTS IN NEARLY ALL AREAS OVER REGIONAL EXTENT.

Figure 3.7. Vertical Diffusivity Profiles (Fig. 3.6 Defines Stability Categories)

influence for the space and time scales of our modeling calculations; therefore, for photochemical/diffusion validations the profiles are taken to be constant all the way to the top.

Reference to Fig. 3.6 shows how the vertical diffusivity values are assigned. Data on the graph are for 100 cm/second to 700 cm/second wind speed. As mentioned previously, a comparison of Figs. 3.5 and 3.6 shows a tighter grouping of points on the temperature gradient plot than there is on the velocity plot; hence, the use of this correlation in place of the velocity formula. Hybridization of these profiles may be a good approach if the vertical mesh is taken to be higher than the inversion base.

Horizontal diffusivities, K_y , were needed for the transverse diffusion tests of the model that are reported elsewhere. The choice of a typical value, 5×10^6 cm^2/s, was based on the Los Angeles tetroon data of Angell and Pack.[33] One can infer a Fickian diffusion coefficient from the horizontal separation of tetroons flying a few hundred meters above the ground. The values grow with time so that some time scale characterizing the problem must be selected. It will be noted from Fig. 3.8 that the value of K_y selected represents a travel time of about one hour. Figure 3.8 shows lateral separation of simultaneously released tetroon pairs as a function of time since release for flights in morning (IFA) and afternoon (IFP) at Idaho Falls, and flights at Atlantic City (ACY) and Los Angeles (LAX). The heavy line represents the mean of these weighted according to number of cases. Also entered are lateral eddy diffusivity (K_y) isopleths based on Fickian theory, and dissipation isopleths (ε) based on similarity theory (data reproduced from Angell and Pack).[33]

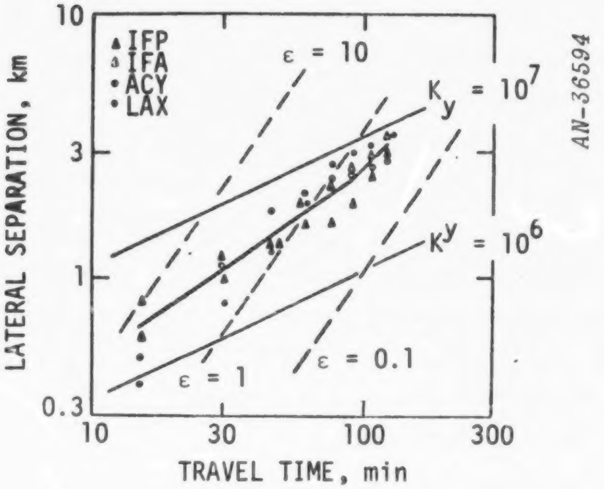

Figure 3.8. Lateral Separation of Simultaneously Released Tetroon Pairs as a Function of Time Since Release (after Ref. 33)

3.4 EMISSION FLUX HISTORIES

For the purposes of production computations, we produced a code that traced air trajectories using a 2-mile interval grid for numerical computations and source inventory compiled by Roberts, Roth, and Nelson.[34] The inputs are wind speeds and headings along line segments of a trajectory. The output is the flux of each pollutant into the air parcel for the time/space-history traced out by the parcel. This code, which was developed by R. Nordsieck prior to the present phase of the work, produces output on punched cards suitable for use as inputs to the GRC photochemical/diffusion model.

The primary revisions made in the emissions model during this study involved (1) the introduction of additional spatial and temporal variations in freeway traffic emissions resulting from vehicle emission rate variations with average speed, and (2) inclusion of a correction factor for surface street emissions to account for the non-uniform temporal distribution of vehicle cold-start emissions.

4 TRANSVERSE DIFFUSION AND ITS EFFECT ON THE GRC MODEL

Two analyses have been conducted to assess the errors incurred in the model calculations due to the omission of transverse diffusion in the semi-Lagrangian formulation. In the first, we have assessed the effects of lateral exchange between adjacent stream tubes. In the second analysis, we have quantified the errors which can result when our Lagrangian control volume passes near an elevated point source, but fails to sweep over it, thus ignoring its contribution that spreads laterally into the control volume. Both of these investigations were performed using our Local Air Pollution Simulation (LAPS) code (see Appendix A, Sec. A.3.2) which incorporates lateral diffusion but is limited to quasi-equilibrium chemistry.

4.1 LATERAL DIFFUSION BETWEEN NEIGHBORING STREAMTUBES

To examine the effect of lateral exchange between "parallel" trajectories, we located a relatively straight trajectory originating at the Commerce station and moving north to Burbank. We then synthesized a parallel trajectory two miles* to the west by simply moving the start point two miles west and assuming an identical wind history. Figure 4.1 shows histories of CO surface flux obtained for these trajectories from our source emissions program. (The fluxes are normalized with respect to air density to yield the somewhat unusual units of meters per minute.) Assuming a 200-m inversion height, and the slightly unstable diffusivity profile shown in Fig. 4.2, the LAPS model was used to simulate atmospheric CO concentrations within two parallel area-source strips 3 km wide.** The lateral cell size was 500 meters, providing six cells over each source strip. Outside boundaries of the horizontal mesh were assumed fully reflecting, simulating a semi-infinite area source on each side. Initial concentrations of CO were set to zero everywhere. Figures 4.3 and 4.4 show the concentration histories obtained along two symmetrically located

---

*Two miles was selected because the minimum resolution which can be expected in our model is set by the two-mile aggregation imposed by the source model.[34]

**The two-mile distance was approximated by 3 km in this test case for convenience in the use of metric units.

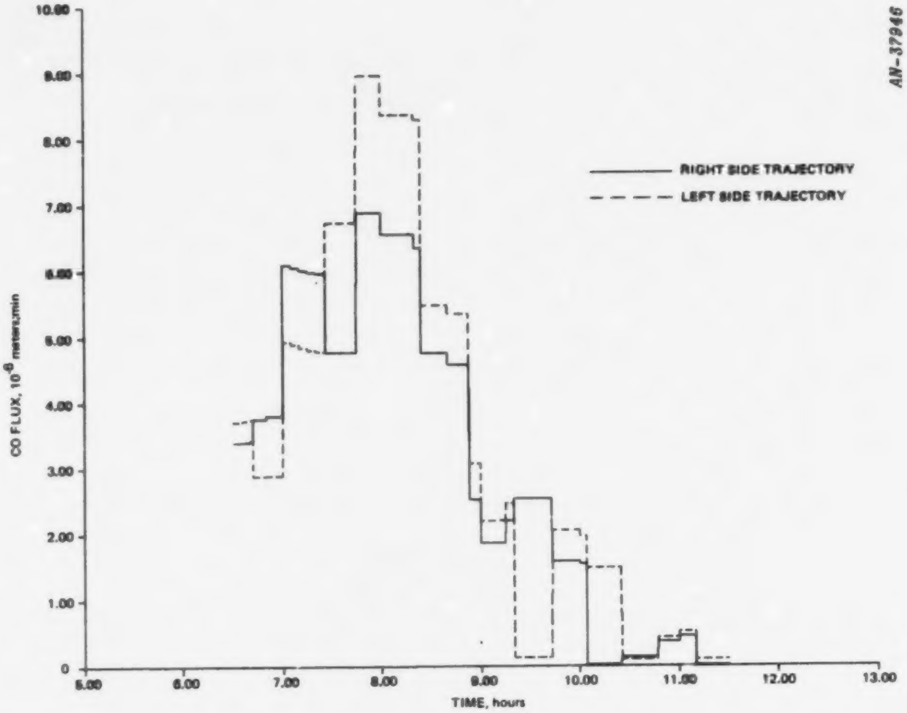

Figure 4.1. CO Flux Histories on Two Neighboring Trajectories

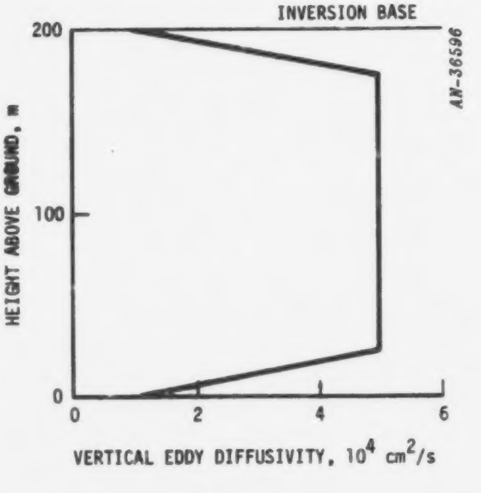

Figure 4.2. Eddy Diffusivity Profile for Neighboring Streamtube Analysis

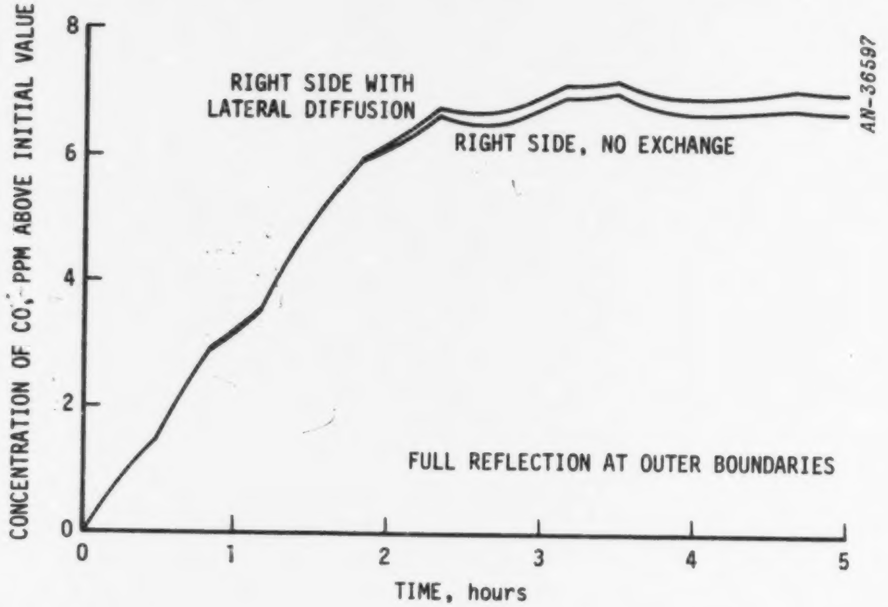

Figure 4.3. CO Concentration Histories on Right-Hand (Commerce) Trajectory

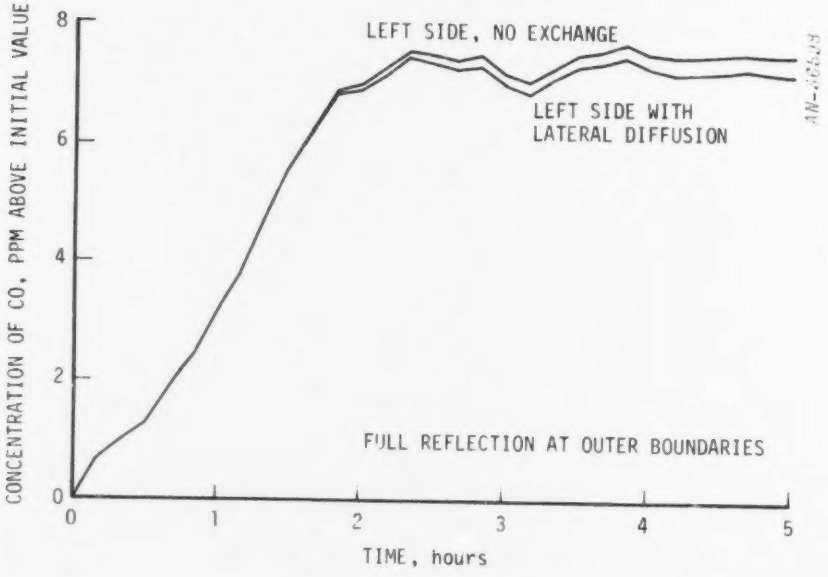

Figure 4.4. CO Concentration Histories on Left-Hand (Synthetic) Trajectory

parallel paths 3.5 km (about 2 mi) apart with and without lateral diffusion (using a lateral eddy diffusivity of 5×10^6 cm^2/s) as discussed in Sec. 3.3. The quantitative differences seem to be small.

To get an idea of what a worst case might be like for the parallel streamtube analysis, we superposed the CO flux histories from 24 test trajectories to indicate the real-world bounds on CO flux histories in the Los Angeles Basin (Fig. 4.5). It was decided that the envelope shown in Fig. 4.6, representing a constant ratio of 3:1 between maximum and minimum, would provide a very acceptable bounding case for two trajectories only two miles apart. Using the simulation parameters described above, the concentration histories shown in Fig. 4.7 were obtained for the worst case comparison.

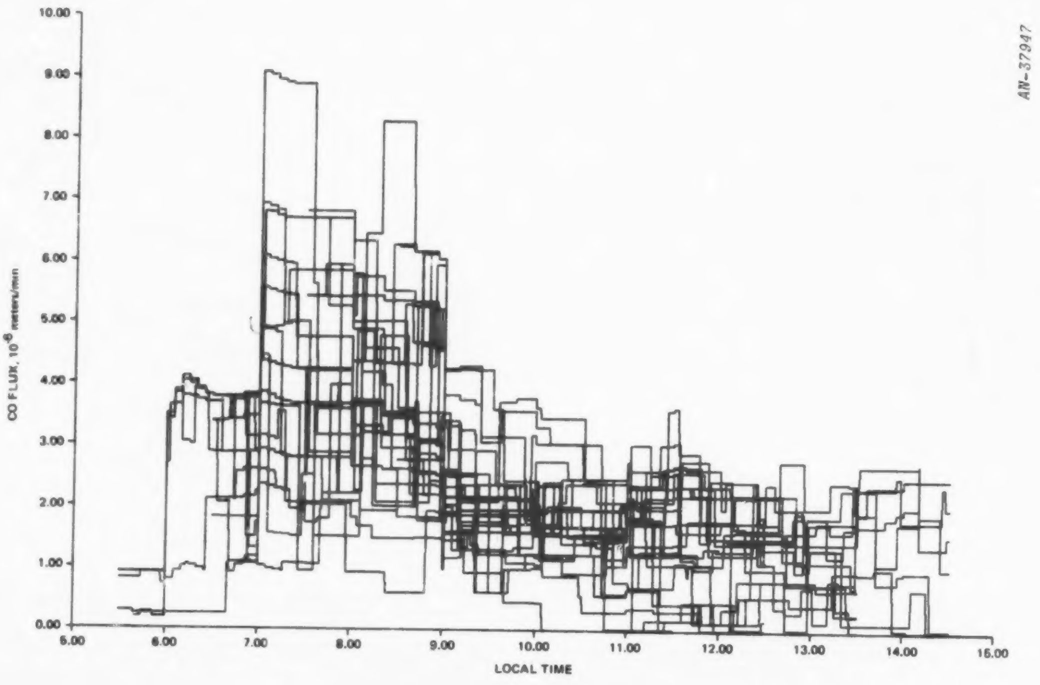

Figure 4.5. Superposed CO Flux Histories for 24 Trajectories

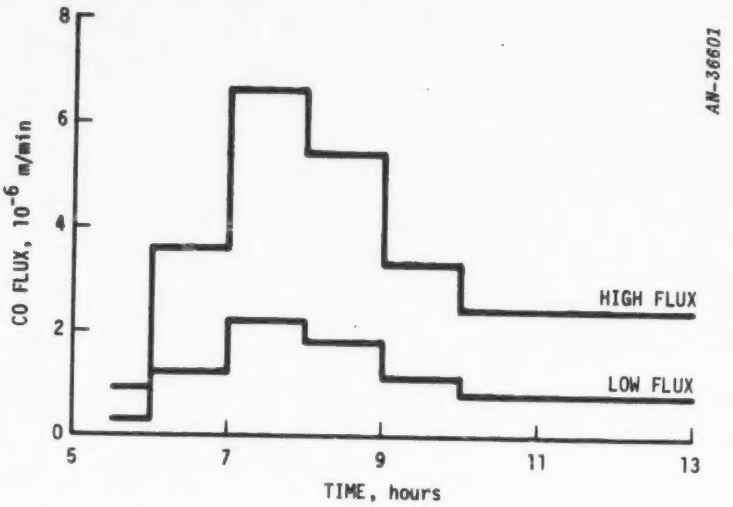

Figure 4.6. Bounding CO Flux Histories for Parallel Trajectory Analysis

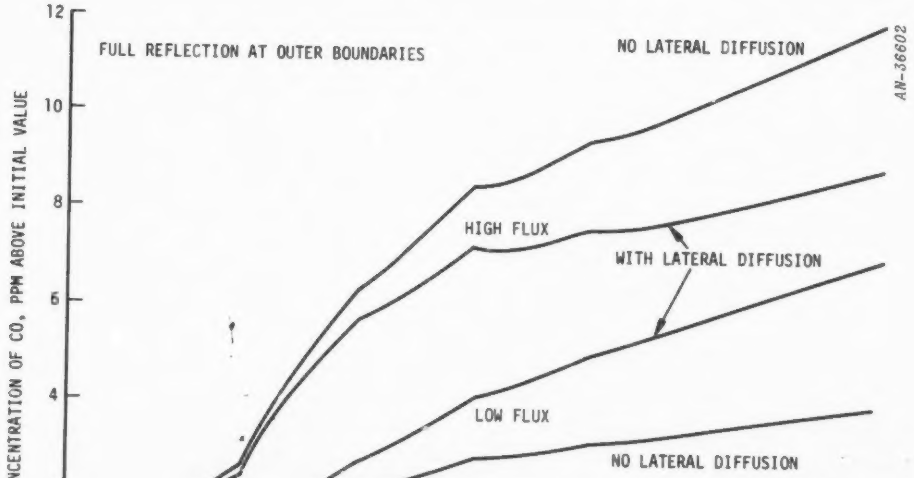

Figure 4.7. CO Concentration Histories for Worst-Case Parallel Trajectories

Table 4.1 summarizes worst case errors that may be encountered under the assumption of zero initial concentration. The fractional error will be lower if the initial concentration is greater than zero. In effect, Table 4.1 shows the worst case errors for increments of concentration rather than for concentration itself. Table 4.2 shows the worst case errors that could be found assuming an initial concentration of 10 ppm of CO, which is a typical early-morning value.

TABLE 4.1

"WORST CASE" BOUNDING ERROR FRACTIONS DUE TO OMISSION OF LATERAL DIFFUSION IN URBAN MODELING ASSUMING ZERO INITIAL CONCENTRATION OF CARBON MONOXIDE

Time	High Flux	Low Flux
5 hr	0.28	0.39
8 hr	0.36	0.44

TABLE 4.2

"WORST CASE" BOUNDING ERROR FRACTIONS DUE TO OMISSION OF LATERAL DIFFUSION IN URBAN MODELING, ASSUMING AN INITIAL CONCENTRATION OF CARBON MONOXIDE OF 10 PPM

Time	High Flux	Low Flux
5 hr	0.12	0.14
8 hr	0.17	0.19

4.2 LATERAL DIFFUSION EFFECTS IN THE VICINITY OF HIGH-FLUX ELEVATED POINT SOURCES

A quantitative assessment of the pollutant contributions of high-flux elevated point sources to neighboring trajectories was performed in a parametric fashion, by determining the ranges of real-world surface fluxes and point source fluxes encountered in the Los Angeles Basin and examining the results of superposing various combinations.

Power plant stacks were chosen as typical high flux elevated pollutant sources, and hence, in order to set background fluxes, we needed to establish the range of surface NO fluxes encountered in the Basin. Proceeding as with the CO fluxes, Fig. 4.8 shows the NO flux histories obtained for our 24 test trajectories. The heavy lines indicate the three fluxes selected from the range of NO fluxes encountered. They are equivalent to 10, 15 and 20 kg/hr/km^2. The source model of Science Applications,

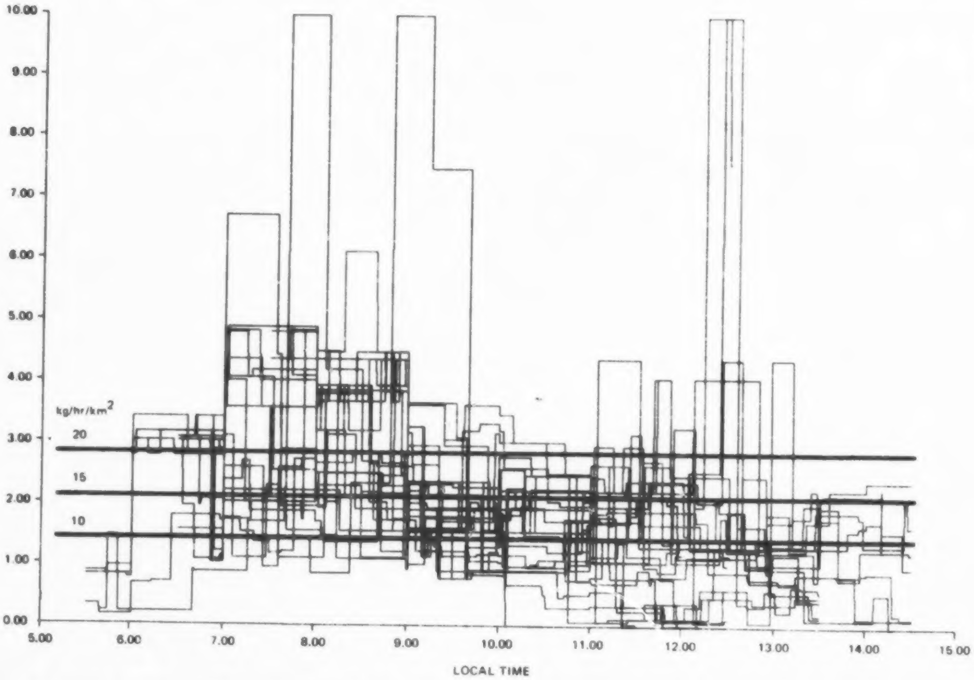

Figure 4.8. Superposed NO Flux Histories for 24 Trajectories

Inc.[34] shows a distribution of power plant NO fluxes ranging up to 532 kg/hr (1172 lb/hr). From this distribution, we chose nominal stack NO fluxes of 60, 200, and 600 kg/hr as including roughly 33%, 67%, and 100% of the power plants on a relative occurrence basis. An effective point source height of 100 meters was used to include the height of an average stack plus the additional plume rise due to jet momentum and buoyancy effects.

The meteorological conditions simulated for these cases included an inversion base height of 183 meters with neutral (2×10^4 cm^2/s) diffusivity below the inversion and very stable (5×10^3 cm^2/s) above. The resulting profile of vertical eddy diffusivities is shown in Fig. 4.9. As before, the lateral diffusivity was set at 5×10^6 cm^2/s. A light wind of 1 m/s (about 2 knots) was assumed.

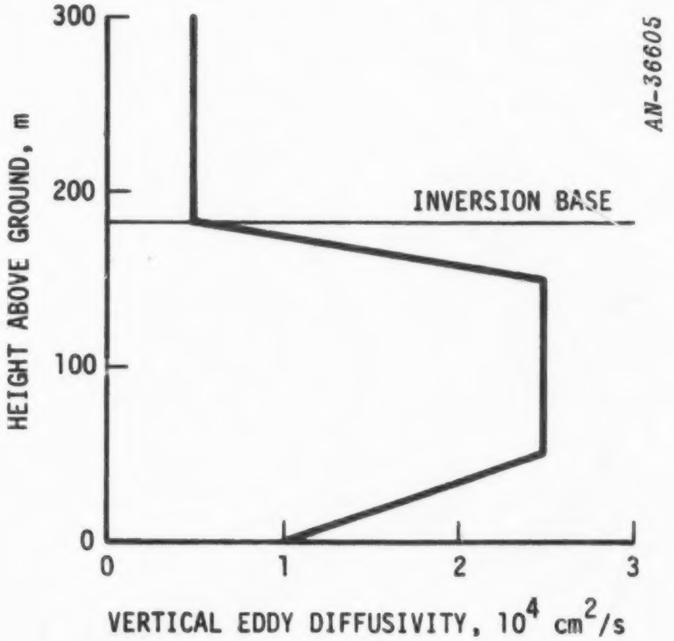

Figure 4.9. Eddy Diffusivity Profile for Elevated Point Source/Lateral Diffusion Analysis

Since the object of these tests was to assess the effect of lateral diffusivity on trajectories missing large point sources, and the basic resolution of our source model is two miles, we have chosen to simulate the average situation in which the stack is centered in a neighboring two-mile-wide path and we are reading concentrations two miles distant at the center of another two-mile swath. Accordingly, Figs. 4.10, 4.11, and 4.12 show NO concentrations at the ground, two miles from the plume centerline for each of the three background NO fluxes combined with stack NO fluxes of 0, 60, 200, and 600 kg/hr. Below these curves, Figs. 4.10, 4.11, and 4.12 plot the corresponding percent error incurred if lateral diffusion were ignored and only the background flux is accounted for. Table 4.3 summarizes the maximum fractional errors associated with each combination of background and stack fluxes. Even under the worst conditions, these error percentages are much smaller than NO-flux uncertainties.

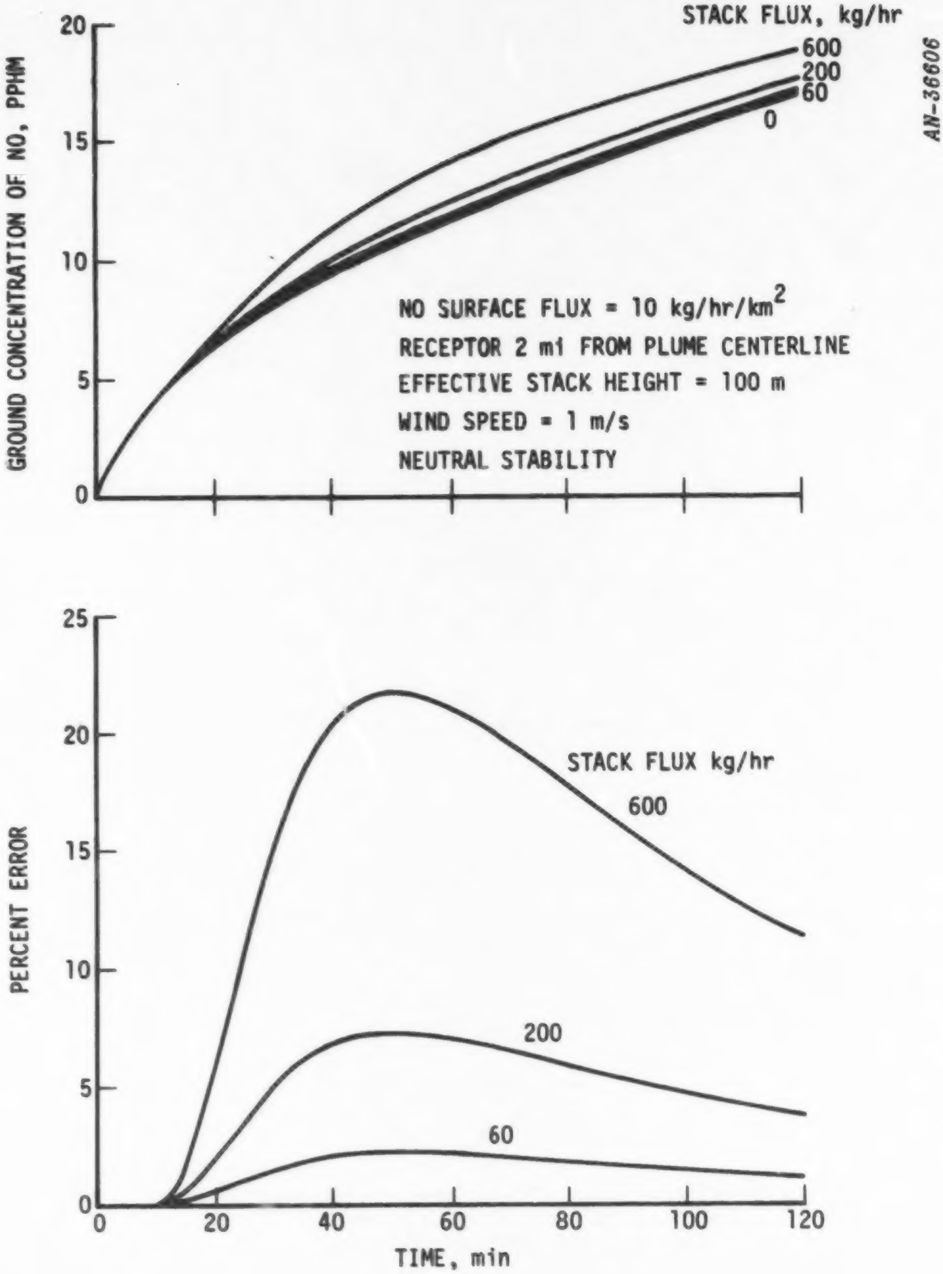

Figure 4.10. Ground Concentration Effects of Elevated Point Sources: 10 kg/hr/km^2 Background Flux

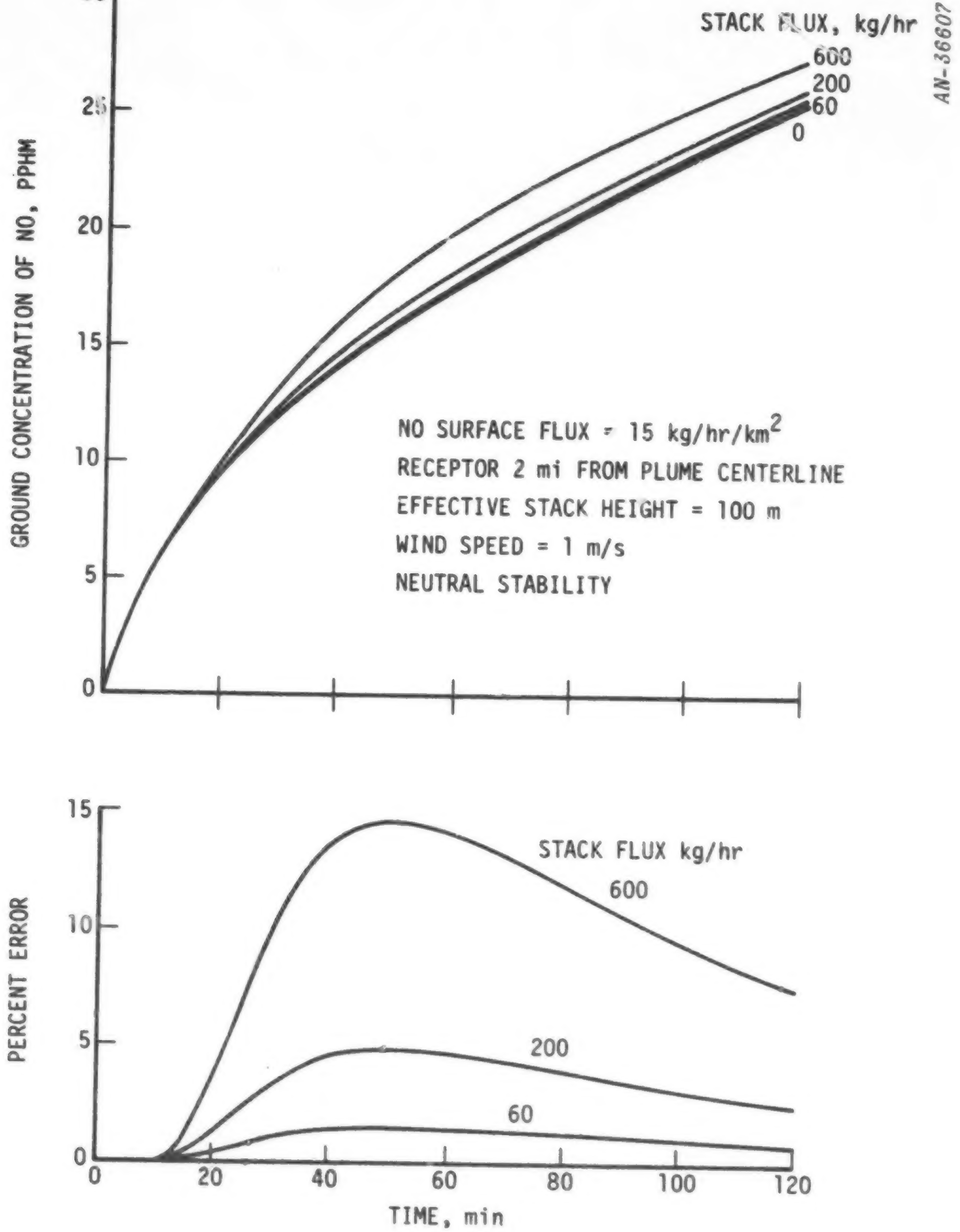

Figure 4.11. Ground Concentration Effects of Elevated Point Sources: 15 kg/hr/km^2 Background Flux

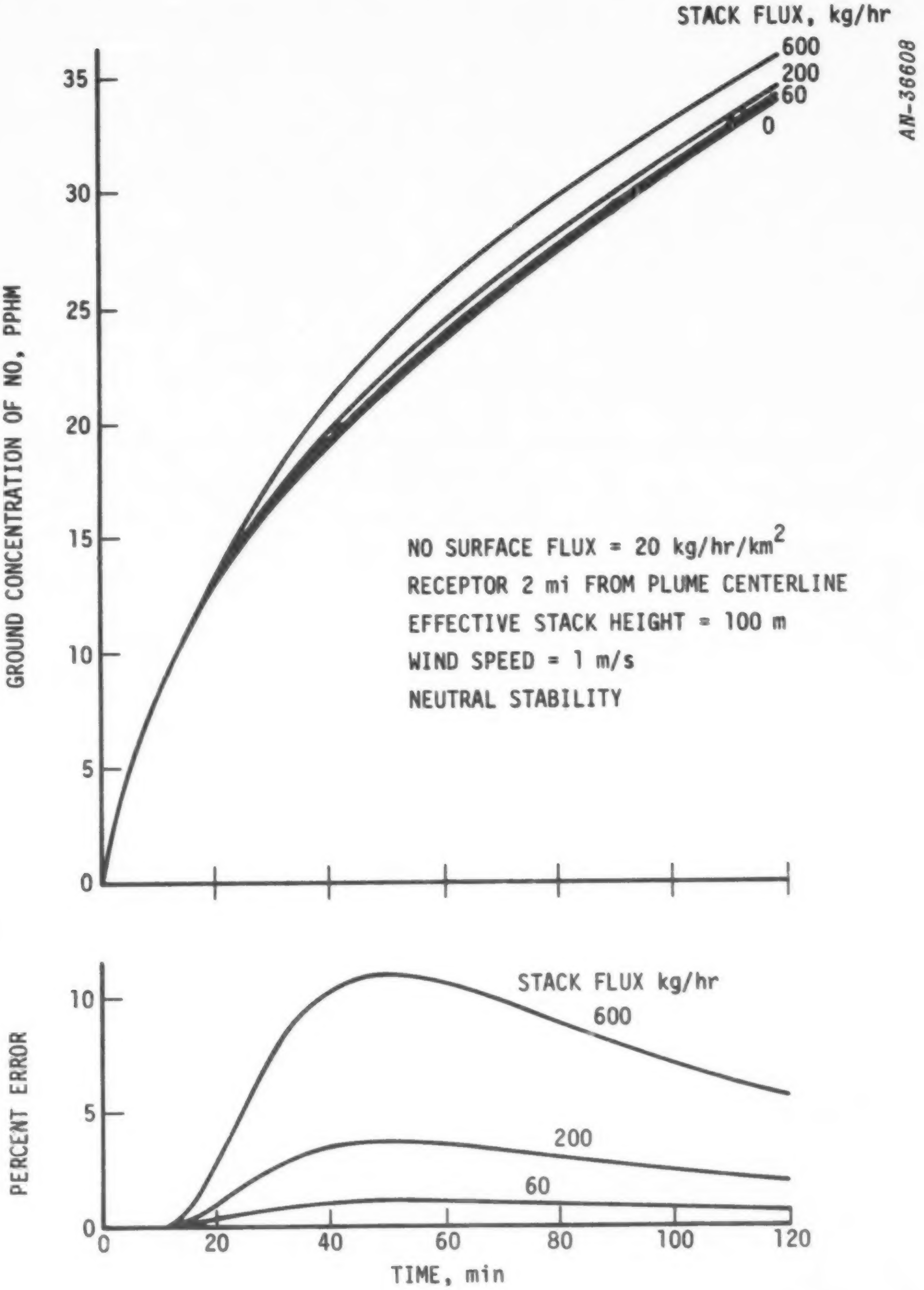

Figure 4.12. Ground Concentration Effects of Elevated Point Sources: 20 kg/hr/km^2 Background Flux

TABLE 4.3

MAXIMUM FRACTIONAL CONTRIBUTION OF AN ELEVATED POINT SOURCE AT A GROUND LOCATION TWO MILES FROM THE PLUME CENTERLINE

Effective Stack Height = 100 m

Neutral Stability, 2 knot wind

		Stack Flux, kg/hr		
		60	200	600
Average Surface Flux, kg/hr/km^2	10	0.022	0.072	0.217
	15	0.015	0.048	0.145
	20	0.011	0.036	0.109

5 VALIDATION STUDIES

5.1 SELECTION OF DAYS FOR MODEL TESTS

The culmination of the improvements in chemistry and meteorology is a set of controlled retests of the GRC Photochemical/Diffusion model and a conversion of the code to IBM 360-compatible form. The selection of days was originally predicated on a consistent basis with the design of the Scott Research Laboratories Los Angeles Basin Program;[35] namely, that morning air movements from Commerce to El Monte would be studied. The design philosophy was that primary pollutants (reactants) would be carefully measured at Commerce with special emphasis on gas chromatographic resolution of hydrocarbon samples. Advection and reaction of the air mass would then occur with the composition of the secondary pollutants (products) indicated by (hopefully) downwind measurements taken at El Monte. To implement this philosophy, we conducted a systematic search for days having morning air trajectories that nearly connected the two stations. The original program design did not consider the use of Los Angeles County Air Pollution Control District station data because they are difficult to obtain and they are not as detailed as the Scott Research Laboratories station data.

According to the field program objectives, our rationale for a requested selection of 9/4/69, 9/15/69, 9/27/69, 10/16/69, 10/29/69, and 11/4/69 was based on air movement calculations. To get these dates, we calculated trajectories that could be used to validate the transport/diffusion module (and ultimately the photochemical/diffusion model). The calculations used the 1969 Scott Research Laboratories data which were collected at Commerce and El Monte in the Los Angeles Basin. We performed a search for trajectories which originated at Commerce in the morning and arrived at El Monte later in the day. The search was accomplished using a special trajectory-generation program designed to compute a wind trajectory between two stations given wind speed and direction data at each station. The program calculates inverse distance-weighted averages of wind speed and direction between the stations and uses these quantities to generate the trajectory. The output of the program consists of the following trajectory descriptors:

1. Geographical coordinates of the air parcel
2. Time, wind speed, and direction of the air parcel at every point in the trajectory
3. Distance of the air parcel from each of the two reference stations

A computer plot of the trajectory can be obtained on an optional basis.

The program has the capability to detect and compensate for anomalies in the data such as missing data points. Moreover, the program warns the user about the existence and nature of the data defects and of the actions taken to overcome the deficiencies. This allows the analyst to assess the reliability of a trajectory.

We considered an air parcel to have "arrived" at El Monte if it passed within one mile of El Monte. The search examined all the trajectories originating at Commerce from 0600 to 0900 for the 72 days (Aug. 28 to Nov. 7) of data available at both Commerce and El Monte. A total of 1368 possible trajectories over the 72 days were computer-analyzed. Only 87 trajectories spread over 12 days were found to satisfy the miss-distance criterion of one mile or less. Additional evaluation of the wind and aerometric data eliminated five of these days, thus leaving only seven possible days with usable trajectories. The seven days are listed below in order of number of trajectories available on each day:

Date	No. of Trajectories	Peak CO (ppm) (Commerce)	Peak O_3 (pphm) (El Monte)
Oct. 16	18	7.9	10.0
Nov. 4	9	25.2	12.0
Sept. 4	9	12.2	18.1
Oct. 29*	8	18.4	19.0
Sept. 6*	6	10.2	14.6
Sept. 15	3	10.0	5.4
Sept. 27	3	5.0	24.5

---

*Missing data

For Sept. 6, El Monte is missing NO_x, HC, and CO data. For Commerce, we found that Oct. 29 is missing the NO measurements for the interval 0600-0730, which is precisely the interval when the trajectories originate. The El Monte data could have been supplemented by LAAPCD Azusa data, except for the hydrocarbon measurements. Supplementing the Commerce data may not have been possible, since no LAAPCD station is located nearby.

The program objectives were then redirected and the original two-station concept was discarded. The newly adopted selection criteria stressed availability of airborne temperature data and high peak oxidant. All but two of the requested dates were discarded in favor of the following set of dates: 9/11/69, 9/29/69, 9/30/69, 10/29/69, 10/30/69, and 11/4/69.

The chemical data for Sept. 29 are satisfactory and the point of closest approach to El Monte is less than a mile. However, the time of closest approach occurs around 1100. Thus for a start time of 0600, we have only a five-hour travel time. The data for September 11 are excellent, but for a 0600 Commerce start, the trajectory misses El Monte by about 6 miles and would require interpolation to estimate the final concentrations. The trajectories for Sept. 30 and Oct. 30 move in a westerly direction from Commerce and would also require interpolation at the destination point.

The decision to obtain Los Angeles County Air Pollution Control District data and to carry out validation studies for these days forced changes in our fundamental approach. Because of critical dependence of model results on initial conditions, we sought trajectories beginning at stations having hydrocarbon data[*] in addition to measurements of other pollutants. With one exception, the trajectories were source-oriented rather than receptor-oriented. As mentioned previously, weighted averages of air quality values were computed from station measurements for each hourly node of each trajectory.

Three days were designated to allow adjustments in parameters. These so-called "hands-on" days are 9/29/69, 9/30/69, and 10/29/69. The remaining three days are reserved for testing the fully adjusted model without manipulation of coefficients. These so-called "hands-off" days are 9/11/69, 10/30/69, and 11/4/69. The hands-off days have lower peak oxidant (generally) than the hands-on days.

5.2 PROGRAM CONVERSION

Conversion of the DIFKIN program for operation on the IBM 360/50 was completed early in the present phase of the work. Specific tasks carried out can be grouped into the following categories:

1. Elimination of nonstandard software which is incompatible with the IBM 360/50.
2. Inclusion of FORTRAN software which is characteristic of the IBM 360/50 and cannot be used in our CDC 6400
3. Testing the accuracy of the solution to a sample problem to determine the effect of the reduced precision of the IBM 360/50 (see Sec. 5.2.1)
4. Determining the differences in running time between CDC 6400 and IBM 360/50 (see Sec. 5.2.2)

---

[*] The stations are Commerce, El Monte, Downtown, East San Gabriel Valley, and West San Gabriel Valley.

5. Producing a punched deck of cards whose character code is that used by the IBM 360/50. (Extended BCD for IBM 360/50 compared to BCD for CDC 6400.)

6. Eliminating diagnostic statements used when the program was being developed.

7. Using a capability of our computer center to generate a source deck with all the statement numbers sequentially ordered for maximum readability.

5.2.1 Precision Test

A sample problem consisting of a polluted air parcel sweeping over a heavily used freeway was run in single-precision mode on both the CDC 6400 and the IBM 360/50 and the results compared. For reference purposes, we recall that the precision of the CDC 6400 and the IBM 360/50 is 14 and 7 decimal digits, respectively. Thus we might expect some difference in the results produced by each machine. Analyzing the answers, we found that they agree to four significant figures and differ by at most two units in the fifth (least) significant digit. Thus the difference is 2 parts in 10,000 at worst. The table below shows the frequency and magnitude of the divergence for one of the eleven species computed; the total number of points sampled is 300.

Units of Difference in Least Significant Digit	Number of Points
0	65
1	227
2	8

Regarding the conversion, two comments are in order. The first is that since the computational technique is unconditionally stable, no problems are anticipated due to amplification of the roundoff error. The second is that for the major species, i.e., NO, NO_2, HC, O_3, CO, the three most significant figures are sufficient for comparison with experimental data.

5.2.2 Timing Test

The test problem ran for a considerably longer time in the IBM 360/50 than in the CDC 6400. For example, total running time for the IBM 360/50 was 18.6 minutes to compute 30 minutes of real time, for a real time/computer time ratio of 1.6:1. For the CDC 6400, the figures are 4.4 minutes of computer time to compute 60 minutes of real time, for a ratio of 14:1. Thus the running time was increased by more than a factor of 8. Recent improvements have greatly improved the speed ratios since these timing tests were conducted. Consequently, the running time for either system should be reduced considerably to reflect current practice.

5.3 ATMOSPHERIC VALIDATION TESTS

5.3.1 Introduction

In this section, we report the results of validation tests carried out for four trajectories on each of the following six days: Sept. 11, 29, 30, Oct. 29, 30, and Nov. 4, all in 1969. Three of the trajectories also serve as baseline cases for the transportation control strategy study which is described in a separate volume.

September 29, 30, and Oct. 29 have been designated to be so-called "hands-on" days for validation purposes. This means that parameter adjustments can be made in order to improve simulations of the measured concentration histories of the various pollutants. The adjustable parameters are the diffusion coefficients and the rate constant of the reaction $OH + HC \rightarrow (b_2)RO_2$, designated by k_4 . The experience gained from working with the hands-on days is then used to develop guidelines for parameter selection to simulate air quality for the remaining three days, Sept. 11, Oct. 30, and Nov. 4. The latter are thus designated "hands-off" days. The guidelines and the inputs that are necessary to apply them are described later in the report.

In addition to the test results, this section also contains descriptions of the test procedures and criteria used in evaluating the model. As a necessary adjunct to model evaluation, data base errors are examined and illustrative examples given. The test results are also assessed on the basis of statistical correlations between predicted and observed concentrations.

A map of the Los Angeles Basin which contains the location of the monitoring stations is included in Fig. 5.1; the legend for the abbreviations used on the map is found in Table 5.1. A list of the trajectories is shown in Table 5.2 and the initial concentrations used in the simulations are in Table 5.3.

5.3.2 Approach and Criteria for Model Evaluation

The approach taken for the hands-on cases was to use CO concentration histories to determine the diffusivity parameters for each trajectory. The diffusivities thus obtained were then applied without change to the same trajectory with the reactive species. Because of spatial variability of meteorological conditions, all the trajectories for a single day could not generally be described by the same diffusivity coefficients. In addition, it was necessary to adjust the rate constant k_4 for the reaction $OH + HC \rightarrow (b_2)\ RO_2$ for some of the reactive cases. Subsequently, guidelines were worked out for determining the diffusivities and k_4 to be used in the hands-off cases. These guidelines appear in Sec. 5.4.

Some remarks are in order about the nature of the test that is applied to the computed concentrations in relation to observed concentrations. Let us begin by reviewing the simulation process: the computed results represent the history of the pollutants in an air parcel which traverses a geographical area following a path determined by the local hourly average wind speed and direction.

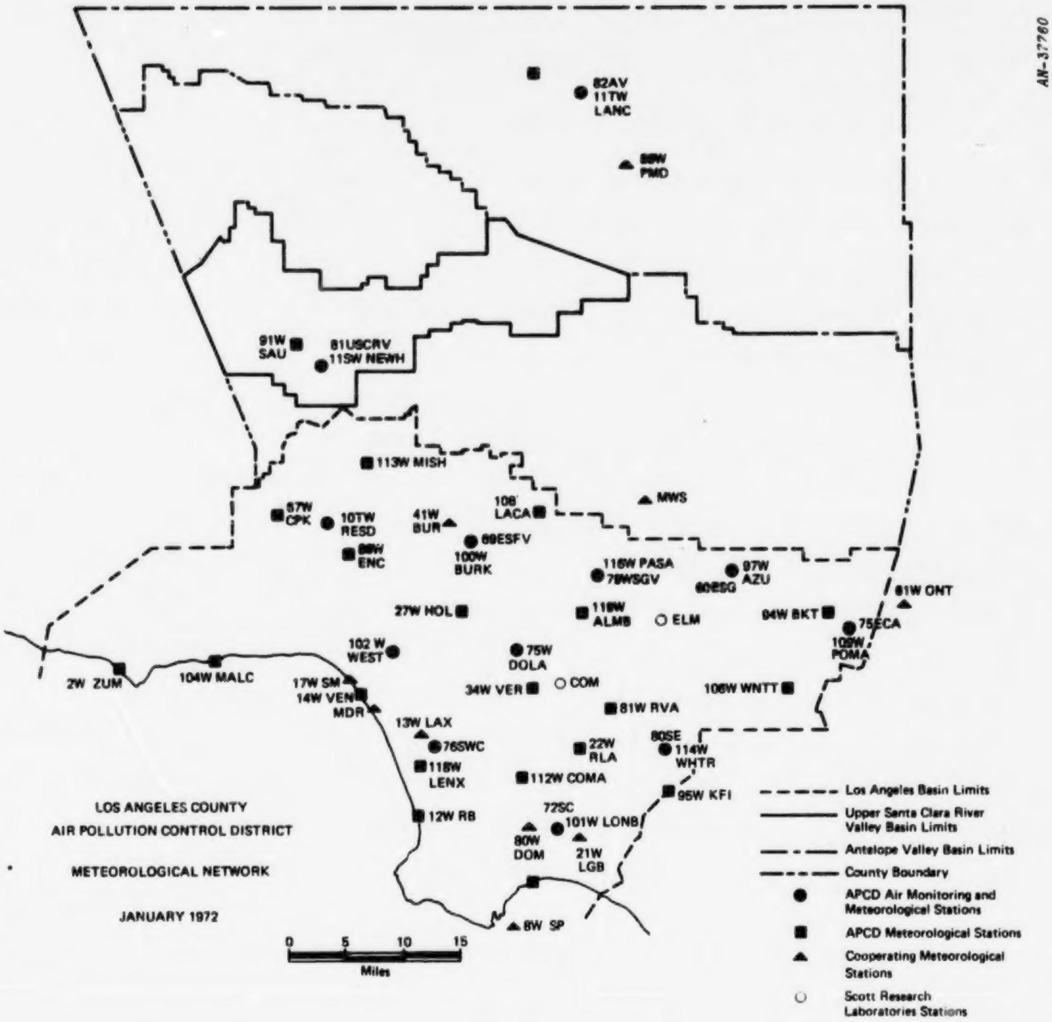
82AV
11TW
LANC
99W
PMD
91W
SAU
81USCRV
115W NEWH
113W MISH
MWS
108
LACA
57W
CPK
10TW
RESD
41W
BUR
69ESFV
88W
ENC
100W
BURK
116W PASA
79WSGV
97W
AZU
80ESG
81W ONT
27W HOL
118W
ALMB
ELM
94W BKT
75ECA
109W
POMA
102 W
WEST
75W
DOLA
2W ZUM
104W MALC
17W SM
14W VEN
MDR
34W VER
COM
106W WNTT
81W RVA
13W LAX
76SWC
22W
RLA
80SE
114W
WHTR
118W
LENX
112W COMA
95W KFI
12W RB
72SC
101W LONB
80W
DOM
21W
LGB
8W SP
LOS ANGELES COUNTY
AIR POLLUTION CONTROL DISTRICT
METEOROLOGICAL NETWORK
JANUARY 1972
0
5
10
15
Miles
Los Angeles Basin Limits
Upper Santa Clara River Valley Basin Limits
Antelope Valley Basin Limits
County Boundary
APCD Air Monitoring and Meteorological Stations
APCD Meteorological Stations
Cooperating Meteorological Stations
Scott Research Laboratories Stations
AN-37760

Figure 5.1. Air Quality and Meteorological Monitoring Network in the Los Angeles Basin

TABLE 5.1

DIRECTORY OF AIR QUALITY AND METEOROLOGICAL MONITORING STATIONS IN THE LOS ANGELES BASIN

Abbreviation	Location
ALMB	Alhambra
AZU	Azusa - East San Gabriel Valley
BRT	Brackett
BUR	Hollywood-Burbank Airport
BURK	Burbank - East San Fernando Valley
COMA	Compton
CPK	Canoga Park
DOLA	Downtown Los Angeles - LAAPCD Headquarters
DOM	Dominguez
ELM	El Monte
ENC	Encino
FOX	Gen. Wm. J. Fox Airfield
HOL	Hollywood
KFI	KFI Transmitter
LACA	La Cañada
LANC	Lancaster
LAX	Los Angeles International Airport
LENX	Lennox
LGB	Long Beach Airport
LONB	Long Beach - South Coast
MALC	Malibu
MDR	Marina del Ray

TABLE 5.1 (Cont.)

Abbreviation	Location
MISH	Mission Hills
MWS	Mount Wilson
NEW	Newhall
NP	Newport Beach
NTB	Los Alamitos Naval Air Station
ONT	Ontario International Airport
PASA	Pasadena - West San Gabriel Valley
PICO	Pico
PMD	Palmdale Airport
POMA	Pomona
RB	Redondo Beach
RESD	Reseda
RLA	Rancho Los Amigos
RVA	Rivera
SAU	Saugus
SM	Santa Monica
SP	San Pedro
VEN	Venice
VER	Vernon
WEST	West Los Angeles
WHTR	Whittier
WNTT	Walnut
ZUM	Zuma Beach

TABLE 5.2

TRAJECTORY IDENTIFICATION TABLE

Trajectory Number	Date	Origin	Start Time	Closest Terminal Station	Final Time
1	Sep 11	Commerce	0530	Rancho Los Amigos	1330
2	Sep 11	Commerce	0630	La Cañada	1330
3	Sep 11	Downtown Los Angeles	0530	West San Fernando Valley	1230
4	Sep 11	Downtown Los Angeles	0630	Mission Hills	1330
5	Sep 29	Commerce	0530	Azusa	1230
6	Sep 29	Commerce	0630	East San Gabriel Valley	1330
7*	Sep 29	Downtown Los Angeles	0530	Walnut	1230
8*	Sep 29	Near Coast	0230	Anaheim	1230
9	Sep 30	Commerce	0530	La Cañada	1130
10	Sep 30	Commerce	0630	La Cañada	1130
11	Sep 30	Downtown Los Angeles	0430	La Cañada	1130
12	Sep 30	Downtown Los Angeles	0530	Burbank	1030
13	Oct 29	Downtown Los Angeles	0530	Whittier	1230
14	Oct 29	Downtown Los Angeles	0630	Walnut	1330
15	Oct 29	Commerce	0630	Walnut	1330
16	Oct 29	El Monte	0830	Azusa	1330
17	Oct 30	Pasadena	0530	Orange County	1330
18	Oct 30	Commerce	0630	Long Beach	1030
19	Oct 30	El Monte	0630	Orange County	1430
20	Oct 30	Downtown Los Angeles	0830	Long Beach	1230
21	Nov 4	Commerce	0530	El Monte	1130
22	Nov 4	Commerce	0630	La Cañada	1230
23	Nov 4	Pasadena	0530	La Cañada	1130
24*	Nov 4	Downtown Los Angeles	0530	Mission Hills	1430

---

*Trajectories used in transportation control strategy study.

TABLE 5.3

INITIAL CONCENTRATIONS USED IN ATMOSPHERIC SIMULATIONS

Trajectory Number	CO, ppm	Initial Concentrations		NO_2, pphm
		NO, pphm	HC, pphm	
1	5.3	25	60	10
2	8	17	60	11.6
3	11	10	25	3
4	14	14	25	3
5	9	39.9	67	11.1
6	12	43.5	77	10.1
7	7	16	40	4
8	7	2	18	9
9	15.9	67.5	117	9.8
10	22	70	129	12
11	13	35	45	5
12	19	38	65	3
13	9	5	30	11
14	11	25	30	15
15	11	30	24	10
16	6	12	30	20
17	6	21	30	13
18	8	48	63	11
19	8.5	23	27	13.5
20	8	13	25	6
21	16	36	100	18
22	23.2	72.6	130	15.4
23	6	3	25	9
24	14	35	40	13

The test that is applied to the computed concentrations consists of comparing the model's results with data which are obtained from air monitoring stations. This is a severe test inasmuch as an attempt is being made to match computation and data in magnitude, time phasing, and space. Consideration of data base errors becomes important in the application of such a test and these are discussed in the next section.

For CO, the criterion of goodness of fit consists of matching the observed concentrations with the computed results. For the reactive species, we focused on matching the computed ozone concentration with the observations. The close photochemical coupling among NO, NO_2, and O_3 in many instances precluded a good match for all three species, since a parameter adjustment made to improve the fit of one of the three would degrade the match of the others. (Such close coupling is obscured in the averaged atmospheric samples used in the comparison process since turbulence effects may interfere--see Appendix A.) Since ozone is generally considered to be the key indicator of photochemical smog, it was felt that a good ozone fit at the possible expense of the others was justified.

5.3.3 Data Base Errors

As was mentioned above, the test of the model consists of comparing the computed concentrations with observations along an air trajectory. However, because of the sparseness of the air quality monitoring network, the monitoring stations will not be on the path of the trajectory as a general rule. Hence, the data used for comparison must be obtained by spatial interpolation (in our case, we use inverse-distance weighting) from those monitoring stations which are nearest to the trajectory's nodes. The model tests compare concentrations computed by the model with concentrations which are interpolated from air monitoring data. Therefore, the spatial interpolation itself can result in large errors that bear no relationship to the validity of the model. An estimate of these errors can be obtained by performing the interpolation for a known monitoring station and then comparing the actual and computed quantities. Such an exercise was carried out using LAAPCD stations 1 (Downtown Los Angeles), 60 (East San Gabriel Valley), and 69 (East San Fernando Valley) for the measured data, and station 79 (West San Gabriel Valley) as the point where the concentration is assumed unknown. The results for ozone showed that the relative error, i.e., |true-computed|/true, ranged from 6% to 63% with an average error of 35% for Sept. 29, 1969. For ozone on Nov. 4, 1969, the error ranged from 0% to 33% with an average of 20%. However, the absolute differences in concentration ranged from 0.3 to 25.8 pphm for Sept. 29 and from zero to 4.1 pphm on Nov. 4. In presenting the results in graphical form as a comparison of model vs data it is the absolute difference, rather than the relative error, which is immediately apparent to the eye. This is clear from Figs. 5.2 and 5.3, which show the interpolated and actual concentrations for ozone on the two days mentioned previously. The actual concentration is measured at station 79 (West San Gabriel Valley) and the stations used for interpolation are 1 (Downtown Los Angeles), 60 (East San Gabriel Valley), and 69 (East San Fernando Valley). Some sources of error in the interpolation are the spatial inhomogeneities in source distribution, meteorological conditions, and terrain. All of these affect the production and flow of pollutants in the area in question and thereby influence the pollutant levels. Indeed, the appropriateness of assuming that the pollutant concentrations at a point are representative of the levels in a region is the basic tenet that comes under scrutiny when one considers the sources of error in the interpolation. Mathematical models such as the one being evaluated in this work may actually help to solve the problem of representativeness by interpolating under constraints which take into consideration the spatial inhomogeneities mentioned above.

The interpolation discussed above was performed using inverse-distance weighting. The same calculation was performed using inverse-distance-squared weighting and the two results were found to be essentially indistinguishable. However, it is unwarranted to draw general conclusions on the basis of this limited test.

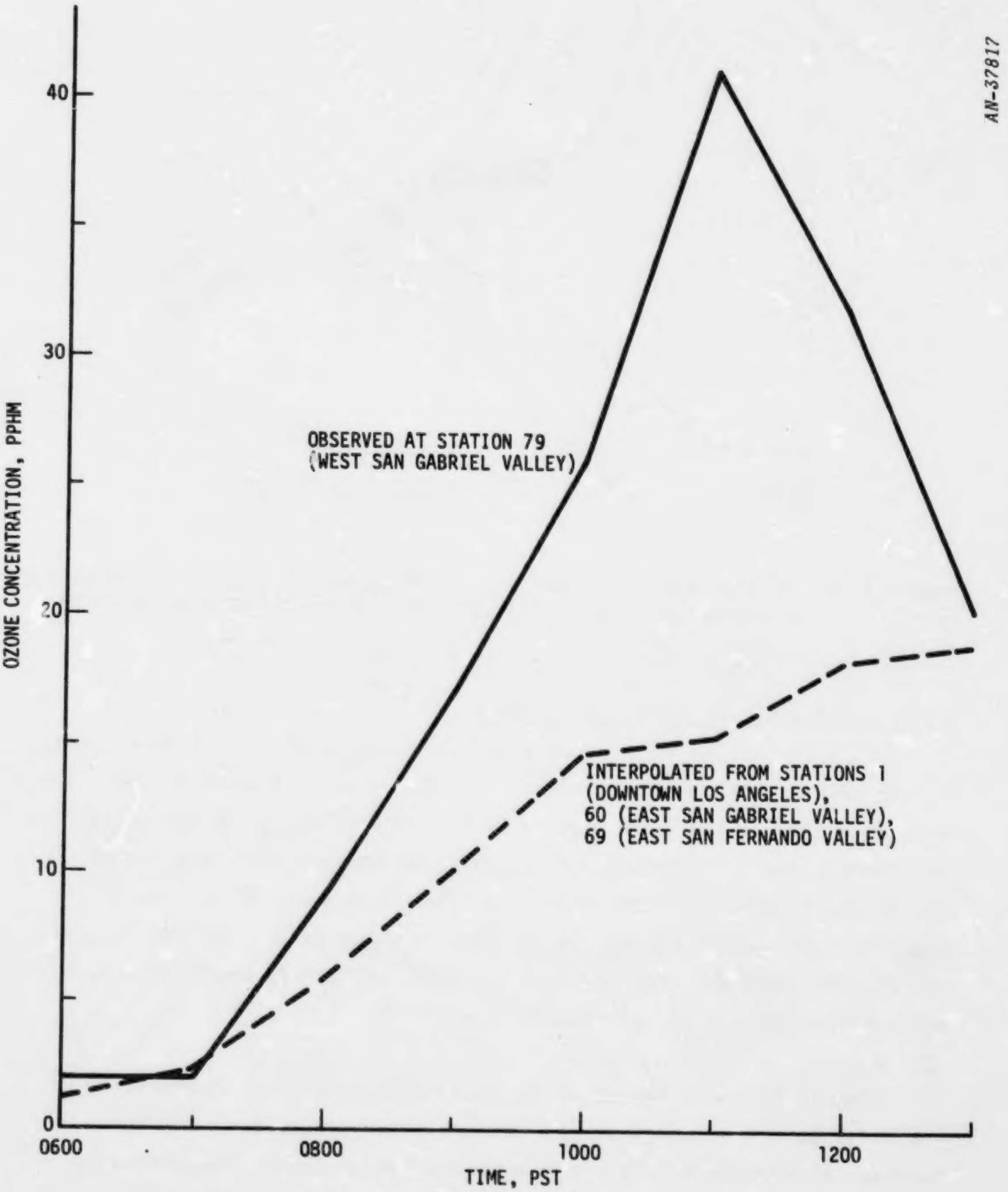

Figure 5.2. Interpolated and Observed Ozone Concentration at a Monitoring Station in the West San Gabriel Valley on September 29, 1969

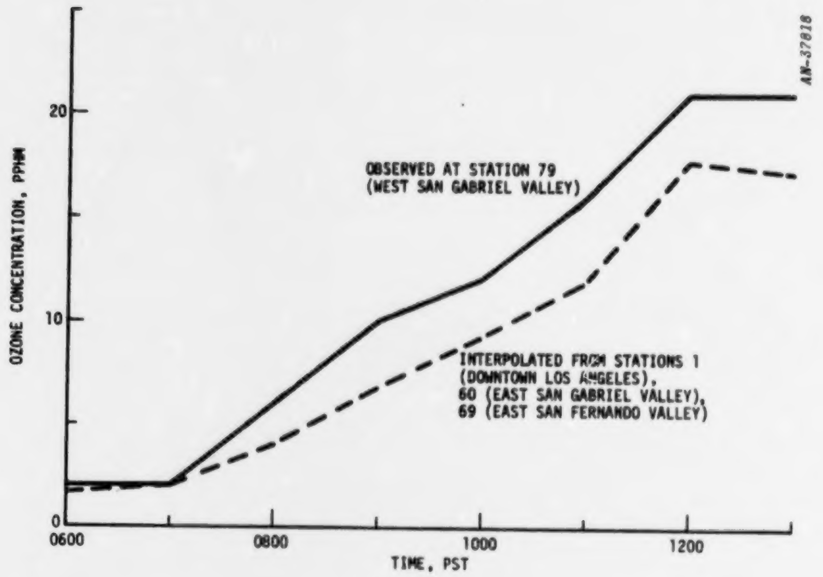

Figure 5.3. Interpolated and Observed Ozone Concentration at a Monitoring Station in the West San Gabriel Valley on November 4, 1969

5.3.4 Assessment of Model Performance

In this section we present a general assessment of the performance of the model. The results for each trajectory are included in Secs. 5.3.5 through 5.3.28, where each case is illustrated by a map of the trajectory and three plots of computed and observed concentrations: one for CO, one for NO and NO_2, and one for ozone. It should be noted that results for reactive hydrocarbon are not shown. This is due to the paucity of hydrocarbon data available for comparison, there being only three hydrocarbon-monitoring stations in Los Angeles County.

One of the most important factors which affect the performance of the model is the accuracy of the initial concentrations of the three fundamental species NO, NO_2, and reactive hydrocarbon. The influence of initial values is especially significant for a trajectory which starts around 0600 or later and runs for eight hours or less. In such a case, the mass of the emitted pollutants is considerably less than the initial mass and as a consequence the computation is greatly influenced by the initial values. Most of the trajectories studied in this report fall in this category. One notable exception is trajectory number 8, which starts at 0230 and has very low initial concentrations. Availability of hydrocarbon measurements constrains the selection of a starting location since there are fewer hydrocarbon-monitoring stations than there are for NO_x or CO. Hence we attempted to reduce the uncertainties in the initial conditions by starting trajectories at places of best-known hydrocarbon levels. In connection with the problem of uncertainty in the initial values, we note that generally we seemed to obtain better results with trajectories which started at Commerce than with those which began in Downtown Los Angeles. This could be attributed to the higher quality of the Commerce data.

The plots of ozone concentration shown in subsequent sections illustrate that the computations matched the observations remarkably well. In order to achieve this, we had to settle for poorer fits for NO and NO_2. Usually, the model results for NO matched the data better than the NO_2 predictions fit the NO_2 measurements. (We recall that this situation also prevailed, although to a smaller extent, in the simulation of the smog chamber experiments.) In several cases, early morning peaks of NO were difficult to reproduce. On the other hand, the NO_2 buildup was generally accurate, but the decay was poorly reproduced, with the NO_2 tending to linger at relatively high concentrations late in the day. This behavior of NO_2 may be due to inadequacies in the kinetics or mixing model for late-time NO_2 behavior. Addition of the reaction of NO_2 with particulates (reaction 2.16) improved the late-time NO_2 decay, but the improvement was small. Increasing k_{16} is not the answer to this problem, because this interferes with late-time RO_2 control, with the result being anomalously high concentrations of RO_2. Additional research is needed to improve the late-time behavior of NO_2.

In the simulation process, we had to reduce NO fluxes consistently to 1/4 of the value estimated from source inventories. This adjustment is consistent with our previous work.[1] The necessity of scaling down the NO emissions arises from the fact that both the NO_x balance and the ozone production diverge greatly from the observed values when the full NO flux is used. Reducing the NO flux to 1/4 of its full value results in predictions which fit the data much more accurately. As discussed previously,[1] these flux reductions may reflect atmospheric loss mechanisms such as surface reactions that are as yet unidentified in any of the field programs.

Statistical Correlation of Computations and Observations

One way of evaluating the aggregate performance of the model is to measure the correlation between computations and observations. This contrasts with the case-by-case presentation of results contained in the next several sections. By examining the relationship between predictions and measurements in a highly aggregated form, it is easy to discern trends in the model's performance. These trends may be useful in obtaining correction factors to improve the predictions. Naturally, the initial concentrations have been excluded from the statistical analysis since their inclusion would bias the correlations.

Correlation coefficients for computed and observed concentrations were obtained for CO and ozone for the set of hands-on cases, the set of hands-off cases, and for both sets together. Table 5.4 shows the values of the coefficients for each of the three groupings. It is clear from

TABLE 5.4

CORRELATION COEFFICIENTS FOR CO AND OZONE

Species	Hands-on	Hands-off	Composite
CO	0.90	0.63	0.80
Ozone	0.94	0.88	0.92

the table that the coefficient for the hands-on cases provides an upper bound of the expected performance of the model, and the coefficient for the hands-off cases, a lower bound. For ozone, the difference between the upper and lower bounds is small, thus indicating a good performance in either situation. The difference is greater for CO, however, indicating a need for additional adjustment in diffusivity parameters in the hands-off cases. It is interesting to note that the lowest correlation coefficient obtained here for CO (in the hands-off cases) matches the highest correlation coefficient obtained by other investigators using another CO diffusion model which employs a combination of Gaussian plume and box models.[36]

Figures 5.4 and 5.5 are scatter diagrams of observed vs predicted concentrations of CO and ozone, respectively. The results of all 24 trajectories are contained in these graphs. The figures also include plots of the least-squares regression line.

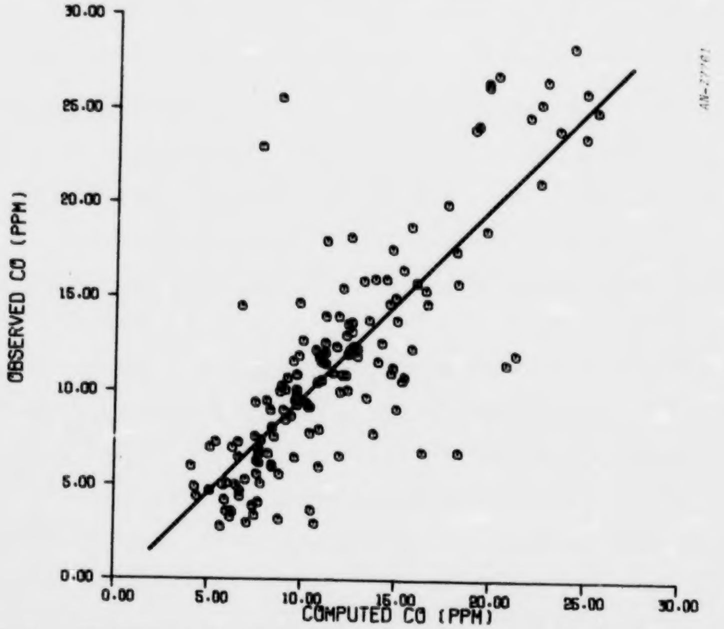

Figure 5.4. Observed Versus Computed Carbon Monoxide Concentration. (Number of Points = 149)

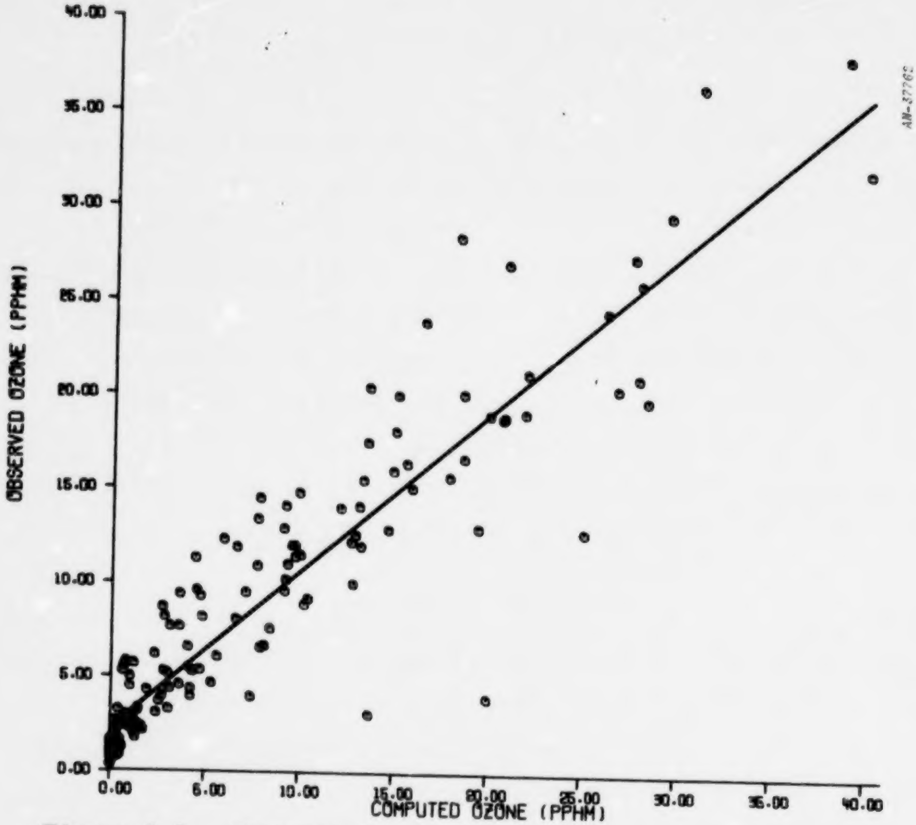

Figure 5.5. Observed Versus Computed Ozone Concentration. (Number of Points = 151)

It is apparent from Fig. 5.4 that for CO the model tends to overestimate the low concentrations; these generally occur in the afternoon. The CO peaks, on the other hand, are underpredicted. For ozone, Fig. 5.5, the model tends to underestimate the low concentrations but to be accurate at medium levels. High ozone concentrations are slightly overpredicted.

The regression lines shown on Figs. 5.4 and 5.5 can be used to correct the predictions and thus obtain a better estimate of the actual concentration. Table 5.5 shows the equations of the regression lines for CO and ozone, together with the standard error of estimate. If we ask what the actual concentration, y , is likely to be given a predicted concentration x , we can obtain an answer from the regression equation. The value of σ , the standard error of estimate, provides a measure of the tolerance which may be assigned to the corrected prediction.

TABLE 5.5

REGRESSION EQUATIONS FOR CO AND OZONE

Species	Regression Equation y = observed x = computed	Standard Error of Estimate (σ)*
CO	$y = 1.007x - 0.346$	3.663 ppm
Ozone	$y = 0.840x + 2.307$	2.109 pphm

$$^{*}\ \sigma = \sqrt{\frac{1}{N} \sum_{1}^{N} (y_o - y_c)^2}$$, y_o = observed concentration

y_c = concentration computed using regression equation

5.3.5 Trajectory No. 1, September 11, 1969, Starts at Commerce at 0530 (Hands-Off)

The simulation of CO agreed very well with the data. However, the results for the reactive species matched the data poorly, with the NO_x balance predicted by the model being greater than is shown by the data. Also, Fig. 5.9 shows that the predicted ozone concentration, denoted by the solid line, is considerably higher than is indicated by the data. This computation was done using the clear-day value of k_1 . However, examination of Fig. 5.102 (Sec. 5.5) shows that for Sept. 11 the value of k_1 at Commerce is much lower than the clear-day value. Since the trajectory meanders around Commerce for most of the day, it is possible that the low values of ozone may be due to the low k_1 . Substituting the Commerce k_1 for the clear-day k_1 yielded the dashed curve shown in Fig. 5.9. The lower k_1 produced much lower values of ozone, but the relatively small ozone peaks shown by the data were still not reproduced by the computation. Nevertheless, the dramatic reduction in ozone obtained using the new k_1 is indicative of the large variations to which the predictions are subject due to the uncertainty in the fundamental input k_1 . Finally, in this case $k_4 = 4 \times 10^3$ ppm^{-1}min^{-1}.

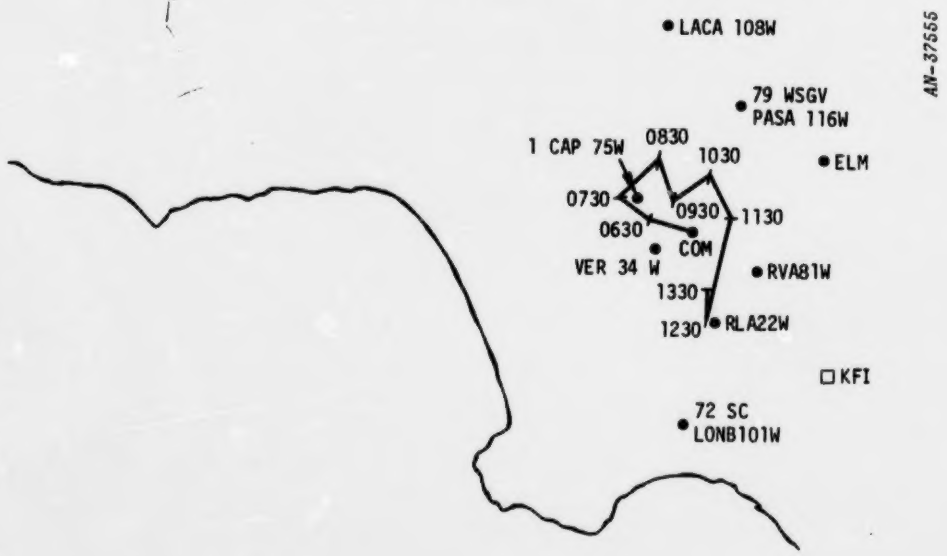

Figure 5.6. September 11, 1969 Trajectory Starting at Commerce at 0530 (No. 1)

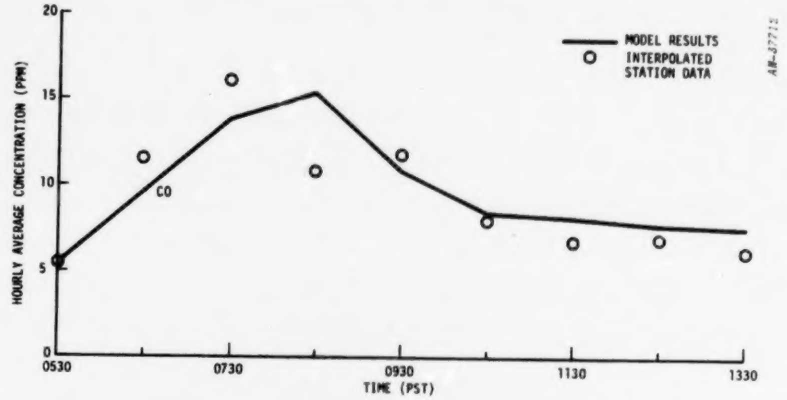

Figure 5.7. Trajectory No. 1--Computed and Observed CO Concentrations

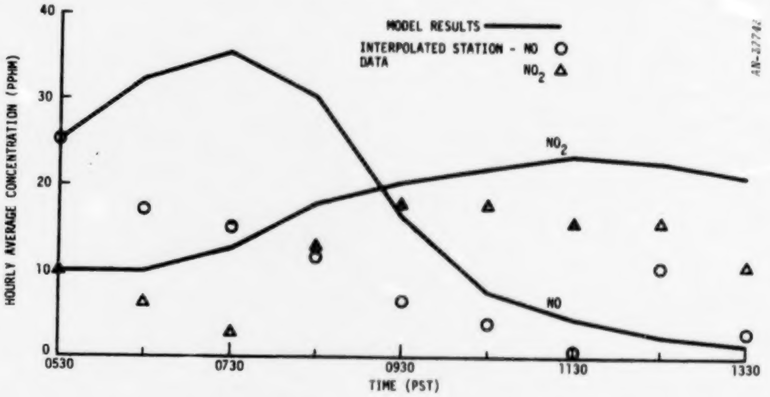

Figure 5.8. Trajectory No. 1--Computed and Observed NO and NO_2 Concentrations

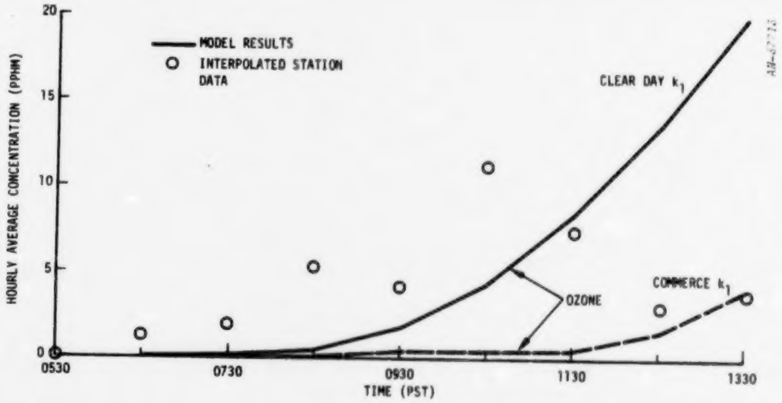

Figure 5.9. Trajectory No. 1--Computed and Observed Ozone Concentrations

5.3.6 Trajectory No. 2, September 11, 1969, Starts at Commerce at 0630 (Hands-Off)

Figure 5.11 shows that the early-morning CO buildup and decay are well reproduced by the model. The low CO concentrations in the afternoon are overestimated, however. (There is no data point at 1230 because it was missing from the observations.) On the other hand, Figs. 5.12 and 5.13 show that the predicted concentrations of the reactive species match the data very well. The computed NO_x balance is very good and the ozone prediction is superior. For this trajectory, $k_4 = 4 \times 10^3$ $ppm^{-1}min^{-1}$.

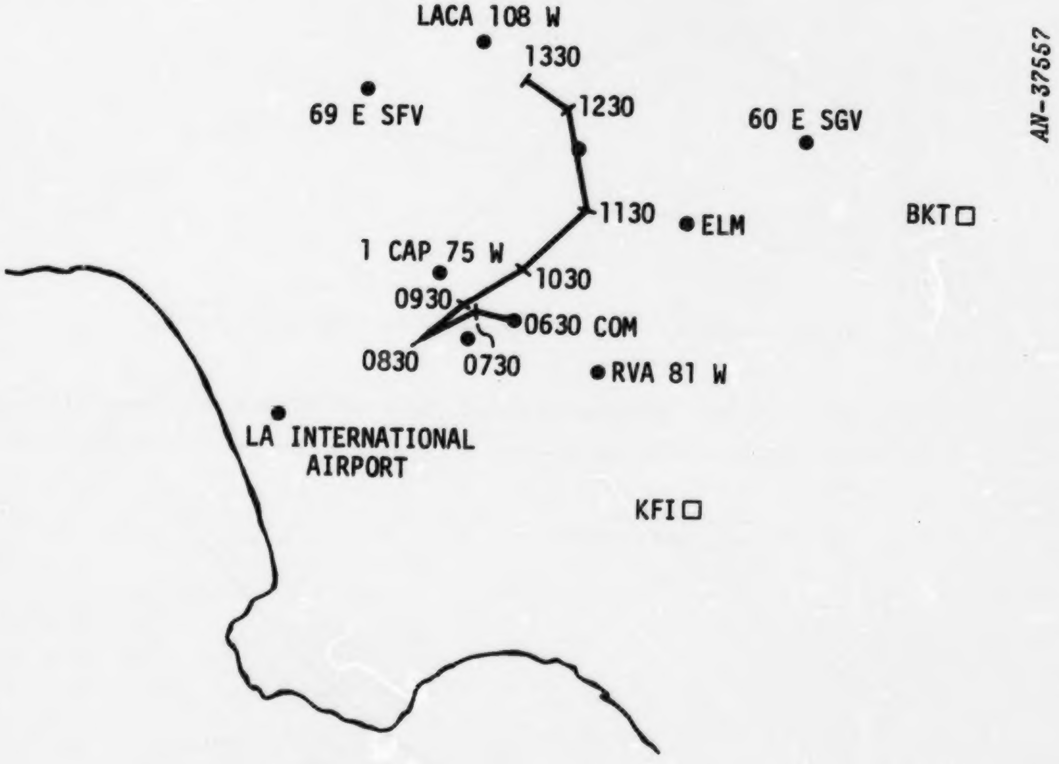
LACA 108 W
1330
1230
69 E SFV
60 E SGV
1130
ELM
BKT
1 CAP 75 W
1030
0930
0630 COM
0830
0730
RVA 81 W
LA INTERNATIONAL AIRPORT
KFI
AN-37557

Figure 5.10. September 11, 1969 Trajectory Starting at Commerce at 0630 (No. 2)

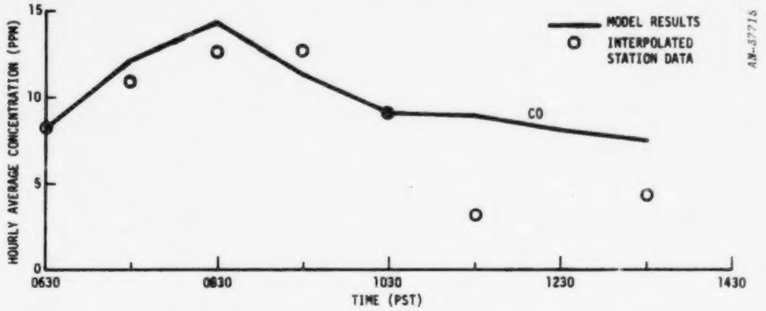

Figure 5.11. Trajectory No. 2--Computed and Observed CO Concentrations

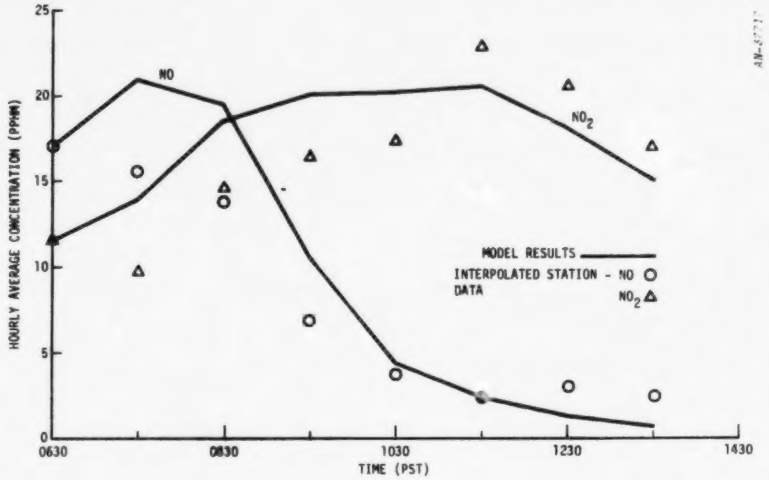

Figure 5.12. Trajectory No. 2--Computed and Observed NO and NO_2 Concentrations

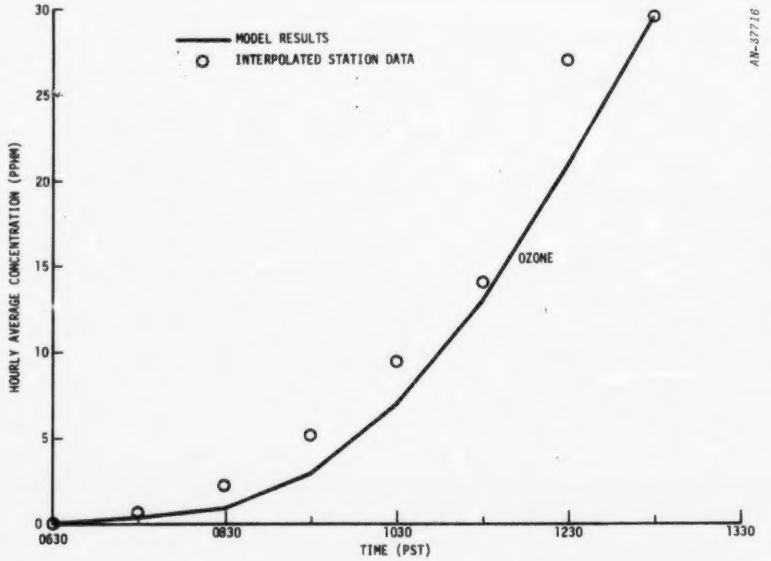

Figure 5.13. Trajectory No. 2--Computed and Observed Ozone Concentrations

5.3.7 Trajectory No. 3, September 11, 1969, Starts in Downtown Los Angeles at 0530 (Hands-Off)

Figure 5.15 shows that the simulation of CO matched the data well. However, the NO_x computation does not match the data, the peaks of NO and NO_2 being much lower than the observations shown in Fig. 5.16. On the other hand, the ozone simulation is remarkably accurate, despite the poor quality of the NO_x predictions. This case is one example where parameter adjustments made to improve the NO_x computations degrade the ozone and vice versa. The value of k_4 used in this case is 4×10^3 $ppm^{-1}min^{-1}$.

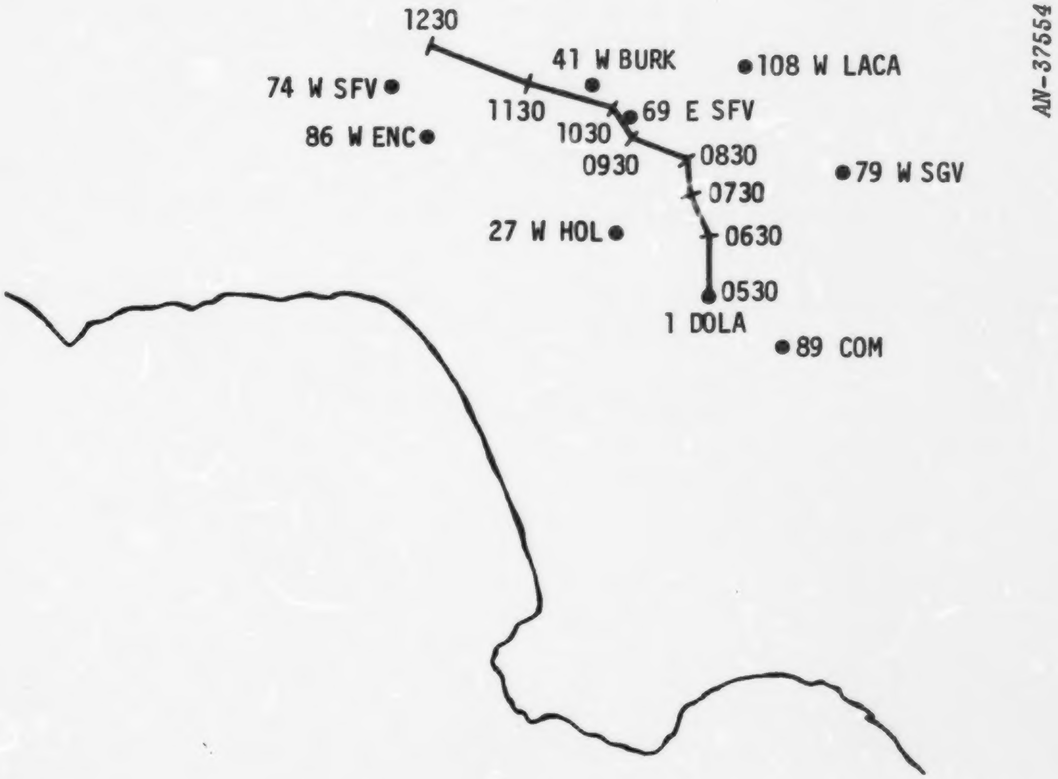
1230
41 W BURK
108 W LACA
74 W SFV
1130
69 E SFV
86 W ENC
1030
0930
0830
79 W SGV
0730
27 W HOL
0630
0530
1 DOLA
89 COM
AN-37554

Figure 5.14. September 11, 1969 Trajectory Starting in Downtown Los Angeles at 0530 (No. 3)

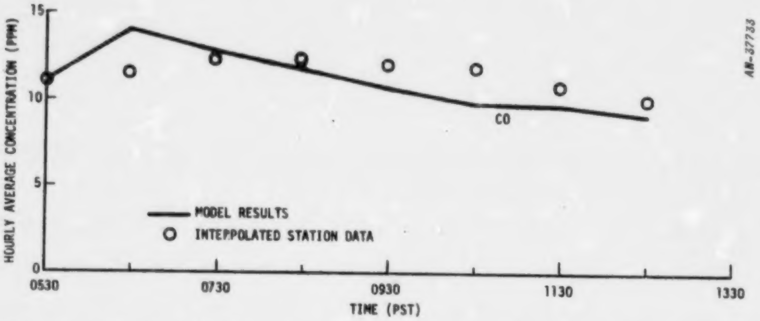

Figure 5.15. Trajectory No. 3--Computed and Observed CO Concentrations

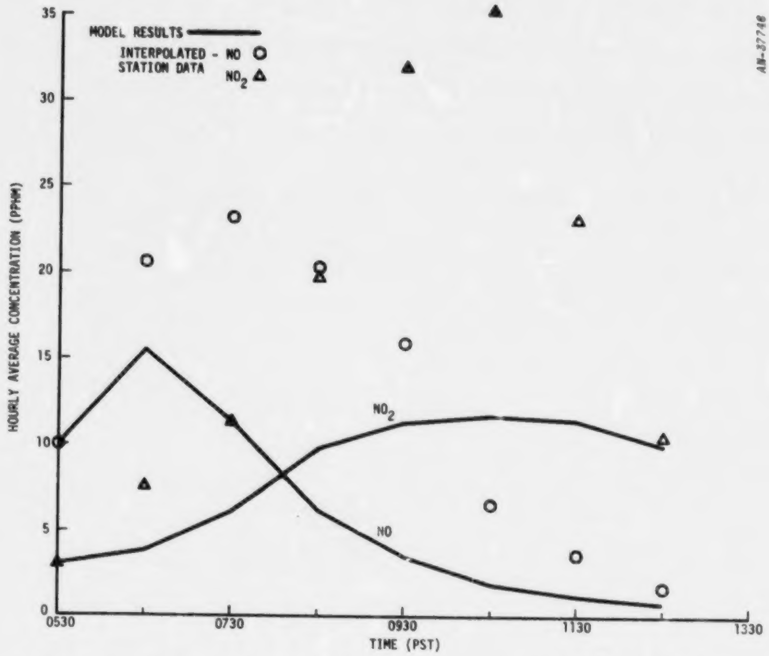

Figure 5.16. Trajectory No. 3--Computed and Observed NO and NO_2 Concentrations

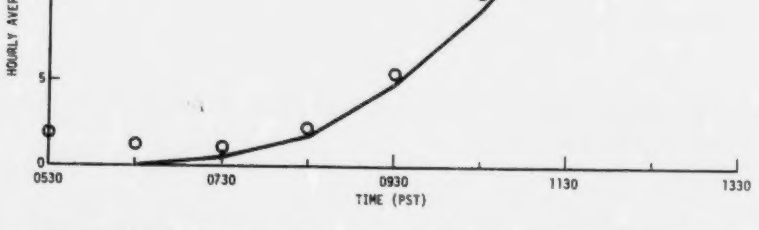

Figure 5.17. Trajectory No. 3--Computed and Observed Ozone Concentrations

5.3.8 Trajectory No. 4, September 11, 1969, Starts in Downtown Los Angeles at 0630 (Hands-Off)

The computed CO, Fig. 5.19, agreed with the data to within 3 ppm, except for the last point which is about 5 ppm higher than the data. As in the previous trajectory, the computed NO_x balance is lower than indicated by the data, but this time the NO predicted by the model matches the data well. Figure 5.21 shows that the computed ozone is generally lower than the measurements, but the differences are certainly within the error margin of interpolation and experimental uncertainty. The value of k_4 used in this simulation was $k_4 = 4 \times 10^3 \text{ ppm}^{-1}\text{min}^{-1}$.

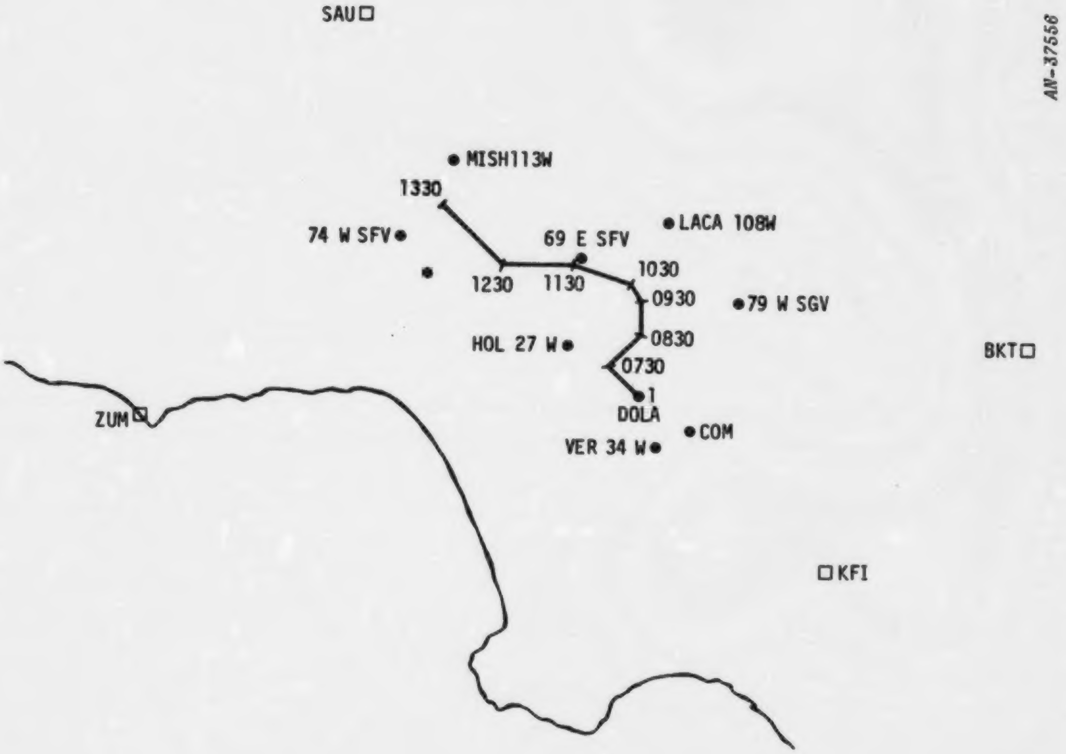

SAU
AN-37558
MISH113W
1330
74 W SFV
69 E SFV
LACA 108W
1230
1130
1030
0930
79 W SGV
HOL 27 W
0830
BKT
0730
1
DOLA
ZUM
COM
VER 34 W
KFI

Figure 5.18. September 11, 1969 Trajectory Starting in Downtown Los Angeles at 0630 (No. 4)

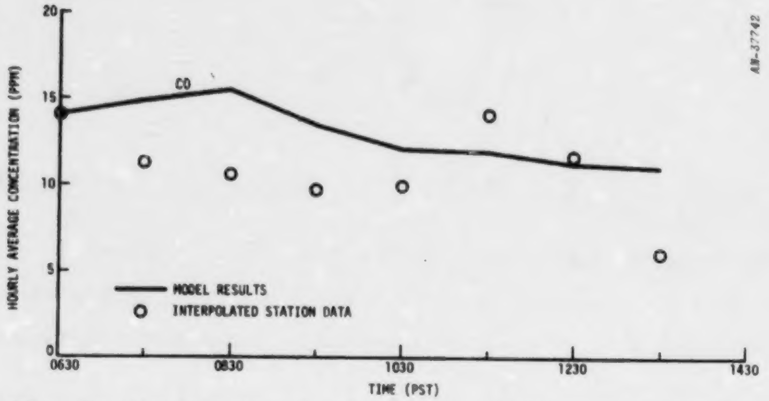

Figure 5.19. Trajectory No. 4--Computed and Observed CO Concentration

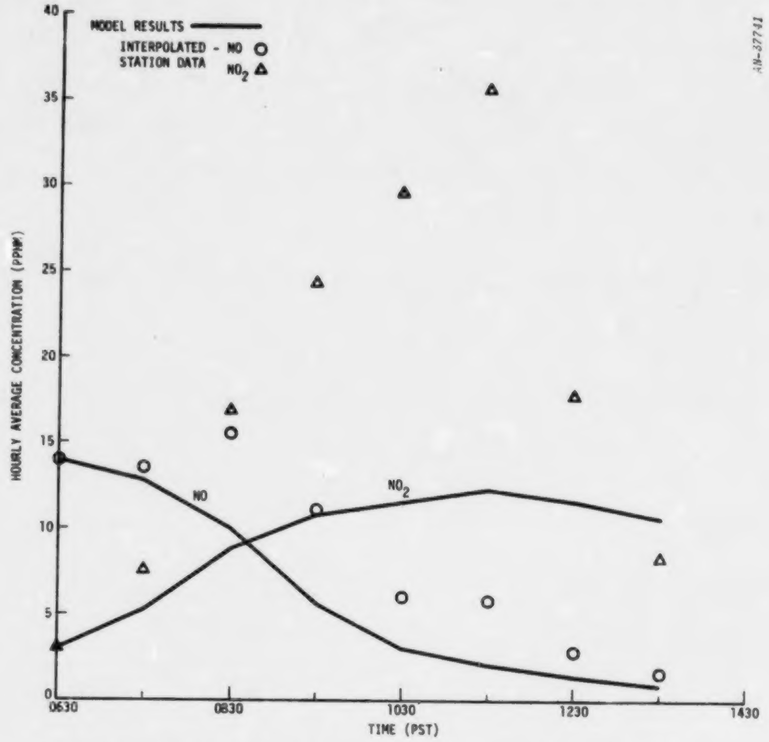

Figure 5.20. Trajectory No. 4--Computed and Observed NO and NO_2 Concentrations

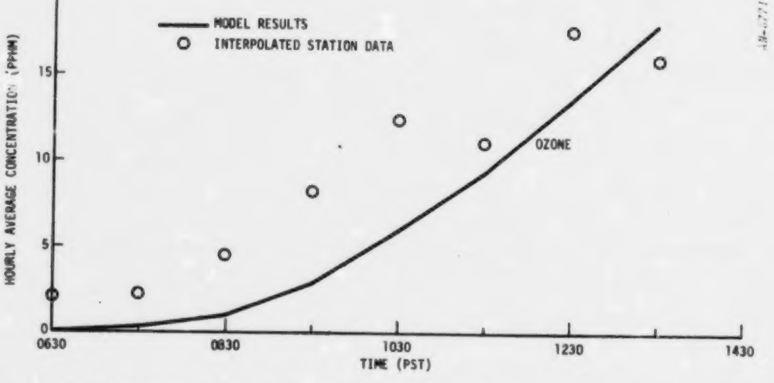

Figure 5.21. Trajectory No. 4--Computed and Observed Ozone Concentrations

5.3.9 Trajectory No. 5, September 29, 1969, Starting at Commerce at 0530 (Hands-On)

This trajectory has the characteristic that it stays in the vicinity of Commerce most of the time from 0530 to 1030. This gives us a greater degree of confidence in the data obtained by interpolation from the various stations along the way.

The CO simulation shows a low peak, but the remaining concentrations are predicted accurately. The simulation of the reactive species shows good agreement with the data, especially for the NO and ozone. The NO_2 buildup is accurately predicted, but the NO_2 decay fits the data poorly. The value of k_4 used was 8×10^3 $ppm^{-1}min^{-1}$.

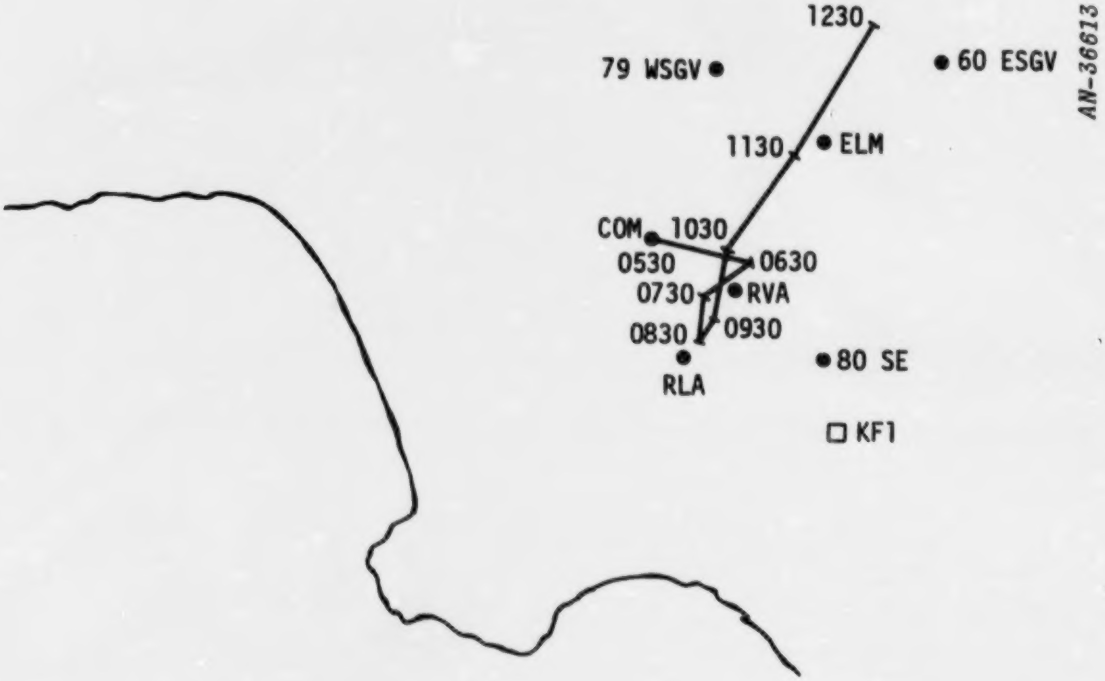
1230
79 WSGV
60 ESGV
AN-36613
1130
ELM
COM
1030
0530
0630
0730
RVA
0830
0930
RLA
80 SE
KF1

Figure 5.22. September 29, 1969 Trajectory Starting at Commerce at 0530 (No. 5)

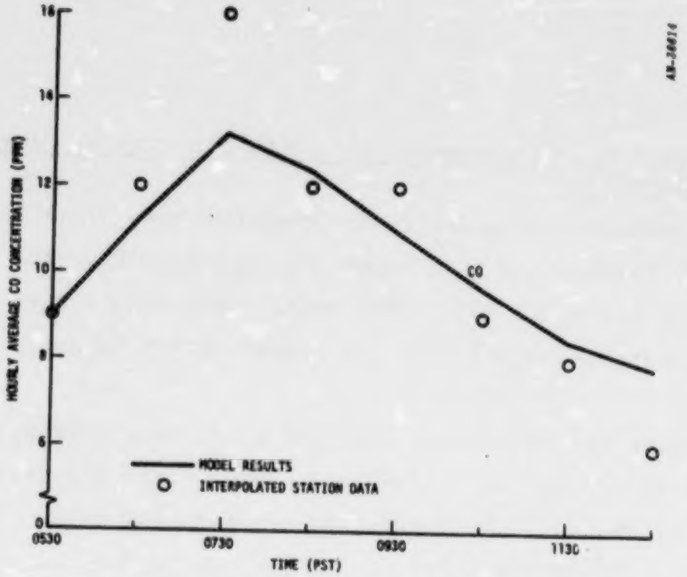

Figure 5.23. Trajectory No. 5--Computed and Observed CO Concentrations

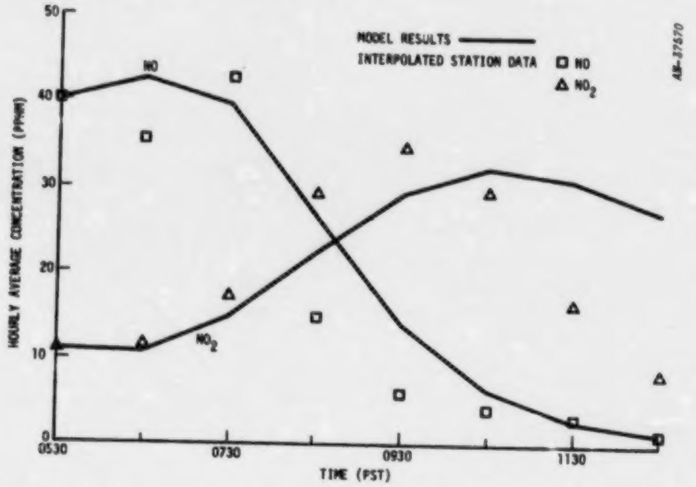

Figure 5.24. Trajectory No. 5--Computed and Observed NO and NO_2 Concentrations

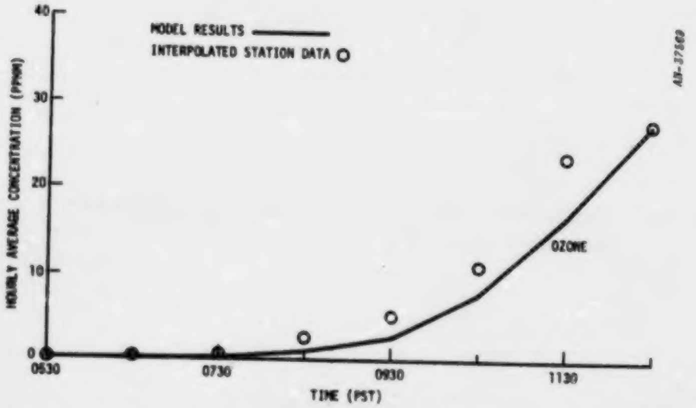

Figure 5.25. Trajectory No. 5--Computed and Observed Ozone Concentrations

5.3.10 Trajectory No. 6, September 29, 1969, Starting at Commerce at 0630 (Hands-On)

This trajectory is similar to the previous one. This time, however, the computed CO buildup and peak match the data closely. The predicted CO decay is accurate until 1030. The model overpredicts the 1130 and 1230 CO concentrations but at 1330 the approximation is good.

The reactive species, Figs. 5.28 and 5.29, show a behavior similar to that in trajectory no. 5: the NO and ozone curves are very well modeled, but for NO_2 only the buildup is close to the data. The value of k_4 was 8×10^3 $ppm^{-1}min^{-1}$.

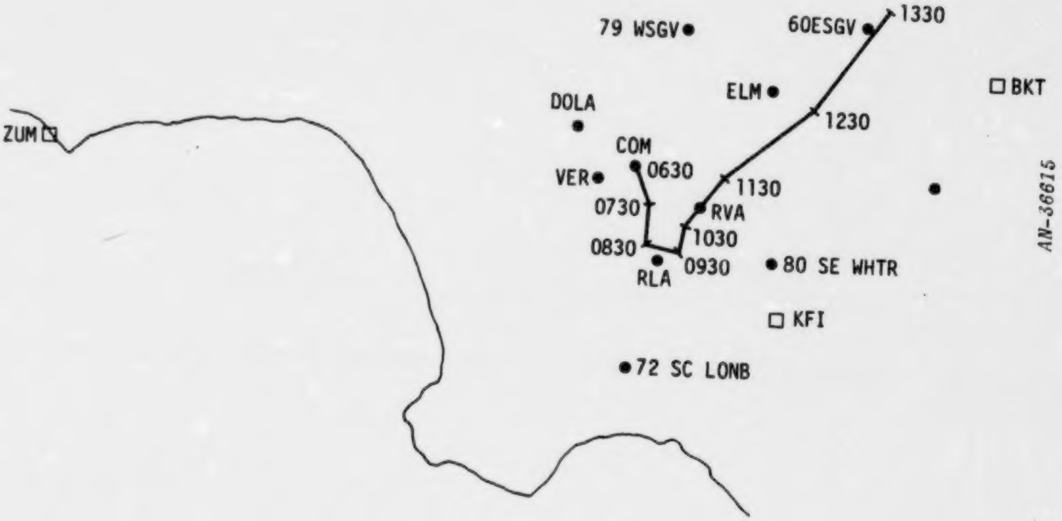
79 WSGV
60ESGV
1330
ELM
BKT
DOLA
1230
ZUM
COM
0630
VER
1130
0730
RVA
1030
0830
0930
RLA
80 SE WHTR
KFI
72 SC LONB
AN-36615

Figure 5.26. September 29, 1969 Trajectory Starting at Commerce at 0630 (No. 6)

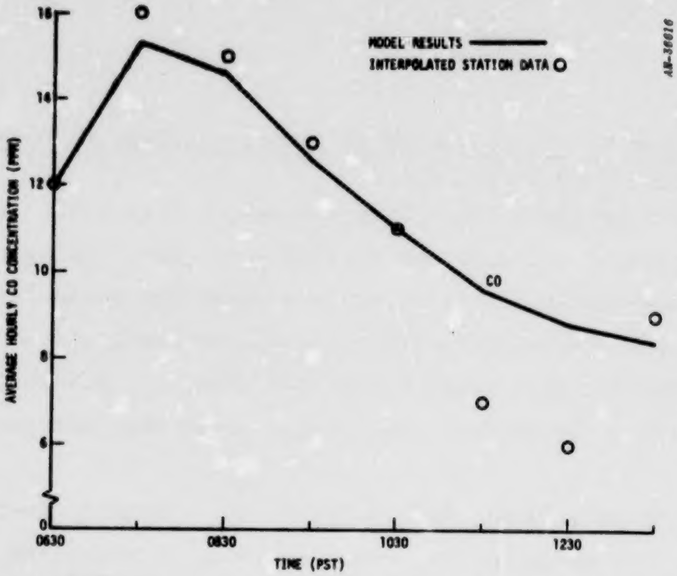

Figure 5.27. Trajectory No. 6--Computed and Observed CO Concentrations

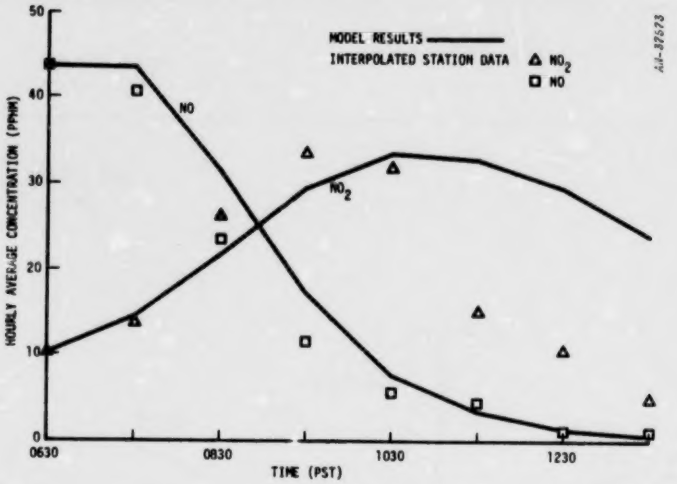

Figure 5.28. Trajectory No. 6--Computed and Observed NO and NO_2 Concentrations

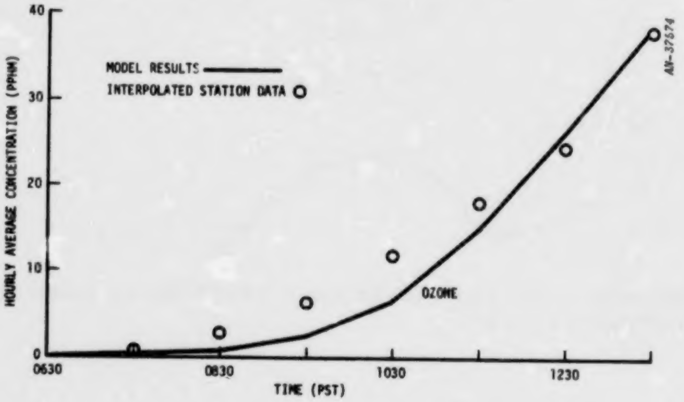

Figure 5.29. Trajectory No. 6--Computed and Observed Ozone Concentrations

5.3.11 Trajectory No. 7, September 29, 1969, Starting in Downtown Los Angeles at 0530 (Hands-on)

The results obtained for CO are shown in Fig. 5.31. The reported 0530 concentration at the downtown station was 3 ppm. Using this initial value yielded very low concentrations throughout the whole day. In order to obtain a better approximation to the data, the initial value was adjusted to 7 ppm and this yielded improved results. However, the predicted peak value of 12 ppm was still 4 ppm lower than the data indicate.

Figure 5.32 shows that the predicted NO_x balance diverges considerably from that shown by the data. In spite of this, the simulation of ozone was very accurate. We might add that no adjustment of the initial concentrations was necessary for simulating the reactive species. The value of k_4 was 5×10^3 $ppm^{-1}min^{-1}$.

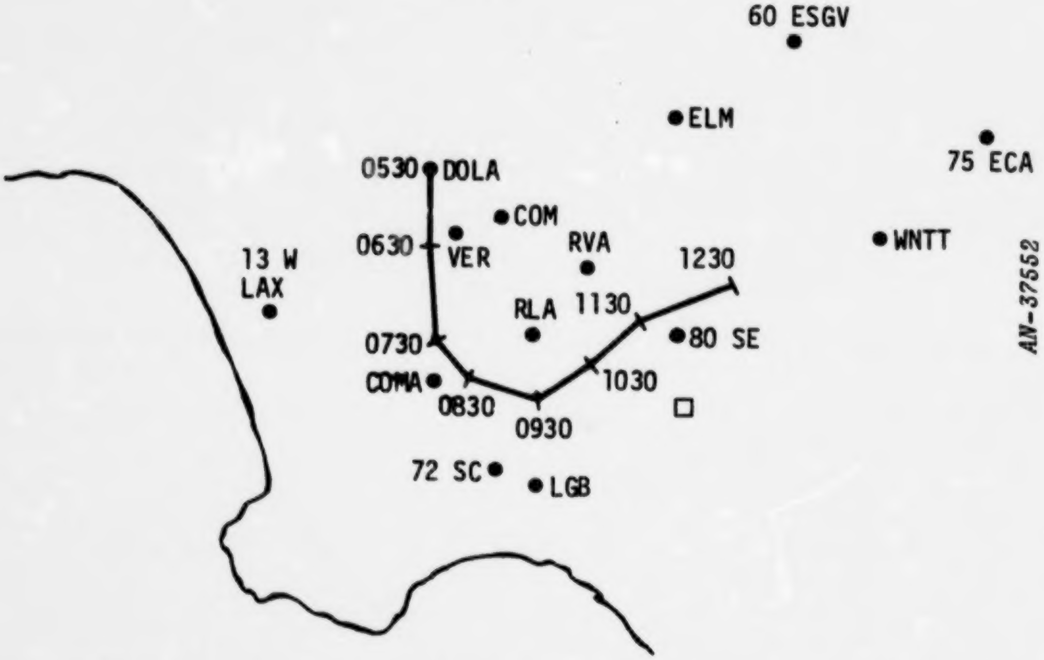
60 ESGV
ELM
75 ECA
0530
DOLA
COM
0630
VER
RVA
1230
WNTT
13 W
LAX
RLA
1130
0730
80 SE
COMA
1030
0830
0930
72 SC
LGB
AN-37552

Figure 5.30. September 29, 1969 Trajectory Starting in Downtown Los Angeles at 0530 (No. 7)

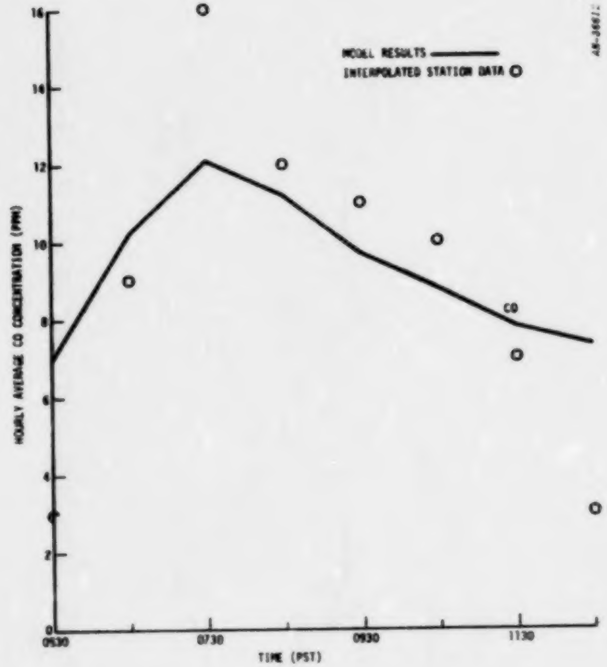

Figure 5.31. Trajectory No. 7--Computed and Observed CO Concentrations

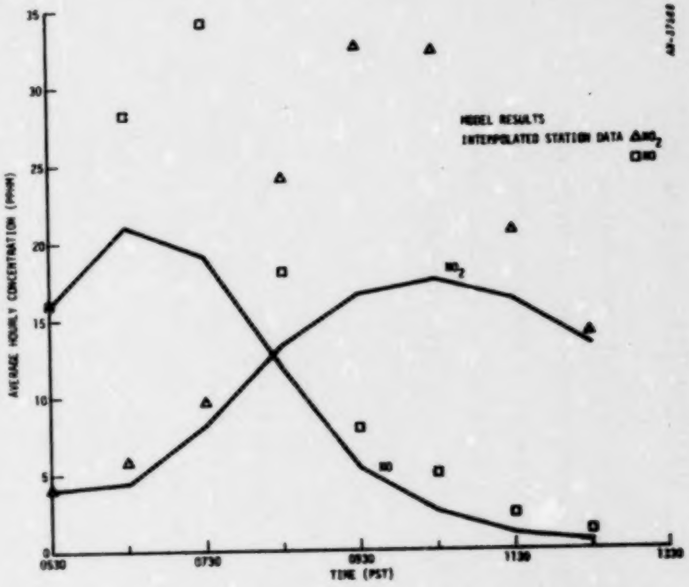

Figure 5.32. Trajectory No. 7--Computed and Observed NO and NO_2 Concentrations

Figure 5.33. Trajectory No. 7--Computed and Observed Ozone Concentrations →

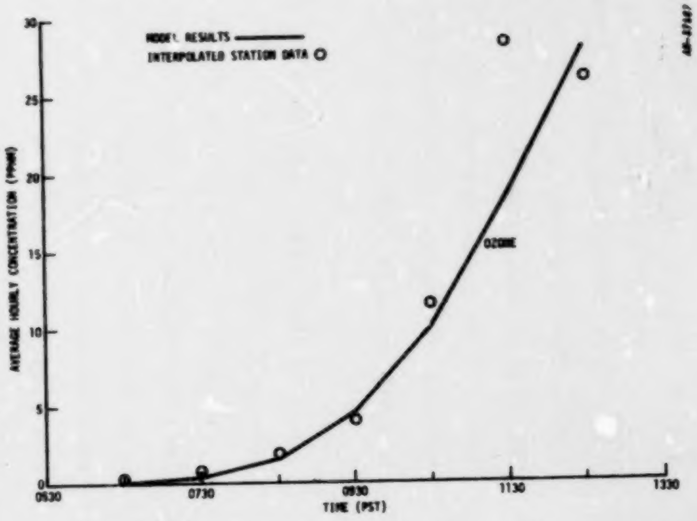

5.3.12 Trajectory No. 8, September 29, 1969, Starting Near Coast at 0230 (Hands-on)

This trajectory was reverse-calculated from the Anaheim station at 1230. The computation of pollution concentrations commenced at 0230 near the Lennox station of the LAAPCD. As was the case with the previous trajectory, we could not fit the CO data using the reported initial concentration of 3 ppm. Adjustment of the initial CO to 7 ppm produced satisfactory results from 0530 to 1130, as is shown in Fig. 5.35.

As with CO , the initial values of NO_x and hydrocarbon were adjusted upward by the ratio 7/3. However, the original initial values were very low and the adjustment did not cause large changes in the simulation. Figure 5.36 shows that the NO simulation does not agree well with the data. It should be noted that the NO data show a second peak at 0930 which is suspect. The computed NO_2 , on the other hand, shows close agreement with the data after 0630. For ozone, Fig. 5.37 shows that the simulation and the data are very closely correlated. The value used for k_4 was $10^4\ \text{ppm}^{-1}\text{min}^{-1}$.

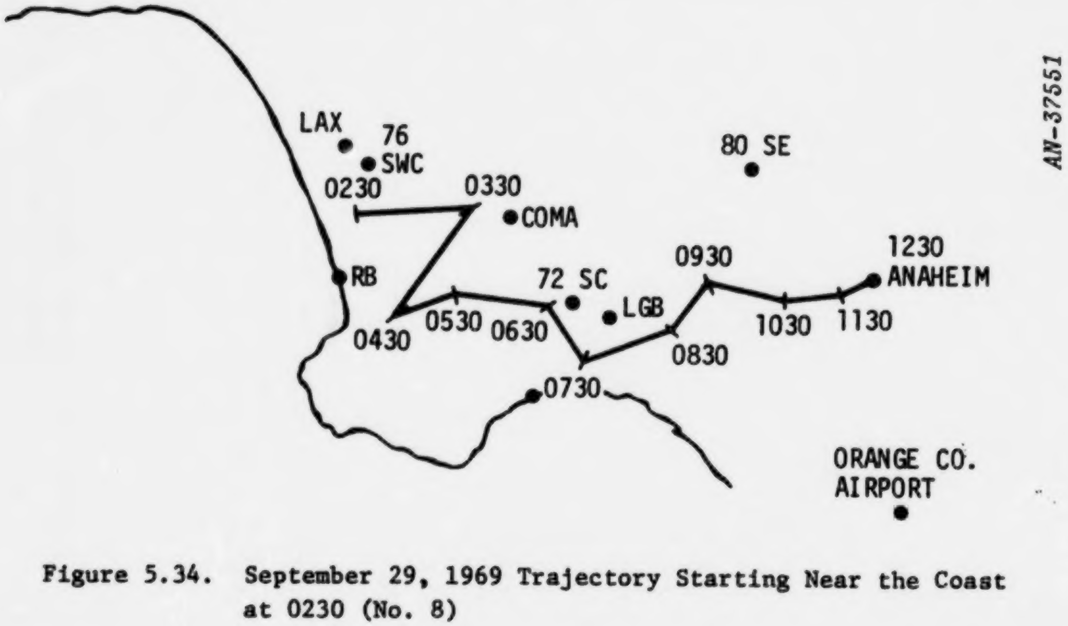

Figure 5.34. September 29, 1969 Trajectory Starting Near the Coast at 0230 (No. 8)

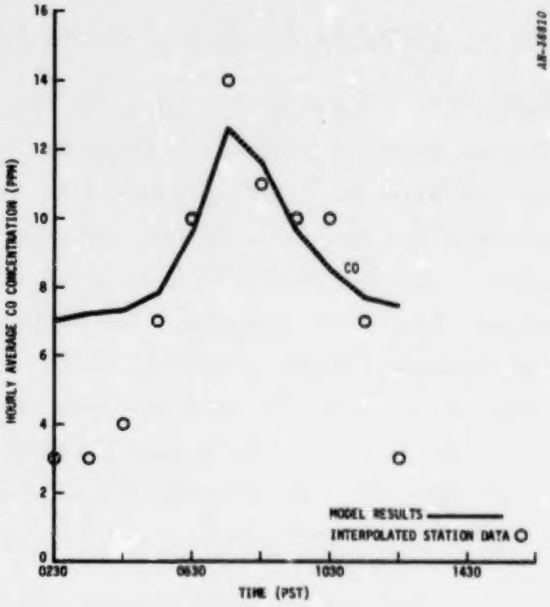

Figure 5.35. Trajectory No. 8--Computed and Observed CO Concentrations

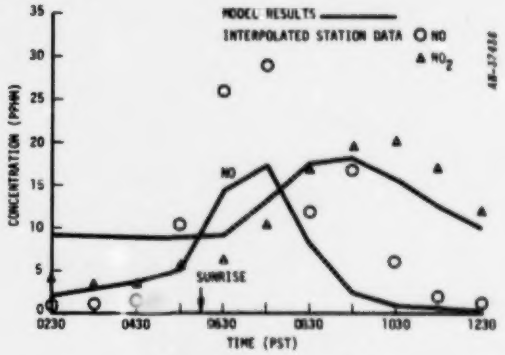

Figure 5.36. Trajectory No. 8--Computed and Observed NO and NO_2 Concentrations

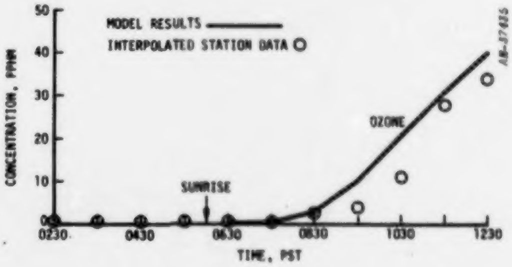

Figure 5.37. Trajectory No. 8--Computed and Observed Ozone Concentrations

5.3.13 Trajectory No. 9, September 30, 1969, Starting at Commerce at 0530 (Hands-on)

Figure 5.39 shows that the predicted CO fits the data well, with the exception of the data point at 0930. In addition, the computed concentration at 0630 is low by about 6 ppm. Figure 5.40 illustrates that the predicted NO matches the data closely but that the NO_2 is considerably overestimated. This situation is typical of the unsatisfactory NO_x balances encountered in the simulations. The computed ozone (Fig. 5.41) is seen to underestimate the early-morning concentrations and then overshoot the 1130 value by 8 pphm. We note that the relatively high ozone concentrations indicated by the observations before 1030 are puzzling inasmuch as very little $NO \rightarrow NO_2$ conversion has taken place prior to 1030. The value of k_4 is $10^4\ ppm^{-1}min^{-1}$.

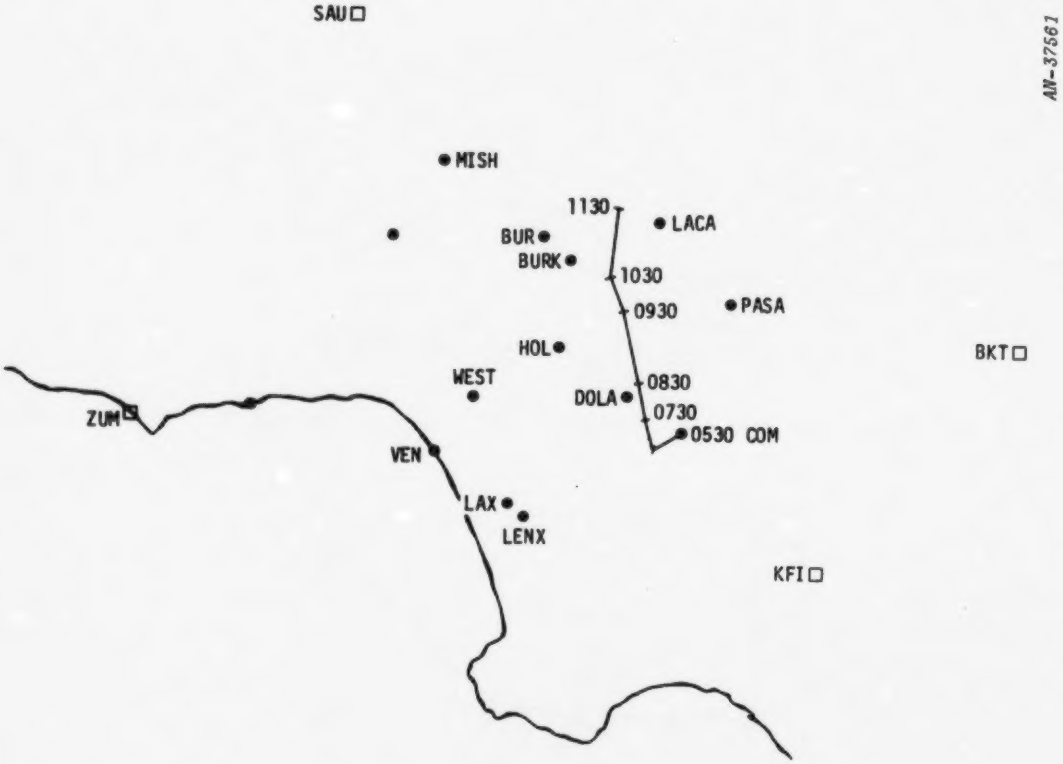
SAU
AN-37561
MISH
1130
LACA
BUR
BURK
1030
0930
PASA
HOL
BKT
WEST
0830
DOLA
0730
ZUM
0530 COM
VEN
LAX
LENX
KFI

Figure 5.38. September 30, 1969 Trajectory Starting at Commerce at 0530 (No. 9)

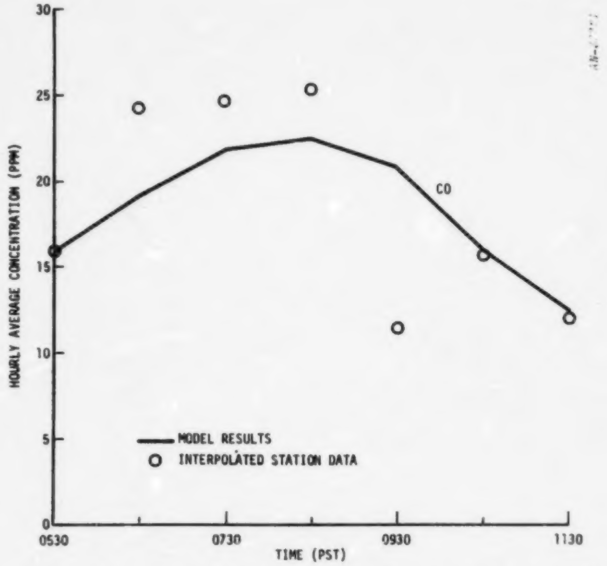

Figure 5.39. Trajectory No. 9--Computed and Observed CO Concentration

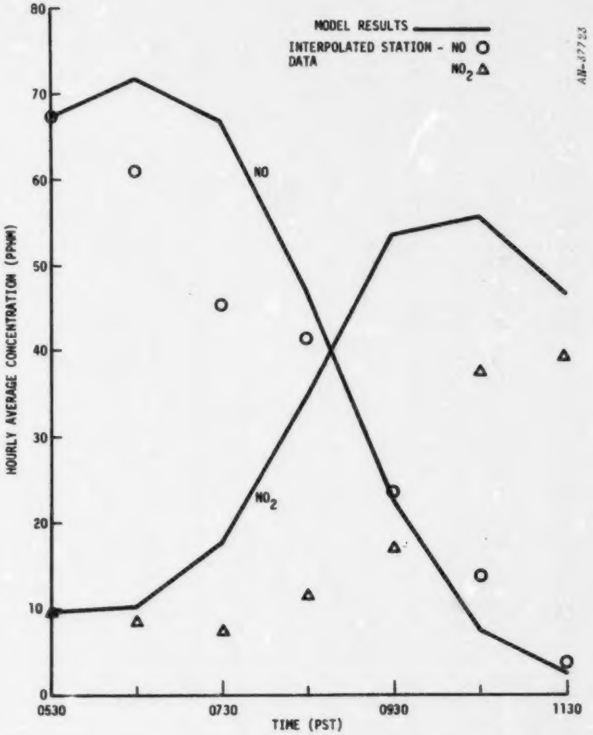

Figure 5.40. Trajectory No. 9--Computed and Observed NO and NO_2 Concentrations

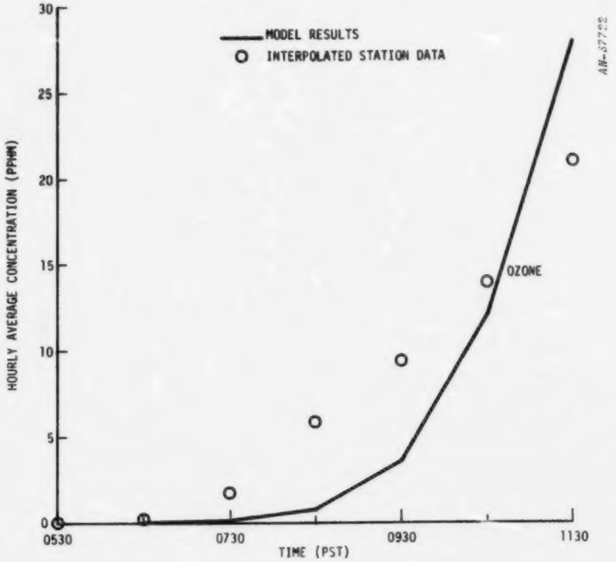

←Figure 5.41. Trajectory No. 9--Computed and Observed Ozone Concentrations

5.3.14 Trajectory No. 10, September 30, 1969, Starting at Commerce at 0630 (Hands-on)

This trajectory follows approximately the same path as trajectory No. 9. However, this time the early-morning values of CO are reproduced very well, as can be seen in Fig. 5.43. As was the case with the previous trajectory, the model is unable to follow the sharp drop in CO concentration which occurs at 0930. For NO it can be seen in Fig. 5.44 that the peak is too high but the decay is fairly accurate. The NO_2 buildup is well reproduced, but the decay is very poor. For ozone, Fig. 5.45, it can be seen that once again the low concentrations are underestimated. In contrast with the previous case, the model is very accurate at the higher ozone levels. The value of k_4 is 10^4 $ppm^{-1}min^{-1}$.

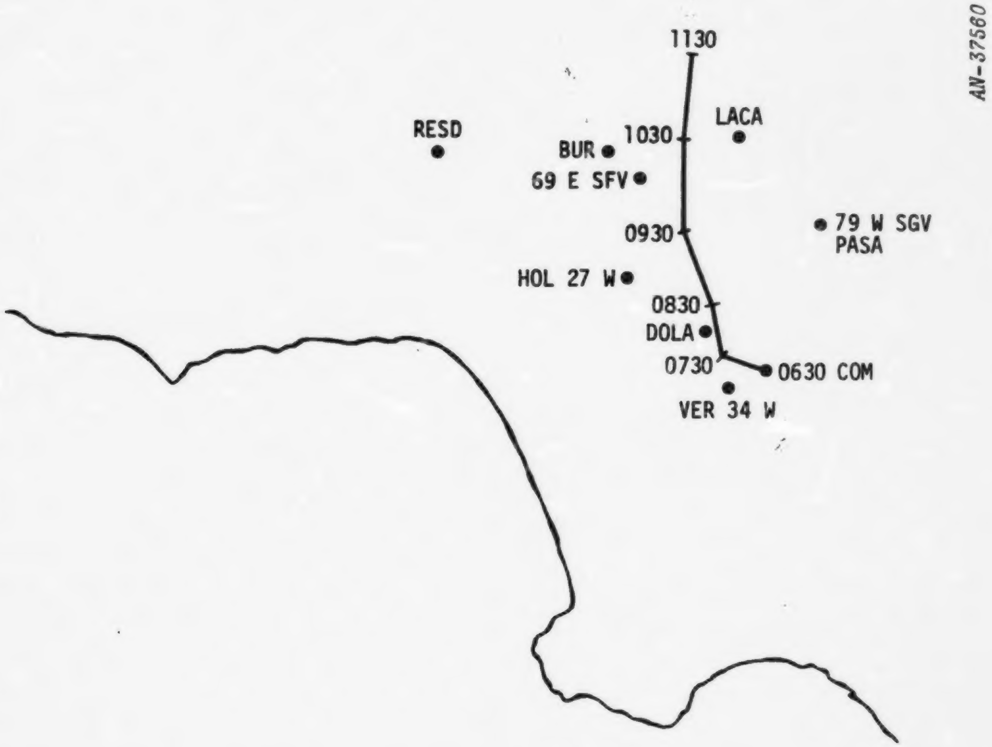
1130
RESD
BUR
1030
LACA
69 E SFV
0930
79 W SGV
PASA
HOL 27 W
0830
DOLA
0730
0630 COM
VER 34 W
AN-37560

Figure 5.42. September 30, 1969 Trajectory Starting at Commerce at 0630 (No. 10)

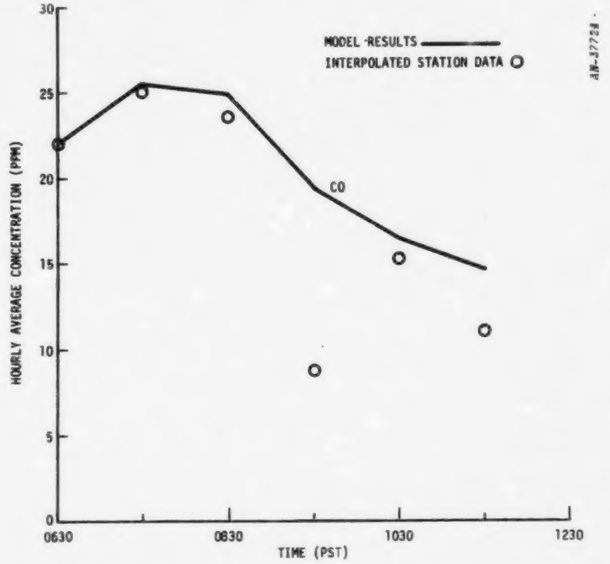

Figure 5.43. Trajectory No. 10--Computed and Observed CO Concentrations

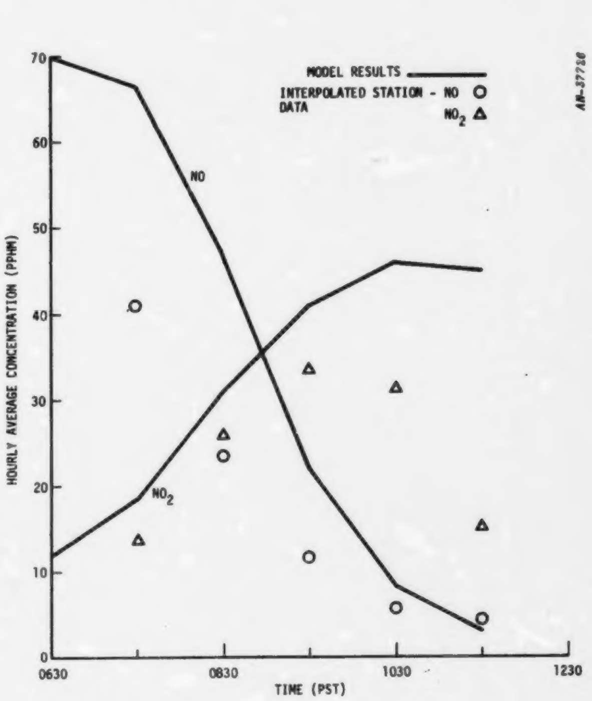

Figure 5.44. Trajectory No. 10--Computed and Observed NO and NO_2 Concentrations

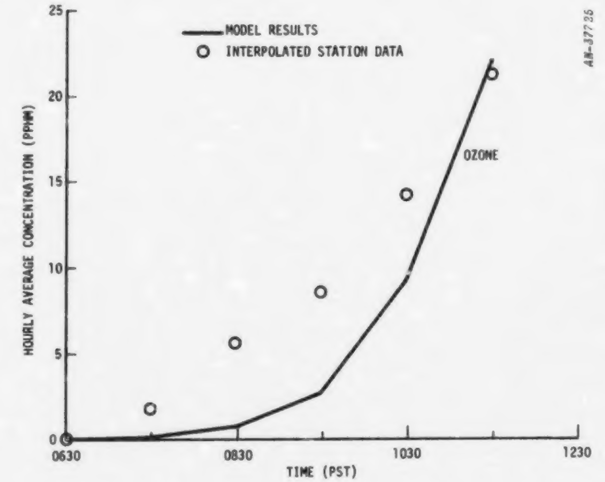

← Figure 5.45. Trajectory No. 10--Computed and Observed Ozone Concentrations

5.3.15 Trajectory No. 11, September 30, 1969, Starting in Downtown Los Angeles at 0430 (Hands-On)

Figure 5.47 illustrates that the CO peak is about 6 ppm too low. This may indicate a deficiency in the strength of the emissions since the diffusivities were set at the lowest value used for very stable atmospheric conditions, 2.5×10^3 cm^2/second . The model is accurate from 0730 to 0930, but does not reproduce the apparent peak after 0930. The reactive species are well modeled. This time the simulated NO_x balance is excellent with the exception of one very high observed concentration of NO_x at 1130. The ozone is only slightly underestimated throughout the trajectory. The value of k_4 used in this case is 10^4 $ppm^{-1}min^{-1}$.

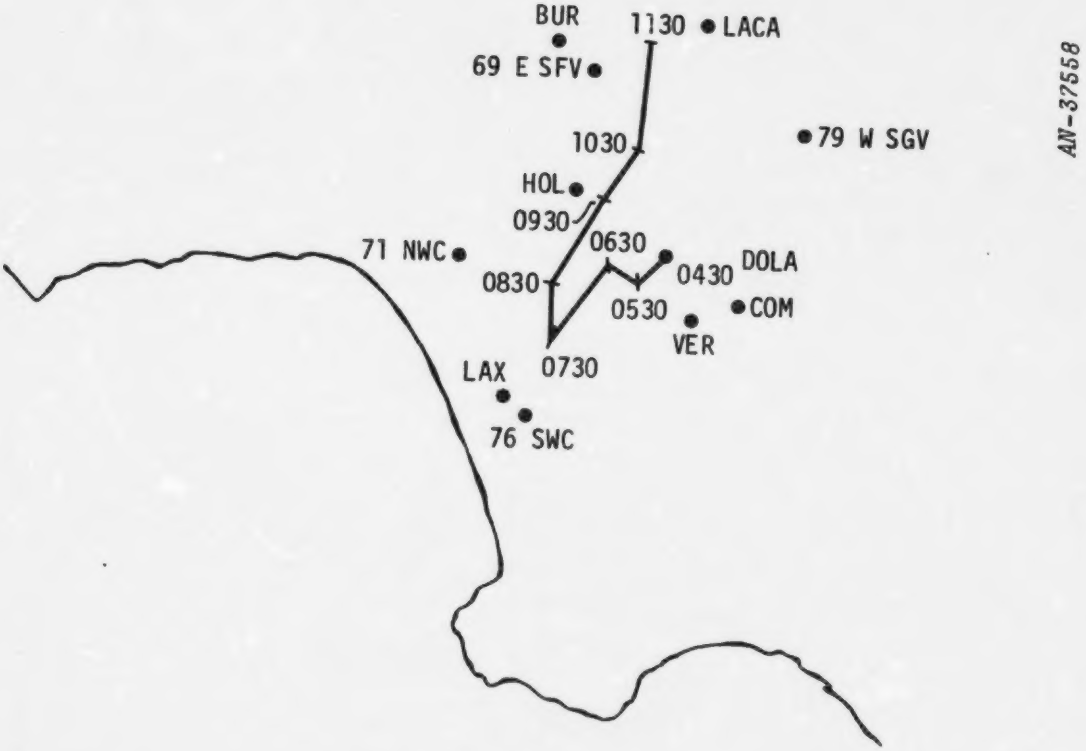
BUR
1130
LACA
69 E SFV
79 W SGV
1030
HOL
0930
0630
71 NWC
0430
DOLA
0830
0530
COM
VER
0730
LAX
76 SWC
AN-37558

Figure 5.46. September 30, 1969 Trajectory Starting in Downtown Los Angeles at 0430 (No. 11)

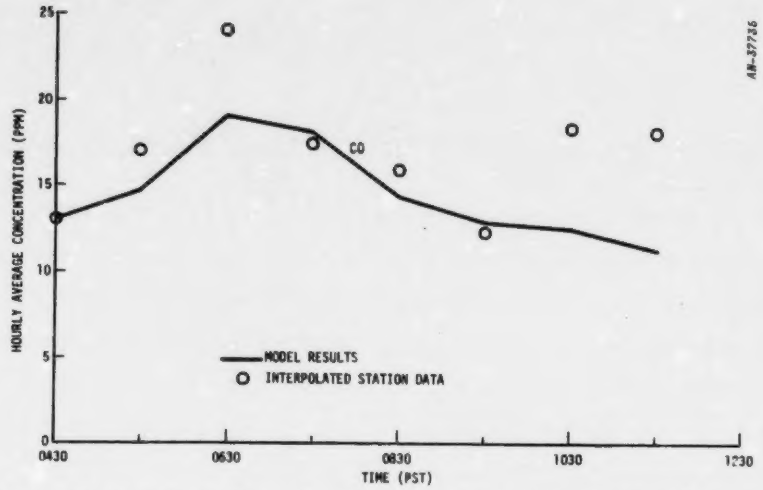

Figure 5.47. Trajectory No. 11--Computed and Observed CO Concentrations

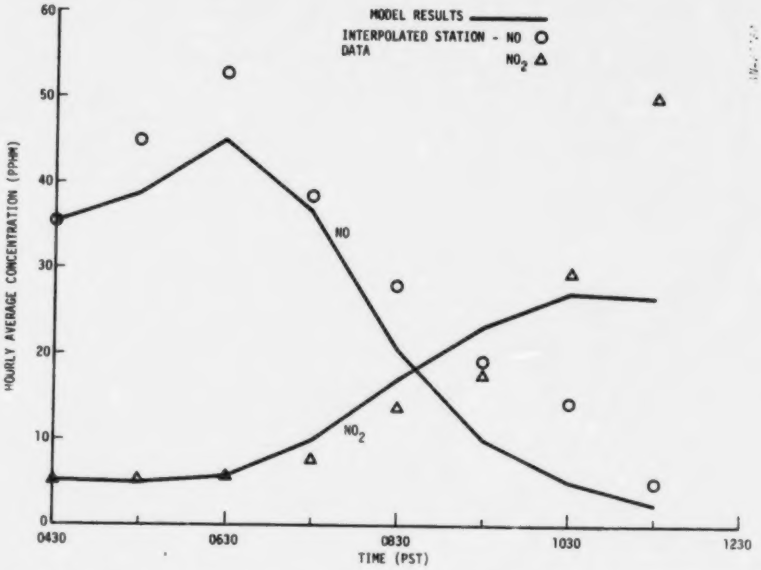

Figure 5.48. Trajectory No. 11--Computed and Observed NO and NO_2 Concentrations

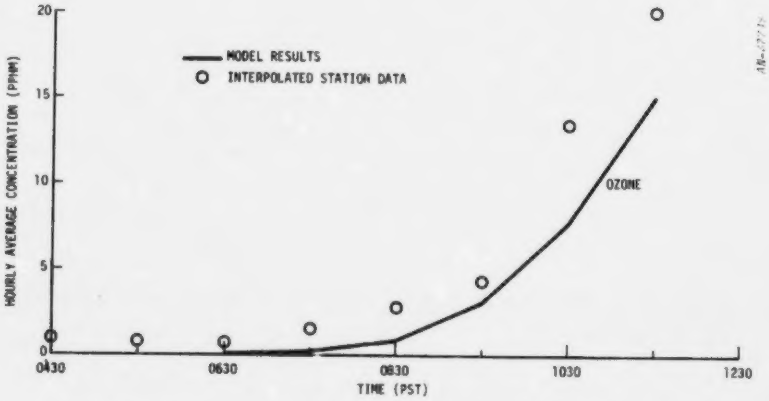

Figure 5.49. Trajectory No. 11--Computed and Observed Ozone Concentrations

5.3.16 Trajectory No. 12, September 30, 1969, Starting in Downtown Los Angeles at 0530 (Hands-On)

The CO simulation shown on Fig. 5.51 indicates good agreement between prediction and observation, with the lower concentrations being overpredicted. On Fig. 5.52, it can be seen that the predicted NO concentrations are low but that the NO_2 computations match the observations accurately. The ozone, Fig. 5.53, is underestimated throughout most of the morning, but the error is small. It should be noted that the observed ozone concentrations which occur from 0730 to 0930 are difficult to reconcile with the high NO concentrations indicated by the data. For k_4, the value used was 10^4 $ppm^{-1}min^{-1}$.

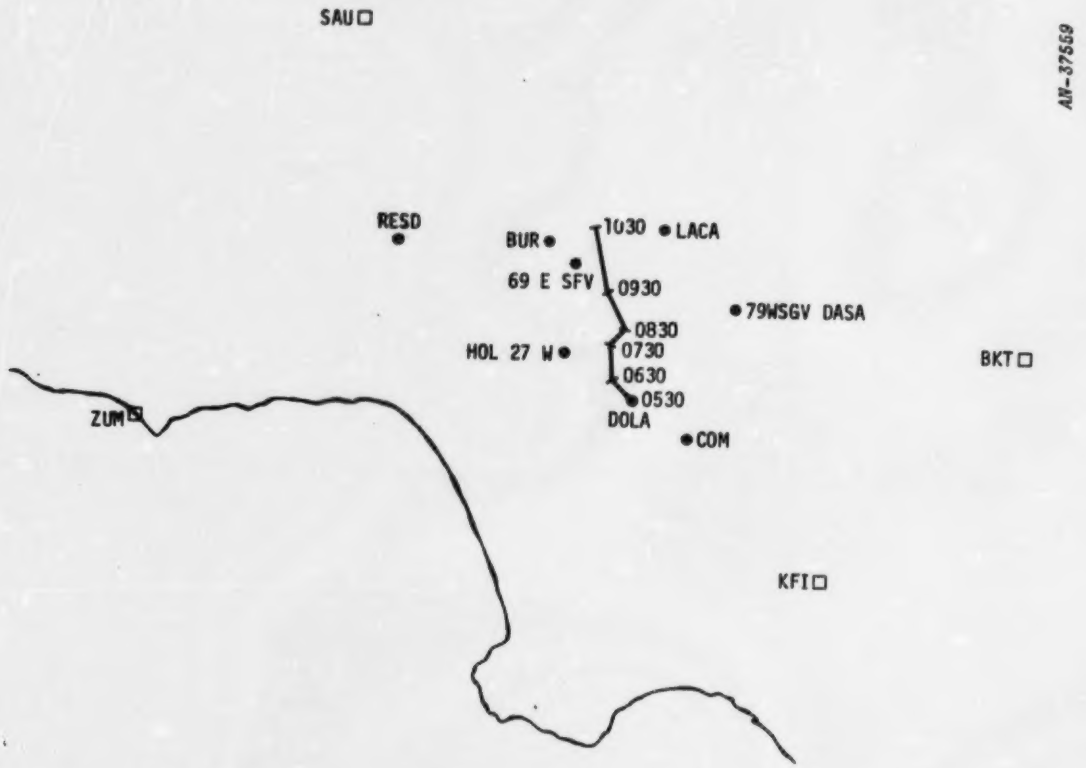
SAU
AN-37559
RESD
BUR
1030
LACA
69 E SFV
0930
79WSGV DASA
0830
HOL 27 W
0730
BKT
0630
0530
ZUM
DOLA
COM
KFI

Figure 5.50. September 30, 1969 Trajectory Starting in Downtown Los Angeles at 0530 (No. 12)

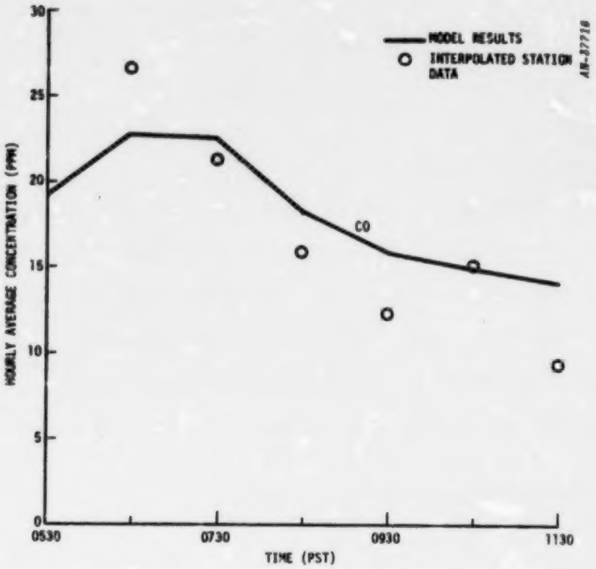

Figure 5.51. Trajectory No. 12--Computed and Observed CO Concentrations

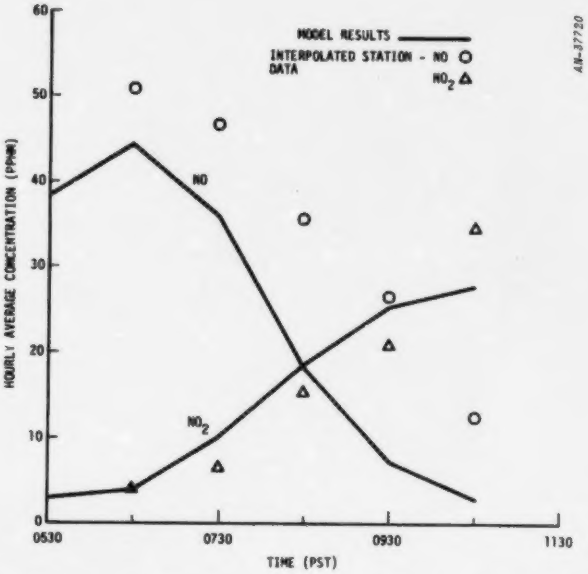

Figure 5.52. Trajectory No. 12--Computed and Observed NO and NO_2 Concentrations

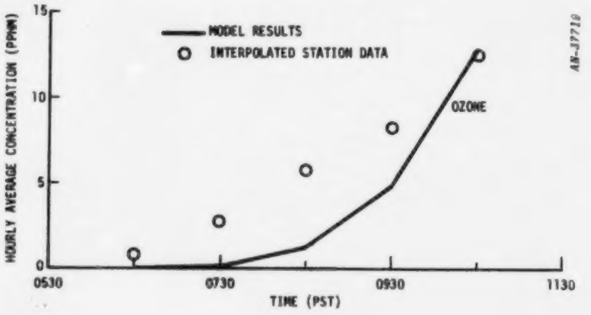

Figure 5.53. Trajectory No. 12--Computed and Observed Ozone Concentrations

5.3.17 Trajectory No. 13, October 29, 1969, Starting in Downtown Los Angeles at 0530 (Hands-On)

Figure 5.55 shows that the simulated CO approximates the data closely. However, from Fig. 5.56 we can see that the NO_x simulation diverges considerably from the data. Despite the low quality of the NO_x simulation, the computed ozone fits the data closely. This is, of course, the result of our emphasis on obtaining accurate ozone predictions. For this trajectory, the value of k_4 used was 4×10^3 $ppm^{-1}min^{-1}$.

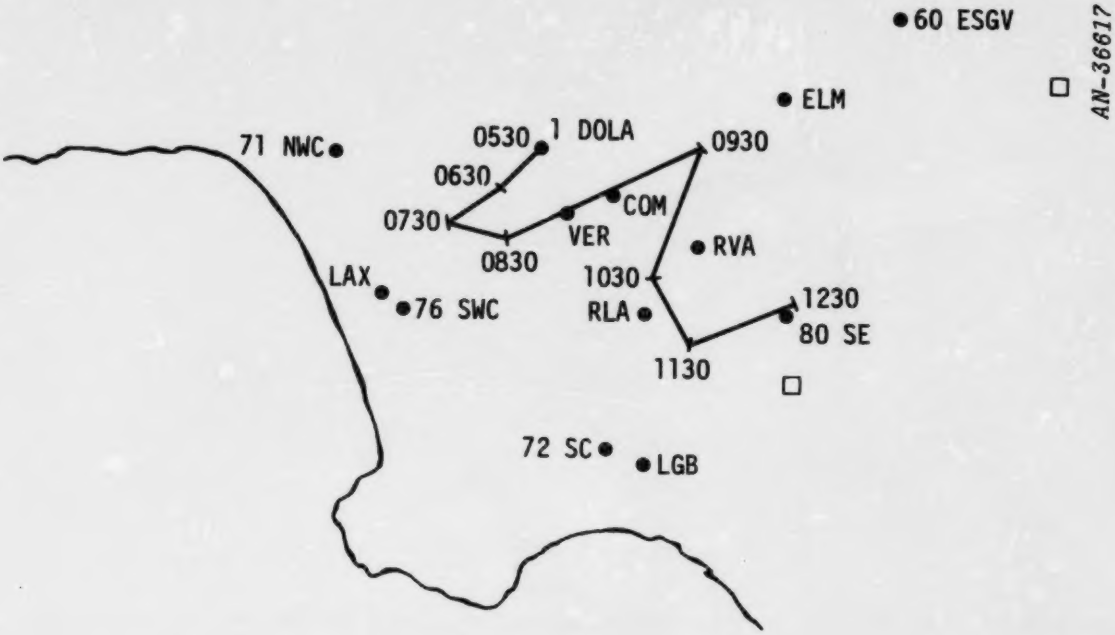
60 ESGV
AN-36617
ELM
71 NWC
0530
1 DOLA
0930
0630
0730
COM
VER
0830
RVA
LAX
1030
76 SWC
RLA
1230
80 SE
1130
72 SC
LGB

Figure 5.54. October 29, 1969 Trajectory Starting in Downtown Los Angeles at 0530 (No. 13)

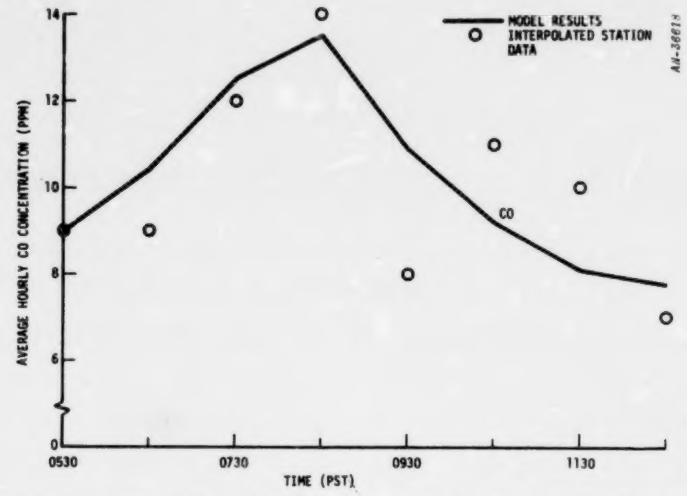

Figure 5.55. Trajectory No. 13--Computed and Observed CO Concentrations

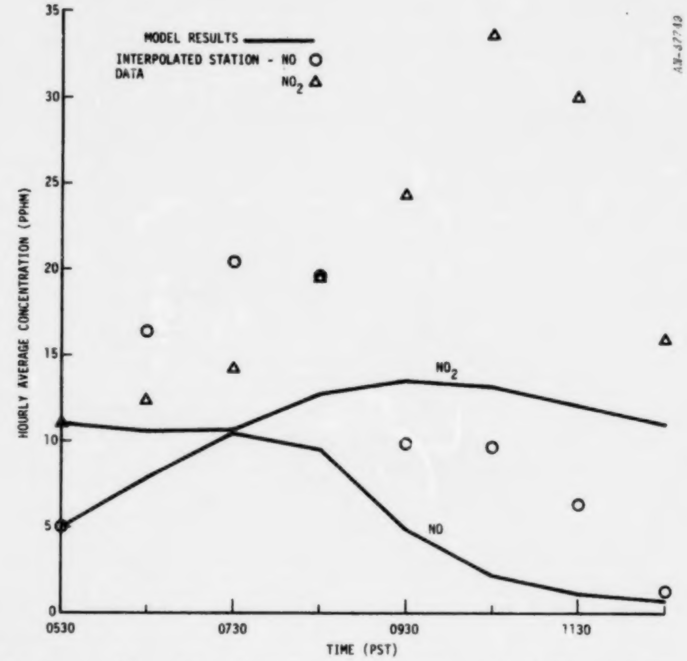

Figure 5.56. Trajectory No. 13--Computed and Observed NO and NO_2 Concentrations

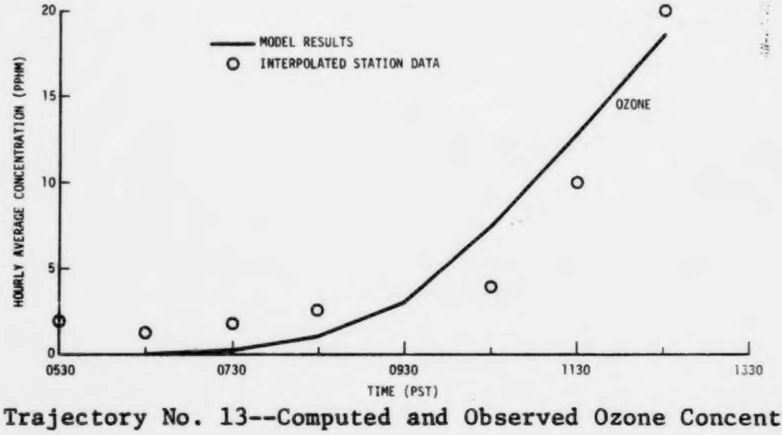

Figure 5.57. Trajectory No. 13--Computed and Observed Ozone Concentrations

5.3.18 Trajectory No. 14, October 29, 1969, Starting in Downtown Los Angeles at 0630 (Hands-On)

From Fig. 5.59 it can be seen that the CO simulation fits the data fairly closely. The CO peak produced by the model is low by 3 ppm. The early-afternoon concentrations of CO are overpredicted.

Figure 5.60 shows that the NO is reproduced very accurately. On the other hand, the simulated NO_2 diverges from the data, the NO_2 peak being low by about 4 pphm and occurring an hour later than indicated by the data. Figure 5.61 shows that the modeling of ozone is remarkably accurate. For this trajectory, the value of k_4 used was 10^4 $ppm^{-1}min^{-1}$.

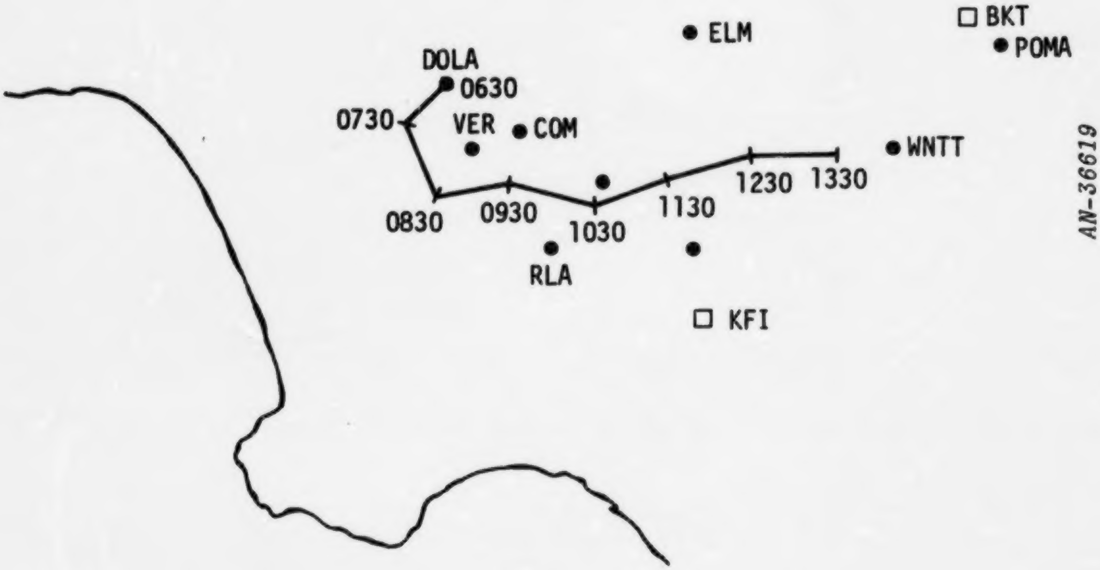
BKT
ELM
POMA
DOLA
0630
0730
VER
COM
WNTT
1230
1330
0830
0930
1030
1130
RLA
KFI
AN-36619

Figure 5.58. October 29, 1969 Trajectory Starting at 0630 in Downtown Los Angeles (No. 14)

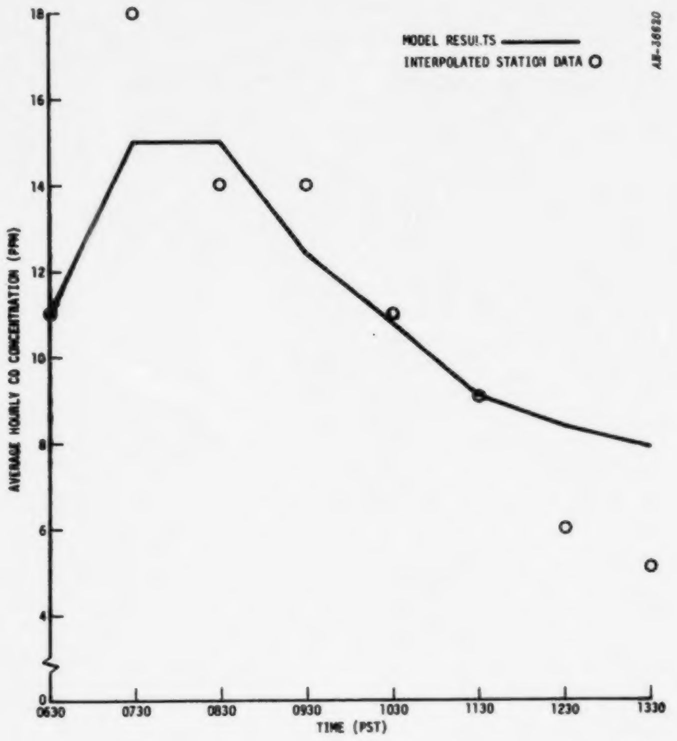

Figure 5.59. Trajectory No. 14--Computed and Observed CO Concentrations

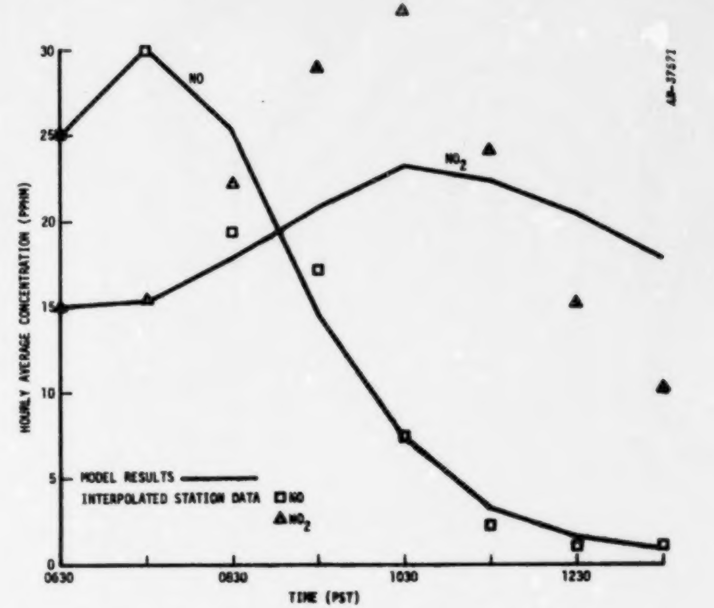

Figure 5.60. Trajectory No. 14--Computed and Observed NO and NO_2 Concentrations

Figure 5.61. Trajectory No. 14--Computed and Observed Ozone Concentrations →

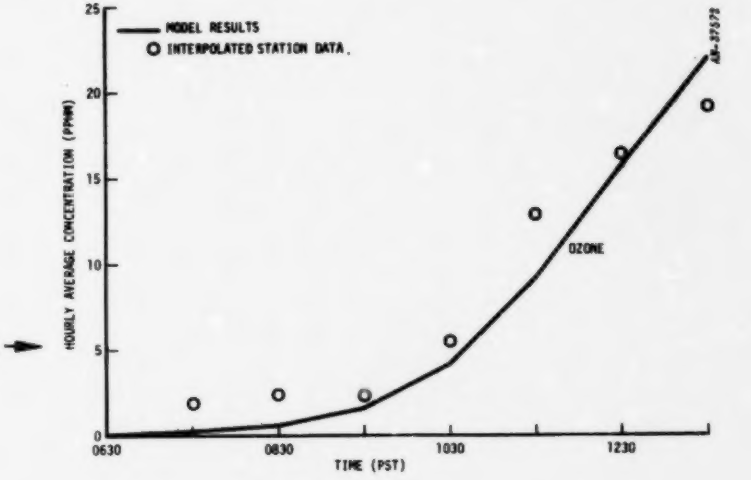

5.3.19 Trajectory No. 15, October 29, 1969, Starting at Commerce at 0630 (Hands-On)

The CO simulation shown in Fig. 5.63 is especially interesting because the double peak shown by the data is reproduced by the model. The maximum difference between data and simulation occurs near the end of the trajectory and is approximately 2.5 ppm. This could be due to greater dispersion near the mountains.

The photochemical simulations (Figs. 5.64 and 5.65) show very good modeling of NO and O_3 . The simulated NO_2 peak is about 3 pphm too low and occurs one hour later than is shown by the data. Inaccuracies in the NO emissions inventory may account for this. The computed end value of NO_2 is 21 pphm compared to about 7 pphm for the data. The high terminal values of NO_2 appear to be a recurring problem in atmospheric photochemical simulations. It is likely that this problem arises from departures from expected photo-chemical equilibrium conditions (see Appendix, Sec. A.2.2). The value of k_4 used in this trajectory was 10^4 $ppm^{-1} min^{-1}$.

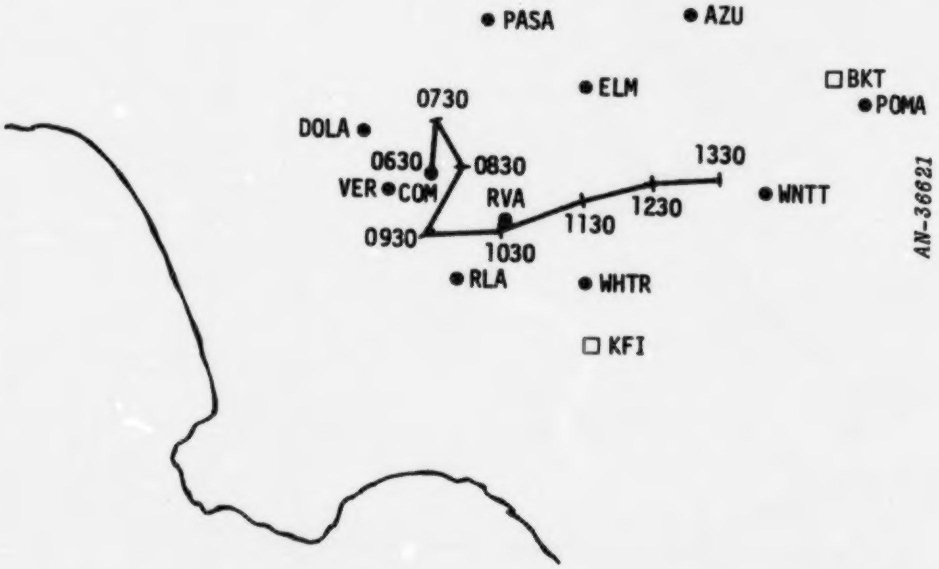

Figure 5.62. October 29, 1969 Trajectory Starting at Commerce at 0630 (No. 15)

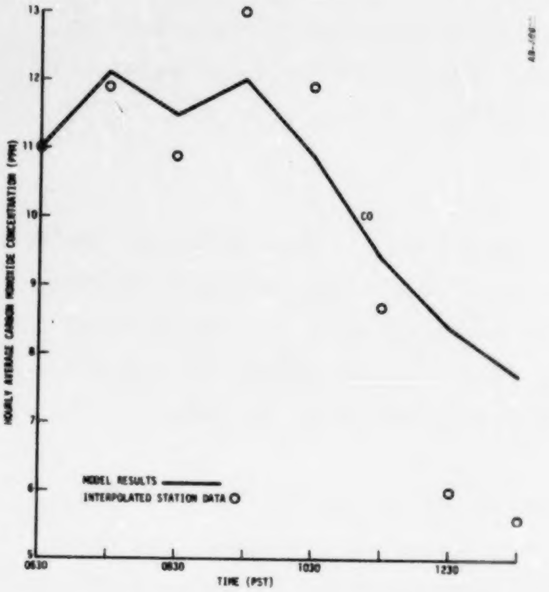

Figure 5.63. Trajectory No. 15--Computed and Observed CO Concentrations

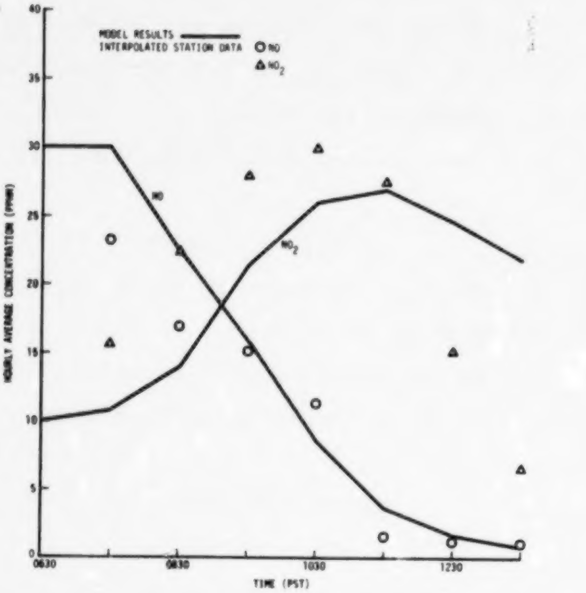

Figure 5.64. Trajectory No. 15--Computed and Observed NO and NO_2 Concentrations

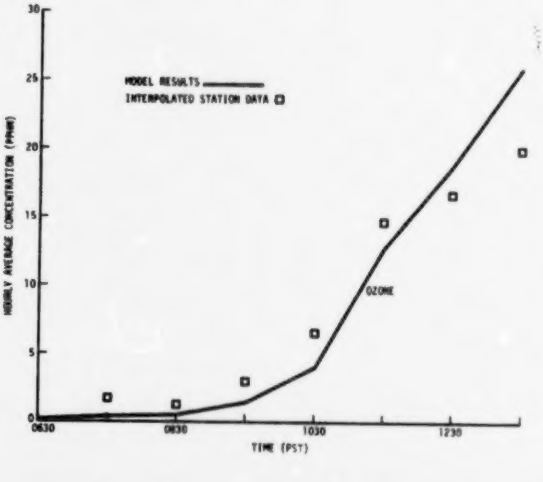

Figure 5.65. Trajectory No. 15--Computed and Observed Ozone Concentrations

5.3.20 Trajectory No. 16, October 29, 1969, Starting at El Monte at 0830

This trajectory shows a reversal in direction of almost 180° at 1030. This may be seen in Fig. 5.66. The high value obtained from the data at 1030 is mostly due to high concentrations reported at the downtown station (1DOLA). In view of the reversal in direction, it is likely that this interpolated quantity is badly off the mark.

The high values shown by the data at the end of the trajectory could not be reproduced by the simulation since the trajectory enters some areas with no sources at all. Location of the sampling sites can induce large deviations from the average for the air mass. The ground value will continue to decrease due to diffusion when source strengths are small.

Figure 5.68 shows that the simulation of NO is very accurate, but that for NO_2 the model produced very poor results. As usual, the ozone simulation, shown in Fig. 5.69, fits the data closely. The value used for k_4 was 10^4 $ppm^{-1}min^{-1}$.

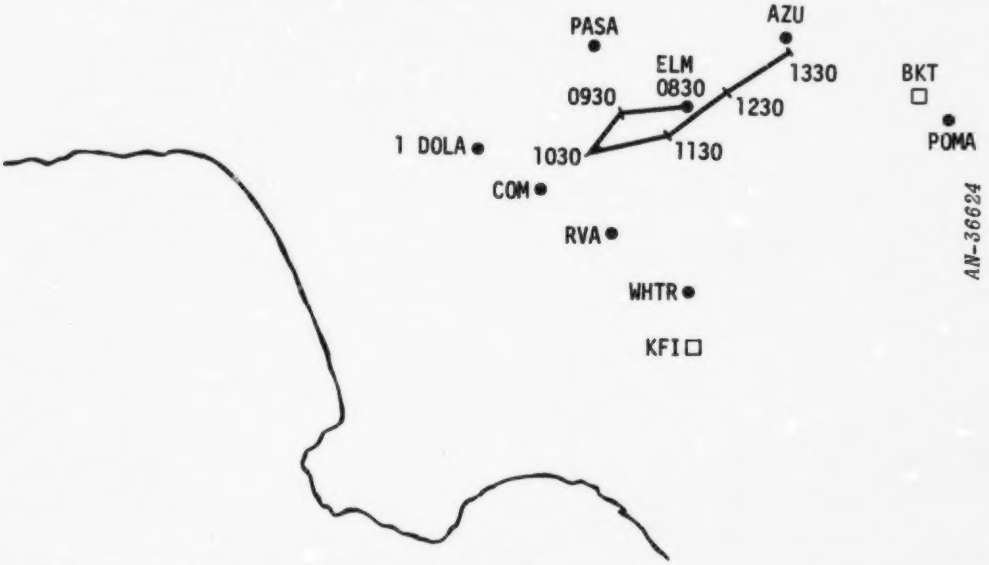

Figure 5.66. October 29, 1969 Trajectory Starting at El Monte at 0830 (No. 16)

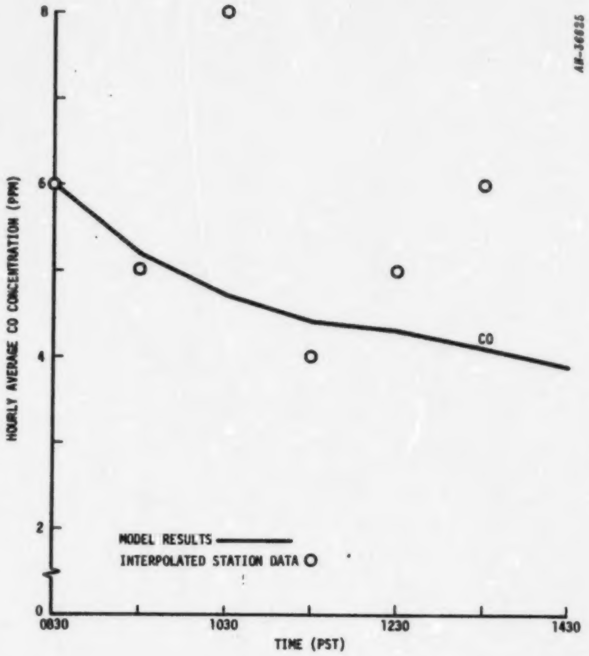

Figure 5.67. Trajectory No. 16--Computed and Observed CO Concentrations

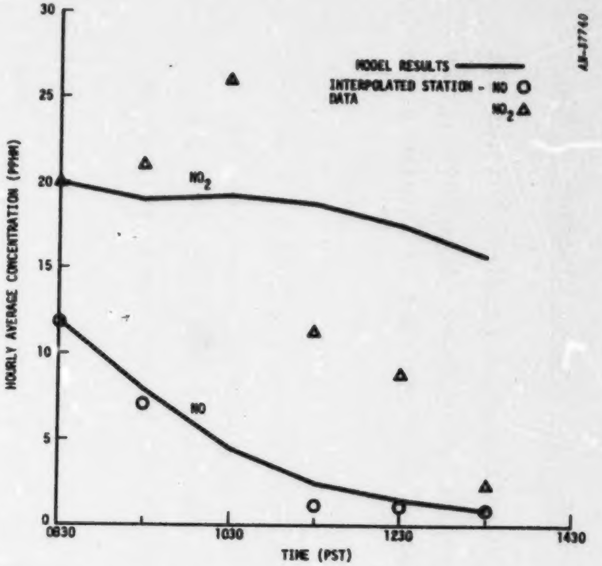

Figure 5.68. Trajectory No. 16--Computed and Observed NO and NO_2 Concentrations

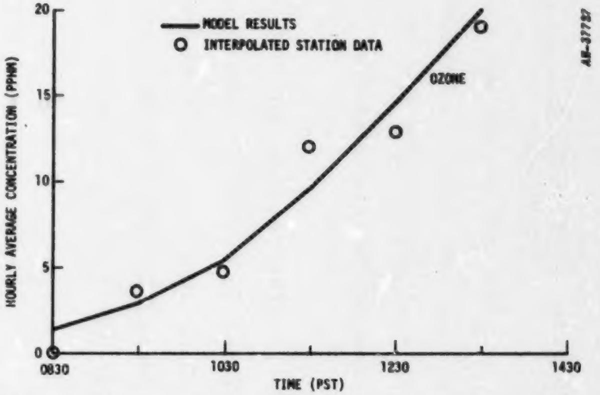

Figure 5.69. Trajectory No. 16--Computed and Observed Ozone Concentrations

5.3.21 Trajectory No. 17, October 30, 1969, Starting at Pasadena at 0530 (Hands-Off)

The trajectory was started at 0730 southeast of Pasadena because all of the CO data for Pasadena are missing for this date. As a result, the initial values used for the various species were obtained by interpolation from neighboring stations.

The results for CO show good reproduction of the buildup phase from 0730 to 0930. The decay part of the concentration curve has the right shape, but the concentrations are about 3 ppm too high. The low points in mid-morning measurements could be due to horizontal intrusions of air directly from the ocean.

The photochemical results show good NO and O_3 simulations. The NO_2 buildup is well modeled, but the NO_2 decay shows a very poor fit of the data. The late morning dip of NO_2 interpolated values may be due to the same dilution mechanisms suggested above for the CO points. The value used for k_4 was 10^4 $ppm^{-1}min^{-1}$.

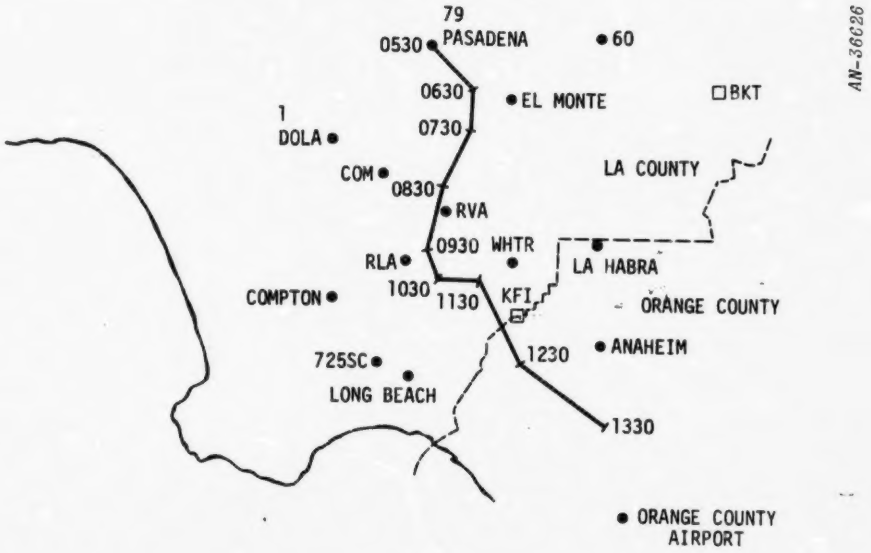
79
PASADENA
0530
60
0630
EL MONTE
BKT
AN-36C26
1
DOLA
0730
LA COUNTY
COM
0830
RVA
0930
WHTR
RLA
LA HABRA
COMPTON
1030
1130
KFI
ORANGE COUNTY
1230
ANAHEIM
725SC
LONG BEACH
1330
ORANGE COUNTY
AIRPORT

Figure 5.70. October 30, 1969 Trajectory Starting at Pasadena at 0530 (No. 17)

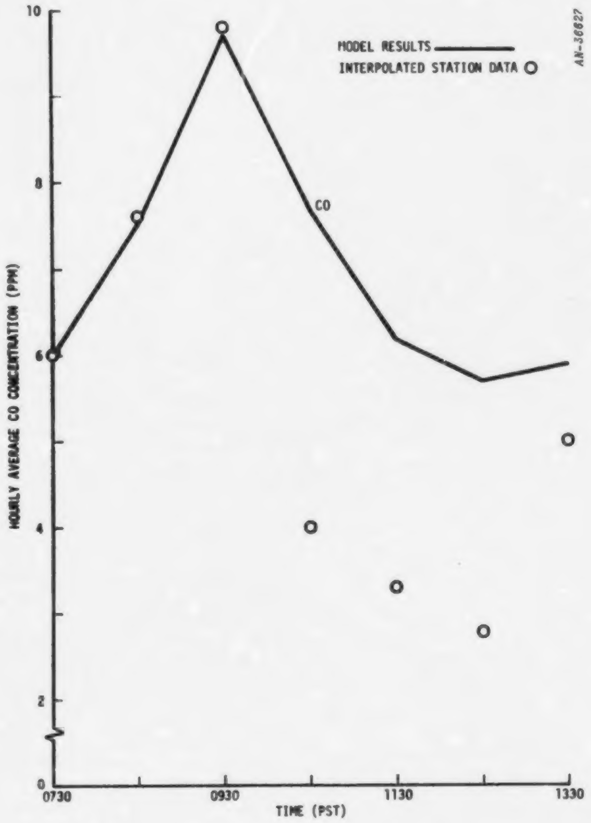

Figure 5.71. Trajectory No. 17--Computed and Observed CO Concentrations

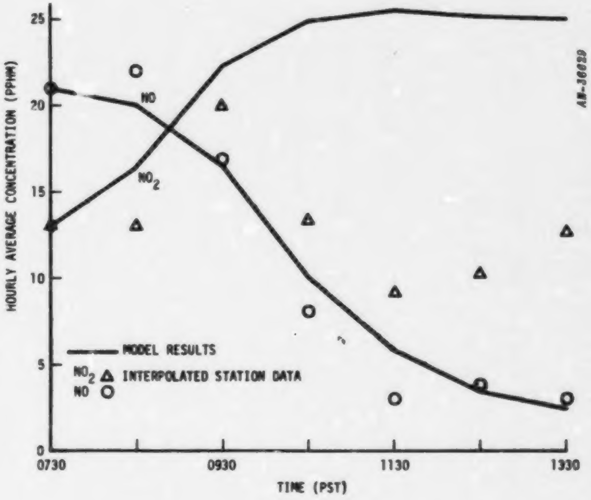

Figure 5.72. Trajectory No. 17--Computed and Observed NO and NO_2 Concentrations

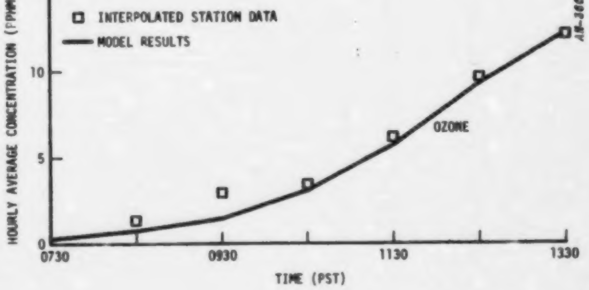

Figure 5.73. Trajectory No. 17--Computed and Observed Ozone Concentrations

5.3.22 Trajectory No. 18, October 30, 1969, Starting at Commerce at 0630 (Hands-Off)

This trajectory is rather short, only 4 hours long, and is interesting because it travels toward the coast early in the morning.

Figure 5.75 illustrates the simulation of CO . The time phasing and shape of the curve agree with the data, but the predicted CO peak is about 2.5 ppm lower than the data. It is noted that there were not available data for 0930.

It can be seen from Fig. 5.76 that the behavior of NO is accurately simulated. The NO_2 buildup is also accurate, but the predicted peak is too low. This trajectory is one of the few examples in which the computed ozone does not fit the data. However, it should be noted that the ozone levels are very low and that the maximum absolute difference is only 4 pphm, although the relative error is considerably greater. The value used for k_4 was 10^4 $ppm^{-1}min^{-1}$.

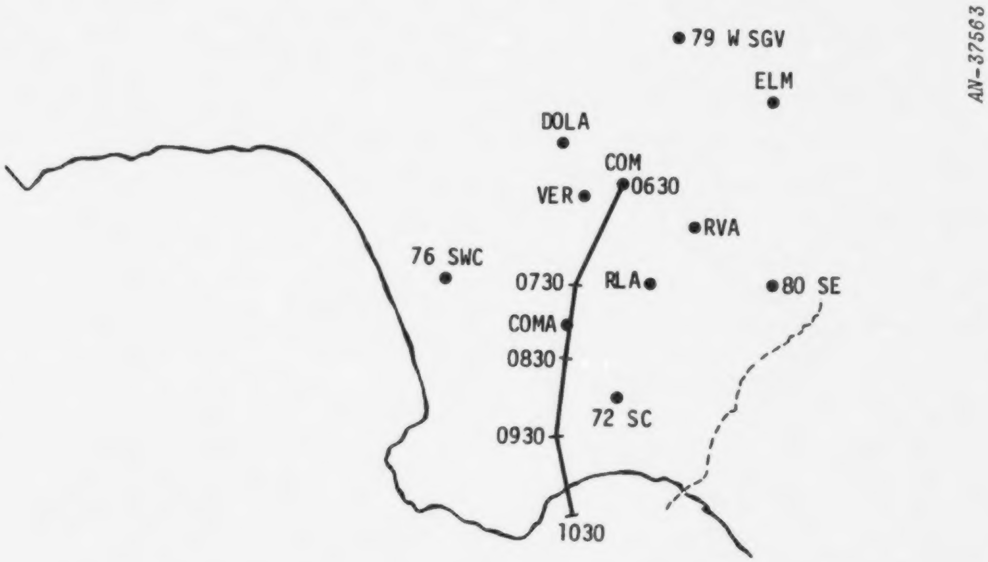

Figure 5.74. October 30, 1969 Trajectory Starting at Commerce at 0630 (No. 18)

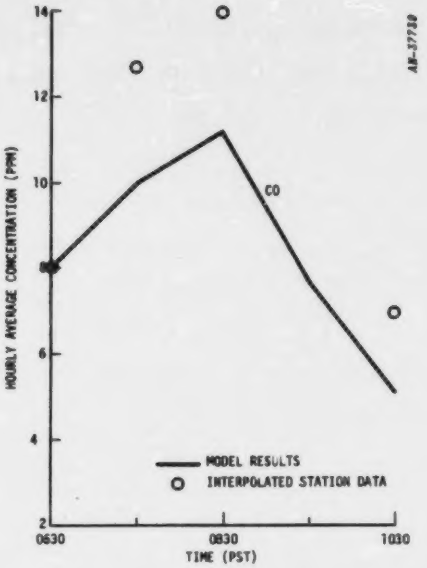

Figure 5.75. Trajectory No. 18--Computed and Observed CO Concentrations

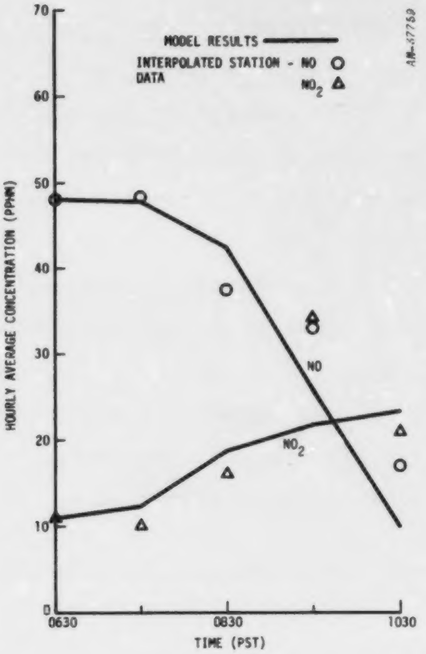

Figure 5.76. Trajectory No. 18--Computed and Observed NO and NO_2 Concentrations

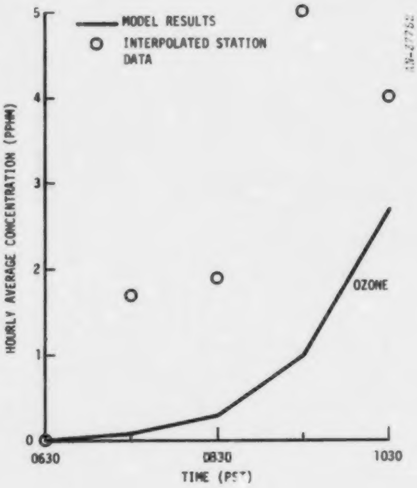

Figure 5.77. Trajectory No. 18--Computed and Observed Ozone Concentrations

5.3.23 Trajectory No. 19, October 30, 1969, Starting at El Monte at 0630 (Hands-off)

The results of the simulation for CO are shown in Fig. 5.79. It can be seen that the model overestimates CO throughout the day. However, the maximum difference between model and data is about 2.5 ppm.

As is generally the case with the reactive species, the NO and ozone predictions are very accurate, as is shown in Figs. 5.80 and 5.81, respectively. The NO_x balance is poor after 1030, however. The NO_2 simulation exceeds the data after 1030. The low NO_2 data at 1130 and 1230 are suspect inasmuch as $NO \rightarrow NO_2$ conversion continues during this interval. The magnitude of k_4 was 10^4 ppm^{-1} min^{-1}.

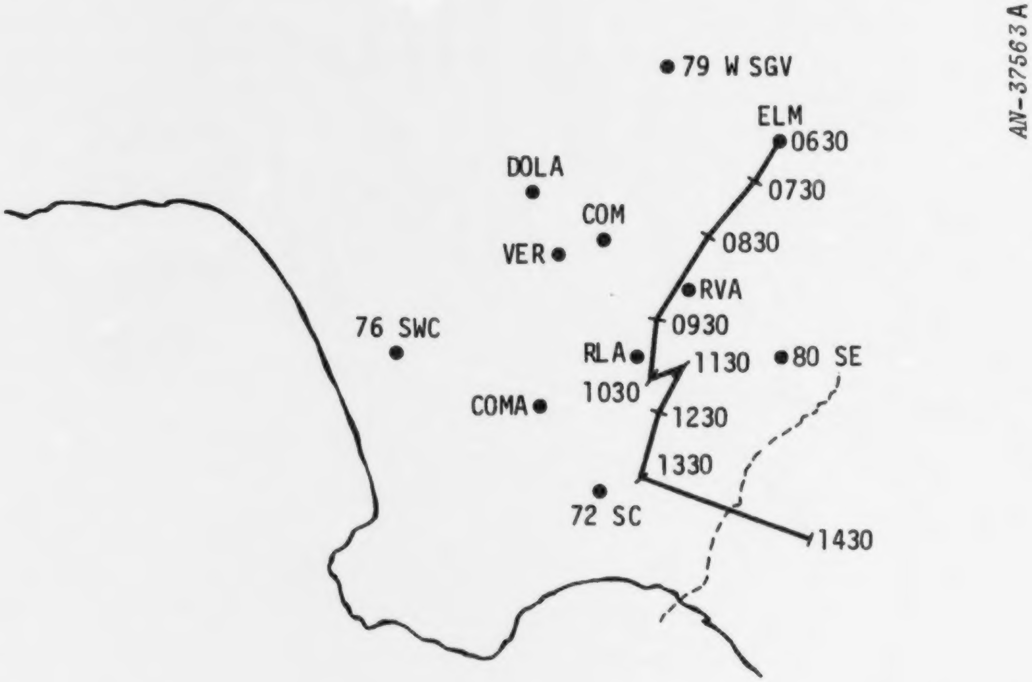
AN-37563 A
79 W SGV
ELM
0630
0730
0830
DOLA
COM
VER
RVA
0930
76 SWC
RLA
1130
80 SE
1030
COMA
1230
1330
72 SC
1430

Figure 5.78. October 30, 1969 Trajectory Starting at El Monte at 0630 (No. 19)

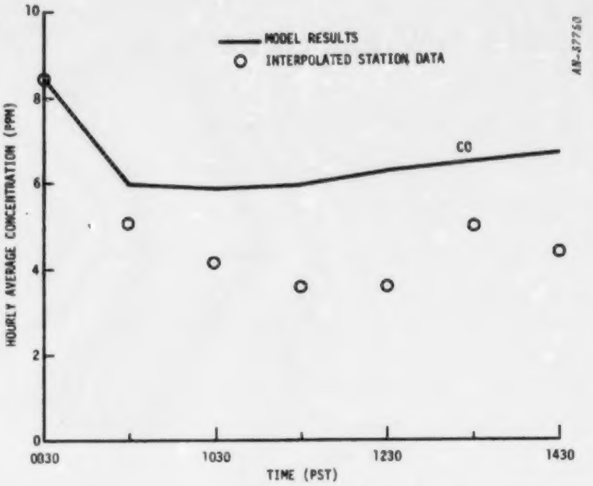

Figure 5.79. Trajectory No. 19--Computed and Observed CO Concentrations

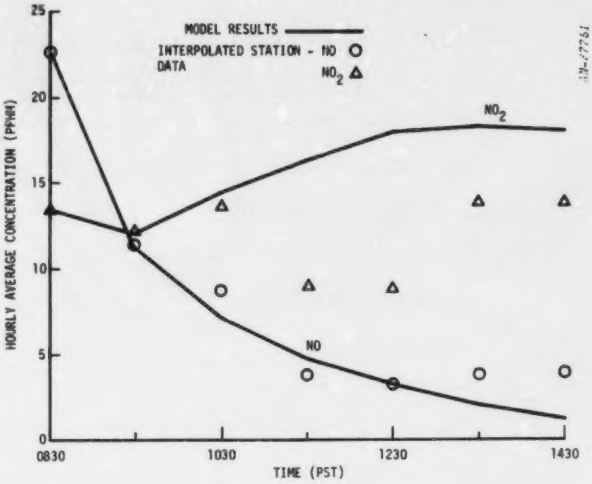

Figure 5.80. Trajectory No. 19--Computed and Observed NO and NO_2 Concentrations

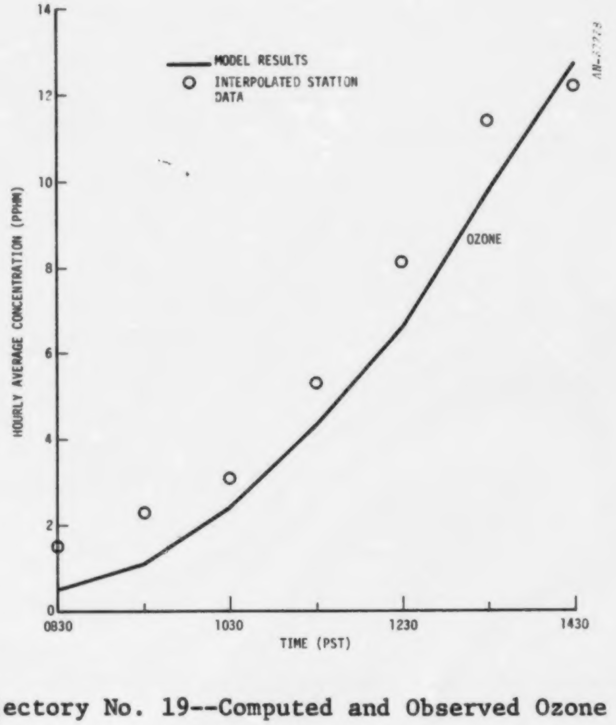

Figure 5.81. Trajectory No. 19--Computed and Observed Ozone Concentrations

5.3.24 Trajectory No. 20, October 30, 1969, Starting in Downtown Los Angeles at 0830 (Hands-off)

The shape of the CO simulation depicted on Fig. 5.83 does not match the data. Nevertheless, the maximum difference between model and data is 2 ppm. The increase in CO concentration after 1030 is due to the filling up of the air parcel, thus reducing the vertical concentration gradient and therefore the vertical diffusion.

For NO_x, the simulation results are inaccurate, as can be seen in Fig. 5.84. However, in Fig. 5.85 the simulated ozone shows once again a very close fit to the data, despite the low quality of the NO_x simulation. We note that it is difficult to believe that so much ozone could coexist with the NO indicated by the data. Finally, the value of k_4 used was 6×10^3 ppm^{-1} min^{-1}.

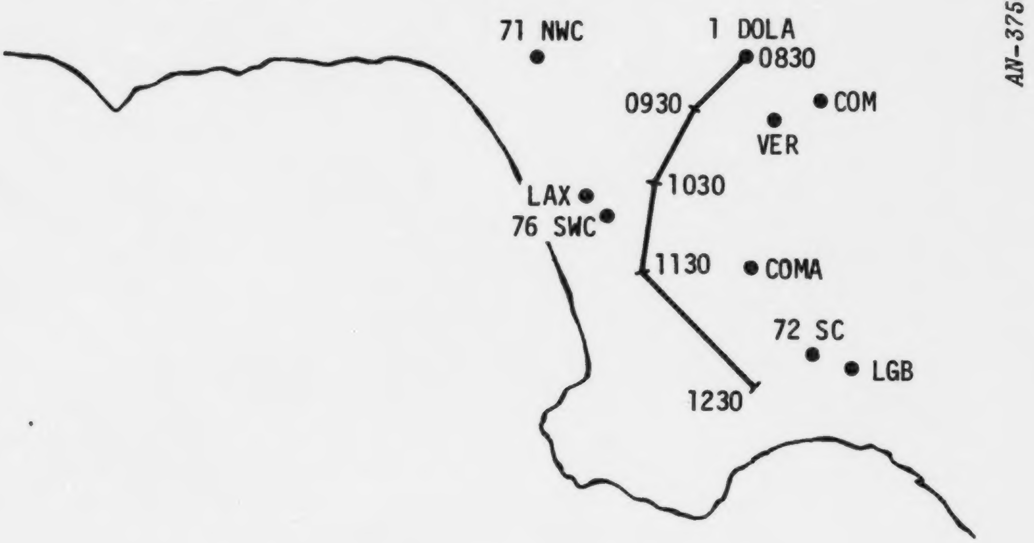

Figure 5.82. October 30, 1969 Trajectory Starting in Downtown Los Angeles at 0830 (No. 20)

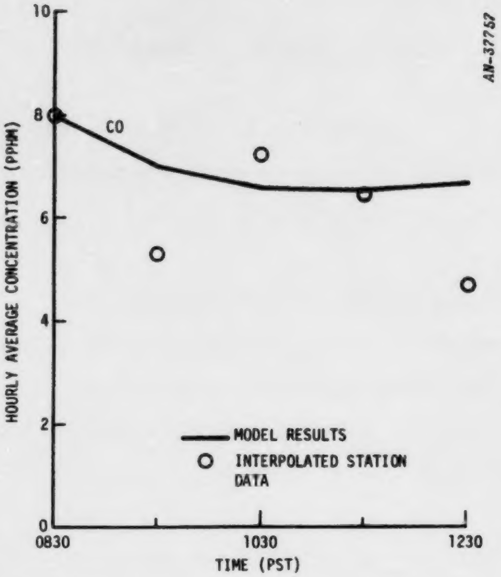

Figure 5.83. Trajectory No. 20--Computed and Observed CO Concentrations

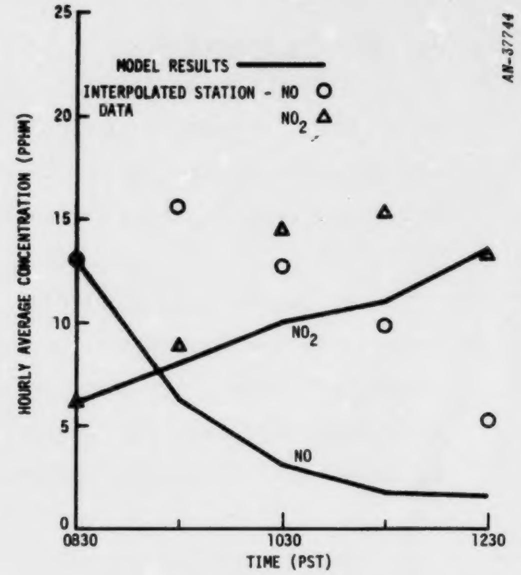

Figure 5.84. Trajectory No. 20--Computed and Observed NO and NO_2 Concentrations

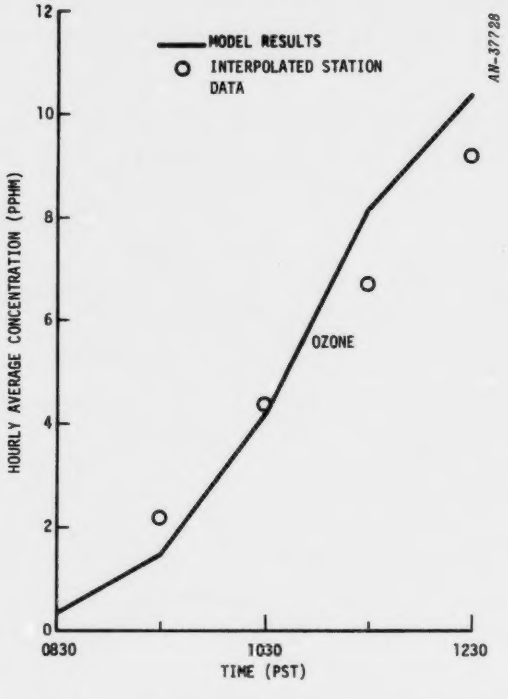

Figure 5.85. Trajectory No. 20--Computed and Observed Ozone Concentrations

5.3.25 Trajectory No. 21, November 4, 1969, Starting at Commerce at 0530 (Hands-off)

This trajectory exhibits a reversal in direction at 0730 and this may introduce inaccuracies in the interpolation process used to calculate the concentrations along the path of the trajectory.

As can be seen from Fig. 5.87, the early-morning CO buildup is underestimated by the model, with the relative error at the CO peak being about 21%. The sharp decay and subsequent increase in concentration seen after 0930 are not properly simulated by the model because the CO emissions are increasing during this part of the trajectory.

The simulation of NO_x illustrated in Fig. 5.88 shows that NO is underpredicted but that NO_2 fits the data accurately. The relatively high concentrations of ozone found in the data (Fig. 5.89) are suspect because the data show high concentrations of NO present throughout the trajectory. Nevertheless, the ozone simulation is accurate, especially at the higher levels. In this trajectory the value assigned to k_4 was 5×10^3 ppm^{-1} min^{-1}.

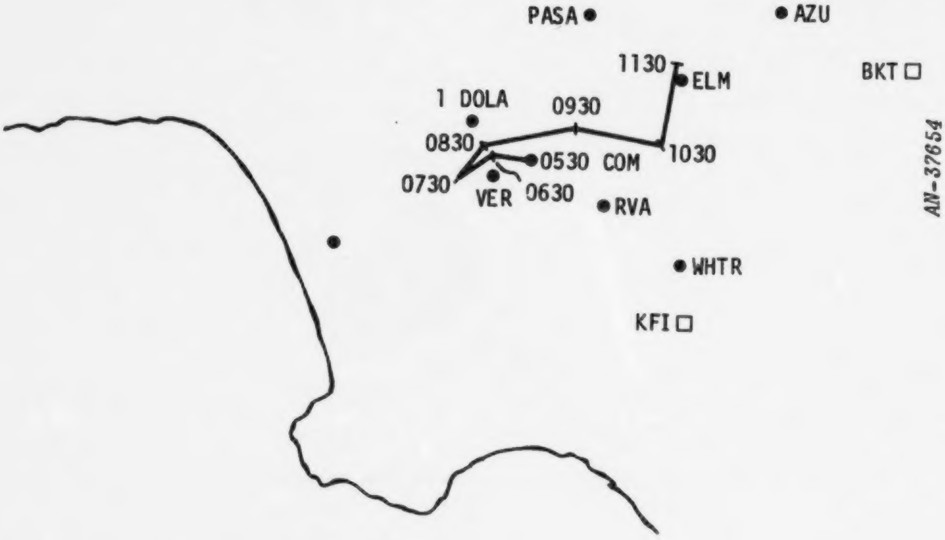

Figure 5.86. November 4, 1969 Trajectory Starting at Commerce at 0530 (No. 21)

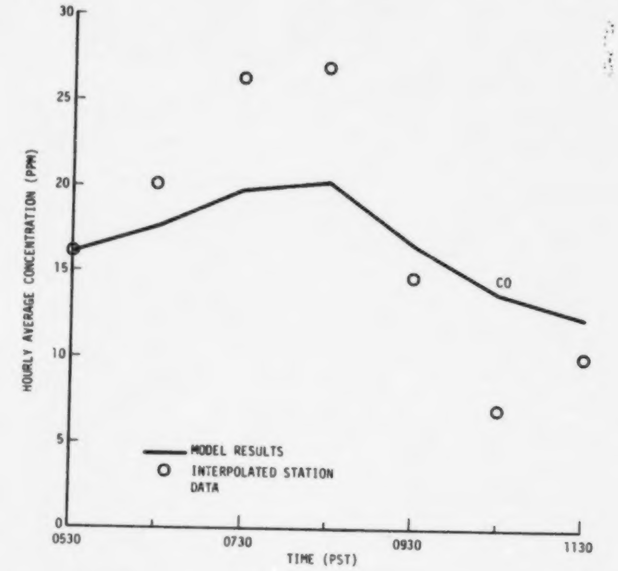

Figure 5.87. Trajectory No. 21--Computed and Observed CO Concentrations

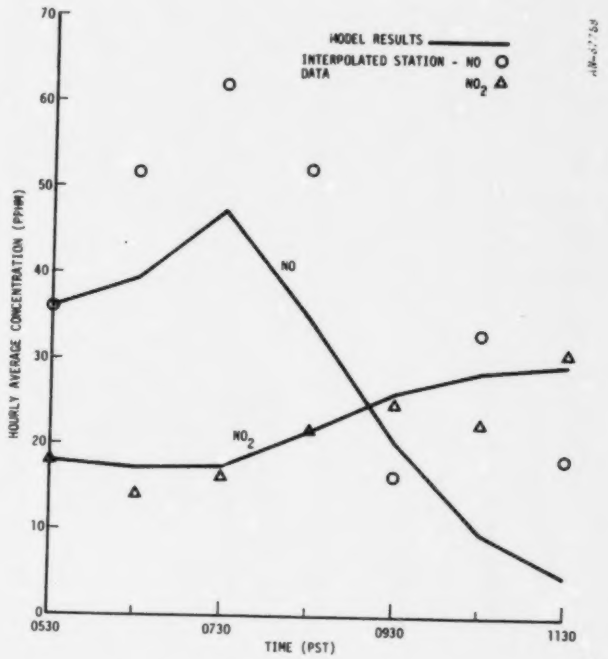

Figure 5.88. Trajectory No. 21--Computed and Observed NO and NO_2 Concentrations

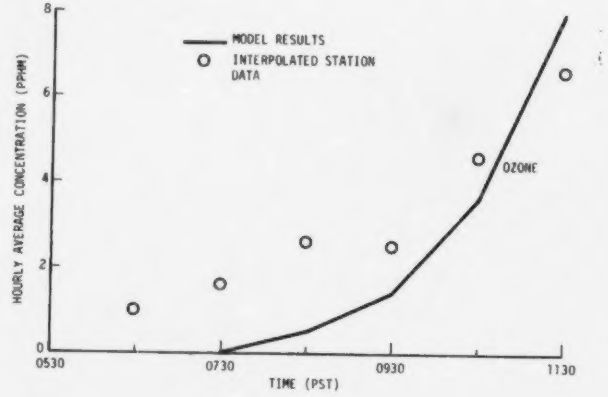

← Figure 5.89. Trajectory No. 21--Computed and Observed Ozone Concentrations

5.3.26 Trajectory No. 22, November 4, 1969, Starting at Commerce at 0630 (Hands-off)

This trajectory also exhibits a reversal in direction at 0730 similar to that found in trajectory No. 21. Thus the caveats mentioned previously regarding the accuracy of the interpolation also apply here.

In contrast with the previous case, Fig. 5.91 shows that the CO buildup is reproduced accurately by the model. However, the CO decay is greatly overestimated by the computation. The CO emissions are high until 0900, at which time they drop to about one-half of the 0900 value.

Figure 5.92 shows that the initial NO level is very high and from Table 5.3 we can see that the initial hydrocarbon concentration is also very high (130 pphm). This hydrocarbon-NO combination portends high NO_2 levels and this is precisely what the simulation produces, as can be seen in Fig. 5.92. The ozone simulation is generally accurate, however, although the ozone peak is overestimated by about 28%. For this trajectory, we used a value of k_4 equal to 10^4 ppm^{-1} min^{-1}.

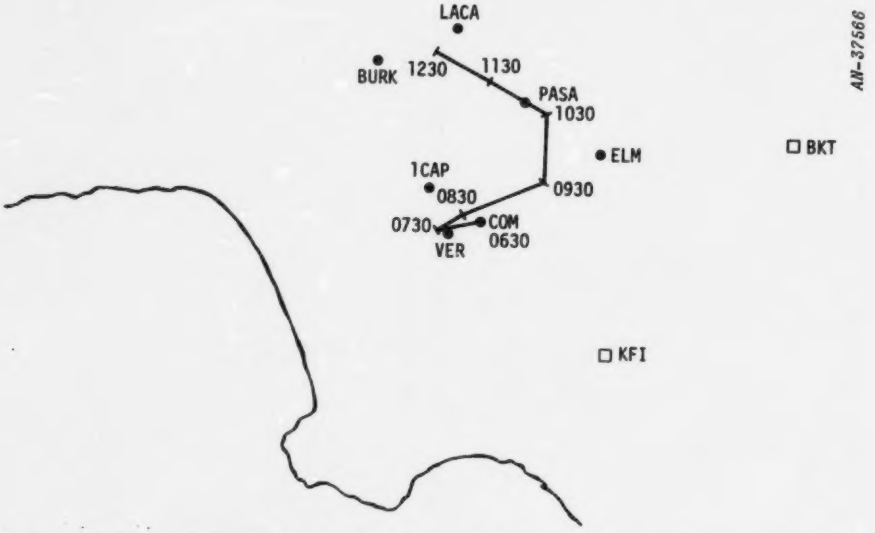

Figure 5.90. November 4, 1969 Trajectory Starting at Commerce at 0630 (No. 22)

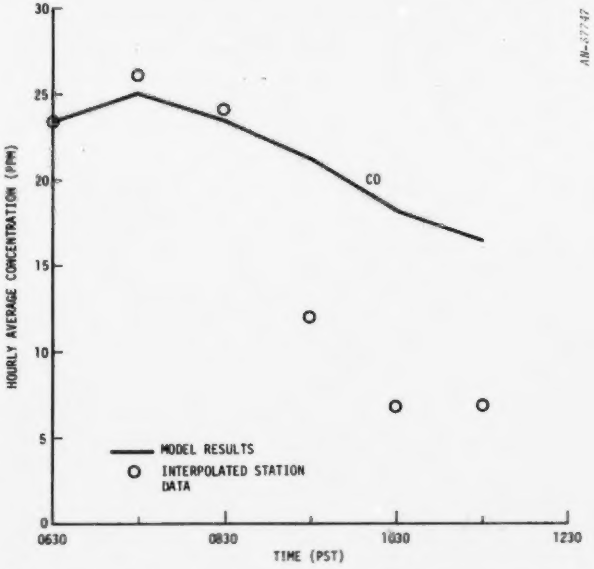

Figure 5.91. Trajectory 22--Computed and Observed CO Concentrations

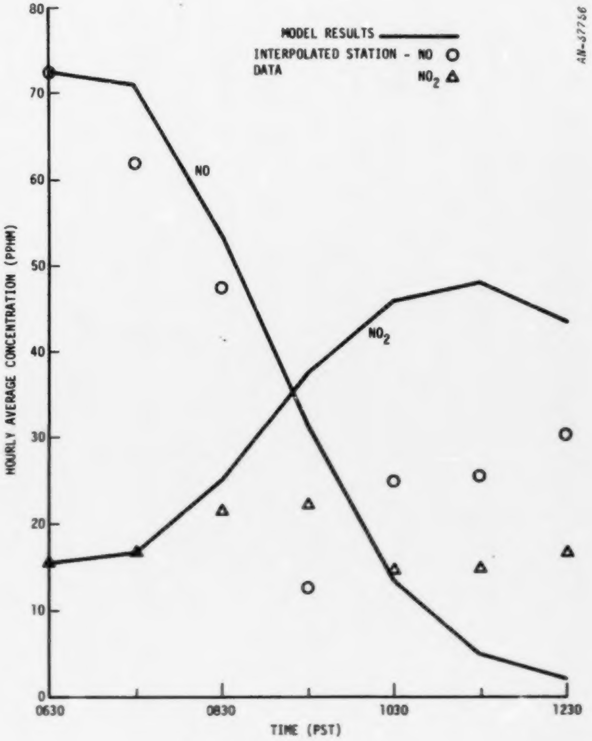

Figure 5.92. Trajectory No. 22--Computed and Observed NO and NO_2 Concentrations

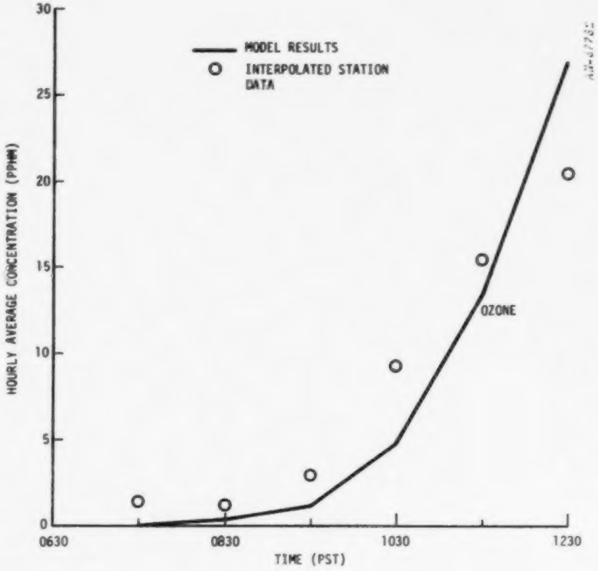

← Figure 5.93. Trajectory No. 22--Computed and Observed Ozone Concentrations

5.3.27 Trajectory No. 23, November 4, 1969, Starting in Pasadena at 0530 (Hands-off)

Figure 5.95 shows that the model underestimates CO concentrations throughout the trajectory. In this case, the strength of the emissions was too low to produce the high values indicated by the data even under highly stable meteorological conditions. Upon investigating the data, it became apparent that the high concentrations from 0630 to 0830 are due to the downtown and Commerce stations which, in view of the path of the trajectory, makes these interpolated concentrations suspect. The suspicion is heightened upon noting that at 0930, when the air parcel is again close to Pasadena, the predicted and observed concentrations are closely matched.

Figure 5.96 shows that the computed NO_x balance is very poor, with the predicted NO and NO_2 considerably below their apparent observed values. As can be seen in Fig. 5.97, the computed ozone accurately reproduces the observations, the largest deviation occurring at 0930. This is puzzling in view of the results obtained for CO at 0930, but with chemical processes at work, it is not surprising. The value used for k_4 was 4×10^3 ppm^{-1} min^{-1}.

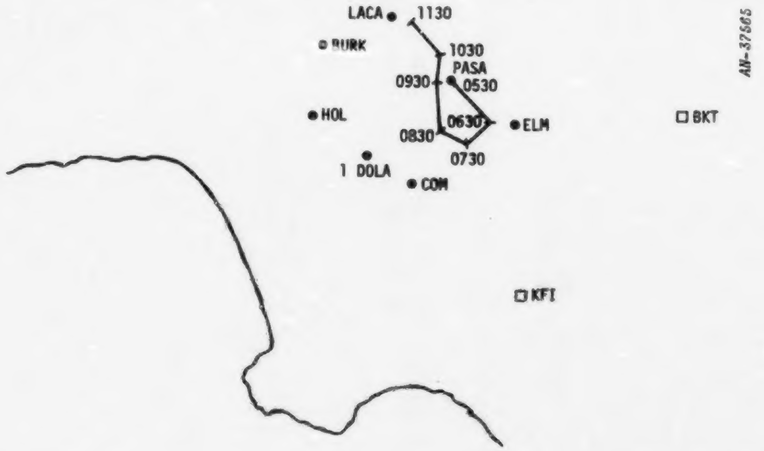

Figure 5.94. November 4, 1969 Trajectory Starting in Pasadena at 0530 (No. 23)

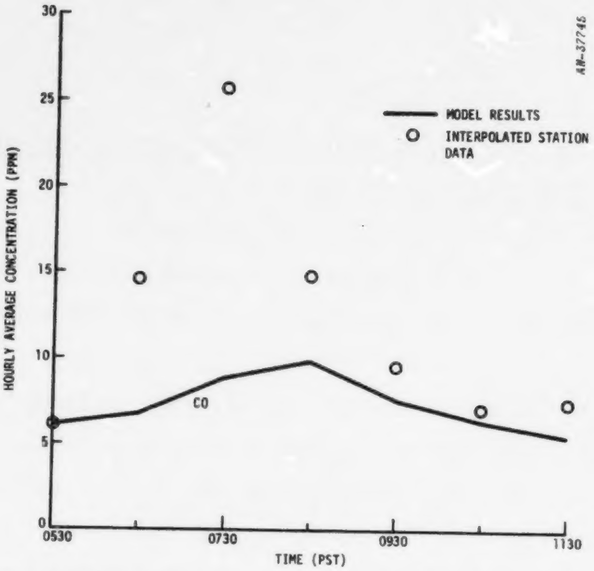

Figure 5.95. Trajectory No. 23--Computed and Observed CO Concentrations

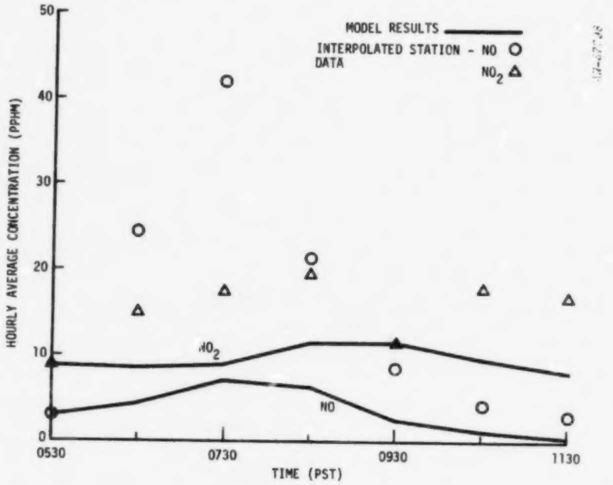

Figure 5.96. Trajectory No. 23--Computed and Observed NO and NO_2 Concentrations

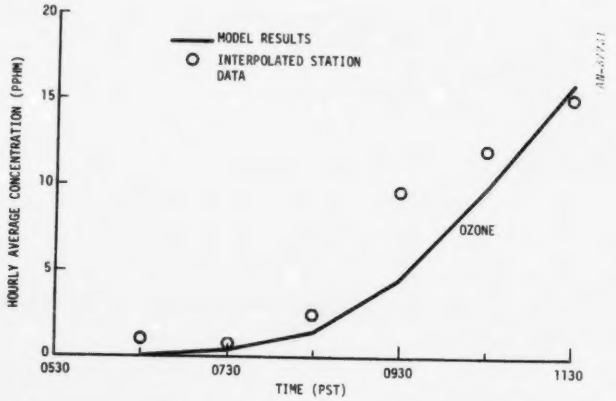

Figure 5.97. Trajectory No. 23--Computed and Observed Ozone Concentrations

5.3.28 Trajectory No. 24, November 4, 1969, Starting in Downtown Los Angeles at 0530 (Hands-off)

The simulation of CO yielded the results shown in Fig. 5.99. The early-morning buildup of CO is accurately simulated. Once again, however, the lower concentrations of CO are overpredicted by the model.

In Fig. 5.100, it can be seen that the NO_x balance is relatively accurate until 0930, although the NO peak is underestimated. After 0930, the computed NO_2 remains too high, while the NO fits the data correctly. For ozone, we see in Fig. 5.101 that the predicted ozone buildup until 1230 is accurate, but after 1230 the model exceeds the data by a maximum of 10 pphm. The value of k_4 used was 10^4 ppm^{-1} min^{-1}.

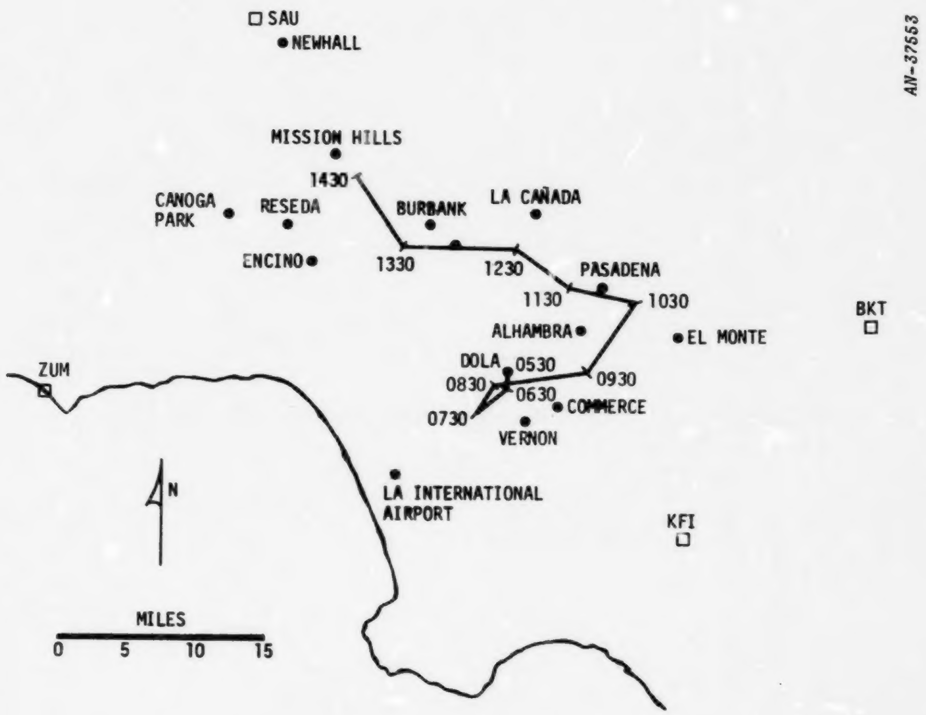

SAU
NEWHALL
AN-37553
MISSION HILLS
1430
CANOGA PARK
RESEDA
BURBANK
LA CAÑADA
ENCINO
1330
1230
PASADENA
1130
1030
BKT
ALHAMBRA
EL MONTE
ZUM
DOLA
0530
0830
0630
0930
COMMERCE
0730
VERNON
N
LA INTERNATIONAL AIRPORT
KFI
MILES
0
5
10
15

Figure 5.98. November 4, 1969 Trajectory Starting in Downtown Los Angeles at 0530 (No. 24)

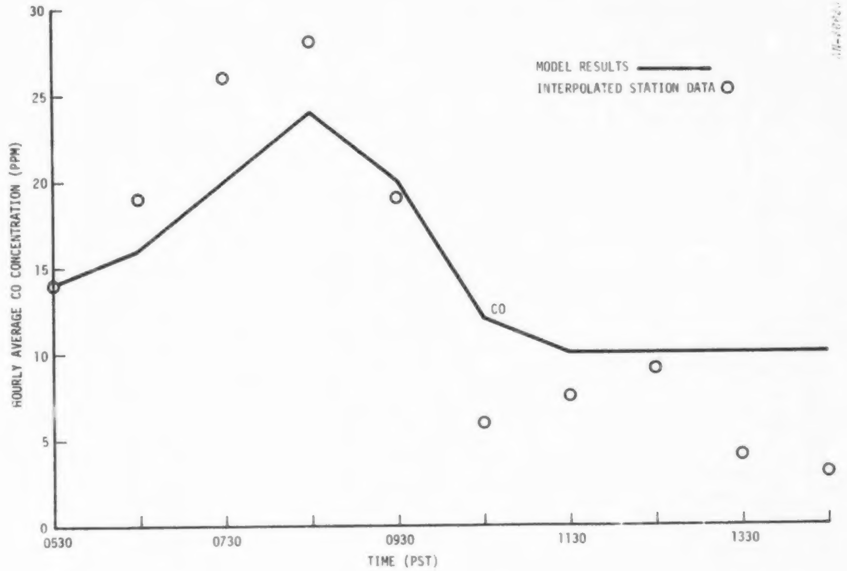

Figure 5.99. Trajectory No. 24--Computed and Observed CO Concentrations

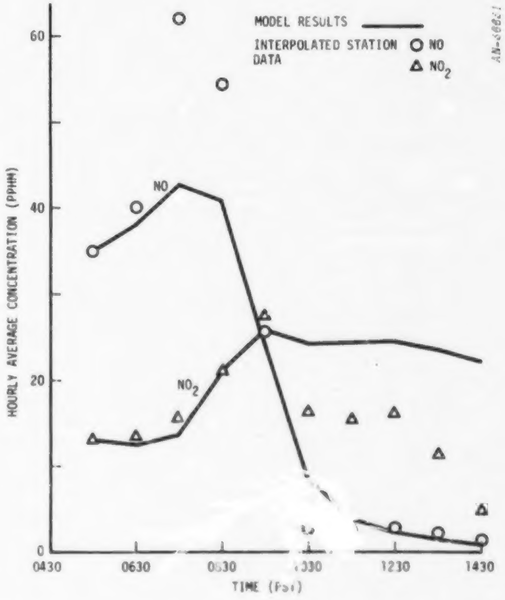

Figure 5.100. Trajectory No. 24--Computed and Observed NO and NO_2 Concentrations

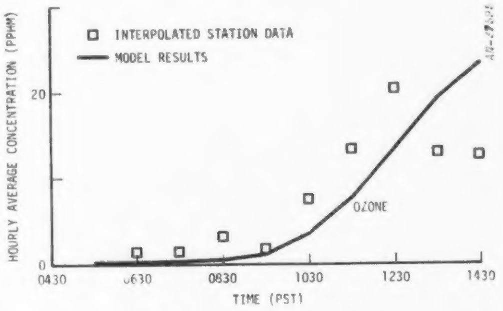

Figure 5.101. Trajectory No. 24--Computed and Observed Ozone Concentrations

5.4 TECHNIQUES FOR MODEL OPERATION

In this section, we describe several basic features of the atmospheric model to assist the prospective model user.

5.4.1 Kinetic Model for Atmospheric Simulation

The chemical model used in atmospheric simulation is basically the same one used to model the smog chamber experiment using a dilute auto exhaust mixture from a vehicle with exhaust hydrocarbon and carbon monoxide emission controls (experiment 231; cf. pp. 37-40 and p. 43). This kinetic model was chosen for atmospheric applications because the smog's kinetics are not likely to be influenced by CO because of its concentrations in experiment 231 and in the atmosphere (cf. p. 36).

The branching factors are features of the smog chamber model which have been retained on moving to atmospheric simulation. Thus we have $b_1 = b_2 = 8$, and $b_3 = 1$. The OH yield factor, y , remains equal to 1/8.

The kinetic model for the atmosphere differs from the smog chamber model mentioned above in that a single hydrocarbon class is used rather than two. The rate constants for the basic atmospheric model are shown in Table 5.6. The constants for reactions 3 and 5 shown in Table 5.6 are rounded mole-weighted averages of the two reaction pairs (3, 3a) and (5, 5a) shown in Table 2.7. The first-order constant for reaction 16 shown in Table 2.7 was halved in the process of parameter adjustment required for atmospheric simulation. (See p. 95 for a discussion of the model's sensitivity to k_{16}.)

The value of the rate constant of the first reaction depends on the intensity of ultraviolet light in the wavelength range 2900-3850 Å. The magnitude of k_1 is treated in the simulation as a function of solar zenith angle, and hence of time of day. See p. 150 for an explanation of the derivation of k_1 and the sources of uncertainty associated with the value of this rate constant.

TABLE 5.6

RATE CONSTANTS USED IN ATMOSPHERIC MODELING STUDIES

Reaction No.	Rate Constant*
1	**
1a	1.32(-5) ppm^{-2} min^{-1}
2	2.67(+1)
3	2.76(+2)
4	***
5	4.0(-3)
6	1.0(+5)
7	2.0(+2)
8	1.5(+3)
9	3.0(+3)
10	†
11	1.0(-3)
12	5.0(-3)
13	4.5(+3)
14	1.4(+1) min^{-1}
15	6.05(+1) min^{-1}
16	1.0(-3) min^{-1}

---

*Units are ppm^{-1} min^{-1} unless otherwise specified.

**This rate constant depends on sunlight intensity and in the simulation it is treated as a function of solar zenith angle, and hence time of day.

***The rate constant for this reaction is given in the section which describes each of the cases tested.

†This reaction is the photodissociation of HONO and its rate constant is obtained from the relation $k_{10} = 3.75 \times 10^{-3} k_1$.

The rate constant for the photodissociation of HONO (reaction 10) is obtained from k_1 using the equation $k_{10} = 3.75 \times 10^{-3} k_1$. This relation results from the assumption that the ratio k_{10}/k_1 is a constant equal to the ratio of the quantities used in the smog chamber simulations. In atmospheric modeling, k_{10} is thus a function of time.

It became necessary to adjust the rate constant of reaction 4 ($OH + HC \rightarrow (b_2)RO_2$) during the simulation process conducted under atmospheric conditions. For this reason, the value of k_4 is given in the sections describing the results of the simulations.

5.4.2 Chemical Inputs

Two inputs are basic to the operation of the chemical model. These are k_1, the rate constant of the reaction $h\nu + NO_2 \rightarrow NO + O$, and k_4, the rate constant of $OH + HC \rightarrow (b_2)RO_2$.

The value of k_1 is of course a function of the intensity of ultraviolet light with wavelength in the range 2900-3850Å. The ultraviolet intensity depends on time of day, time of year, geographical location, and weather conditions. In our simulations, we have used values of k_1 which correspond to clear-day conditions, i.e., no overcast. Thus the magnitude of k_1 used is an upper bound of the actual value. This can be seen in Figs. 5.102-5.107 in Sec. 5.5.

The derivation of the clear-day value of k_1 is accomplished by means of the relationship between k_1 and solar zenith angle given by Leighton.[18] The solar zenith angle is a function of time of day, time of year, and geographical location. Using solar ephemeris tables, a table of solar zenith angles is generated for the specific times and places of interest. Given the solar zenith angle, the value of k_1 is then determined. In our model, we update k_1 at 10-minute intervals, but this is arbitrary and can be changed to match the integration step size.

The value of k_4 is determined by the concentrations of NO, NO_2, and reactive hydrocarbon at the start of the trajectory or at sunrise, whichever is later. Thus k_4 is dependent on the initial mixture of pollutants. We recall that this is in agreement with findings in the validation of the chemical model using smog chamber data for the more reactive mixtures such as propylene/NO_x and auto exhaust/NO_x. During the atmospheric simulations, k_4 ranged from 4×10^3 to 10^4 ppm^{-1} min^{-1}. The rules for determining k_4 will not be exact because of uncertainties in the initial concentrations. The variability of emissions from case to case is another factor which affects the choice of k_4. Thus a plot of k_4 on a graph with ordinate equal to NO_x concentration and abscissa equal to reactive hydrocarbon concentration reveals some scatter in the values of k_4 relative to the quantities HC/NO_x and HC + NO_x. However, some trends are apparent from such a plot and we have used these to establish our guidelines. In any event, we note that the range of values of k_4 is not large, and that by far the most frequent values of k_4 are 4×10^3 and 10^4 $ppm^{-1}min^{-1}$. Based on these frequencies of appearance, we can formulate a general rule: if $HC/NO_x \geq 1.7$, then $k_4 = 4 \times 10^3$ $ppm^{-1}min^{-1}$; otherwise, $k_4 = 10^4$ $ppm^{-1}min^{-1}$. However, a more involved, but more exact set of guidelines for selecting k_4 is as follows:

1. If $HC/NO_x \geq 1.7$, then $4 \times 10^3 \leq k_4 \leq 5 \times 10^3$ ppm^{-1} min^{-1}
2. If $HC/NO_x < 1.7$, then $6 \times 10^3 \leq k_4 \leq 10^4$ ppm^{-1} min^{-1}
3. If $HC/NO_x \leq 1.2$ or if $HC + NO_x > 1.8$ ppm, then $k_4 = 10^4$ ppm^{-1} min^{-1}
4. If $1.4 < HC/NO_x < 1.5$ and 1.2 ppm $< HC + NO_x <$ 1.4 ppm, then $k_4 = 8 \times 10^3$ ppm^{-1} min^{-1}

5.4.3 Meteorological Inputs

The three basic meteorological inputs are the maximum inversion base height, a table of inversion heights as functions of time, and the diffusivity parameters. Establishing general guidelines for selecting these inputs is a difficult task; this is especially true for the last two quantities. The spatial and temporal variability of meteorological conditions impose a high degree of difficulty in trying to devise general rules. Thus one would expect the inversion height, for example, to attain different maximum levels at different locations. Similarly, the changes of inversion height with time can be expected to show spatial variability. Therefore, we must have information about inversion base height as a function of time for each trajectory. This information can be obtained from plots of inversion height isopleths for various times for an entire geographical region. Given a description of the path of the trajectory, the required inversion base data are then obtained from these plots for the trajectory in question in a straightforward manner.

Determining the diffusivity parameters is somewhat more difficult. In this case, the required data consist of profiles of temperature as a function of height and time. These data determine the stability classes and from these the diffusivity coefficients can be obtained using Fig. 3.7. The time variation of the stability class determines the time dependence of the diffusivity coefficients. Results from our simulations indicate that a likely value of diffusivity in the very stable case is $2.5 \times 10^3\ \mathrm{cm}^2/\mathrm{s}$, rather than $5 \times 10^3\ \mathrm{cm}^2/\mathrm{s}$ as shown in Fig. 3.7. The other values of diffusivity shown in Fig. 3.7 were used without change in the simulations.

5.5 SOURCES OF UNCERTAINTY DUE TO SOLAR RADIATION AND PARTICULATE REACTIONS

In the course of any serious evaluation process, any systematic validation-check of a simulation model demands these two things:

1. A quantitative characterization of each uncertainty entering the model

2. A clear identification of the sensitivity of the model outputs to each uncertainty in the inputs

Many efforts in the past several years have been concentrated on the second aspect enumerated above. Indeed, we and others have run parametric analyses until the results are almost intuitive to any worker in the field. Unanswered questions still surround the first requirement, however. These questions need not be a source of mystery because straightforward well-planned investigations can be designed to get the answers. No new discoveries of laws of physics or chemistry will be necessary, but rather, the commitment of resources that concentrate on finding out what is really happening. Suggestions for the future are embodied in Sec. 6; however, for now, we must content ourselves with identifying and assessing the uncertainties in both the input data and the validation data base.

The primary process in the production of photochemical smog is the photodissociation of nitrogen dioxide to form nitric oxide and atomic oxygen. Our rate constants for this reaction are derived in two ways. In the first, we assume clear skies and deal with the atmospheric transmission of radiation in the dissociation bands according to a zenith angle derived from time of day, day of year, and location on the earth's surface. In the second method,[26] Eppley ultraviolet detector readings are calibrated to the clear-day curve of k_1 versus solar zenith angle. The cosine correction presupposes the preponderant contributions to be from direct rather than scattered ultraviolet radiation. As will be seen, this leads to significant errors only at large zenith angles.

Using these two methods, we have explored the uncertainty in k_1 that occurs for predictions that assume clear day values. Figures 5.102 through 5.107 show diurnal k_1 variations for each of the six data days.

It can be seen from the figures that the departures of the actual k_1 from the theoretical clear-day values can be rather large. As might

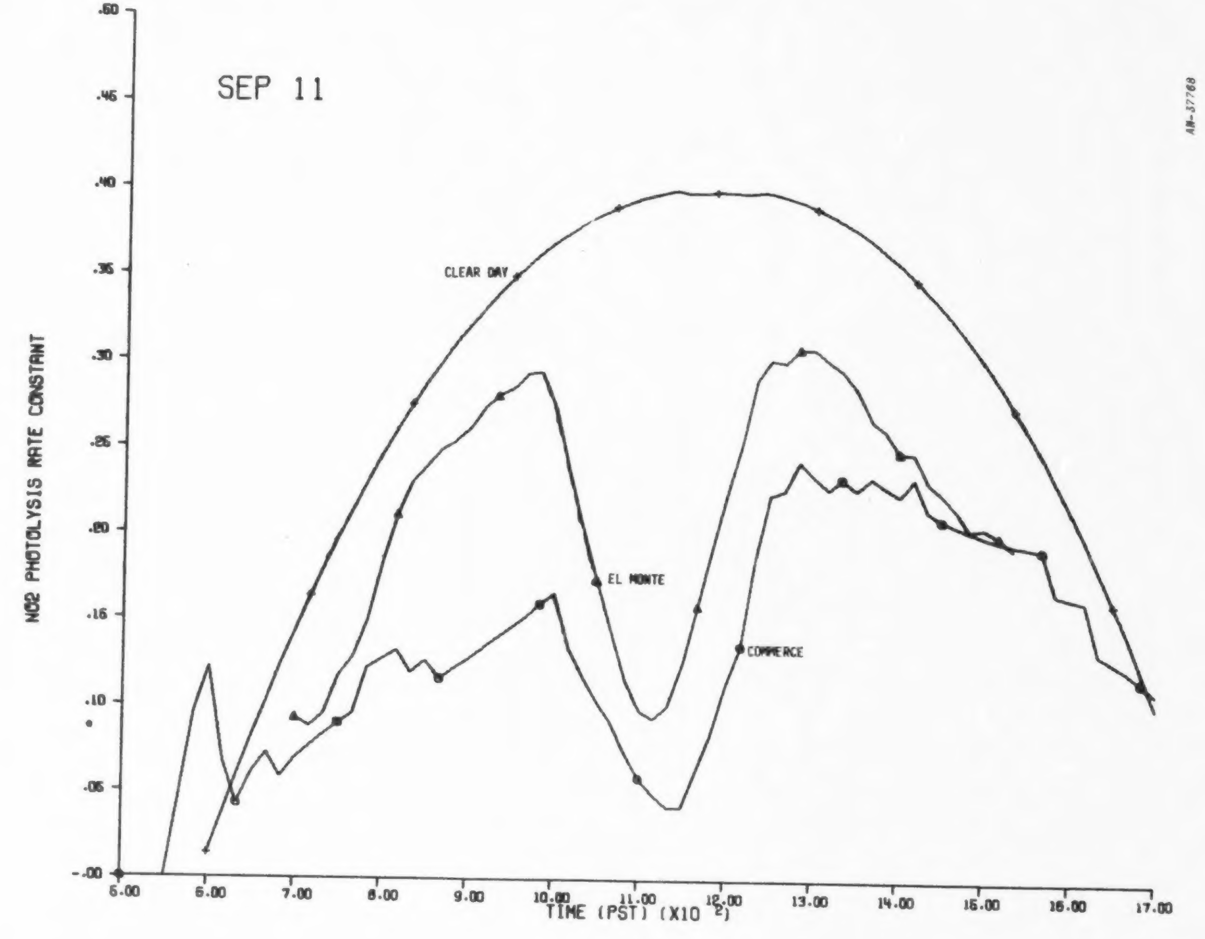

Figure 5.102. NO_2 Photolysis Rate Constant, k_1, for September 11, 1969

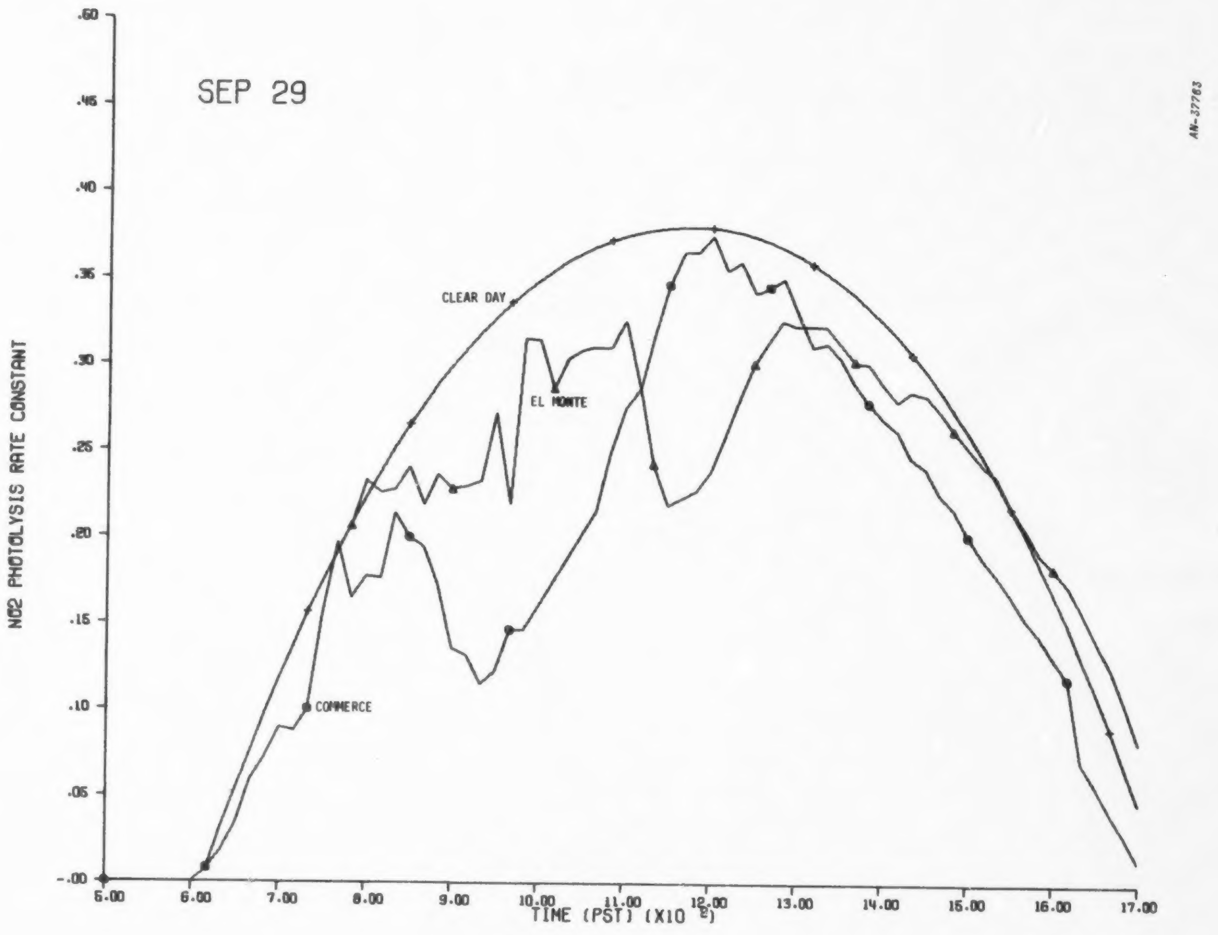

Figure 5.103. NO_2 Photolysis Rate Constant, k_1, for September 29, 1969

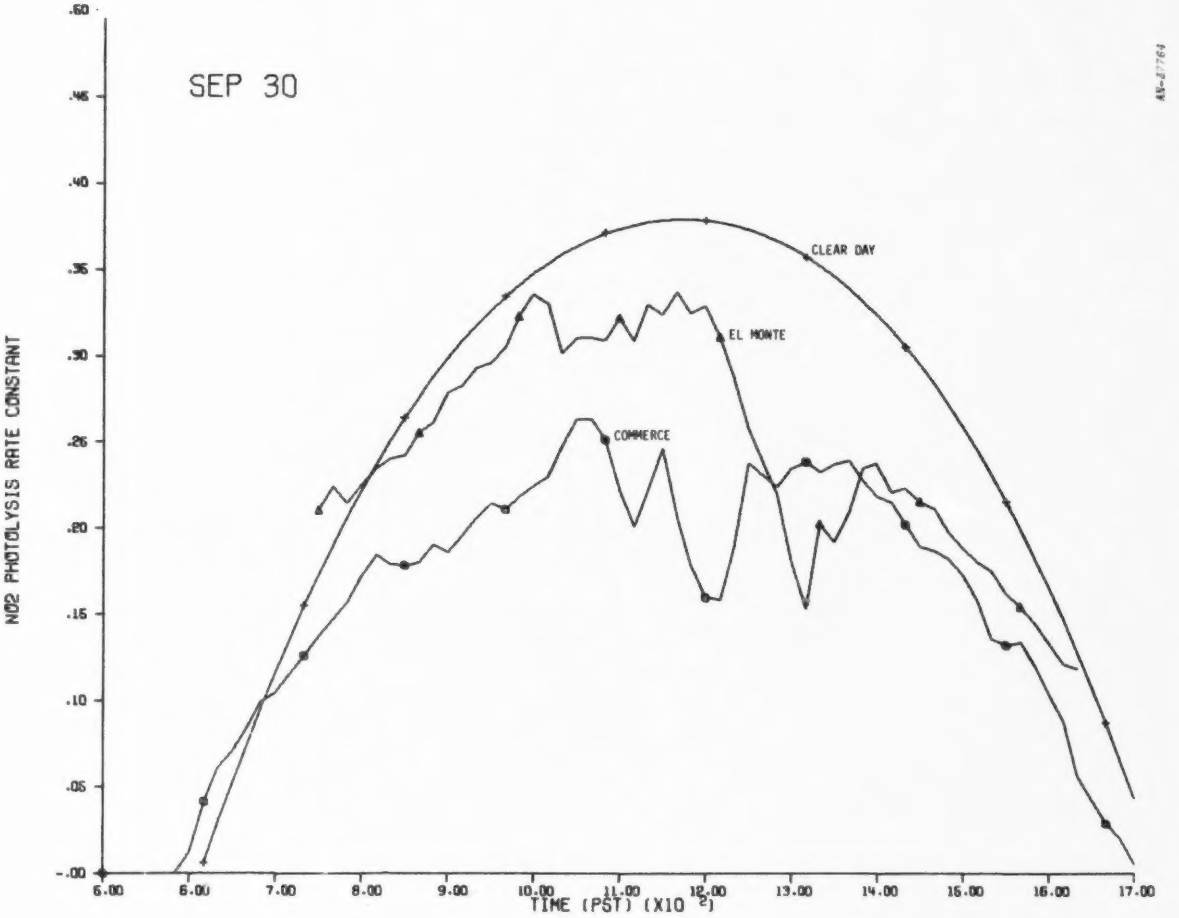

Figure 5.104. NO_2 Photolysis Rate Constant, k_1, for September 30, 1969

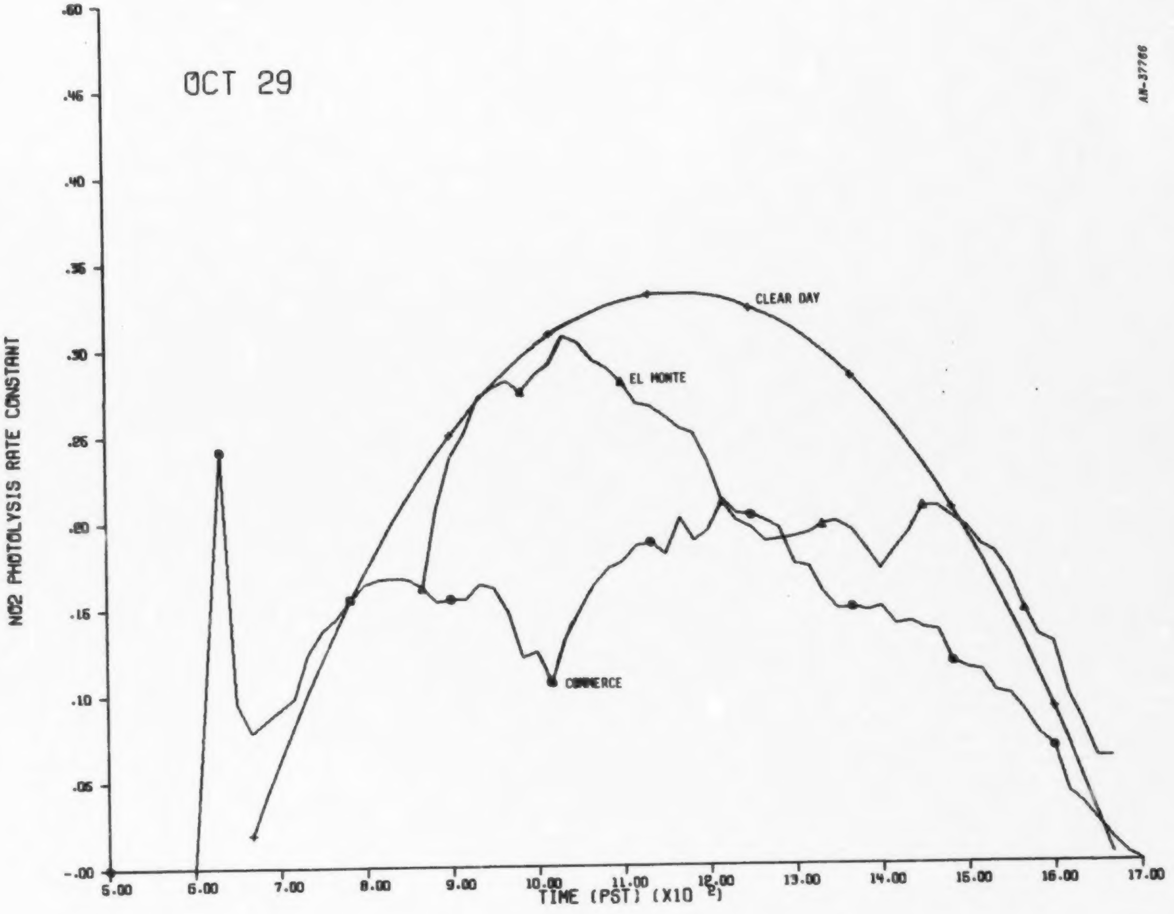

Figure 5.105. NO_2 Photolysis Rate Constant, k_1, for October 29, 1969

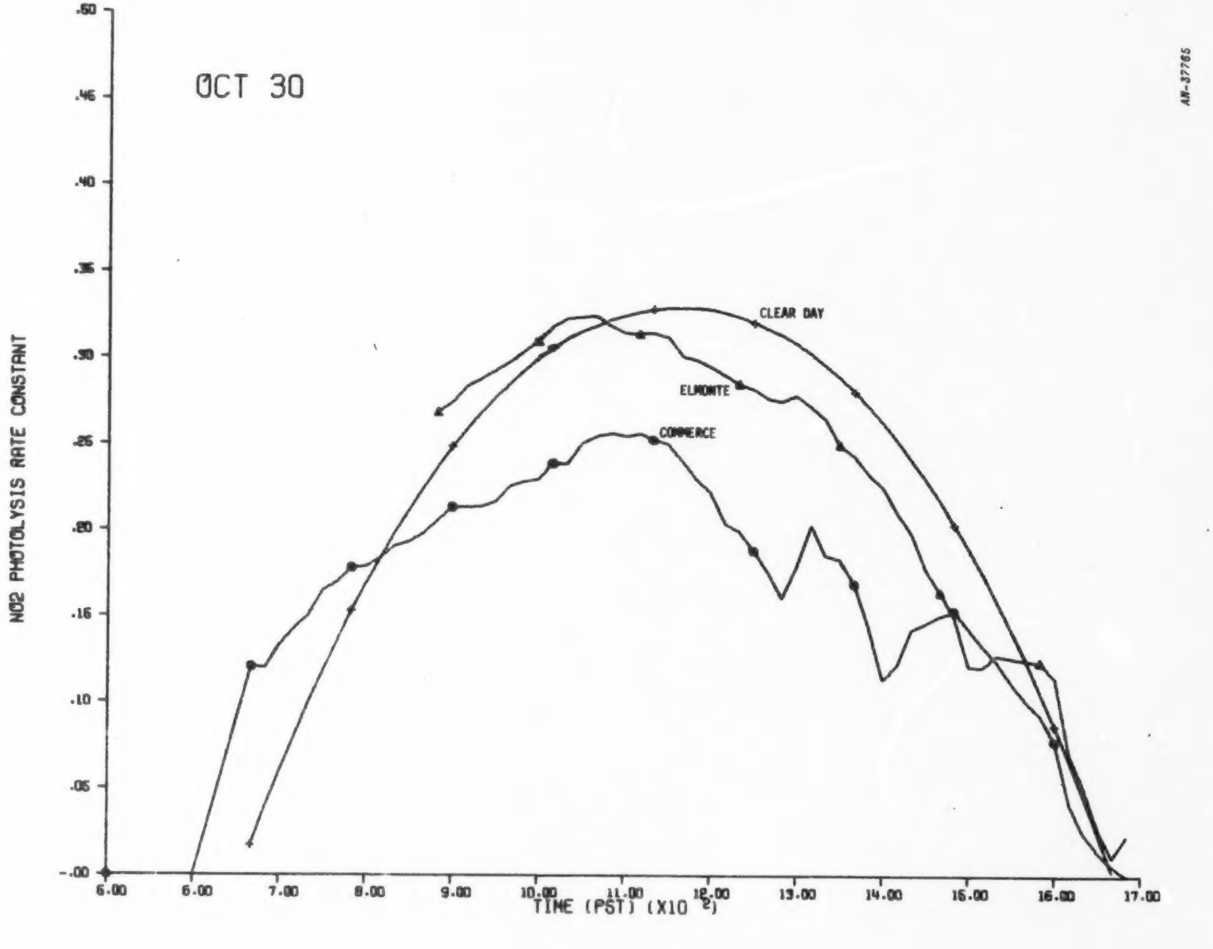

Figure 5.106. NO_2 Photolysis Rate Constant, k_1, for October 30, 1969

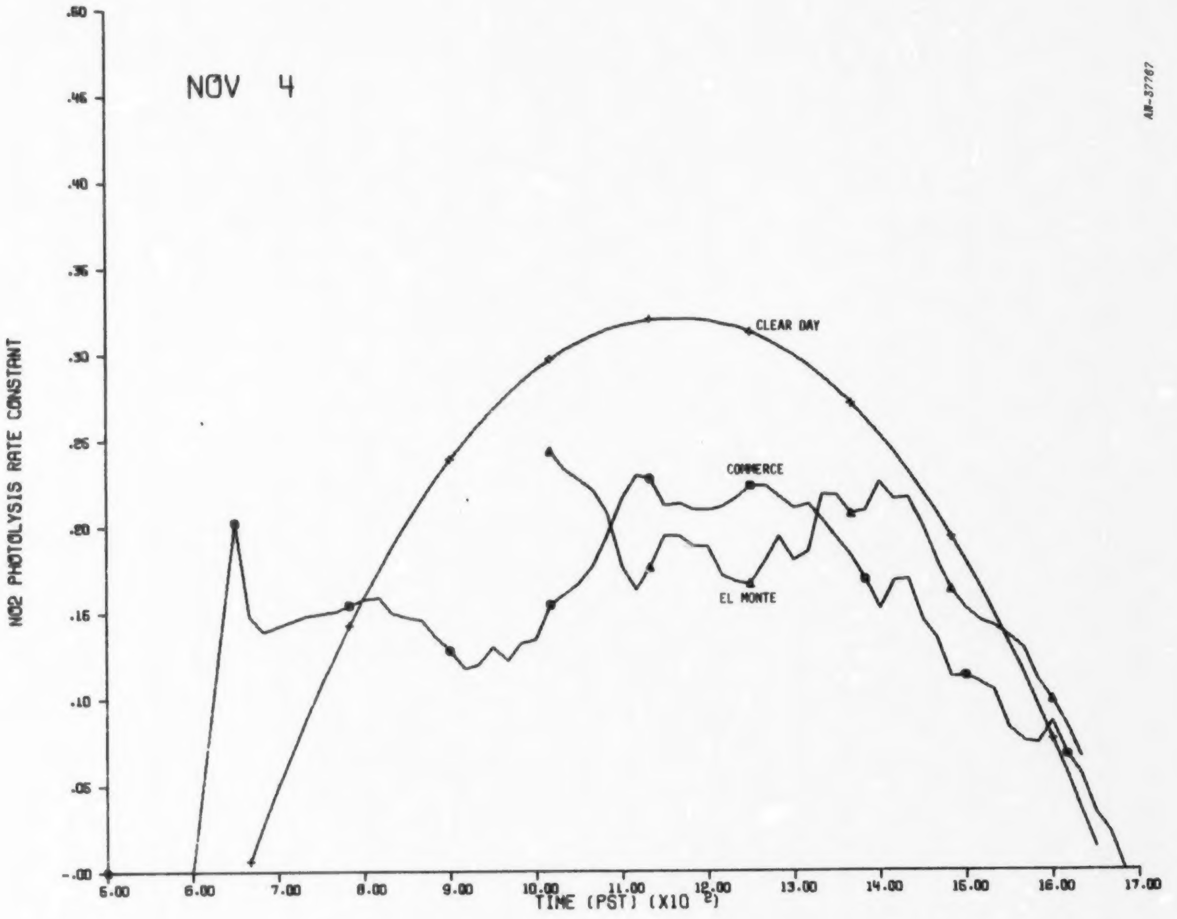

Figure 5.107. NO_2 Photolysis Rate Constant, k_1, for November 4, 1969

be expected, there also exist marked differences in the value of k_1 at different locations in the Los Angeles Basin, in this case Commerce and El Monte. The ratio of (theoretical k_1/actual k_1) ranges from unity at a few points to 8/1 on September 11. As a general rule, the theoretical k_1 is higher by a factor of 1.5 or 2 for Commerce and by about 1.3 for El Monte.

To ascertain the magnitude of the uncertainty introduced, we ran parallel cases using the Commerce values of k_1 as well as the clear-day values for the trajectory starting near Pasadena at 0730 on October 30, 1969 and ending west of Pomona at 1330. This is by no means the worst case, as is easily ascertained from the Fig. 5.106. The result of the test was that the concentrations of NO_x were perturbed very little, but the peak ozone concentration was lowered from 13 pphm using the clear-day k_1 to 9 pphm using the Commerce k_1, a relative change of about 31%. Such a margin of error is significant and must be borne in mind in assessing the expected accuracy of the computed concentrations in view of the uncertainties in the inputs. Interestingly enough, however, in this particular case (see Fig. 5.73), the simulation using the clear-day k_1 is actually very close to the measured data and using the Commerce k_1 would have degraded the simulation if no other rate constants were adjusted to compensate for the lower ozone values. In closing, we note that another case has been tested using the data for September 11 since it shows the largest departures from theoretical values (see Sec. 5.3.5).

Another source of uncertainty is the influence of NO_2 + particulate reactions. It will be recalled that such a lumped reaction, reaction (2.16), was introduced in the kinetic model in simulating smog chamber experiments involving auto exhaust in which the presence of aerosol was observed (see Sec. 2.5.4). Introducing this reaction produced a better simulation of the disappearance of NO_x from the system.

The sensitivity of the model to changes in the rate constant of this reaction was tested during the atmospheric validation runs. The effect of increasing k_{16} was to lower the NO_2 concentration and to increase the ozone concentration late in the day. The sensitivity of the NO_2 peak was negligible compared to the sensitivity of ozone. However, the sensitivity of the end value of NO_2 almost matches that of O_3. This interaction can be explained by realizing that in the kinetic model, the reaction $NO_2 + O_3$ is very strong at late times when NO_2 and O_3 are high; thus removing NO_2 will cause the O_3 to increase. As an example, we ran tests using the November 4, 1969 trajectory with $k_{16} = 10^{-3}\ \text{min}^{-1}$ and $k_{16} = 2 \times 10^{-3}\ \text{min}^{-1}$. The peak ozone went from 25 to 32 pphm and the peak NO_2 underwent a negligible change. The concentration of NO_2 at the end of the trajectory was reduced from 21 to 16 pphm.

6 CONCLUDING REMARKS

These findings establish progress milestones in the understanding of chemical kinetics and atmospheric dynamics underlying air pollution models.

Systematic investigations of laboratory smog chamber experiments have provided significant insights into the air chemistry of urban atmospheres. Although the artifices of the apparatus prevent direct applicability to the atmosphere, important qualitative features are highlighted by computer simulations of chamber studies. Mixtures of various hydrocarbons with nitric oxide were modeled. The hydrocarbons included propylene, toluene, toluene/n-butane, and auto exhaust from vehicles with and without exhaust emission controls. Added chain-breaking reactions for smog chambers improved the predictions markedly. These, along with previously added[24] OH + HC reactions, give consistent behavior for various initial mixtures placed in the chamber. Incorporation of recently reported rate data narrowed the options for adjustable parameters (according to our ground rules, at least), but improved the validations overall. As might be expected for a complex nonlinear system, the nonuniqueness of the rate constants was discovered for validation of a given experiment; that is, an entire set of rate constants could be moved through several orders of magnitude and preserve the same computed results. Selection of the best set was made using benchmark values that have recently come out of the laboratory. Rank order and proportionality of hydrocarbon reactivity indices were shown to bear a direct relationship to the set of rate constants for hydroxyl attack of the hydrocarbons. This built further confidence in our previously adopted procedure[27] of reactivity scaling of smog chamber reaction rates to model atmospheric systems.

Model methodology was substantially improved in several areas. The logic for air trajectory computation has been systematized by generalizations derived from many hand calculations using actual data. Consistency checks between tetroon trajectories and calculated ground trajectories revealed some large sources of uncertainty that are not considered in air pollution models. The dominance of stratification over wind shear was incorporated in changes in the calculation of vertical turbulent mixing coefficients. While previous formulations stressed wind speed dependence, the newly adopted methods depend on potential temperature gradients. The impermeable inversion base assumption was abandoned for upper boundary conditions. Vertical mesh intervals were extended well above the inversion base with assignment of vertical diffusion coefficients controlling upward mixing according to local stability conditions. Thus the inversion base was traced through the mesh by varying the diffusion coefficient in time and space. While the present work did not reexamine the source inventories, many changes were made to assure direct comparison with other model results. Extensive improvements in the computer implementation of source models permitted a high degree of responsiveness to the frequent alterations.

Turbulent diffusion transverse to the wind was assessed to evaluate possible errors due to mass exchange between neighboring stream tubes. As suspected previously, only minor perturbations are introduced by lateral mixing perpendicular to the path of an air parcel. The case of side-by-side trajectories was tested using the GRC three-dimensional time-dependent LAPS code which is especially adapted to treat conditions of large transverse gradients in emission fluxes that typify localized large sources. Worst-case carbon monoxide area sources were tested using the extreme values of fluxes determined from dozens of actual air trajectories over the Los Angeles Basin. The spread of power plant stack plumes from off-trajectory sources into the control volume was investigated for a wide range of parametric conditions of point emission and area emission strengths. To insure realism, the parametric values were selected from the actual inventory statistics. Even the largest percentage errors are not likely to exceed other uncertainties due to model inputs. Systematic examination of validation trajectories relative to these findings showed that transverse diffusion errors are far smaller than other sources of uncertainty in the model inputs.

With the chemical and meteorological improvements, the validation results have been more gratifying than ever before. Consistency in assumptions for both the kinetic rates and the diffusion parameters can be maintained to model a wide variety of cases without ad hoc adjustments. Our abandonment of the single-receptor validation criterion placed much more rigorous constraints on the model tests than had been originally anticipated. Each hourly trajectory node has an interpolated set of concentrations based on neighboring station values. Therefore, we seek to match the shape of each pollution history rather than just matching values at the end point. Despite these more severe requirements, both diffusion and photochemical validations were remarkably successful.

Some problems remain that are critical to the future success of simulation modeling. It is likely that they stand alone by now as the main obstacles to further fidelity improvements. Following this reasoning, one realizes the need to establish closer coupling between modelers and measurers than has been the case in the past. The continuity that is thus assured will build the scientific foundations needed to attack air pollution abatement problems on a rational basis.

Finally, of the myriad topics for additional research which are worthy of note, we wish to single out a few which should improve future models when the problems posed have been solved. In what follows, the order of discussion of the topics has no particular significance.

The first subject that merits some discussion is the need for a new measurement of the rate constant of the reaction $NO_2 + O_3 \rightarrow NO_3 + O_2$. In our model, this rate constant had to be reduced by a factor of 10 in order to achieve accurate reproduction of smog chamber experiments. Since this reaction appears to be rate-controlling at late times when NO_2 and O_3 have reached high concentrations, and since the available measurements of this rate constant are rather old (1949 and 1957) a new measurement is warranted.

A second topic of interest is whether HONO exists in the atmosphere in significant amounts (around 1 pphm). Should this not be the case, the chain-breaking structure of the kinetic model will have to be revised. A corollary to this question is that if HONO is found in the atmosphere, then the rate constant of the reaction $h\nu + HONO \rightarrow OH + NO$ needs to be determined. There appears to be no measurement of this rate constant at the present time.

Thirdly, additional investigation is needed to ascertain the nature of NO_2-scavenging processes in the atmosphere. The possibility that heterogeneous reactions may play a significant role must be included in such a study. Such knowledge would help us to improve the late-time behavior of NO_2 in the simulations.

APPENDIX A

A VIEW OF FUTURE PROBLEMS IN AIR POLLUTION MODELING*

---

*This first appeared as General Research Corporation TM-1631, March 1972 and was subsequently published in Proceedings of Summer Computer Simulation Conference, Simulation Councils, Inc., LaJolla, Calif., June 1972, pp. 1013-1027. Research reported in this document was originated through independent efforts, not under a Government contract or program.

- **Preceding page blank**

A.1 INTRODUCTION

Vigorous steps in abating air pollution demand heavy investments both in the public and private sectors. In addition, second-generation cleanup measures are likely to add personal inconveniences to the already growing financial burdens. Large dollar outlays and the need for public support demand that decision-makers have reliable means of evaluating alternative abatement strategies.

Mathematical air quality models are quantitative tools that will play a central role in evaluating the environmental aspects of decisions. These decisions may take the form of regulations aimed at rolling back existing pollution or of minimizing the environmental damage potential of future public works projects. For abating existing sources, implementation planning must show how control regions will achieve ambient air quality standards within a specific number of years. This requires predictions of absolute levels of air pollution. For assessing impact of projected sources, a statement must be filed that demonstrates that these sources will not cause environmental damage. This, too, requires predictions of absolute levels of air pollution. These requirements impose stringent demands on the best air quality models presently available.

For planning long-range strategies on a national scale, the objective is to choose rationally from among a field of alternative abatement actions. The selection criterion is built around maximum benefit/cost ratios. Thus, the long-range considerations require measurements of alternatives on a relative scale. Currently available air quality models will be very useful in fulfilling this less stringent requirement.

Unfortunately, the time scale on implementation plans and impact statements is much shorter than that on national planning goals. It is already becoming evident, however, that the costs of really massive rollback strategies far outstrip our ability to pay over the short time intervals required by recent statutes. Consequently, we will be forced to analyze less ambitious plans in order to define optimum steps toward pollution abatement. This realization may be many months or even years away, but when its effects are felt, it will require the best products of the modeler's art.

This paper takes two directions in assessing these future needs: first, it highlights some scientific problem areas that need immediate attention; and, second, it suggests some ways of adapting models for abatement analysis applications. Any approach to the unsolved phenomenology problems inevitably leads to greater degrees of complexity in the model. In direct opposition to this trend stands the need for sweeping simplifications in practical adaptations of the models. More likely than not, the air quality model will be but one of the many modules in any realistic abatement simulation. The conflict between pure and applied efforts can be resolved only by a high degree of communication between the researchers and the planners.

In the realm of phenomenology, we examine two potential sources of error in predicting atmospheric reaction rates. One involves gas-solid interactions on urban surfaces and on aerosol particles. The other arises from turbulent fluctuations of reactant gas concentration. Experimental evidence of the problems is cited and research approaches to its solution are outlined in each of the two cases. Analytical corrections to the air quality models are proposed.

Systems implementation schemes are then considered to define the fidelity level that the models must achieve. A hierarchy of different versions emerges from the various objectives that are set forth. For some cases, the versions are already available, but for others, only a sketch plan of the specifications can be given.

A.2 PHYSICAL INTERACTIONS WITH POLLUTANT REACTION RATES

A.2.1 Gas-Solid Interactions

Urban surfaces near ground level and particle surfaces distributed through the mixing layer can serve as reaction sites for gas molecules impinging on them. If these effects compete significantly with homogeneous reactions, appropriate sink mechanisms must be introduced into atmospheric models. Indeed, this has already been done for oxides of nitrogen in our earlier work. Briefly summarizing, we noted[27] that the observed buildups of carbon monoxide and hydrocarbon during morning peak traffic were well modeled by the values of emission fluxes and atmospheric diffusion coefficients in the literature. On the other hand, the sum of $(NO + NO_2)$ was grossly overpredicted as shown in Fig. A.1 (Curve A). On the graph, the symbol "r" refers to the oxidation rate reduction (below that of pure propylene) and symbol "f" to the fraction of the inventory value NO_x emission flux used.

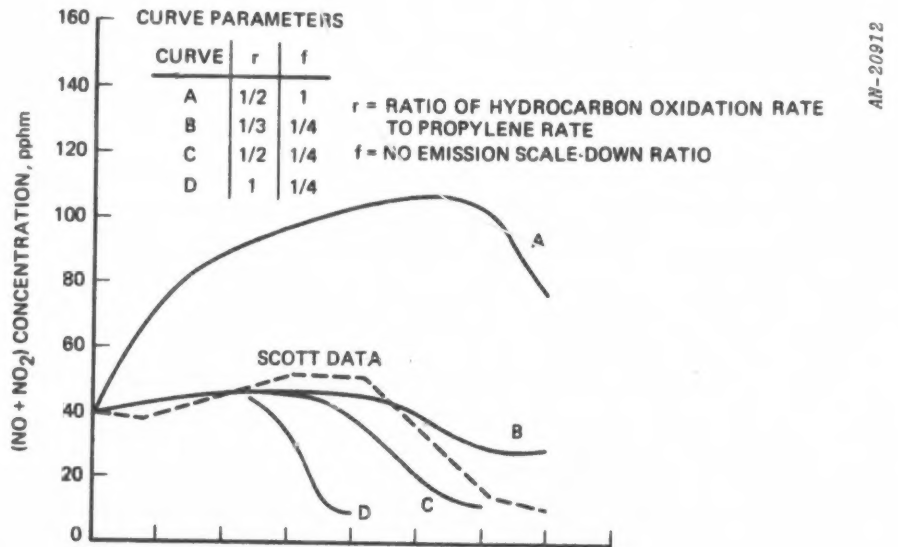

Figure A.1. $(NO + NO_2)$ - Concentration Ground Level Huntington Park

Due to an apparent rapid removal of nitrogen oxides from the gas phase, the published values of emission rates had to be reduced by a factor of four to offset the losses. Note that the first 2.5 hours of buildup are practically unaffected by the choice of reaction rates (over a factor of three). Although flux reduction is an ad hoc correction for these results, it may not be generally applicable to all types of surfaces or to all types of days or even to all times during a given day. Figure A.2 illustrates the difficulty very clearly. It displays averages of the CO/NO_x mole ratios for groups of 1968 data measured by Scott Research Laboratories.[35] It is intended that CO be regarded as an inert tracer so that variations between observed ratios and source ratios reflect loss of NO_x . This removes uncertainties due to dilution and other interferences. Types 1, 2, and 3 denote high oxidant days and Type 0, low oxidant days. The factor of four (between source values and air

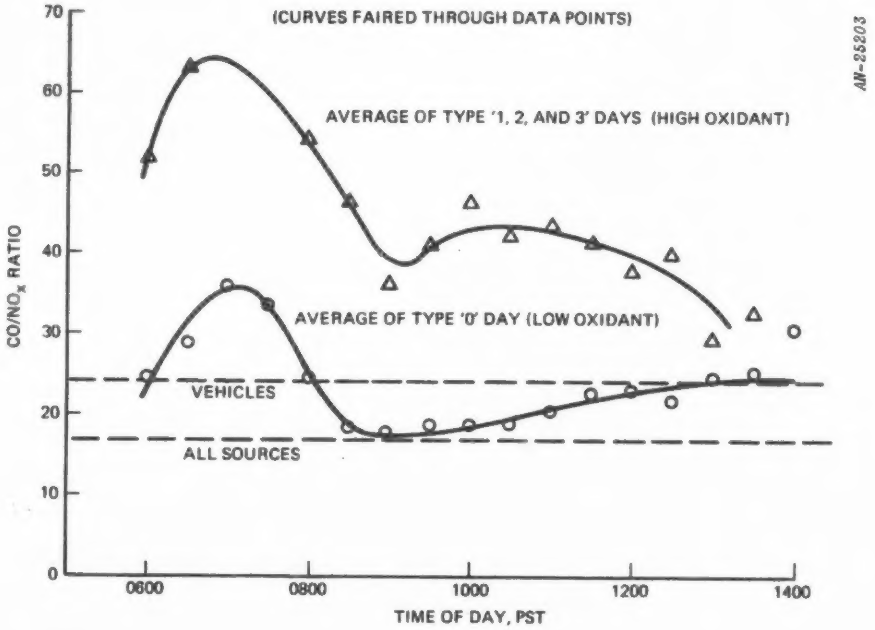

Figure A.2. CO/NO_x Ratios for Huntington Park 1968 values) shows up clearly at the morning traffic peak for high oxidant days. Low oxidant days exhibit far lower discrepancies between source ratios and ambient air ratios.

These bits of evidence show the nature of the problem but they do not indicate a truly general solution. Indeed, the deficit of gas phase nitrogen oxides has been observed for years in laboratory photooxidation experiments in smog chambers. Gay and Bufalini[9] give an excellent review of these problems and demonstrate that analysis of surface-adsorbed products greatly improves the nitrogen balance in these experiments. Substantial uptake of pollutants in soils has been demonstrated in experimental studies[37,38,39] reported in the literature. From these results, ground absorption can be deduced or estimated. They average out to the following very approximate values (in $mg/m^2 \cdot hr$): ~1 for ozone, ~8 for carbon monoxide and ~3 for nitrogen dioxide. It is important to note that the ozone value is for atmospheric background concentration (~0.05 ppm) while the CO and NO_2 values are for tens or hundreds of ppm in a 10-liter vessel. Aldaz[37] assumes that the surface reaction rate must be first-order in the ozone concentration, but the Inman and Ingersoll results[38] show a linear concentration decay of CO suggesting zero-order. Before any of the reported values can be used in models, the concentration (and possibly temperature) dependence of the uptake rates must be determined. It is of interest, nevertheless, to compare these values with the emission fluxes averaged over the Los Angeles basin area. For oxides of nitrogen (as NO_2) the emissions are approximately 10 $mg/m^2 \cdot hr$ (against 3 estimated for soil uptake) and for carbon monoxide it is approximately 100 (against 8 estimated for soil uptake). Therefore, these preliminary indications are consistent with our model adjustments and with the observed atmospheric CO/NO_x ratios; namely, that there could be significant perturbation of the NO_x-balance, but only minor effects on the CO-balance. Surface uptake of ozone has been regarded as the major global sink for this gas; however, Ripperton and Vukovich[40] indicate that gas phase removal may also be important even at background conditions. Some of our early calculations for a fully catalytic ground surface suggest that gas-phase reactions dominate the ozone balance in polluted air to within a few meters of the ground.

Modeling the uptake at the ground is a simple matter of adding boundary conditions to the finite-difference approaches that simulate air quality for distributed sources. As indicated above, the lack of reliable data is the main obstacle. Algorithms are already developed for the flux boundary condition at (or near) the ground level. In general, this logic is suitable only for zero-order surface reactions, but minor modifications would generalize it to the nth-order uptake processes. The modifications would substitute kc^n for the constant flux now in the boundary conditions.

Now turning to the gas-solid interactions at particulate surfaces, we begin with the evidence cited by Lundgren:[41]

> On days of heavy smog, very hygroscopic, crystalline-like particles were found to comprise over half of the particulate dry weight in the 0.5-1.5 μm diameter size range. These crystalline particles were analyzed by X-ray diffraction and identified as ammonium nitrate.

It has been known for some time (see for example, Ref. 42) that Los Angeles aerosol has anomalously high fractions of nitrate when compared with that from other cities. Altshuller and Bufalini[3] cite smog chamber experiments with auto exhaust emphasizing the rapidity of conversion of nitrogen oxides to particulate nitrate. They urge that further field work be undertaken to determine atmospheric rates of conversion.

Oxygen-atom reactions with particulate matter were discounted by Leighton and Perkins.[43] They carried out a calculation of the mean displacement during the gas-phase lifetime of an O-atom. For a high particle loading (1 mg/m^3), they then estimated the total volume of the spheres of influence of the particles. It accounted for less than 10^{-4} of the volume of the gas, thereby forming a basis for neglecting the influence on O-atom chemistry.

We can undertake a somewhat more detailed analysis of other pollutants by carrying out some calculations for simultaneous gas-phase and surface reactions in the neighborhood of a particle. The physical picture is a steady state diffusion of a reactive species toward the particle surface. For steady state, the governing equation is

$$D\nabla^2 n_i + w_i = 0 \tag{A.1}$$

where D = Diffusion coefficient

n_i = Number density of ith species

w_i = Net production rate of ith species in the gas phase

The form of the production term is predicated on a high level of chemical activity for species i. This is based on a constant strong source s_i opposed by a series of fast reverse reactions that consume species i at a rate of $k_g n_i$ where k_g is a composite of gas-phase rate constants (for reactions with q other species) and concentrations given by

$$k_g = \sum_{j=1}^{q} (1 - \delta_{ij}) k_{ij} n_j \tag{A.2}$$

where $\delta_{ij} = 1 \quad ; \quad i = j$

$\delta_{ij} = 0 \quad ; \quad i \neq j$

so that for the gas phase production term we use

$$w_i = s_i - k_g n_i \tag{A.3}$$

Outside of the range of influence of the particle, we can calculate the homogeneous stationary state number density of species i by setting $w_i = 0$ giving

$$n_\infty = \frac{\varepsilon_i}{k_g} \tag{A.4}$$

Incorporating spherical symmetry and substituting Eq. A.3 in Eq. A.1, we get

$$D\left(\frac{d^2n_i}{dr^2} + \frac{2}{r}\frac{dn_i}{dr}\right) - k_g n_i = -s_i \qquad \text{(A.5)}$$

The heterogeneous reaction enters the problem in the boundary condition at the particle surface ($r = r_0$) where we assume a first-order reaction balancing the influx of the _i_th species.

$$-D\left.\frac{dn_i}{dr}\right]_{r=r_0} = -k_s n_{io} \qquad \text{(A.6)}$$

where k_s is the rate constant for the surface reaction.

The homogeneous reaction is approached at an infinite distance from the particle

$$\lim_{r\to\infty} n_i = n_\infty \qquad \text{(A.7)}$$

which corresponds to the vanishing first and second derivatives on the left-hand side of Eq. A.5. Solving Eq. A.5 subject to Eqs. A.6 and A.7, we can obtain by elementary methods the result

$$\frac{n_i}{n_\infty} = 1 - \left(\frac{1}{1 + \frac{D}{k_s r_o} + \frac{\sqrt{k_g D}}{k_s}}\right)\frac{r_o}{r}\exp\left[-\sqrt{\frac{k_g}{D}}\,(r - r_o)\right] \qquad \text{(A.8)}$$

which closely resembles the classical Debye equation for an ion in an electrolyte solution. Equation A.8 expresses an exponential decay from the ambient level into the surface of the particle. The e-folding distance is approximately the length a typical molecule travels before it reacts. At small fractions of the e-folding distance from the particle surface, the reciprocal r-dependence dominates. The coefficient of the decay term brings in the influence of the surface reaction.

It is instructive to examine limiting cases of the surface concentration by setting $r = r_o$ in Eq. A.8. For a very small diffusion coefficient (D) the molecules of species i are insulated from the surface by a thin film. At the surface the concentration is zero because every molecule that penetrates the film is consumed at the surface on arrival. This is the diffusion-controlled limit, and it results in a zero surface concentration. At high values of k_g, the presence of the surface or the diffusion process has very little effect and we have approached the homogeneous reaction limit. The free-molecule limiting case where surface reaction rate is the controlling feature occurs with very small reactive particles. Thus if $r_o << D/k_s$ and if $k_s >> k_g D$, this limit is approached.

For cases of interest in air pollution, it is useful to compare the magnitudes of the terms in Eq. A.8. Assume that the mean particle diameter is 0.5 μm. The diffusion coefficient is of the order of 0.1 cm^2/s, and for active species in photochemical air pollution $k_g \sim 0.004\ s^{-1}$. The least certain of all the constants is the surface reaction coefficient k_s. Kinetic theory sets the upper limit on k_s by the frequency of molecular collisions Γ_i, on a unit area.

$$\Gamma_i = n_{io} \sqrt{\frac{kT}{2\pi m_i}} \qquad (A.9)$$

where m_i = Molecular mass of ith species

k = Boltzmann's constant

T = Absolute temperature

Now k_s can be derived directly from Eq. A.9 by applying a collision efficiency η. This is the fraction of collisions that result in surface reaction. The value of η, a measure of chemical surface efficiency, is determined by the surface coverage of reactant partners and by the activation energy required to make a reaction occur. Combining Eqs. A.6 and A.9 with the concept of collision efficiency, we obtain

$$k_s = \eta \sqrt{\frac{kT}{2m_i}} \qquad \text{(A.10)}$$

For nitric oxide at 300°K, this gives a value of $\sim(1.2 \times 10^4 \eta)\ \mathrm{cm \cdot s^{-1}}$. The measurements of Aldaz ahow values of η for ozone on active surfaces in excess of 10^{-4} (for the case of juniper). At the time of this writing, we do not have values available for oxides of nitrogen, but if 10^{-4} is used, then k_s is of the order of unity.

Using these estimates, we get the following values for the parameters in Eq. A.8: $(D/k_s r_o) \simeq 3 \times 10^3$, $(k_g D)^{1/2}/k_s \simeq 2 \times 10^{-2}$, and $\sqrt{D}/k_g \simeq 5$ cm. This indicates that the second term (which is the fractional species deficit in the neighborhood of the particle) is always small and that the full value of concentration n_∞ is exposed to the surface. Thus we are in the regime that is dominated by surface reactions even if collision efficiencies range as high as $\eta \simeq 10^{-2}$. This simplifies particle uptake estimations considerably because Eq. A.9 can be used directly with the ambient gas concentration at the surface ($n_{io} \simeq n_\infty$) if the efficiency factor is applied to the particle flux Γ_i.

Let us turn to the task of placing an upper limit on the role of particles in competition with gas phase reactions in photochemical smog. To obtain numerical comparisons between the rates, we must specify some gas phase reactions and assign some concentration values. Table A.1 summarizes some typical conditions on a smoggy day in Los Angeles.

TABLE A.1

CONCENTRATIONS (ppm) AND GAS PHASE RATE CONSTANT ASSUMED FOR COMPARATIVE ANALYSIS

Species	Early Time (~6-9 AM)	Late Time (~midday)
Ozone	$5.5 \times 10^{-3*}$	2×10^{-1}
Nitric Oxide	1×10^{-1}	$2 \times 10^{-3*}$
Nitrogen Dioxide	1×10^{-1}	5×10^{-2}
Oxygen Atom	$8 \times 10^{-9*}$	$5 \times 10^{-9*}$
NO_2 Dissociation Rate Constant	0.22 min^{-1}	0.30 min^{-1}

---

*Computed from stationary state relationships.

The footnote on the table refers to the reaction steps chosen to characterize gas phase rates. These elementary processes are:

$$h\nu + NO_2 \xrightarrow{k_{11}} NO + O \tag{A.11}$$

$$O + O_2 + M \xrightarrow{k_{12}} O_3 + M \tag{A.12}$$

$$NO + O_3 \xrightarrow{k_{13}} NO_2 + O_2 \tag{A.13}$$

where species M is any collision partner. This mechanism comprises the fastest gas phase reactions that influence the species in Table A.1.

For calculating the starred concentrations, we assumed stationarity for O-atom giving

$$c_O = \frac{k_{11} c_{NO_2}}{k_{12} c_{O2} c_M} \tag{A.14}$$

and for ozone giving

$$c_{O_3} = \frac{k_{11} c_{NO_2}}{k_{13} c_{NO}} \tag{A.15}$$

where c denotes ppm concentration of the subscript species. Rate constants for reactions (A.12) and (A.13) were assumed to be 1.32×10^{-5} ppm^{-2} min^{-1} and 40 ppm^{-1} min^{-1} consistent with some of our modeling calculations.[44] In a later section, we express caution about using Eq. A.15 because of possible turbulence interference effects; however, for the present purposes we will assume that we have properly averaged concentrations for use in stationary state calculations. Since all of the stoichiometric coefficients in the reaction cycle are unity, stationarity permits us to calculate a single gas phase reaction rate characterizing all of the transformations in the cycle.

The gas reaction rate for reactions (A.12) and (A.13) at early time is 2.2×10^{-2} ppm^{-1} min^{-1}, and at late time it is 1.5×10^{-2} ppm^{-1} min^{-1}. To get upper bounds on the surface rates using Eq. A.9, we will need to know the surface area per unit volume. Following Leighton and Perkins,[43] we assume $r_o = 0.25$ μm and a specific gravity of unity. For an aerosol loading of 200 μg/m^3 (which is typical for Los Angeles smoggy days) this gives a surface area of 6.08×10^{-6} cm^2 per cm^3. Using Γ for each species from Eq. A.9, calculations can be made for the collision rate of each species on the aerosol surfaces. This gives the upper limit for the surface reaction effect. Ratios of surface to gas phase rates are shown for this limit in Table A.2. If the ground level ozone flux measurements of Aldaz[37] apply also to aerosol surfaces, efficiency factors in the range of 10^{-6} to 10^{-4} reduce all of the numbers in Table A.2 to insignificant levels. On the other hand, if there is a moderate degree of surface activity on the aerosol particles (say 10^{-2} collision efficiency), we see from Table A.2 that the morning NO_x levels could be seriously affected.

TABLE A.2

UPPER LIMIT OF (SURFACE RATE/GAS PHASE RATE) RATIO*

Species	Early Time (~6-9 AM)	Late Time (midday)
Ozone	8.5×10^{-1}	$4.5 \times 10^{+1}$
Nitric Oxide	$2.0 \times 10^{+1}$	6.0×10^{-1}
Nitrogen Dioxide	$1.6 \times 10^{+1}$	$1.1 \times 10^{+1}$
Oxygen Atom	2.1×10^{-6}	2.0×10^{-6}

---

*For conditions in Table A.1 and for 200 μg/m^3 of 0.5-μm-diameter particles.

This possibility deserves serious consideration in view of the atmospheric nitrogen balance results we cited above. In some of the smog chamber experiments reported by Gay and Bufalini,[9] the majority of the oxides of nitrogen loaded initially show up in the solid phase after only a few hours of irradiation. Finally, it should be noted from Table A.2 that our results agree with those of Leighton and Perkins[43] for oxygen atoms; namely, that gas-particle interactions are negligible by several orders of magnitudes even if oxygen atoms react at 100% efficiency with the aerosol. The influence of surface reactions on ozone concentration can become moderate in the later stages of smog formation.

The critical factor in assessing the impact of these findings is the surface reaction efficiency as well as the order of the reaction. If these quantities were more accurately known, it would be possible to tell which of the surface processes must be included. Not covered in the above discussion are the large families of organic radicals and compounds that may also react with aerosol surfaces. Certainly the hydrocarbon reaction rates are much smaller than those discussed; therefore, heterogeneous reactions could contribute very significantly. The intermediates such as RO, RO_2, and HONO and the products like aldehydes and alkyl nitrates must also be investigated.

Having identified the significant processes, we can incorporate them into the air quality model by adding sink terms to the continuity equation for each species. Such a term would depend on a rate constant, the particulate level, and probably the species concentration raised to some power greater than zero. These reaction terms could be lumped in with others. If, for example, a high degree of correlation were found between ozone and aerosol levels, the ozone terms could be augmented to account for heterogeneous removal mechanisms. There may also exist product species which become detached from the particles. If a surface is coated with loosely bound B-molecules, an impact of an A-molecule on the surface might be followed by ejection of an AB-molecule. It is clear that a great deal of research is yet to be done in this field.

Before leaving the question of gas-solid interactions, we should not fail to mention the possible effects of attenuation of incident sunlight by the aerosol, particularly in the ultraviolet. Since the photodissociation primary processes are most sensitive to the ultraviolet input, there may be a significant reduction of the reaction rates without a commensurate reduction in total incident solar energy. In one version of our model, Eppley detector readings can be used directly to get the rate constants.* This automatically accounts for ultraviolet attenuation down to ground level. When such data are not available, any significant reduction in rate constant must be accounted for by solving a radiation transfer equation over the dissociation band of wavelengths. To the best of our knowledge, this is not a part of existing atmospheric pollution models. Of course, before extensive development of any new simulation logic is undertaken, the class of cases where the effect is important must first be identified. This done, it will be necessary to delineate the regime with certain parametric criteria.

---

*This calibration was based on a particular filter system having a 0.3-0.4 μm bandpass.

A.2.2 Turbulent Fluctuation Interactions

The second area of needed research is the influence of concentration inhomogeneities upon atmospheric reaction rate calculations. As an air parcel moves over an array of different emission sources, turbulence folds in the gases of different composition. The nonuniformity manifests itself as blobs that become less and less distinct due to the combined action of diffusion and reaction. Attempts to describe such phenomena have formed a body of theory for turbulent fields of scalar quantities. Unfortunately, little supporting evidence in the form of actual observations is available for the testing of such theory. We can, nevertheless, utilize some of the grosser aspects of the theory for model improvements if some appropriate experimentation is done.

The specific problems arising due to fluctuating concentrations can be clarified by considering the reaction between the pollutants NO and O_3. The reaction of ozone and nitric oxide in polluted air rapidly produces nitrogen dioxide and molecular oxygen. Characteristic reaction times for part-per-hundred-million level concentrations of the reactants (O_3 and NO) might range from several seconds to a minute or more. This reaction is opposed by the photodissociation of NO_2 which has a two or three minute characteristic reaction time in bright sunlight. The resulting quasi-equilibrium, therefore, can respond relatively rapidly to changing reactant stoichiometry. (Reactions (A.11), (A.12), and (A.13) in the previous section form the mechanism in question.) If concentration changes are induced by turbulent mixing, which may be characterized by the same time scales, there is an interaction between the turbulent fluctuations and the mean reaction rates.

Here is what is observed: suppose we station ourselves at some point and measure the atmospheric reactant concentrations with good time resolution. Typical records (see Fig. A.3) will show that there is significant anticorrelation between O_3 and NO concentration. For example, one-minute O_3 and NO readings from the first 20 minutes of this sample have a cross-correlation coefficient of -0.742 (see Table A.3). Consequently, if we calculate the mean reaction rate from

$$\frac{dc_{NO}}{dt} = -kc_{NO}c_{O_3} \tag{A.16}$$

we find that the fluctuations introduce a correction into the rate because

$$c_{NO} = \bar{c}_{NO} + c'_{NO} \tag{A.17}$$

and

$$c_{O_3} = \bar{c}_{O_3} + c'_{O_3} \tag{A.18}$$

where bars denote means and primes, fluctuations. Insertion of Eqs. A.17 and A.18 in Eq. A.16, followed by averaging, gives

$$\overline{\frac{dc_{NO}}{dt}} = -k\bar{c}_{NO}\bar{c}_{O_3}\left[1 + \left(\frac{\overline{c'_{NO}c'_{O_3}}}{\bar{c}_{NO}\bar{c}_{O_3}}\right)\right] \tag{A.19}$$

Note that if there is vanishing correlation between the two concentrations, the parenthetical factor is unity. Negative correlation will clearly reduce the reaction rate in Eq. A.19 (the amount depends on fluctuation intensity).

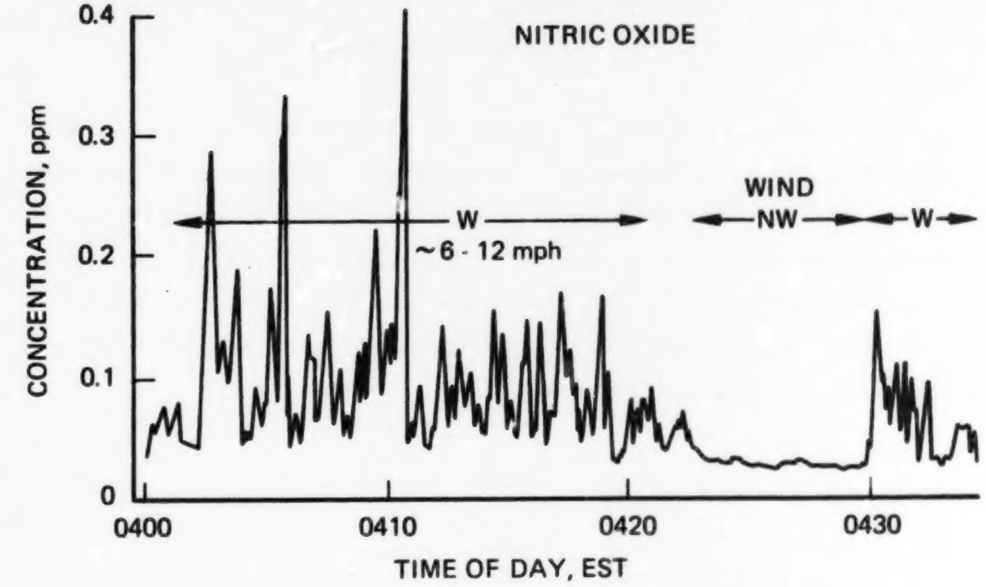

AN-34285

Figure A.3a. Chemiluminescent Measurements in New York - 1970(44)

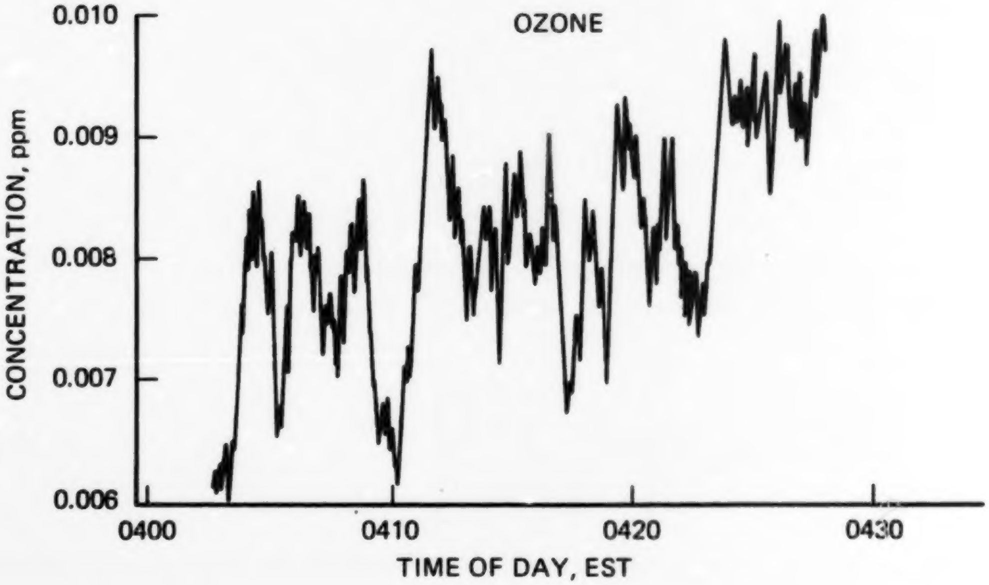

Figure A.3b. Chemiluminescent Measurements in New York - 1970(44)

TABLE A.3

FORD/NEW YORK DATA[44] (FIRST 20 MINUTES)

Input Data

ID Time After 0400 EST	X NO ppm	Y O_3 ppm
2.	0.150000	0.006150
3.	0.117000	0.006150
4.	0.052000	0.008120
5.	0.090000	0.007780
6.	0.057000	0.008240
7.	0.070000	0.007620
8.	0.063000	0.007940
9.	0.097000	0.007330
10.	0.122000	0.006420
11.	0.055000	0.007970
12.	0.080000	0.009140
13.	0.088000	0.007710
14.	0.058000	0.007080
15.	0.067000	0.007480
16.	0.060000	0.007980
17.	0.098000	0.007480
18.	0.064000	0.008480
19.	0.078000	0.007300
20.	0.054000	0.009070
Mean Values =	0.080000	0.007655
Correlation Coefficient =	-0.742	

In earlier work,[26] we tested the quasi-equilibrium of the three-reaction cycle given in reactions (A.11), (A.12), and (A.13). It will be recalled that ozone quasistationarity requires that

$$k_{11}\bar{c}_{NO_2} = k_{13}\bar{c}_{O_3}\bar{c}_{NO_2} \qquad (A.20)$$

neglecting the turbulence effects on reaction (A.13). Based on 10-minute averaged concentrations, Fig. A.4 shows the systematic departure from Eq. A.20 in the direction of too high an apparent rate for reaction (A.13). To suppress inaccuracies in small NO readings, we have omitted those values less than (or equal to) one part per hundred million (pphm). One explanation for the departure may be reactions besides (A.11), (A.12) and (A.13) playing a significant competitive role. Modeling calculations for these conditions have as yet failed to reveal such reactions. Another hypothesis is instrument inaccuracies at high ozone level. Figure A.5 shows the results of back-calculating what the ozone meter (MAST) response would have to be to bias the measurements as suggested in the data in Fig. A.4. To achieve quasiequilibrium, we would need an instrument that would read 20 or 25 pphm when the actual value is 5 or 6. This extent of inaccuracy is unlikely especially since it has been reported that MAST instrument readings are consistently below the true values. This correction is even in the wrong direction to support the plausibility of a response curve passing through the data of Fig. A.5. Detailed background on data analysis and the calculations of rate constants is given in an earlier publication.[24]

Two possible explanations of the breakdown of $O_3/NO/NO_2$ quasistationarity will now be considered. The first is the obvious possibility of interference from competing reactions. The second is the effect of turbulence on the rate of reaction (A.13). For these investigations, we will make use of our mathematical model of the chemical-kinetic aspects of photochemical smog.

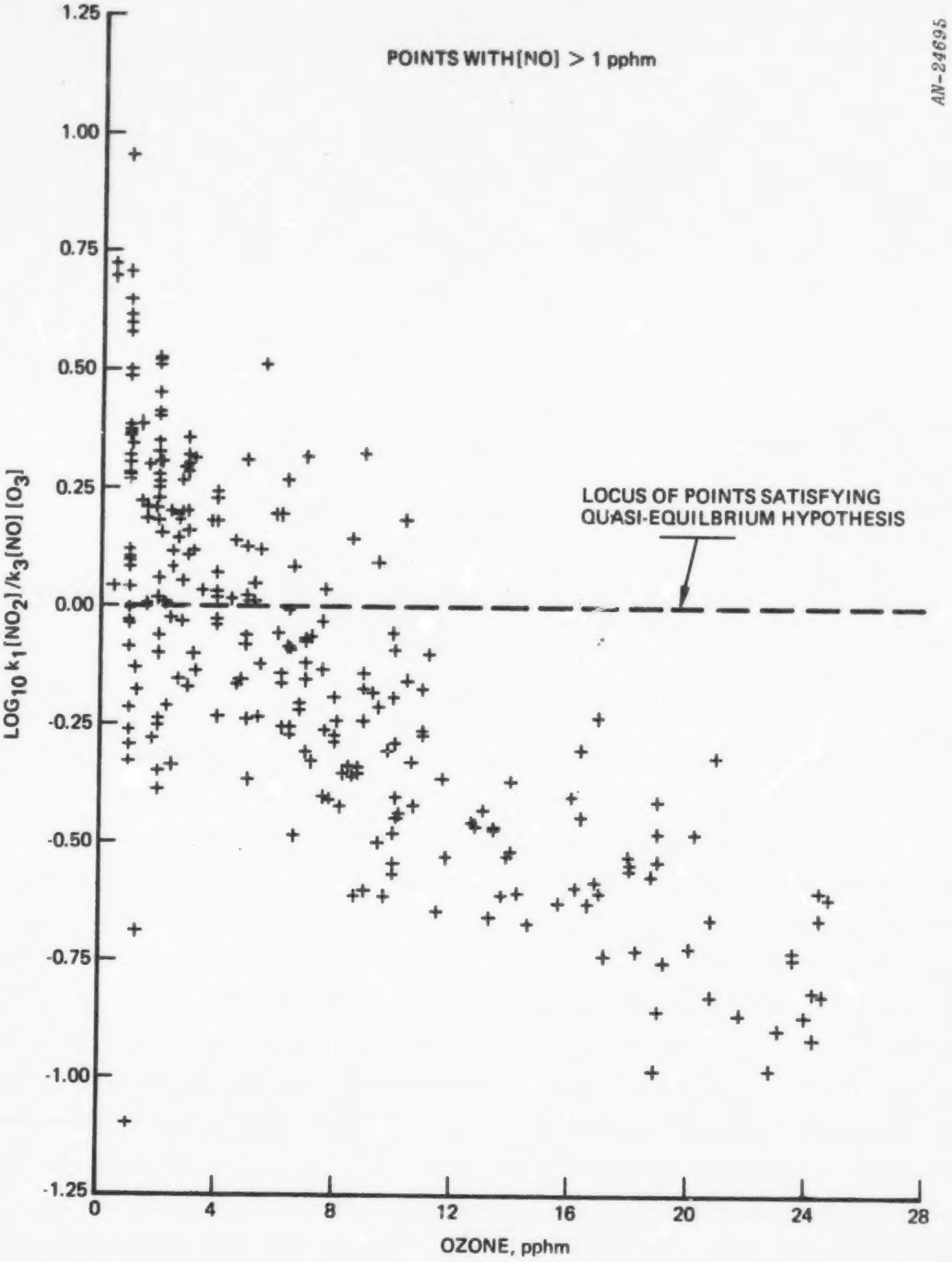

Figure A.4. Quasiequilibrium Test for 1969 Ground Data at El Monte--High NO Levels

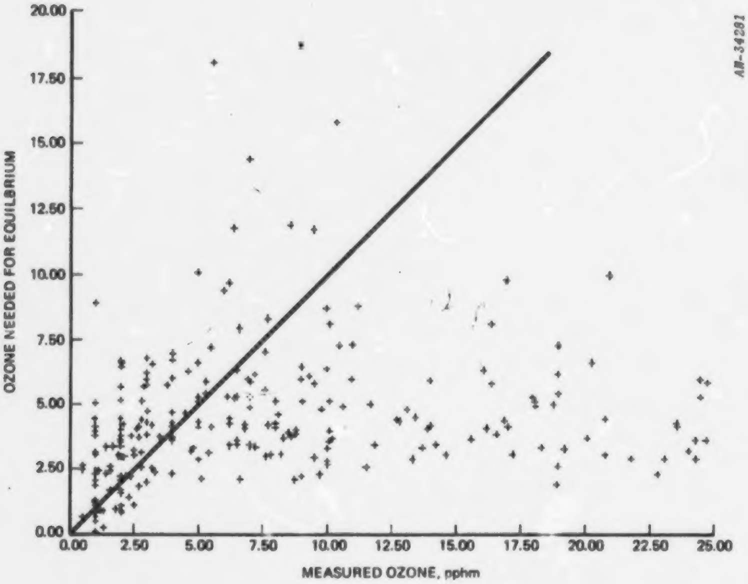

Figure A.5. Ozone Inaccuracies Needed to Explain the Departures from Quasiequilibrium in Figure A.4

To determine the effect of competing reactions, we used a 14-reaction, 10-species model of photochemical smog. As reported in previous work,[24,13] the computed concentrations simulated accurately the experimental work of Altshuller, et al.[45] Using the results of this simulation, we computed the ratio $k_{11}[NO_2]/k_{13}[O_3][NO]$ with the rate constants fixed at $k_{11} = 0.4\ min^{-1}$ and $k_{13} = 0.4\ pphm^{-1}\ min^{-1}$. A plot of the logarithm of the ratio versus ozone concentration is shown in Fig. A.6. It [illegible] apparent that the ratio is different from unity and that the departure increases with increasing ozone. However, the maximum value of the logarithm is only 0.04, indicating that the ratio is very close to unity compared with the atmospheric deviations shown previously. It seems reasonable to conclude from this that the interference from other reactions is negligible and that O_3, NO, and NO_2 closely approach quasiequilibrium under the static conditions that prevail in a smog chamber.

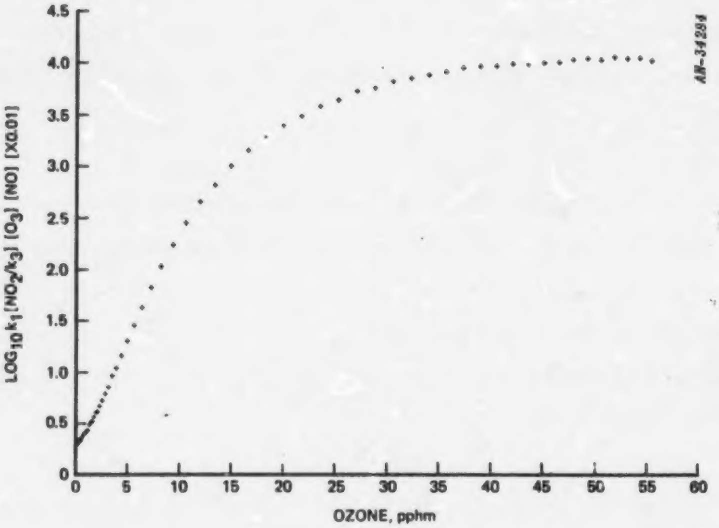

Figure A.6. Quasiequilibrium in a Simulated Smog Chamber Experiment

---

In Fig. A.6, it should also be noted that the trend away from equilibrium is in a different direction from that found in the Los Angeles data (Fig. A.4). This may be significant inasmuch as it implies an excess of NO_2 and a deficiency of NO and O_3. We are well aware that this effect could be due to the model. Nevertheless, if the effect is accepted as real, this implies that what was observed under atmospheric conditions is probably not due to interfering reactions. This is in agreement with a statement by Schuck and Stephens,[46] who claim that quasiequilibrium holds in the presence of competing hydrocarbon reactions inasmuch as the rates for these reactions are very low. However, they go on to claim that quasiequilibrium holds in the Los Angeles atmosphere, but offer no evidence to support their assertion. Finally, we note that the pair of reactions

$$NO_2 + O_3 \rightarrow NO_3 + O_2$$

$$NO + NO_3 \rightarrow 2NO_2$$

suggested by Leighton[42] as likely candidates for interference, would produce results that contradict the data of Fig. A.4. In fact, these reactions would perturb quasiequilibrium in the direction indicated in Fig. A.6.

The above arguments are based on the premise that the smog chamber experiment represents the principal chemical processes that really occur in the atmosphere. Many more known (as well as unknown) chemical interactions take place in urban air and thus it is always possible that some reactions may be interfering with the $O_3/NO/NO_2$ cycle in a manner which produces the observed results.

It is apparent from Eq. A.19 that turbulent fluctuations have the effect of modifying the rate of reaction (A.13). The apparent validity of the quasi-equilibrium hypothesis is going to be affected if we use the product of time-averaged concentrations instead of the time average of the product of concentrations. This notion is in agreement with Leighton's caveat about the effect on stationarity of rapid changes in concentration.

Having identified the turbulence interference problem in air pollution modeling, let us now consider some methods of attacking it. To provide further insight into the problem, experimental data like those shown in Figs. A.3 and A.4 must be obtained simultaneously; namely, time-resolved concentrations of O_3, NO, NO_2, temperature, and ultraviolet input.

The monitoring station should be located at each of two types of urban environment: one in an area dominated by distributed transportation emission sources and another generally downwind from intense nitric oxide sources). The first provides low fluctuation tests and the second, high fluctuation tests. The data obtained in such a program would provide direct evidence as to whether the apparent deviations from quasiequilibrium were due to fluctuation interferences. Diagrams like Fig. A.4 could be constructed both from time-averaged reaction rates and from rates derived from time-averaged concentrations. Comparisons would test explicitly the hypotheses advanced above.

Another phase of needed experimental research must be done in the laboratory. Its objective is the construction of a theoretical approach for inclusion of rate corrections in computer simulation models. The method of attack in the experiment must be designed to yield fundamental information on turbulent flow reaction rates. Thus it must incorporate a well-understood (necessarily simple) reaction system in a controlled turbulent mixing process such that reaction-time/mixing-time ratios are adjustable and near unity. This difficult set of specifications is being approached in an experiment in progress at TRW Systems under the direction of R. G. Batt.[47] It involves the N_2O_4 dissociation reaction in a free shear layer in a low speed wind tunnel. Optical probes are employed for concentration measurements in addition to conventional aerodynamic instrumentation. Other tunnel experiments for studying the effect may also be conceived. An expected end result of the experiment is a measure of steady concentration fields and velocity fields as well as the ensemble of turbulent statistical properties.

Theoretical treatments based on both the field and lab findings must be undertaken in parallel in order to give model modifications that account for any mixing interferences with chemical reactions. Theoretical interpretation of the laboratory experiments will give a detailed treatment of a reactive plume mixing into a background flow under steady conditions. Coupled with the flow field through time-averaged velocity and concentration is a fluctuation budget equation like

$$\frac{\partial f_i}{\partial t} = \frac{\partial}{\partial z}\left(D_f \frac{\partial f_i}{\partial z}\right) + D\left(\frac{\partial c_i}{\partial z}\right)^2 - \varepsilon_i \qquad \text{(A.21)}$$

where $f_i = \bar{c}_i'^2$, the mean square fluctuation of species i

D_f = A diffusion coefficient for fluctuation transport

D = Turbulence diffusivity

ϵ_i = Dissipation of fluctuations

This equation for total fluctuation content might incoporate the statistical approaches of Bugnolo[48] and Corrsin[49-51] in integrated forms. It holds for a reaction that is second-order in species i . As an approximation, one might assume $D_f \sim D$. The dissipation term consists of two components, one due to diffusive smearing of fluctuations[52] and another due to reactive destruction of fluctuations.[51] We can approximate these by

$$\epsilon_i \sim 12 \frac{D_m}{\lambda_i^2} f_i + 4k_i \bar{c}_i f_i \qquad \text{(A.22)}$$

which expresses the two effects respectively with its two terms. The new symbols are defined as follows:

D_m = Molecular diffusivity

λ_i = Microscale of concentration fluctuations

k_i = Second-order reaction rate constant for ith species

Application of Eq. A.21 to the laboratory results will show how chemical dissipation of species fluctuations is influenced by chemistry. This effect then feeds into the equations for mean concentrations through the reaction rate terms (e.g., Eq. A.19). The validity of the theoretical approach can be checked by computer modeling of the mean and fluctuating concentrations in the experiment. A key aspect of this validation procedure is a knowledge of the transport and reaction coefficients. Consequently, it is essential to keep both the chemical system and the flow field as simple as possible rather than to attempt to construct a physical scale model of an urban airshed.

Applications of the research findings in air pollution simulation models will require considerable simplification because inadequate knowledge of coefficients and complexities of geometry make an elegant treatment inadvisable; however, the research is needed to tell us where the approximations are valid. Quantitative implementation of rate corrections can take the form of gross parameters like a plume gradient criterion to tell when a correction is needed and a mixing delay time that is a function of scale length and velocities. The mixing delay time in turn can be introduced into a correction factor that is formally applied in the chemical rate portion of the simulation logic.

All of the details of these formulations are yet to be worked out; hence, it seems imperative that this be investigated in the immediate future. The large discrepancies observed between our notions of the inorganic kinetics and the observations cannot be ignored. Until their sources are discovered and rectified in the simulation models, it seems unwise to mount extensive validation efforts that repeatedly apply existing approaches to more and more time-averaged air quality data.

A.3 SYSTEMS IMPLEMENTATIONS OF PHOTOCHEMICAL/DIFFUSION MODELS

A.3.1 Few Runs/High Fidelity

For evaluation studies of emission source contributions, the influence of specific control measures can be determined by running only a few simulations. This approach yields the marginal decrease in air quality ascribable to a particular emitter and, therefore, indicates what marginal improvements might be bought by imposing controls. Most frequently this type of inquiry is served adequately by the simulation of relatively few pollution scenarios. Choices from an array of technological alternatives for controls will be the result of these simulations; therefore, the model should have high fidelity for this application.

An example of the "few runs/high fidelity" mode of air quality simulation is our study of the influence of morning vehicle start emissions on photochemical smog.[13] We sought the answer to the question "What degradation of air quality is directly ascribable to motor vehicles starting up in the morning?" Despite many statements to the contrary, the answer is not merely the fractional emissions due to cold starts. Diffusion and chemistry introduce non-linearities which preclude simple scale-up. To investigate the air quality effects, we ran simulations with and without starting emissions.

The model was used with aerometric data from the Los Angeles basin to study the buildup of air pollution as it is affected by starting emissions. The procedure relates meteorological factors, time/space traffic distributions, and ultraviolet solar radiation with the photochemical atmospheric mechanisms involved in air pollution. (Averaging over the dailv activities of motor vehicles may not give an adequate description of the most severe conditions.)

Table A.4 shows two of the main findings from the simulation. First, that air quality effects vary with pollutant and, second, that

TABLE A.4

AIR QUALITY EFFECTS FOR 1974 TRAJECTORY

(Ratios of concentration with cold-start to concentration without cold-start)

Time	Species	Spatially Uniform Start Distribution	Decentralized Start Distribution
1400 hours	O_3	1.039	1.042
1400 hours	NO_2	1.024	1.026
Peak	CO	1.125	1.136

the geographical distribution of starts has no significant effect. (The density of morning starts for the nonuniform cases was assumed to be three times as high at the outer edge of populated areas as it was at the Federal building downtown varying linearly in a radial direction.) The numerical comparisons drawn from the table depend on the fidelity of the model. Some significance can be attached to the larger effect on peak CO than that on photochemical pollutants. The combined action of reaction and diffusion attenuates the start-effect for O_3 and NO_2 . These patterns emerged after only a very few simulations were carried out.

A.3.2 Moderate Number of Runs/Moderate Fidelity

Studies of local problems over a wide range of conditions demand more runs than the example described above. On the other hand, the reduction in scale from regional to local permits us to use a less detailed physical and chemical formulation from a simplified version of the photochemical/diffusion model. Exemplifying this type of approach is the analysis of air quality impact for a proposed high-capacity roadway. The larger number of cases arises from a multiplicity of factors derived from a many-dimensioned parameter space. For several miles of roadway near an urban area, background source intensity and receptor sensitivity might both vary widely. Hourly traffic loadings change sharply from hour to hour and meteorological conditions can exhibit large seasonal variations. Every year, the emission characteristics of the vehicle population are altered by the replacement units that have current control systems. Finally, the impact of the roadway can be fairly assessed only if we simulate the route corridor with the facility and compare this with the alternative of traffic diversion over the surrounding network of surface streets. Indeed, these variations of parameters multiply into literally hundreds of specific cases.

An example of a reduced-fidelity model suitable for this task is LAPS,[*] a code that we have recently developed and put into operation. The key simplification leading to the efficiency features of the model is the choice of coordinate system. The Lagrangian frame of reference is chosen so that the downwind distance coordinate is replaced with time, with air parcels traced through a streamline system. This coordinate system is illustrated in Fig. A.7. Streamline curvature can be neglected in the local areas of freeways; hence, for the free flow above the roadway, the air parcel representations are planar control surfaces moving along streamlines. Each control surface that sweeps with the wind along the streamlines has superimposed upon it a spatial grid. This grid consists of intervals in the vertical and crosswind directions. Finite-difference methods are used for the vertical diffusion differential equations. In particular, the Crank-Nicolson technique is employed. For diffusion in the lateral direction, Gaussian dispersion is employed. Horizontal diffusion, therefore, is treated as an algebraic correction that runs concurrently with the finite-difference solutions of the vertical diffusion equations, permitting spatial variation of the vertical diffusion coefficient. An optional feature of LAPS is the inorganic portion of the smog chemical mechanism involving the $NO/O_3/NO_2$ cycle. With two dimensional diffusion and limited chemistry, LAPS is considerably faster running than our regional code DIFKIN.[**]

---

[*] Local Air Pollution Simulator.

[**] DIFfusion and KINetics.

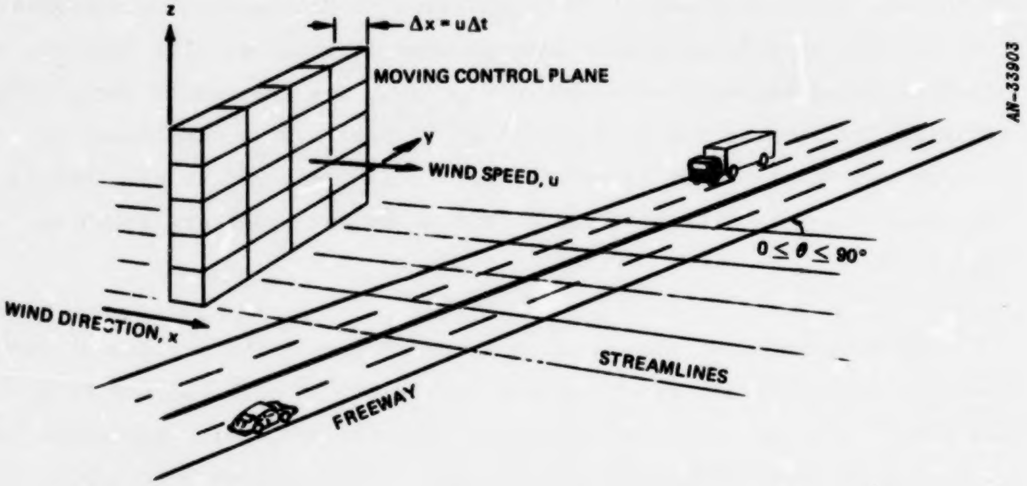
z
Δx = uΔt
MOVING CONTROL PLANE
y
WIND SPEED, u
0 ≤ θ ≤ 90°
WIND DIRECTION, x
STREAMLINES
FREEWAY
AN-33903

Figure A.7. LAPS Coordinate System

Inputs to the program consist of wind direction, wind speed, vertical and horizontal diffusion parameters and the whole set of descriptors that characterize emission sources. Output values of concentrations as functions of time are obtainable by specifying what receptor locations are of interest. For example, in a particular environmental impact study, the concentration on a nearby school playground might be desired. If that were the case, the model could give a history of concentration at that location.

Stagnant conditions are calculated by determining the dispersion from the roadway under zero wind (but not zero diffusion). This is done by centering the mesh on the roadway and computing the pollutant spread in a plane normal to the road centerline.

A set of three typical cases serves to demonstrate the capability of the GRC model to simulate the dispersion of nonreacting pollutants in the vicinity of a freeway with various wind directions. The freeway, a six-lane depressed section shown in Fig. A.8, was assumed to carry 100,000 vehicles/day. Using the geometry shown in Fig. A.9, a wind speed of 1.3 mph was simulated at angles (θ) of 0°, 30°, and 90° to the roadway. The resulting CO distributions predicted by the model are shown in Fig. A.10.

As an example of the speed of the LAPS model, the problem of computing the CO concentration at 100 points in a vertical plane normal to a freeway for 8 hours of real time required 3 minutes of central-processor time on a Control Data 6400 computer. The computation interval for this problem was 0.1 minute; the output intervals were 1 minute for ground concentration profiles and 30 minutes for vertical data maps.

To illustrate how the fidelity of the model captures the ozone-depression effect near a freeway, we can examine the same input conditions as above for a one mile per hour crosswind. Background levels are chosen to be typical of the Los Angeles basin well into a midsummer day. Figure A.11 shows the reduction in ozone as the nitric oxide from the vehicles mixes in and feeds the $NO + O_3 \rightarrow NO_2 + O_2$ reaction. Downwind of the roadway, ambient air dilutes the emissions with air containing a higher level of ozone. Consequently, the nitric oxide decreases back down to a level near ambient.

Since the chemistry is handled by a simple algorithm based on quasi-stationary state, this technique is suitable for running the many cases we will encounter for future problems of air quality impact evaluations. Turbulent mixing effects of vehicle wakes are treated internally by aerodynamic formulas for the locally enhanced diffusion coefficients. Source geometries are not restricted to roadways. Airports, central power stations and other source concentrations can also be treated as inputs to the LAPS code.

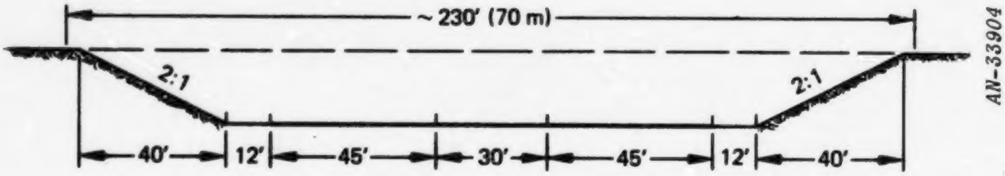
~ 230' (70 m)
2:1
2:1
40'
12'
45'
30'
45'
12'
40'
AN-33904

Figure A.8. Cross Section of Depressed Six-Lane Freeway

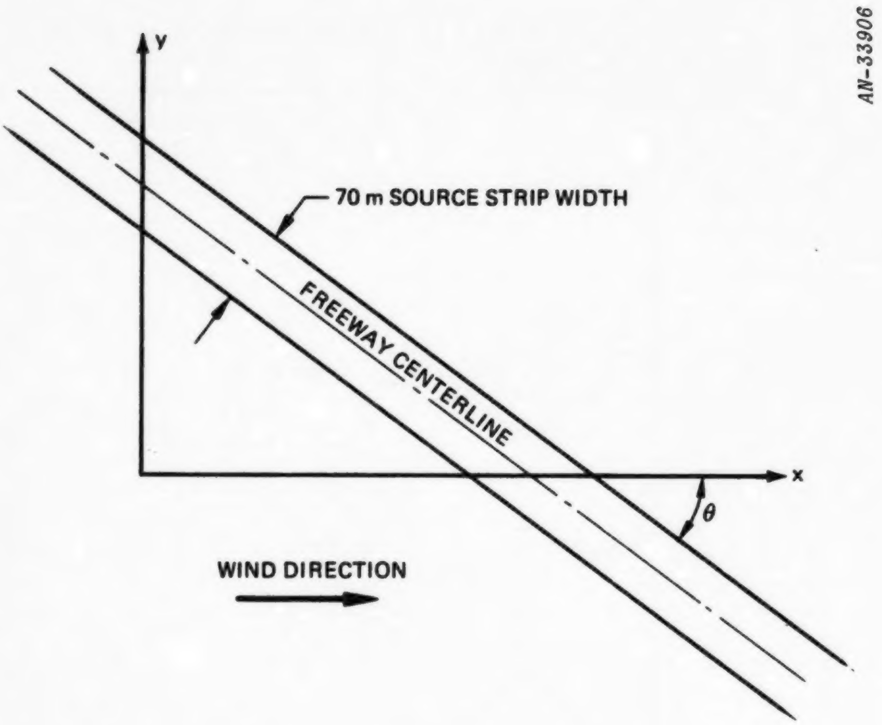
AN-33906
y
70 m SOURCE STRIP WIDTH
FREEWAY CENTERLINE
x
θ
WIND DIRECTION

Figure A.9. Wind-Oriented Coordinate System

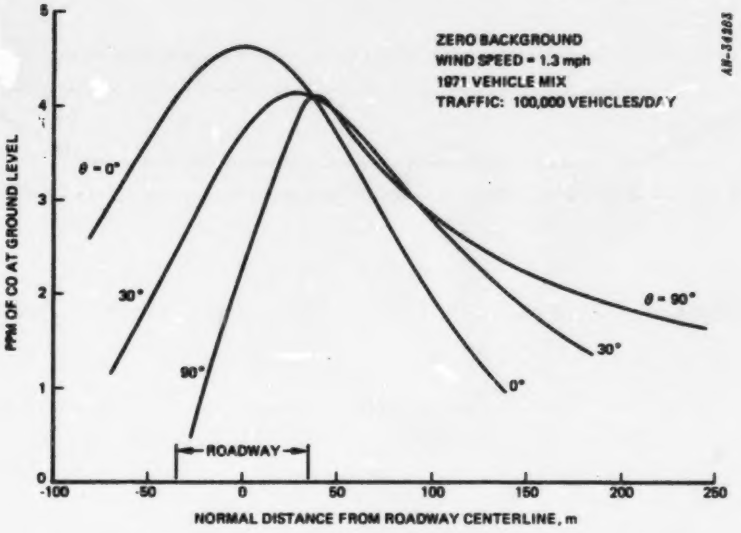

Figure A.10. CO Concentration Profiles Normal to Roadway at Various Wind Aspect Angles

---

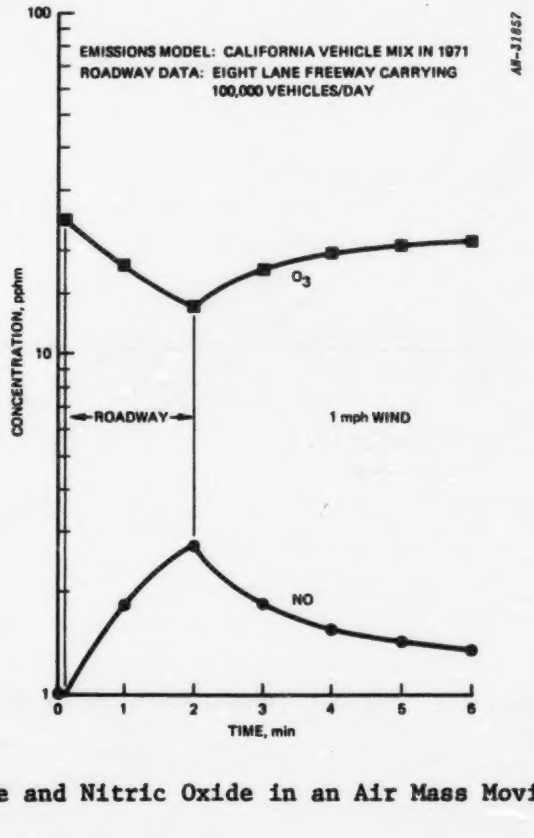

Figure A.11. Ozone and Nitric Oxide in an Air Mass Moving Over a Roadway

A.3.3 Many Runs/Low Fidelity

The deeper we penetrate into future problems of pollution abatement, the more respect we gain for the sometimes subtle, but tightly coupled problems of economic externalities and political realities. Staggering social costs are now beginning to appear on the horizon as the burden we must bear to improve the environment. The job of standard-setting, which has nearly run through its first round, only sets quantitative targets in this quest for better air and water quality. Actions to achieve the goals result in multiple feedbacks of money and material, that may either damage or benefit humanity depending on what value system we adopt.

Models such as the Implementation Planning Program[53] have endeavored to relate all of these factors for the steps needed to improve air quality. Since the air pollution simulation is only a small part of an ensemble of logical functions, it must, of necessity, be highly simplified. The sacrifice of fidelity in these applications is believed to be well justified by the need for many runs. For its scope (particulates and SO_2 from stationary sources) and for the limited availability of data, the IPP simulation did an admirable job of laying out the significant issues. Its weaknesses highlighted the specific needs for better quantitative information, particularly in the area of damage assessment and the inclusion of mobile sources.

Future models of this type will need chemistry in the air module because nearly all pollutants of interest are reactive. Refined cost figures will be needed in the economic modules to reflect advances in control technology. Aggregate damage indices may be incorporated in the form of summations or in integrals such as

$$D_{ij} = \iint \rho_j(x,t)\,\Phi_i(c_i)\; d\sigma\; dt$$

where D_{ij} = damage index due to the ith species acting on the jth type of receptor

ρ = population density of jth receptor

Φ_{ij} = impact function for ith species on jth receptor

c_i = concentration of ith species

x = location

t = time

σ = area

This will be an objective index that goes beyond the mere question "Does it or does it not exceed ambient standards?" It can be tied to ambient standards by normalizing the impact function. Say, for example that the impact of pollutant i on receptor j goes up like the nth power of c_i so that the expression

$$\Phi_{ij} = (c_i/c_{is})^n$$

permits a comparative assessment of all species if c_{is} is the ambient standard. Contributions can be collected by forming a total damage on receptor j by summing all of the D_{ij} over all i.

Now the use of this index in systems analysis requires a model that spreads over all of the receptors, not just a few monitoring stations. An important feature of future work will be reducing the three-dimensional, time-dependent air pollution simulations to a usable size. One key to this reduction lies in a "black box" chemical model. The black box functions in a chemical sense like the Maxwell Demon operates in the kinetic sense; i.e., while the Demon sorts out molecules in a certain energy range, the black box converts NO molecules to NO_2 molecules in photochemical smog according to the hydrocarbon decomposition products that are present. The black box transfer function will need parameters depending on reactivity, HC/NO_x ratio and, perhaps, temperature, humidity, and aerosol levels. The function, which must be obtained from curve fits of extensive kinetics simulations, will replace a dozen or more coupled differential equations. If the Lagrangian fluid dynamic frame is retained in the systems model, this simplification is essential, since many, many, simulations will be required to supply values for the integrand of D_{ij} over an urban region.

Future applications of this simplified air quality model will find it coupled with economic input/output models, transportation network simulations, land use models, and energy managment models (possibly all at the same time). Of course if this line of development is allowed to grow unchecked, it invariably leads into the fantasy world of some systems analysts who are unafraid to take on the universe.

Pollution abatement strategies are limited more by human institutions and resources than by technological advances. Thus, an important class of future problems in simulation will involve live participants in the loop. Invariably, actual decisions on incremental changes take directions other than those selected by system optimization procedures. This happens because the latter procedures are incomplete with respect to variables and constraints. With people operating in a simulated abatement scenario, the quantitative models are used as feedback generators, but they do not control the action. This application of gaming has been instituted in the APEX and CITY exercises already under evaluation by the Environmental Protection Agency. They will serve as training devices as well as testbeds for policy experiments.

The usefulness of these games will depend heavily on the credibility of the feedback models that tell the decision maker how much his decision costs and what effects it will have in many sectors including that of environmental quality. Nevertheless, these models must simulate many alternatives rapidly to enhance the value of the game even if it must be at the expense of some fidelity.

A.4 SUMMATION

Tight implementation schedules and tough regulations have been laid out to abate pollution. The urgency of policies already adopted has led to hasty actions in some cases. It is imperative that the research community concentrate on some of the ill-defined areas that may contain the key elements of understanding the consequences of air pollution control decisions.

Mathematical simulation models at the very least provide a logical framework that highlights the unknowns. At the most, they will serve as predictive tools in evaluating the impact of rulemaking and decision-making. As we have moved into the science of air pollution simulation, we have discovered some serious deficiencies in present-day approaches. The neglect of heterogeneous processes omits possibly the most important cleanup processes for oxides of nitrogen. Unexplained shifts in HC/NO_x ratios are observed in morning air samples. The largest discrepancies occur on the worst smog days. Turbulent chemical kinetics are untouched in contemporary simulation approaches. These effects may well be responsible for apparent shifts several hundred percent away from quasiequilibrium states believed to govern the major pollutants, ozone and oxides of nitrogen in urban environments.

This paper has assembled some suggestions for the attack on each problem. These attacks are based on systematic gathering of observational evidence followed by careful data analysis feeding into refinements or corrections to the simulation models. Unfortunately, many uses will be demanded of the models before these issues are faced. Some of the expressions derived in the preceding sections will serve at least as criteria for setting rough levels of confidence in existing models. The urgency of the problems at hand must be used as a stimulant for the needed research rather than an excuse to overlook the deficiencies in our present understanding of the problems.

With the mature development of certain air quality simulation techniques, a hierarchy of models will emerge embracing a wide range of fidelity levels. The large variety of applications anticipated places demands on operating speed in some cases while other cases are characterized by needs for precision in certain types of predictions. The examples cited in the closing section highlight these differences.

Despite consultant advertising that touts "complete modeling capabilities for air pollution simulation," we can still see some exciting possibilities for new research. This new work will fill significant voids in the basic fiber of which the "complete" models are made. But simply building models is not enough. They must be molded into useful forms by creating special algorithms, by inventing approximations, by designing input/output structures that meet the dynamic demands of air quality management.

REFERENCES

1. A.Q. Eschenroeder and J.R. Martinez, Concepts and Applications of Photochemical Smog Models, General Research Corporation TM-1516, June 1971 (to be published as an ACS Monograph in Advances in Chemistry).

2. A.P. Altshuller and J.J. Bufalini, "Photochemical Aspects of Air Pollution: A Review," Photochemistry and Photobiology, Vol. 4, 1964, pp. 97-146.

3. A.P. Altshuller and J.J. Bufalini, "Photochemical Aspects of Air Pollution: A Review," Environmental Science and Technology, Vol. 5, No. 5, January 1971, pp. 39-64.

4. K. Westberg and N. Cohen, The Chemical Kinetics of Photochemical Smog as Analyzed by Computer, AIAA Third Fluid and Plasma Dynamics Conference Paper No. 70-753, Los Angeles, June 29-July 1, 1970.

5. T.A. Hecht and J.H. Seinfeld, "Development and Validation of a Generalized Mechanism for Photochemical Smog," Env. Science and Technology, Vol. 6, No. 1, January 1972, pp. 47-57.

6. H. Niki, E.E. Daby and B. Weinstock, "Mechanisms of Smog Reactions", Advances in Chemistry, 1972 (in press).

7. D.H. Stedman, E.D. Morris, Jr., E.E. Daby, H. Niki, and B. Weinstock, The Role of OH Radicals in Photochemical Smog, American Chemical Society Division of Water Air and Waste Chemistry, Chicago, Illinois, September 13-18, 1970.

8. J.R. Holmes, A.D. Sanchez, and A.H. Bockian, Atmospheric Photochemistry: Some Factors Affecting the Conversion of NO to NO_2, Pacific Conference on Chemistry and Spectroscopy, San Francisco, October 6-9, 1970.

9. B.W. Gay and J.J. Bufalini, "Nitric Acid and the Nitrogen Balance of Irradiated Hydrocarbons in the Presence of Oxides of Nitrogen," Environmental Science and Technology, Vol. 5, No. 5, May 1971, pp. 422-425.

10. M. Dodge, private communication, May 26, 1972.

11. M. Dodge, private communication, July 11, 1972.

Preceding page blank

12. P.L. Hanst, "Mechanism of Peroxyacetylnitrate Formation", *J. Air Pollution Control Association*, Vol. 21, No. 5, May 1961, pp. 269-271.

13. J.R. Martinez, R.A. Nordsieck, and A.Q. Eschenroeder, *Morning Vehicle-Start Effects on Photochemical Smog*, General Research Corporation CR-2-191, June 1971.

14. F. Stuhl, private communication, Ford Motor Co., Scientific Research Staff, June 1, 1972.

15. J. Anderson, private communication, University of Pittsburgh, June 7, 1972.

16. E.A. Sutton, "Chemistry of Electrons in Pure-Air Hypersonic Wakes," *AIAA Journal*, Vol. 6, No. 10, October 1968, pp. 1873-1882.

17. K. Schofield, "An Evaluation of Kinetic Rate Data for Reactions of Neutrals of Atmospheric Interest," *Planetary and Space Sciences*, Vol. 15, 1967, pp. 643-670.

18. P.A. Leighton, *Photochemistry of Air Pollution*, New York Academic Press, 1961.

19. G. Schott and N. Davidson, "Shock Waves in Chemical Kinetics: The Decomposition of N_2O_5 at High Temperatures," *Journal of American Chemical Society*, Vol. 80, p. 1841 (1958).

20. S. Jaffe and H.W. Ford, "The Photolysis of Nitric Acid at 3660Å and 25°," *Journal of Physical Chemistry*, Vol. 71, p. 1832 (1967).

21. W.R. Greiner, "Hydroxyl Radical Kinetics VI., Reactions with Alkanes in the Range 300°-500°K, *J. Chem. Phys.*, 53, 1970, pp. 1070-1076.

22. J. Heicklen, K. Westberg, and N. Cohen, *The Conversion of NO to NO_2 in Polluted Atmospheres*, Pennsylvania State University Center for Air Environment Studies Publication 115-69, July 1969.

23. K. Westberg, N. Cohen, K.W. Wilson, "Carbon Monoxide: Its Role in Photochemical Smog Formation", *Science*, Vol. 171, March 12, 1971, pp. 1013-1015.

24. A.Q. Eschenroeder and J.R. Martinez, *Further Development of the Photochemical Smog Model for the Los Angeles Basin*, General Research Corporation CR-1-191, March 1971.

25. A.P. Altshuller, "An Evaluation of Techniques for the Determination of the Photochemical Reactivity of Organic Emissions", *JAPCA*, Vol. 16, No. 5, May 1966, pp. 257-260.

26. A.Q. Eschenroeder and J.R. Martinez, Analysis of Los Angeles Atmospheric Reaction Data from 1968 and 1969, General Research Corporation CR-1-170, July 1970.

27. A.Q. Eschenroeder and J.R. Martinez, Mathematical Modeling of Photochemical Smog, General Research Corporation IMR-1210, December 1969. Also a paper presented at the AIAA Eighth Aerospace Sciences Meeting, January 1970.

28. J.K. Angell, D.H. Pack, L. Machta (R. Dickson, and W.H. Hoecker), "Three-Dimensional Air Trajectories Determined from Tetroon Flights in the Planetary Boundary Layer of the Los Angeles Basin", Journal of Applied Meteorology, Vol. 11, No. 3, April 1972, pp. 451-571.

29. M.A. Estoque, "A Numerical Model of the Atmospheric Boundary Layer", Journal of Geophysical Research, Vol. 68, 1968, pp 1103-113.

30. C.R. Hosler, "Vertical Diffusivity from Random Profiles", Journal of Geophysical Research, Vol. 74, No. 28, December 20, 1969, pp. 7018.

31. A.Q. Eschenroeder and J.R. Martinez, A Modeling Study to Characterize Photochemical Atmospheric Reactions to the Los Angeles Basin Area, General Research Corporation CR-1-152, November 1969, p. 18.

32. F. Pasquill, Atmospheric Diffusion, Van Nostrand, London, 1962.

33. J. Angell and D. Pack, "Mesoscale Diffusion Derived from Tetroon Flights", USAEC Meteorological Information Meeting, Atomic Energy of Canada Limited, Chalk River, Ontario, AECL-2787, September 1967.

34. P. Roberts, P. Roth, and C. Nelson, Contaminant Emissions in the Los Angeles Basin--Their Sources, Rates, and Distributions, Systems Applications, Inc., Report 71 SAI-6, March 1971 (Appendix A).

35. Final Report on Phase I, Atmospheric Reaction Studies in the Los Angeles Basin, Vols. I and II, Scott Research Laboratories, June 30, 1969.

36. F.L. Ludwig, A.E. Moon, W.B. Johnson, R.L. Mancuso, A Practical Multipurpose Urban Diffusion Model for Carbon Monoxide, Stanford Research Institute, September 1970.

37. L. Aldaz, "Flux Measurements of Ozone Over Land and Water," Journal of Geophysical Research, Vol. 74, No. 28, December 20, 1969, pp. 6943-6946.

38. R.E. Inman, and R.B. Ingersoll, "Note on the Uptake of Carbon Monoxide by Soil Fungi," Journal of the Air Pollution Control Association, Vol. 21, No. 10, October 1971, pp. 646-647.

39. F.B. Abeles, L.E. Craker, L.E. Forrence, and G.R. Leather, "Fate of Air Pollutants: Removal of Ethylene, Sulfur Dioxide and Nitrogen Dioxide by Soil," Science, Vol. 173, No. 4000, September 3, 1971, pp. 914-916.

40. L.A. Ripperton, and F.M. Vukovich, "Gas Phase Destruction of Tropospheric Ozone," Journal of Geophysical Research, Vol. 76, No. 30, October 20, 1971, pp. 7328-7333.

41. D.A. Lundgren, "Atmospheric Aerosol Composition and Concentration as a Function of Particle Size and of Time," Journal of the Air Pollution Control Association, Vol. 20, No. 9, September 1970, pp. 603-608.

42. J. Cholak, L.J. Schafer, D.W. Yaeger, and R.A. Kehoe, "The Nature of the Suspended Matter," Chapter VIII in Air Pollution Foundation Report No. 9, An Aerometric Survey of the Los Angeles Basin, August-November 1954.

43. P.A. Leighton, and W.A. Perkins, Photochemical Secondary Reactions in Urban Air, Air Pollution Foundation Report No. 24, August 1958.

44. E. Daby, Ford Motor Company, private communication. (Full results to be published in Journal of Air Pollution Control Association, Vol. 22, No. 4, April 1972.)

45. A.P. Altshuller, S.L. Kopczynski, W.A. Lonneman, T.L. Becker and R. Slater, "Chemical Aspects of the Photo-oxidation of the Propylene-Nitrogen Oxide System," Environmental Science and Technology, Vol. 1, No. 11, November 1967, pp. 889-914.

46. E.A. Schuck and E.R. Stephens, "Oxides of Nitrogen," Advances in Environmental Sciences, Vol. 1, New York, John Wiley and Sons, 1969, pp. 73-118.

47. R.G. Batt, T. Kubota and J. Laufer, Experimental Investigations of the Effect of Shear-Flow Turbulence on a Chemical Reaction, AIAA Reacting Turbulent Flows Conference Paper, San Diego, June 1970.

48. D. Bugnolo, "Effects of a 'Mixing-in-Gradient' on the Spectrum of the Electronic Density in a Turbulent Weakly Ionized Gas," Journal of Geophysical Research, Vol. 70, No. 15, August 1965, pp. 3725-3734.

49. S. Corrsin, "Statistical Behavior of a Reacting Mixture in Isotropic Turbulence," Phys. Fluids, Vol. 1, No. 1, January-February 1958, pp. 42-47.

50. S. Corrsin, "The Reactant Concentration Spectrum in Turbulent Mixing with a First-Order Reaction," J. Fluid Mech., 1961, pp. 407-416.

51. S. Corrsin, "Further Generalization of Onsager's Cascade Model for Turbulent Spectra," Phys. Fluids, Vol. 7, No. 8, August 1964, pp. 1156-1159.

52. J. Hinze, Turbulence: An Introduction to Its Mechanism and Theory, McGraw Hill, New York, 1959, p. 224.

53. Air Quality Implementation Planning Program, TRW Systems Group SN11130, November 1970.